UNIVERSIDAD DE CANTABRIA

ESCUELA DE DOCTORADO DE LA UNIVERSIDAD DE CANTABRIA

DOCTORADO EN INGENIERÍA DE COSTAS, HIDROBIOLOGÍA Y GESTIÓN DE SISTEMAS ACUÁTICOS (IH2O)

TESIS DOCTORAL

Desarrollo de una metodología para obtener proyecciones de evolución de la línea de costa frente al cambio climático considerando diferentes escalas temporales y espaciales en un marco de incertidumbre

---

PhD THESIS

Development of a methodology to obtain climate change projections of coastline evolution considering multiple time and spatial scales in an uncertainty context

---

Presentada por:
Moisés Álvarez Cuesta

Dirigida por:
Prof. Iñigo J. Losada
Dra. Alexandra Toimil

SANTANDER, SEPTIEMBRE DE 2022

A mis padres y a mis abuelos

Agradecimientos

Quiero comenzar dando las gracias a mis directores de tesis, Iñigo Losada y Alexandra Toimil. Gracias Iñigo por haber puesto a mi disposición todos los medios necesarios para la realización de este trabajo, por haberme dado la oportunidad de iniciarme en la investigación y por tu generosidad. Gracias Alex por haber marcado el cauce de la tesis, por tu dedicación y por haber estado disponible en todo momento.

Es justo reconocer que el trabajo que aquí se recoge no hubiese sido posible sin la ayuda de mis compañeros de IHCantabria. Agradezco a Adrián Acevedo y a Héctor Lobeto su ayuda en temas de modelado y clima de oleaje. A Patricia González-Lamuño su gran apoyo durante los inicios en esta andadura. Mención especial merece mi amigo David Lucio, en cuyo modelo estadístico se apoya una parte de esta investigación. Igualmente, agradezco a Sheila Abad su inestimable ayuda a la hora de trabajar con información geográfica. Agradezco a todos mis compañeros de la planta dos los buenos momentos que hemos vivido dentro y fuera del Instituto.

Mi mayor reconocimiento es para mis padres, Soledad y Generoso, por ser los artífices de que haya llegado hasta aquí. Gracias por vuestro apoyo y amor sin condiciones y por vuestra infinita paciencia con mi muchas veces árido carácter. Gracias a mis abuelos, Paz y Blas, entre otras muchas cosas, por haber construido el cimiento sobre el que camino.

Tal y como recoge José Luis Borges en su obra, la poesía gauchesca, de la aplicación de la ley de la causalidad se sigue que el menor de los hechos presupone el inconcebible universo, e inversamente, que el universo necesita del menor de los hechos. Contextualizando la reflexión a este trabajo de investigación, son algunas más las personas que de una forma u otra han contribuido a que llegue este momento. Por ello, les estoy inmensamente agradecido, y espero que estas palabras sirvan como muestra de mi reconocimiento.

Resumen

Integrar los efectos del cambio climático en un problema de ingeniería de costas consiste en aplicar los métodos tradicionales basados en la física de los procesos o guiados por datos, pero con consideraciones adicionales por el hecho de desconocer los forzamientos futuros. En primer lugar, tener en cuenta la incertidumbre en las dinámicas futuras, con los recursos computacionales actuales, requiere de modelos eficientes que gestionen los cientos de simulaciones necesarias en marcos probabilísticos. En segundo lugar, la escala temporal del cambio climático implica ser capaz de modelar, en el largo plazo, todos los procesos costeros relevantes y sus interacciones. En tercer lugar, a pesar de la escala global del cambio climático, la adaptación tiene lugar en escalas regionales y locales que definen la extensión requerida por el modelado. Finalmente, la definición de una planificación efectiva implica evaluar el impacto en la costa de diferentes actuaciones basadas en soluciones naturales o grises. Por tanto, para apoyar la toma de decisiones y evaluar el riesgo asociado al cambio climático en la costa, se requieren metodologías y modelos confiables y eficientes capaces de simular la respuesta de las zonas costeras durante decenas de años, en escalas espaciales regionales y locales bajo múltiples escenarios climáticos posibles del futuro.

En este contexto, esta tesis doctoral pretende contribuir al estado del arte del modelado de la erosión e inundación en la costa considerando el cambio climático. Para ello, se desarrolla un marco para el análisis de impactos costeros que incluye un conjunto de herramientas, modelos y metodologías compatibles con los condicionantes impuestos por el cambio climático y orientados hacia una mejor estimación del riesgo y a al diseño de estrategias de adaptación efectivas. En primer lugar, se desarrolla un modelo de evolución de la línea de costa basado en la física de los procesos y enriquecido por datos. El modelo resuelve procesos longitudinales y transversales así como el efecto de intervenciones antrópicas en escalas de decenas de años y usa observaciones para ajustar automáticamente sus parámetros libres. El modelo es un híbrido entre los modelos puramente basados en la física, que confían en un conocimiento potencialmente incompleto del medio natural, y los modelos guiados por datos que se basan en la extrapolación del comportamiento observado. Una vez validado, el modelo se emplea para pronosticar la respuesta de un tramo costero fuertemente antropizado considerando la incertidumbre asociada al oleaje y al nivel del mar futuros. Del modelado se obtiene importante información para la gestión de la costa y la adaptación como el retroceso permanente, el área de playa perdida, la posición de la línea de costa durante la época estival, la contribución relativa de los diferentes procesos físicos a los cambios en la línea de costa y el retroceso extremo debido a tormentas. A continuación, se aborda el problema de la inundación costera desarrollando una metodología probabilística que integra las proyecciones de erosión. La metodología se fundamenta en dos pilares, un emulador de tormentas a escala regional y en la actualización del modelo digital del terreno presente considerando la erosión costera futura. Para esto último, las proyecciones de evolución de la línea de costa son trasladadas al modelo digital del terreno, empleado en el cálculo de la inundación, aplicando las reglas cinemáticas en perfil de los diferentes procesos modelados. El acoplamiento de la erosión y la inundación en la escala del cambio climático permite mejorar sustancialmente las proyecciones de riesgo

y evaluar la respuesta de la costa considerando los procesos de forma holística, de forma similar a como ocurre en la realidad. Finalmente, el modelo de evolución de la línea de costa se combina con el método de generación de la topobatimetría y un modelo avanzado de propagación del oleaje. Como resultado, se obtiene un modelo morfológico capaz de evaluar la evolución temporal de la costa en la mayoría de las playas de arena del mundo.

Abstract

Integrating the effects of climate change in any coastal engineering problem consists of implementing traditional physics- or data-driven methods applied in the field, but with additional considerations due to the unknown nature of the future drivers. First, accounting for uncertain forcings with present-day computational resources needs efficient models to manage the hundreds of simulations required in probabilistic frameworks. Second, the temporal scale at which climate change occurs implies being able to model, in the long-term, all the relevant coastal processes and their interactions. Third, in spite of the global nature of the climate change problem, adaptation plans take place regionally and locally, defining the extent of the modelling. Fourth, effective adaptation planning entails evaluating different nature-based and hard engineering interventions and their impacts on the coast. Therefore, reliable and efficient models capable of handling decadal simulations in regional and local spatial scales in natural and engineered coasts under multiple future climate scenarios are key for evaluating climate change-derived risks and to support informed decision-making.

In this context, this dissertation aims to make progress in the state of the art of coastal erosion and flood modelling considering climate change. To this end, a modelling framework that consists of a set of tools, models and methodologies fulfilling the conditions imposed by climate change and oriented to produce better risk estimates and designing effective adaptation strategies, is developed together with several conceptual advances. Firstly, a physics-based and data-enriched shoreline evolution model is built. The model solves longshore and cross-shore processes, the effect of engineering interventions at the decadal scale and uses observations to automatically calibrate its model parameters. The model is a hybrid between the physics-based approaches that rely on a potentially incomplete knowledge of the physical system and the data-driven models that produce forecasts based on the extrapolation of the past observed behaviour. Once the model is validated, it is used to forecast the shoreline evolution accounting for uncertain future waves and water levels at a highly anthropized coastal stretch. Relevant information for coastal planning and adaptation like the permanent coastline retreat, the area of beach loss, the tourist-season shoreline position, the relative contribution of individual physical processes to shoreline change and the extreme coastline retreat during storms are obtained. Coastal flooding is subsequently tackled and a methodology to develop erosion-enhanced probabilistic flooding projections is tuned up. The methodology relies on two pillars, a regional-scale storm emulator and a method to update the current digital terrain model to account for coastal erosion. To this end, shoreline projections are spatially upscaled to a digital terrain model used for flood modelling by applying simple profile kinematics associated with the individual shoreline change processes. Coupling flooding and erosion at the climate change scale allows to substantially improve risk analysis estimates and to evaluate the coastal response considering the different processes in a holistic way, similarly as it occurs in nature. Finally, the shoreline evolution model is combined with the method to update the topobathymetry and an advanced wave propagation model to generate a novel morphological model capable of reproducing the complete evolution of the nearshore at most of the sandy coastal settings worldwide.

CONTENTS

LIST OF FIGURES

LIST OF TABLES

LIST OF ACRONYMS

ADCIRC . . . . Advanced Circulation Model
ASMITA . . . . Aggregated Scale Morphological Interac-
    tion between Tidal inlets and the Adjacent coast

CA . . . . Coupling Approach
CERC . . . . Coastal Engineering Research Center
COCOONED . . . . Coupled Cross-shore, long-shore, and fore-
    dune Evolution model
CoSMoS-COAST . . . . Coastal Storm Modelling System, Coastal
    One-line Assimilated Simulation Tool
CT . . . . Cross-shore Transport
CNRM . . . . Centre Nationale des Recherches Météorologiques

DA . . . . Data Assimilation
DWS . . . . Dynamic Wave Set-up

FA . . . . Flooded Area

GCM . . . . Global Climate Model

EKF . . . . Extended Kalman Filter
EMODnet . . . . European Marine Observation and Data
    network

GEV . . . . Generalized Extreme Value function
GIS . . . . Geographic Information System
GOW . . . . Global Ocean Waves

HADG . . . . Hadley Centre
HR . . . . High Resolution

IGN . . . . Spanish National Geographic Institute (*In-
    stituto Geográfico Nacional*)
IH-LANS . . . . IH Long-term Anthropized coastlines Sim-
    ulation tool

IH-LANSloc . . . . IH Long-term Anthropized coastlines Simulation tool for local-scale studies

ISPL . . . . Institute Pierre-Simon Laplace

IPCC . . . . Intergovernmental Panel on Climate Change

LST . . . . Longshore Transport

LR . . . . Low Resolution

LT . . . . Long Term

MDM . . . . Multivariate Directional Model

MID . . . . Metamodel ID

MME . . . . Monthly-scale Multivariate Emulator

MITERD . . . . Spanish Ministry for the Ecological Transition and the Demographic Challenge (*Ministerio para la Transición Ecológica y el Reto Demográfico*)

MHL . . . . Mean High water Line

NMSE . . . . Normalized Mean Square Error

OECD . . . . Organisation for Economic Cooperation and Development

OTIS . . . . Oregon State University Tidal Prediction Software

PNOA . . . . National Plan for Airborne Orthophotography (*Plan Nacional de Ortofotografía Aérea*)

RANS . . . . Reynolds-Averaged Navier-Stokes

RCM . . . . Regional Climate Model

RCP . . . . Representative Concentration Pathway

RMSE . . . . Root Mean Square Error

RBF . . . . Radial Basis Function

RFSM-EDA . . . . Rapid Flood Spreading Model, Explicit Diffusion with Acceleration

ROMS . . . . Regional Ocean Modelling System

SCAPE . . . . Soft-Cliff and Platform Erosion

SLR . . . . Sea Level Rise

SROCC . . . . Special Report on the Ocean and Cryosphere in a Changing Climate of the IPCC

ST . . . . Short Term

SWAN . . . . Simulating Waves Nearshore

SWASH . . . . Simulating Waves till Shore

TB . . . . Topobathymetry

TWL . . . . Total Water Level

XBeach . . . . Extreme Beach model

LIST OF SYMBOLS

$\boldsymbol{G}$	Kalman Gain
g	Acceleration of gravity
γ	Depth breaking coefficient
γ_k	Geometric shape function at point k
h_r	Depth of the reef crest
H_s	Significant wave height
H_b	Breaking wave height
k	Wave number
K_c	Cross-shore transport coefficient
K_1	Longshore transport coefficient
K_e	Sediment bypass reduction coefficient
K_N	Bottom roughness length scale
K_t	Transmission coefficient
L	Wave length
$\boldsymbol{M}$	Offshore wave and water level properties
N	Wave action
N_v	Number of plant stems per square meter
$\boldsymbol{P}$	Process covariance matrix
$\boldsymbol{\Psi}$	State vector
Φ	Normal distribution
Q	Longshore transport
q	Sediment sink or source
Q_b	Percentage of breaking waves
$\boldsymbol{Q}$	Process noise matrix
$q_c(\eta)$	Cross-shore distribution of the longshore transport
R_{SLR}	Retreat due to SLR
R	Measurement error
ρ_s	Density of sediment
ρ	Density of water
SS	Storm surge
S_{tot}	Source terms in the wave action balance equation
σ	Relative frequency
T_p	Peak period
T_m	Mean period
$\tan \beta_n$	Nearshore slope
$\tan \beta_f$	Foreshore slope
$\tan \beta_s$	Surfzone slope

$T_{\boldsymbol{\theta} i}(\boldsymbol{\theta})$ . . . . Unimodal multivariate von Mises distribution

$\boldsymbol{TW}$ . . . . Transects to wave grid interpolation matrix

$\boldsymbol{U}$ . . . . Current velocity

vlt . . . . Unresolved processes trend

$\boldsymbol{WT}$ . . . . Wave grid to transects interpolation matrix

W_b^* . . . . Width of the breaking zone

ξ_p . . . . Iribarren's number

Y . . . . Shoreline position

Y_l . . . . Longshore shoreline position

Y_c . . . . Cross-shore shoreline position

CAPÍTULO 0

RESUMEN

0.1. Introducción

En este capítulo se presenta un resumen en castellano del documento original de tesis redactado en inglés. Este resumen condensa los principales resultados del trabajo de investigación y sus conclusiones. Para una información más detallada, se remite al lector interesado a la versión extendida en inglés.

0.1.1. Motivación y estado del arte

Las zonas costeras juegan un papel socio-económico relevante a nivel mundial ya que están densamente pobladas, albergan infraestructuras críticas y acogen intercambios económicos esenciales como el turismo, las pesquerías o el transporte marítimo. Actualmente, el 10 % de la población mundial vive en una estrecha franja por debajo de los 10 metros de elevación y esta tasa se espera que aumente en el futuro (Jones and O'Neill, 2016). Las proyecciones de población pronostican que el número de personas viviendo en las zonas costeras aumentará un 66 % en 2060 con respecto al año 2000, alcanzando 1,000[1] millones de personas (Neumann et al., 2015). Las zonas costeras son también

---

[1]A lo largo del documento, la coma se emplea como separador de miles y el punto como separador decimal.

importantes desde un punto de vista socioeconómico. En 2010, la economía global asociada al mar contabilizó un valor añadido de 1.5 trillones de dólares americanos con contribuciones relevantes de la extracción offshore de gas y crudo, del turismo costero y marítimo, de los equipamientos portuarios y marítimos y de los empleos en industrias ligadas al mar (Melet et al., 2020). En el futuro cercano (2030), la economía del mar experimentará un crecimiento que puede alcanzar los 3 trillones de dólares confiando en la extracción de combustibles fósiles y en el turismo (OECD, 2016). Por otro lado, los ecosistemas costeros son ricos en flora y fauna. Son uno de los más productivos del planeta gracias a las pesquerías y juegan un papel regulador y de protección esencial (Duarte et al., 2013; Narayan et al., 2016; Beck et al., 2018; Reguero et al., 2021).

A pesar de su importancia, las zonas costeras están amenazadas por la erosión y la inundación. A partir de 30 años de observaciones obtenidas a mediante de imágenes de satélite, Luijendijk et al. (2018) estimó que el 24 % de las playas de arena del mundo sufren erosión, mientras que la mayoría de los espacios costeros protegidos están en zonas necesitadas de aportes sólidos. Mentaschi et al. (2016) calculó a partir de información satelital que las pérdidas de terreno emergido entre 1984 y 2015 (28,000 km^2) doblaron al terreno ganado al mar y concluyeron que el factor humano es el principal causante del daño. Por otro lado, más de 100 millones de personas ocupan terrenos por debajo de las mareas vivas actuales (Kulp and Strauss, 2019) y la cantidad de población expuesta a eventos de inundación de baja tasa de recurrencia dobla esta cantidad (Dullaart et al., 2021). Los deltas, donde las aguas continentales se encuentran con las oceánicas, también están en riesgo. Syvitski et al. (2009) resaltó que durante la primera década del siglo veintiuno, el 85 % de los deltas experimentaron inundaciones severas fundamentalmente debidas a factores antrópicos, resultando en la inmersión episódica de 260,000 km^2.

En las próximas décadas, la erosión y la inundación continuarán el acoso a las zonas costeras de una forma más intensa debido al cambio climático (Nicholls and Cazenave, 2010; Ranasinghe, 2016; Collins et al., 2019). Los niveles medios del mar han ido aumentado durante el siglo pasado (Hay et al., 2015; Fasullo et al., 2016) y se espera

que sigan progresando alcanzando tasas sin precedentes durante las próximas décadas debido al calentamiento global (Kopp et al., 2014; Jevrejeva et al., 2016; Hermans et al., 2021). Adicionalmente, el cambio climático está aumentado la potencia del oleaje (Reguero et al., 2019) y alterando sus regímenes medio y extremal (Hemer et al., 2013; Lobeto et al., 2021a), las mareas meteorológicas (Little et al., 2015; Muis et al., 2020), la actividad de los ciclones tropicales (Bloemendaal et al., 2022; Gori et al., 2022) y las mareas astronómicas (Idier et al., 2017; Haigh et al., 2020). Como resultado de las interacciones entre los diferentes forzamientos, las cotas de inundación en la costa aumentan más rápidamente que el nivel medio del mar (NMM), proyectando al alza el número de eventos de rebase un orden de magnitud con respecto a los niveles presentes (Almar et al., 2021). La mitad de las playas de arena están en peligro de desaparecer a fin de siglo (Vousdoukas et al., 2020b). Los niveles del mar extremos integrando NMM, marea astronómica, marea meteorológica y oleaje expondrán anualmente la mayoría de las costas del mundo al evento que en la actualidad se repite, de media, una vez cada 100 años (Vousdoukas et al., 2018b) a partir del 2050, incluso en escenarios bajos (1.5°C) de aumento de temperatura (Tebaldi et al., 2021). Si no se implementan medidas de adaptación, el aumento en los niveles de exposición y peligrosidad en Europa impulsarán los daños anuales esperados desde 1.25 billones de euros en el presente, hasta cifras de entre 93 y 961 billones de euros a fin de siglo (Vousdoukas et al., 2018a) y la migración global de entre 1.6-5.6 millones de personas debido a la erosión costera implicará costes que podrían llegar a un trillón de euros (Hinkel et al., 2013). De forma similar, el riesgo de inundación en las principales ciudades costeras del mundo alcanzará niveles sin precedentes desde las pérdidas de 6 billones de euros en el año 2005 hasta un trillón de dólares americanos o más en 2050 (Hallegatte et al., 2013).

La respuesta a la pregunta de cómo evolucionarán las zonas costeras bajo los efectos del cambio climático es extremadamente incierta, ya que resulta de la intersección de las ingenierías civil y de costas y de las ciencias sociales, políticas, atmosféricas, oceánicas y de la tierra. Sin embargo, el papel trascendental de la ingeniería a la hora de condicionar la evolución de las costas es ampliamente reconocido en la literatura (Vitousek et al., 2017b), principalmente mediante medidas de adaptación (Brown et al., 2014;

Vousdoukas et al., 2020a). Para evitar las altamente probables y extremas pérdidas socio-económicas, se necesitan proyecciones de riesgos de erosión e inundación robustas para ayudar a los tomadores de decisión a escoger las mejores estrategias de adaptación considerando las fuentes de incertidumbre (Toimil et al., 2021a). Para ello, modelos de impacto confiables son esenciales para pronosticar la erosión y la inundación, calcular el riesgo, identificar los puntos críticos y evaluar las medidas de adaptación. Un modelo de impacto ideal debe ser capaz de resolver los procesos físicos relevantes y sus interacciones en la escala temporal del cambio climático (décadas), en la escala espacial de la adaptación (local a regional) y eficiente computacionalmente para poder muestrear la incertidumbre inherente al clima futuro mediante múltiples simulaciones (Ranasinghe, 2020; Toimil et al., 2020a). Además, las incertidumbres debidas al conocimiento incompleto del sistema costero deben se minimizadas mediante el enriquecimiento de las ecuaciones de la física mediante observaciones empleando algoritmos de asimilación (Splinter and Coco, 2021) o métodos de aprendizaje de máquinas (Wang et al., 2022), que se beneficiarán de los avances en observación remota y de la disponibilidad de bases de datos abiertas de campañas satelitales mundiales (Turner et al., 2021).

Se han realizado avances considerables en el modelado de la erosión gracias al desarrollo de modelos multi-proceso de complejidad reducida (Vitousek et al., 2017c; Toimil et al., 2017a; Robinet et al., 2018; Antolínez et al., 2019; Tran and Barthélemy, 2020); al empleo de observaciones mediante asimilación (Long and Plant, 2012; Vitousek et al., 2017c; Ibaceta et al., 2020); y a la consideración de diversas fuentes de incertidumbre desde la parametrización de los modelos (d'Anna et al., 2020), el NMM (d'Anna et al., 2021; Thiéblemont et al., 2019), diferentes cronologías de oleaje (Toimil et al., 2017a; Vitousek et al., 2021; d'Anna et al., 2022a), diferentes escenarios futuros de oleaje (Zacharioudaki and Reeve, 2011; Bamunawala et al., 2020) o una combinación de distintas fuentes (Toimil et al., 2021a). Del mismo modo, se han desarrollado varios modelos de inundación de complejidad reducida válidos para el estudio de impactos del cambio climático (Bates and De Roo, 2000; Gouldby et al., 2008; Leijnse et al., 2021), se han afinado esquemas de asimilación para reducir la incertidumbre en el modelado de la inundación (Muñoz et al., 2022; Nguyen et al., 2022), se han adaptado modelos mate-

máticos para reproducir estadísticamente los forzamientos (Rueda et al., 2016; Lucio et al., 2020) y se han implementado técnicas de metamodelado eficientes para el cálculo de impactos en la costa (Anderson et al., 2021). Los efectos de la inundación y la erosión se han combinado en la escala temporal de tormentas en estudios forenses (Gharagozlou et al., 2020; van Ormondt et al., 2020) y de cambio climático (Passeri et al., 2018; Grases et al., 2020). También se han incorporado los cambios de largo plazo en unos pocos estudios de inundación empleando gran variedad de técnicas (Passeri et al., 2016; Lentz et al., 2016; Stripling et al., 2017; Grilli et al., 2017; Erikson et al., 2017). Hasta la fecha, no existe un modelo único que sea capaz de resolver de forma holística la erosión y la inundación en las escalas relevantes del cambio climático de forma eficiente, pero sí se han desarrollado marcos de análisis para proyectar los impactos costeros del cambio climático. El CoSMoS americano (del inglés *Coastal Storm Modeling System*) (Barnard et al., 2019) es un gran ejemplo de marco integrado de análisis, ya que combina un conjunto de modelos numéricos (Vitousek et al., 2017c; Erikson et al., 2017; Limber et al., 2018) para evaluar la el riesgo de inundación futuro considerando el ANMM y los cambios en la línea costa. Sin embargo, existen lagunas importantes en cuanto a la consideración de la incertidumbre, pues sólo se considera un modelo climático de oleaje y marea meteorológica y las tormentas del futuro no consideran todas combinaciones de forzamientos estadísticamente posibles que puedan generar inundación. El modelado de la línea de costa integra las ecuaciones clásicas con observaciones pero no considera los efectos de las actuaciones antrópicas. La inundación se calcula empleando un modelo hidrodinámico ejecutado en perfiles y los mapas de inundación mediante interpolación espacial. Las cotas del terreno se actualizan considerando la evolución de la línea de costa, pero la cinemática del perfil es excesivamente simple.

De la revisión del estado del arte, se pone de manifiesto que no existe un marco de modelado capaz de reproducir la respuesta de la costa en cuanto a erosión e inundación que combine: a) los procesos relevantes a múltiples escalas y sus interacciones, b) el efecto de estructuras antrópicas y de soluciones basadas en la naturaleza, c) la incertidubmre en los forzamientos futuros, d) las interacciones entre la inundación y la erosión y f) técnicas de metamodelado eficientes para el cálculo de las cotas de inunda-

ción empleando modelos de procesos. Por ello, esta investigación pretende desarrollar un conjunto de modelos, herramientas y metodologías para el estudio de impactos de erosión e inundación integrando: el muestreo apropiado de la incertidumbre en el clima futuro, el estado del arte en técnicas de observación remota de la tierra, nuevos modelos de evolución de la morfología de la costa basados en la física- procesos y de complejidad reducida, el modelado riguroso de los efectos de intervenciones humanas mediante soluciones grises tradicionales y basadas en la naturaleza, el modelado probabilístico de tormentas y una metodología novedosa para integrar las proyecciones de erosión en los estudios de inundación.

0.1.2. Objetivos y marco de trabajo

El objetivo general de esta investigación es el desarrollo de un marco de análisis de impactos compuesto de diferentes modelos, herramientas y metodologías orientadas a mejorar los análisis de riesgo de erosión e inundación y la adaptación al cambio climático. El hilo conductor del trabajo es comprender cómo la línea de costa responde ante diferentes forzamientos y a continuación, emplear estos cambios para predecir la respuesta de la morfología costera y obtener mejores proyecciones de inundación. Especial atención se debe prestar a las escalas de largo y corto plazo y a sus interacciones, para así poder determinar su peso relativo en la respuesta de la costa y guiar a los tomadores de decisiones.

Para logar el objetivo principal, se han propuesto los siguientes objetivos específicos:

Objetivo 1: Desarrollo de un modelo de evolución de la línea de costa. El modelo debe resolver los principales procesos que contribuyen a la evolución de la línea de costa, los efectos de las intervenciones antrópicas y se debe beneficiar de la disponibilidad de bases de datos globales de observaciones remotas mediante técnicas de asimilación. El modelo debe ser eficiente para poder muestrear la incertidumbre climático y modular, para poder adaptarse a los últimos avances en modelado y asimilación.

Objetivo 2: Desarrollo de una metodología para obtener proyecciones de evolución de la línea de costa considerando la incertidumbre climática. La

metodología debe considerar proyecciones de oleaje y marea meteorológica de diferentes modelos climáticos y escenarios de concentraciones y diferentes trayectorias de ANMM. Asimismo, el modelo debe incorporar estrategias eficientes de propagación para regionalizar las realizaciones del oleaje y nivel del futuro a la costa y junto con el modelo de evolución, debe producir series temporales de evolución de la línea de costa que consideren la incertidumbre en el clima y sirvan para ayudar a la toma de decisiones en la costa.

Objetivo 3: Desarrollo de una metodología para incluir el efecto de la erosión a múltiples escalas en las proyecciones de inundación. La incertidumbre en el clima debe considerarse mediante la generación estadística y la simulación de tormentas a escala regional en diferentes escenarios futuros. Para ello, se debe combinar un emulador sintético de tormentas a escala regional con el modelado de la inundación empleando metamodelos que integren técnicas estadísticas y numéricas. Adicionalmente, la metodología deber ser capaz de incorporar los cambios unidimensionales de la línea de costa obtenidos a partir de modelos de evolución y generar proyecciones de inundación que consideren los cambios en la morfología de la costa.

Objetivo 4: Desarrollo de un modelo de evolución de la morfología costera para estudios a escala local. El modelo debe resolver todos los procesos que gobiernan la evolución de la línea de costa y actualizar de forma dinámica la morfología costera. La propagación sobre batimetrías irregulares debe ser considerada mediante el empleo de modelos de propagación avanzados. Asimismo, se deben incorporar los beneficios en cuanto a reducción de incertidumbre en el modelado mediante algoritmos de asimilación y los efectos de intervenciones humanas y soluciones basadas en la naturaleza en la respuesta de la costa.

Para la consecución de los objetivos propuestos, el marco de trabajo se orienta en torno a un principio guía: alcanzar la mejor representación posible de la evolución de la costa en múltiples escalas en el contexto del cambio climático. Esto se resalta en el bucle cerrado representado en la Figura 0.1.

Para ello, se ha implementado un modelo de evolución de la línea de costa que considera los procesos longitudinales y transversales, el efecto de las actuaciones antrópicas e incorpora un algoritmo de asimilación de observaciones. Una vez validado, se ha desarrollado una metodología para proyectar la evolución de la línea de costa considerando la incertidumbre climática. A continuación, se ha generado una metodología novedosa para incorporar el efecto de los cambios futuros de la línea de costa en las proyecciones de inundación. Finalmente, la investigación vuelve al principio guía de conseguir una mejor representación de la respuesta de la costa integrando los distintos avances conseguidos. Como resultado, se ha obtenido un nuevo modelo de evolución morfológico fruto del acoplamiento entre el modelo de evolución de la línea de costa, la herramienta de actualización de la topobatimetría y un modelo avanzado de propagación del oleaje. El modelo devuelve como salida no sólo la evolución de la línea de costa sino la evolución completa de la morfología, que puede ser empleada de forma directa en modelos de inundación.
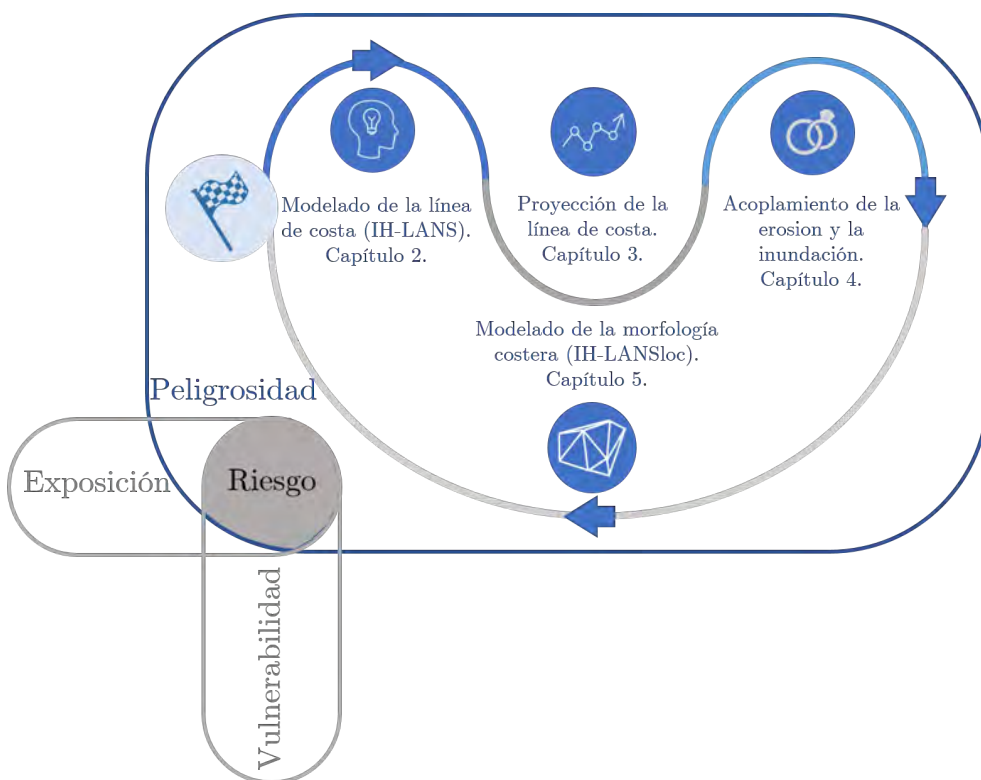
Figura 0.1: Representación gráfica del marco de trabajo y alcance. En azul los elementos abordados en el estudio y en gris el resto de componentes del riesgo.

Combinando los resultados obtenidos a partir de esta investigación con exposición y vulnerabilidad se pueden obtener estudios estudios de riesgo y diseñar estrategias de adaptación siguiendo el marco general del IPCC (Wong et al., 2014; Oppenheimer et al., 2019; Collins et al., 2019), tal y como se describe en la Figura 0.1.

0.2. Desarrollo y validación de IH-LANS

En esta sección se introduce un nuevo modelo de evolución de la línea de costa, llamado IH-LANS por sus siglas en inglés *Long-term ANtrhopized coastlines Simulation tool*. IH-LANS se ha diseñado para su aplicación en estudios regionales de la respuesta a largo plazo de la línea de costa en zonas altamente antropizadas. En IH-LANS se combina un módulo de propagación híbrido que integra técnicas estadísticas y numéricas con un modelo de evolución de la línea de costa que asimila observaciones. El modelo de evolución de la línea de costa resuelve procesos de transporte longitudinal y transversal y los efectos de actuaciones antrópicas. En cada simulación, los cambios en la línea de costa debidos a la acción del oleaje y nivel se evalúan a la vez que se reduce la incertidumbre en la calibración de los parámetros libres del modelo empleando un filtro extendido de Kalman que permite asimilar observaciones. Para probar el rendimiento del modelo, IH-LANS se aplica en un tramo costero de 40 km de longitud altamente antropizado en la costa Mediterránea. El modelo se ejecuta durante el periodo 1990-2020 empleando información de alta resolución espacio-temporal y observaciones de la línea de costa extraídas a partir de imágenes de satélite. La evolución de la línea de costa se representa con éxito (<10 m de error medio cuadrático, RMSE) al tiempo que se consideran los efectos de rellenos, la construcción y demolición de espigones, escolleras y diques a lo largo del tiempo. La eficiencia del modelo convierte a IH-LANS en una herramienta potente para la gestión de la costa y la adaptación al cambio climático.

0.2.1. Estructura y funcionalidades del modelo

La estructura del modelo se funda en tres elementos clave que son: 1) un módulo eficiente de transformación del oleaje en dos pasos que combina propagación a la costa mediante técnicas híbridas (estadístico-numéricas) y una rutina de propagación a rotura; 2) un modelo de evolución de la línea de costa multiproceso que considera procesos longitudinales y transversales; y 3) un algoritmo de asimilación para la calibración de los parámetros libres del modelo.
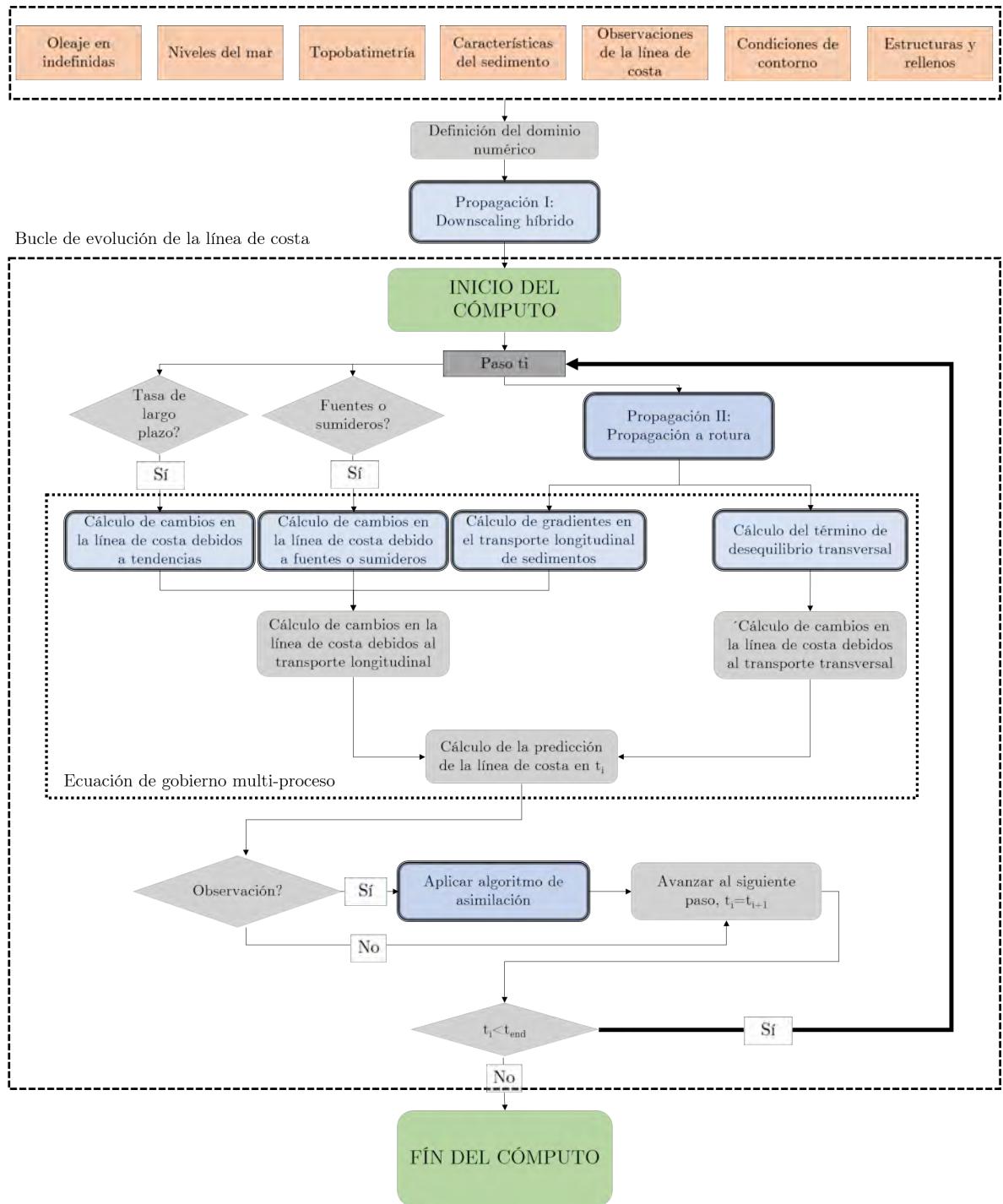
Figura 0.2: Flujo de cálculo de IH-LANS.

El proceso de cálculo de IH-LANS se muestra en la Figura 0.2. El primer paso consiste en recolectar todas las entradas necesarias en la zona de estudio que son: oleaje y niveles en profundidades indefinidas, batimetría, características del sedimento, observaciones de la línea de costa, intercambios sedimentarios en los límites de la zona de

estudio y la parametrización de las intervenciones antrópicas. A continuación se define el dominio numérico, compuesto por la malla computacional para la propagación del clima marítimo en indefinidas y la discretización en transectos de la línea de costa. El oleaje en la costa se obtiene en un conjunto de puntos predefinidos combinando técnicas estadísticas y de propagación numérica. A continuación, el oleaje se propaga a rotura en un paso independiente, para así alimentar al modelo de evolución de la línea de costa.

La ecuación multiproceso de evolución de la línea de costa consta de cuatro módulos (Ecuación 0.1). Tres de esos módulos, que son el módulo de gradientes en el transporte longitudinal siguiendo la expresión del CERC (USACE, 1984), el módulo de fuentes y sumideros de sedimento y el módulo de procesos no resueltos; son responsables de los cambios en la línea de costa debido a procesos longitudinales. Por otro lado, los procesos transversales debidos a cambios en el oleaje y en el nivel se modelan según el modelo de Toimil et al. (2017a) basado en Miller and Dean (2004).

Conocer los raíles (transectos) que guían la evolución de la línea de costa permite obtener, para cada transecto, la serie temporal de observaciones de la línea de costa antes de resolver la ecuación de gobierno. Por ello, con el fin de facilitar el acoplamiento entre los procesos longitudinales y transversales y el esquema de asimilación, se ha aplicado una discretización basada en transectos fijos para resolver la ecuación de evolución de la línea de costa:

$$
\underbrace{\frac{\partial Y}{\partial t}}_{\text{Cambios totales línea de costa}} = \underbrace{\frac{\partial Y_l}{\partial t}}_{\text{Cambios tte. longitudinal}} + \underbrace{\frac{\partial Y_c}{\partial t}}_{\text{Cambios tte. transversal}}
$$

$$
\frac{\partial Y_l}{\partial t} = \underbrace{-\frac{1}{B+d_c}\frac{\partial Q}{\partial x}}_{\text{Gradientes tte. longitudinal}} + \underbrace{\frac{1}{B+d_c}q}_{\text{Fuentes y sumideros}} + \underbrace{vlt}_{\text{Procesos no resueltos}}
$$

$$
\frac{\partial Y_c}{\partial t} = \underbrace{K_c^{+/-}[Y_c^{eq} - Y_c]}_{\text{Tte. transversal}}
$$

$$(0.1)$$

dónde Y es la distancia, medida a lo largo del transecto, desde el punto en tierra del perfil a la costa (linea de pleamar media), y corresponde a la suma de la posición de

la línea de costa asociada a procesos longitudinales (Y_l) y a transversales (Y_c). B es la altura de la berma, d_c se refiere a la profundidad de cierre, $\frac{\partial Q}{\partial x}$ se corresponde con los gradientes en el transporte longitudinal, $\frac{q}{B+d_c}$ representa las fuentes y sumideros de sedimento, vlt es la tendencia debida a procesos no resueltos en el modelado, $K_c^{+/-}$ es la tasa de acreción/erosión transversal y Y_c^{eq} es la posición transversal de equilibrio.

La Ecuación 0.1 se resuelve en cada paso de tiempo e incluye los efectos de estructuras antrópicas si existen. Asimismo, IH-LANS verifica si existen observaciones disponibles en ese instante, y si es así, actualiza los parámetros libres del modelo y la predicción de la línea de costa mediante el filtro extendido de Kalman.

0.2.1.1. Transformación del oleaje

La propagación del oleaje desde indefinidas a rotura se realiza en dos pasos (Figura 0.3). El primer paso consiste en la propagación desde indefinidas a la cabeza de los perfiles. Este proceso no se ve alterado por cambios morfodinámicos, ya que los puntos en costa a los que se propaga se encuentran a mayores profundidades que el cierre del perfil. Para ello, se emplea una técnica de propagación siguiendo la propuesta por Camus et al. (2013) pero ligeramente modificada para incluir información espectral detallada (particiones espectrales) de modelos globales de oleaje. Se realiza en cuatro etapas: 1) recolección de las variables climáticas y generación del dominio de cálculo, 2) selección de un conjunto representativo de estados de mar mediante el algoritmo de maxima disimilitud, 3) propagación numérica mediante el modelo SWAN (Booij et al., 1999) de los casos seleccionados y reconstrucción mediante interpolación multivariada del clima marítimo en los puntos costeros empleando funciones de base radial.

El segundo paso consiste en la propagación a rotura considerando asomeramiento, refracción y difracción inducida por estructuras antrópicas. La obtención de la línea de rompientes implica resolver procesos no-lineales actuando en una topobatimetría activa. En estudios locales, es posible acoplar un modelo numérico de propagación que resuelva los procesos relevantes con la ecuación de gobierno de la línea de costa. En este caso, un paso adicional necesario consiste en adaptar la batimetría activa dependiendo del mo-

vimiento de la línea de costa como en Robinet et al. (2018). Sin embargo, para estudios regionales, la propagación a rotura implementada en IH-LANS se simplifica considerando asomeramiento lineal, refracción uni-dimensional, leyes empíricas de difracción y un criterio de rotura basado en la profundidad. Para ello, se aplica la ecuación de conservación de energía, se emplea la ley de Snell para modelar la refracción, la rotura por profundidad se considera mediante un coeficiente de rotura (γ) de 0.55 y las leyes de difracción empíricas de Kamphius (2000) y Dabees (2000) se utilizan para corregir las propiedades en rotura del oleaje por efecto de espigones y diques. En este caso, no es necesario resolver la evolución de la topobatimetría activa, ya que el nexo de unión entre los cambios morfológicos e hidrodinámicos es la orientación media de la topobatimetría. Ésta se emplea al evaluar la refracción mediante la ley de Snell y se obtiene a partir de la posición de la línea de costa.
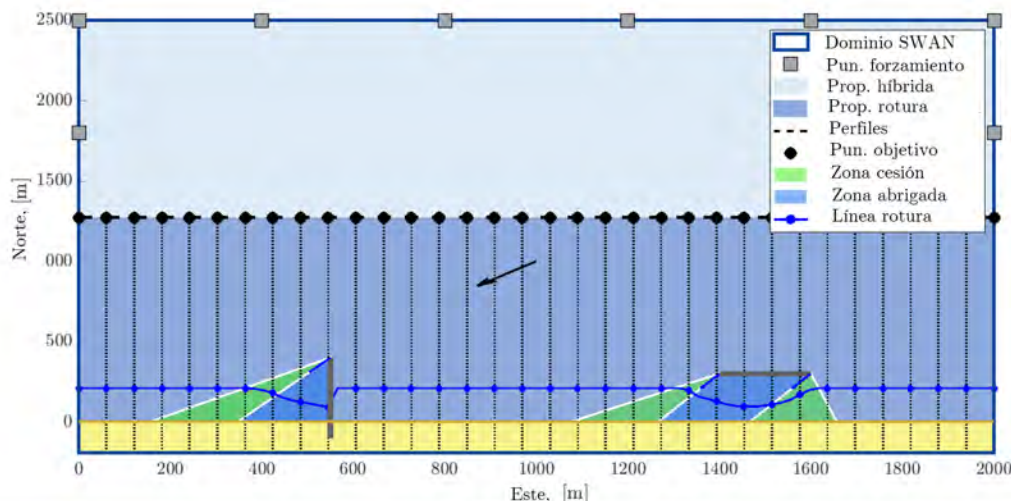
Figura 0.3: Esquema de las técnicas de propagación empleadas para obtener las propiedades del oleaje en rotura.

0.2.1.2. Transporte longitudinal

Los cambios morfológicos debidos a gradientes en el transporte longitudinal se producen en la topobatimetría activa, que se extiende desde la profundidad de cierre calculada según (Hallermeier, 1980) y la berma. El transporte longitudinal se evalúa considerando la ecuación del CERC (USACE, 1984) corregida en función de la capacidad de retención

de sedimentos de las estructuras antrópicas presentes:

$$Q = K_e Q_0 \tag{0.2}$$

donde Q es el transporte neto, K_e es el coeficiente de reducción en el transporte longitudinal debido a estructuras que atrapen sedimento y Q_0 es el transporte longitudinal según la formulación del CERC. La ecuación del CERC considera que la componente longitudinal de la energía del oleaje es el mecanismo que moviliza el transporte longitudinal de sedimentos y considera mediante la modificación de Ozasa and Brampton (1980) el efecto de los gradientes longitudinales de altura de ola. Sin embargo, diferentes formulaciones (Kamphius, 1993; Mil-Homens et al., 2013; Van Rijn, 2014) pueden ser implementadas en IH-LANS con facilidad.

Los espigones, entendidos como estructuras impermeables perpendiculares a la costa, bloquean el transporte longitudinal de sedimentos. En IH-LANS se modela esta capacidad de retención mediante el coeficiente K_e, que varía entre 0 y 1 en función de la anchura de la zona de transporte de sedimentos, la distribución transversal del transporte longitudinal $q_c(\eta)$ y la distancia desde el extremo offshore de la estructura y la línea de costa en el lado expuesto o de barlomar (L_e). Siguiendo a Kristensen et al. (2016), el transporte de sedimentos ocurre en una banda que excede hacia el mar la anchura de la zona de rompientes W_b^* en un 25 %. Asimismo, la $q_c(\eta)$ se asume uniforme siguiendo a Hanson (1989). Por tanto, el coeficiente de retención K_e es:

$$K_e = 1 - \frac{L_e}{1.25 W_b^*}, \quad K_e \in [0, 1] \tag{0.3}$$

Las escolleras limitan el sedimento movilizable y previenen el retroceso de la línea de costa en su trasdós. Para aplicar esta condición de forma realista, si la posición de la línea de costa retrocede por detrás de una escollera, se introduce una limitación en el transporte de sedimentos para respetar la condición de no franqueabilidad siguiendo el procedimiento iterativo descrito en Hanson and Kraus (1986).

Por otro lado, los diques exentos generan cambios en la línea de costa debido a las

alteraciones en el flujo en su zona abrigada. En la fase de saliente, los patrones de difracción controlan la evolución de la línea de costa debido a gradientes la altura de ola y dirección por difracción. Asimismo, si se forma un tómbolo, las tasas de transporte de sedimentos también se alteran para prevenir que la línea de costa sobrepase la estructura. Esto se consigue de forma similar, pero inversa, a la redistribución de sedimento debido a una escollera.

0.2.1.3. Transporte transversal

El transporte transversal se modela según Toimil et al. (2017a), que se basa en la formulación de Miller and Dean (2004). Se asume que cambios en oleaje y niveles generan una respuesta en la línea de costa respetando la conservación del volumen en un perfil de equilibrio. Como la mayoría de modelos transversales de equilibrio, la formulación matemática se basa en una ecuación cinética en la que el desequilibrio con respecto a un estado de referencia genera cambios en la línea de costa. La posición de equilibrio de la línea de costa Y_c^{eq} es:

$$Y_c^{eq} = \Delta y_0 + R_{ANMM} + \Delta y_{eq}(t) \tag{0.4}$$

dónde Δy_0 es un parámetro empírico que asegura que las fluctuaciones se producen en torno a una posición media de base. Para poder sumar la contribución de los diferentes módulos de la ecuación de gobierno, la posición base cross-shore Y_c^{eq} se asume que es cero si el R_{ANMM} es nulo. R_{ANMM} es el retroceso según la ley de Bruun (Bruun, 1962) por aumento del nivel medio del mar y $\Delta y_{eq}(t)$ es la posición de equilibrio que depende del oleaje, de la marea astronómica y del set-up del oleaje:

$$\Delta y_{eq} = -W_{bc}^* \left(\frac{0.106 H_{s_{bd}} + MM + MA}{B + d_{bd}} \right) \tag{0.5}$$

siendo d_{bd} la produndidad de rotura, W_{bd}^* la anchura de la zona de rompientes según el perfil de equilibrio de Dean $W_{bd}^* = \left(\frac{H_{s_{bd}}}{\gamma A} \right)^{3/2}$, MM la marea meteorológica y MA la marea astronómica.

0.2.1.4. Fuentes y sumideros de sedimento

En el caso de intercambios episódicos de sedimento (e.g. rellenos o dragados), la tasa de evolución de la línea de costa se calcula en función del volumen total de sedimento movilizado, la duración y el polígono que define la extensión de la actuación. Intercambios permanentes o persistentes como descargas sólidas de ríos o retroalimentaciones de sedimento se deben especificar mediante tasas de evolución constantes o variables en el tiempo.

0.2.1.5. Tendencia de largo plazo

La tendencia a largo plazo (vlt) considera todos aquellos procesos no resueltos de cualquier tipo que contribuyen a la evolución de la línea de costa. Como Vitousek et al. (2017c), este término es de origen empírico y se obtiene mediante asimilación de observaciones. En el inicio de la simulación vlt es igual a cero pero cambia a medida que existen datos para asimilar y el comportamiento observado no es atribuible a los procesos modelados de forma explícita en la Ecuación 0.1. Este término es especialmente útil en el caso de fuentes o sumideros estacionarios cuya contribución a los cambios en la línea de costa es desconocida inicialmente.

0.2.1.6. Asimilación de observaciones

La asimilación de observaciones mediante filtros de Kalman permite emplear observaciones dispersas para calibrar, de forma automática, las predicciones y los parámetros libres del modelo (Long and Plant, 2012). La predicción del modelo y los parámetros libres, en un determinado paso de tiempo, definen el vector de estado, que se corresponde con los valores mínimos para hacer avanzar el modelo un paso de tiempo. Cada vector de estado actualizado se calcula de forma recursiva a partir del estado previo y de la observación disponible. Esto se consigue promediando la predicción del modelo y la observación mediante la ganancia de Kalman, estimada al propagar la matriz de covarianza, que depende de la incertidumbre inicial del vector de estado, el ruido inherente del modelo y el error en la medida.

El algoritmo de asimilación basado en el filtro extendido de Kalman permite obtener parametrizaciones estacionarias o variables en el tiempo haciendo variar el ruido inherente del modelo. Una vez que los parámetros libres del modelo han convergido en un conjunto óptimo, la amplitud de la matriz de covarianza propagada se reduce, y converge al ruido inherente del proceso. Si el ruido inherente del proceso es pequeño, se tenderá a parametrizaciones estacionarias y valores más grandes implicarán que la matriz de covarianza propagada tenga la suficiente flexibilidad para acomodar variaciones no estacionarias en los parámetros libres como en Ibaceta et al. (2020). Sin embargo, durante el periodo de predicción, la relación entre los parámetros libres y las dinámicas es desconocida, lo que impide la implementación de parametrizaciones no estacionarias. Por ello, en ausencia de una metodología robusta que permita considerar la no estacionariedad en las formulaciones de procesos, la hipótesis de estacionariedad se ha adoptado en este estudio.

En IH-LANS se han implementado dos variantes del algoritmo de asimilación dependiendo del acoplamiento de los procesos longitudinales y transversales en el filtro de Kalman. Por un lado, la implementación independiente considera de forma desacoplada los procesos longitudinales y transversales dentro del algoritmo de asimilación. Por otro, la implementación conjunta incluye, de forma acoplada, los procesos longitudinales y transversales según el trabajo de Vitousek et al. (2017c) y de Long and Plant (2012).

0.2.2. Casos sintéticos de estudio

Se han elaborado siete casos sintéticos de estudio para validar la correcta implementación de las rutinas de propagación, la implementación numérica de la ecuación de gobierno de la línea de costa y del algoritmo de asimilación. Los experimentos detallados cubren las siguientes funcionalidades: 1) evolución de la línea de costa tras un espigón considerando difracción y bypass de sedimento, 2) evolución de la línea de costa tras una escollera, 3) formación de saliente tras diques exentos, 4) efecto de fuentes de sedimento variables en el tiempo, 5) asimilación de observaciones en procesos longitudinales, 6) asimilación de observaciones en procesos transversales y 7) asimilación de observaciones considerando procesos longitudinales y transversales.

0.2.2.1. Actuaciones antrópicas: espigón, escollera, relleno y dique exento

En la Figura 0.4a, la evolución de la línea de costa tras un espigón calculada en IH-LANS se compara con la solución analítica de Pelnard-Considère (1956). Los resultados de ambas aproximaciones son similares, sin embargo se aprecian diferencias debido a la sombra que genera la difracción en el lado abrigado del espigón y al modelado del bypass variable de sedimento considerado en la solución numérica.

La habilidad del modelo para reproducir la evolución de la línea de costa tras una escollera se muestra en la Figura 0.4b. Asimismo, también se representa la evolución de la línea de costa en el caso de no estar protegida. Se aprecia cómo el sedimento que inicialmente estaba frente a la defensa se desplaza hacia un extremo de la playa buscando la perpendicular al flujo de energía y exponiendo la escollera en el lado opuesto.

En la Figura 0.4c se representa la dispersión de un vertido de sedimento depositado en el tramo central de la playa. Debido a la acción del oleaje, el sedimento se redistribuye haciendo que la línea de costa progrese de forma uniforme hacia el mar.

Finalmente, la Figura 0.4d se muestra la capacidad de IH-LANS para modelar la respuesta de la línea de costa tras un dique exento. Para ello se calcula la distancia del tómbolo final al dique exento (x) analizando diques de diferente longitud (L) y distancia inicial a la orilla (S) y se compara con la solución empírica de Hsu and Silvester (1990).

0.2.2.2. Asimilación: transporte longitudinal, transversal y combinado

Con el fin de testear el algoritmo de asimilación de observaciones, en los diferentes ejemplos se ejecuta IH-LANS en cuatro configuraciones: 1) una simulación de de referencia con los parámetros libres *verdaderos* del modelo, 2) una simulación en la que se alteran los parámetros libres del modelo y no se asimilan observaciones, 3) una simulación que se inicializa con los parámetros libres alterados de la simulación 2) pero se asimilan observaciones de la simulación 1) y 4) igual que la 3) pero añadiendo error en las observaciones. En todos los casos, las observaciones de la simulación de referencia se toman
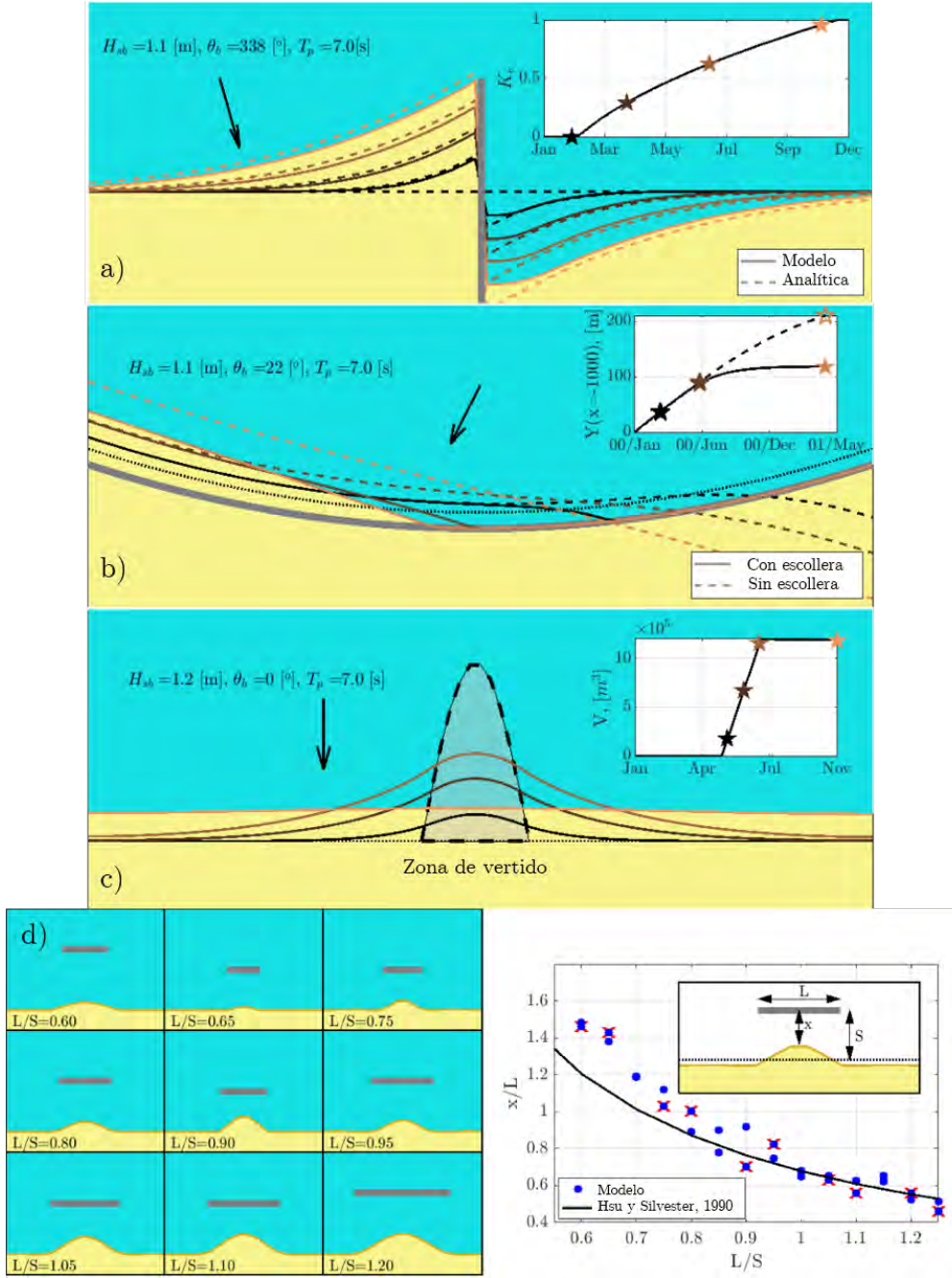
Figura 0.4: Resumen de las estructuras implementadas en IH-LANS.

cada 15 días y el error en la simulación 4 se supone igual a 10 m de RMSE. De esta forma, se pretende emular las características de las observaciones obtenidas a partir de imágenes de satélite.

En la Figura 0.5 se muestra la evolución de la línea de costa tras un dique exento considerando únicamente el transporte longitudinal. Se aprecia como las cuatro simulaciones

tienden a una posición de equilibrio en tres años, y de como el algoritmo de asimilación durante el periodo sombreado en gris, es capaz de converger hacia el parámetro óptimo $K_1 = 400 \ m^{1/2}/hr$ incluso en el caso de observaciones con 10 m de RMSE (línea roja).
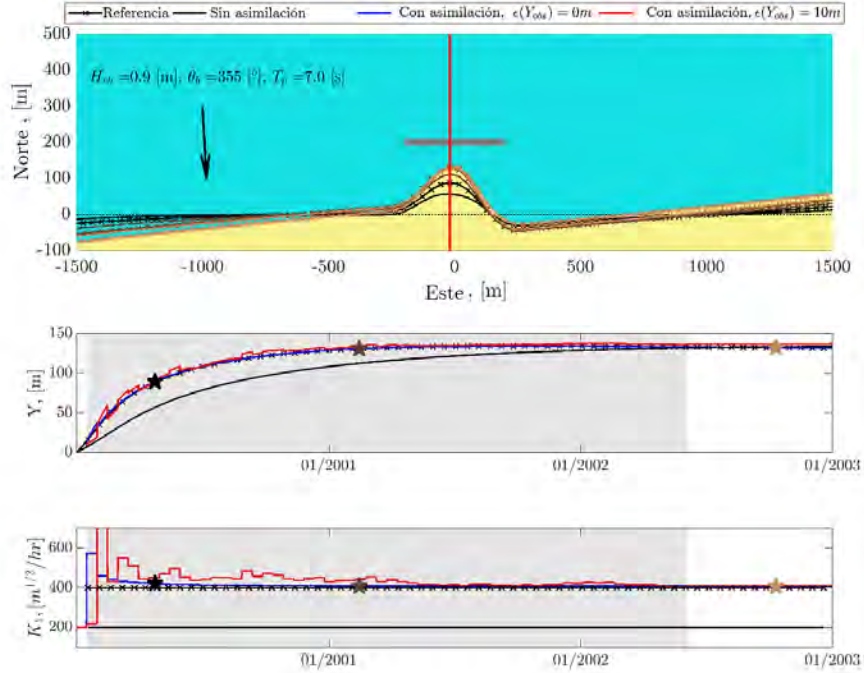
Figura 0.5: Asimilación de observaciones considerando el transporte longitudinal.

La capacidad del modelo de asimilar observaciones considerando parámetros de erosión y acreción diferentes ($K_c^{+/-}$) en el modelo transversal se pone de manifiesto en la Figura 0.6. En este caso, la simulación en la que se asimilan observaciones sin error (línea azul) converge al conjunto óptimo de parámetros ($K_c^{+/-}$) mientras que si se introduce un error en las observaciones, la posición de la línea de costa (línea roja en el primer panel) converge hacia la línea de referencia (línea negra con marcadores) pero con un error relativo de los parámetros libres asimilados ($K_c^{+/-}$) con respecto a los de referencia en el entorno al 35 %. Por tanto, se pone de manifiesto la complejidad de calibración del transporte transversal, debido fundamentalmente a que actúa a una escala temporal más breve que el transporte longitudinal. Sin duda, para obtener mejores predicciones, se necesita progresar en las técnicas de observación remota para así disminuir el error en las observaciones y aumentar su frecuencia de muestreo.
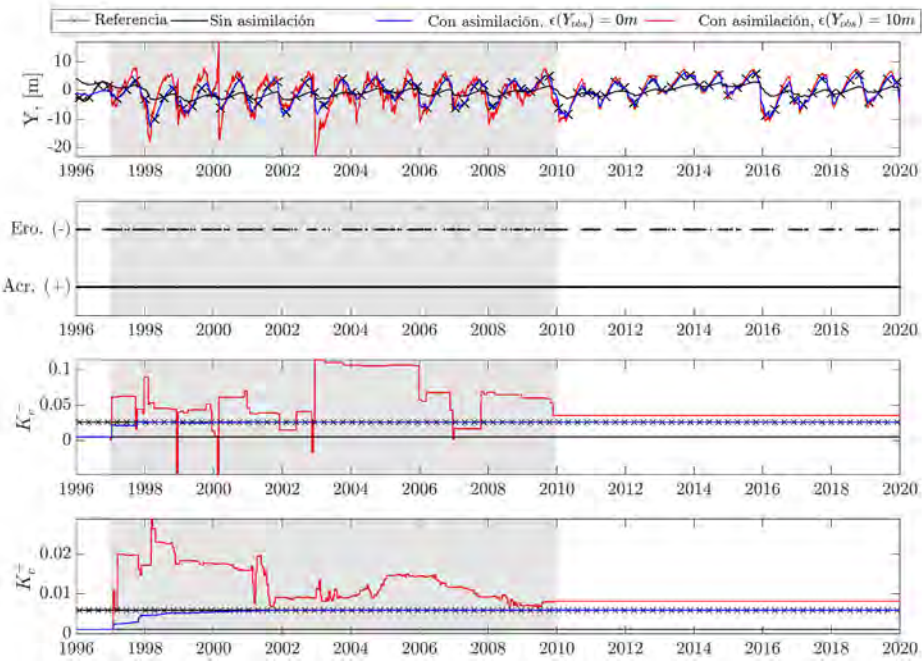
Figura 0.6: Asimilación de observaciones considerando el transporte transversal.

Finalmente, en la Figura 0.7, se muestra la capacidad del modelo de asimilar observaciones de procesos longitudinales y transversales de forma conjunta. En este caso, se testean dos enfoques diferentes de asimilación, la asimilación independiente (líneas azules) y la asimilación conjunta similar a Vitousek et al. (2017c) (líneas rojas). Se muestra la evolución temporal de la línea de costa total (Y), la línea asociada al trasporte longitudinal (Y_l) y la línea asociada al trasporte transversal (Y_c), así como los parámetros de transporte longitudinal (K_1) y transversal ($K_c^{+/-}$). Las concusiones referidas a los procesos analizados de forma individual en las Figuras 0.5 y 0.6, prevalecen en el caso del análisis conjunto en la Figura 0.7. La asimilación en el transporte longitudinal, de una escala temporal superior al transversal, converge hacia el conjunto óptimo de parámetros incluso en el caso de existir ruido en las observaciones. El transporte transversal es más sensible a errores en las observaciones pero la evolución temporal de la línea de costa coincide satisfactoriamente con la evolución de la simulación de referencia. Sin embargo, la clave del análisis reside en la comparación de las dos técnicas de asimilación. Se aprecia cómo la asimilación conjunta (trazo rojo) da lugar a una línea de costa que coincide casi a la perfección con la línea de costa total, a costa de atribuir pesos erróneos a la suma de los procesos longitudinales y transversales (ver paneles tercero y

cuarto de la primera columna). Como alternativa a la asimilación conjunta, se propone la asimilación independiente, que desacopla en la asimilación los procesos longitudinales y transversal evitando interacciones incorrectas. Sin embargo, para poder asimilar de forma independiente procesos longitudinales y transversales, se debe desagregar la serie temporal de observaciones en procesos longitudinales y transversales. Para ello, y aprovechando su diferente escala temporal, los procesos longitudinales se aproximan por la media móvil de tres años mientras que el residuo se atribuye a los procesos transversales. Asimismo, se pueden aplicar otras técnicas de atribución en función de la escala temporal (Montaño et al., 2021).
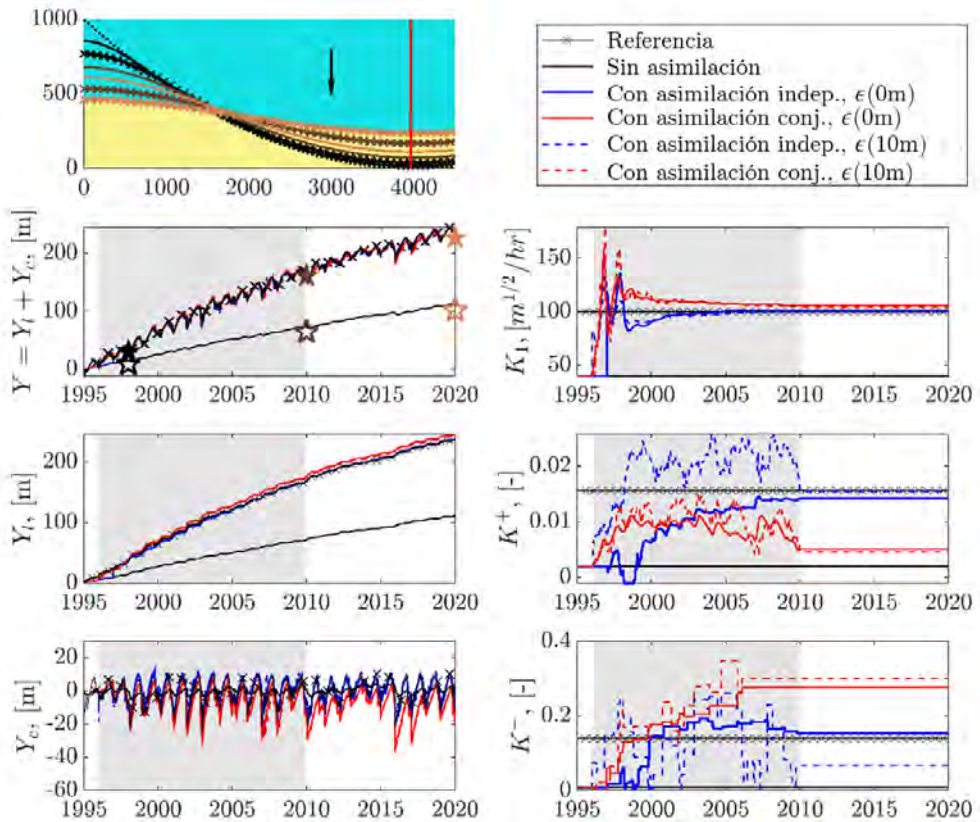
Figura 0.7: Asimilación de observaciones considerando el transporte longitudinal y transversal combinado.

0.2.3. Caso de aplicación

Para validar la capacidad predictiva del modelo, se ejecuta IH-LANS en un tramo de costa real fuertemente antropizado. Tras recolectar todos los datos de partida (dinámicas en indefinidas, batimetría, caracterísiticas del sedimento, observaciones de la línea de costa, condiciones de contorno de transporte de sedimentos y parametrización de estructuras), se elabora el dominio numérico para la propagación y la discretización en transectos de la línea de costa. A continuación, se resuelve la ecuación de gobierno de la línea de costa, que se alimenta de las dinámicas en rotura. El modelo se ejecuta durante el periodo de 1990-2020 y los resultados se calibran y validan con observaciones obtenidas a partir de imágenes de satélite. Para evitar los problemas de la asimilación conjunta, se aplica la asimilación independiente de procesos longitudinales y transversales.
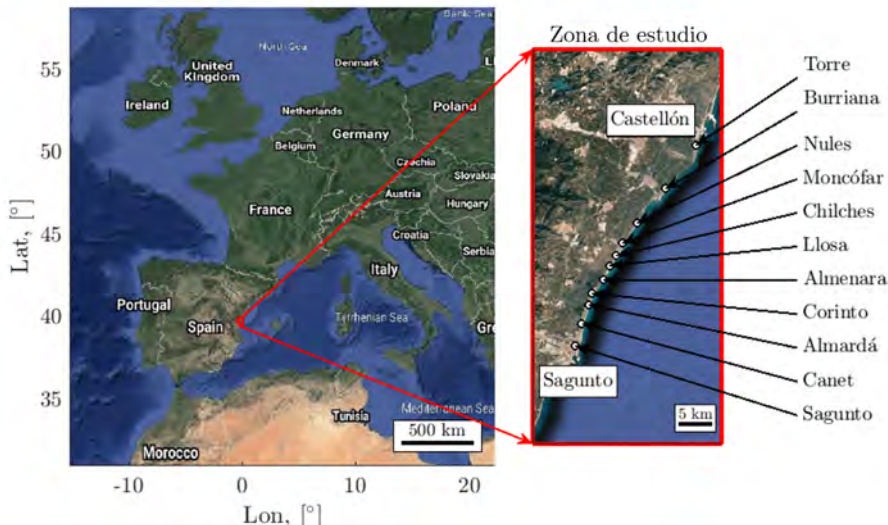
Figura 0.8: Localización de la zona de estudio.

0.2.3.1. Zona de estudio

La zona de estudio es un tramo de 40 km en el Mediterráneo, entre Castellón y Valencia, Figura 0.8. El clima de oleaje medio se caracteriza por oleajes poco energéticos pero con un ángulo de incidencia oblicuo con respecto a la orientación de la batimetría, lo que alimenta un intenso transporte de sedimentos de norte a sur. La construcción de

grandes puertos en Castellón, Burriana y Sagunto, generan zonas de acumulación y de erosión alternadas que se han tratado de corregir puntualmente mediante actuaciones basadas en espigones y regeneraciones.

0.2.3.2. Entradas del modelo

En primer lugar se confecciona el dominio de cálculo para la regionalización a costa. Para ello se define una malla general de 500 metros de resolución anidada a tres mallas de detalle de 50 metros de resolución en la que se ejecutará SWAN. La línea de costa se discretiza en transectos separados 200 metros aunque con correcciones puntuales para captar fenómenos morfológicos locales.

A continuación, se emplea el oleaje offshore y la marea meteorológica en el periodo 1990-2020 obtenidos a partir de regionalizar dinámicamente los campos atmosféricos del ERA5 empleando modelos de procesos en un grid de 0.08° de resolución. La marea astronómica se obtiene a partir de la reconstrucción armónica del modelo global TP-XO7.2. La topobatimetría se forma uniendo el modelo digital del terreno del Intituto Geográfico Nacional (IGN), la batimetría costera a partir de las campañas de campo del Ministerio para la Transición Ecológica y el Retro Demográfico (MITERD) en 2009 y la batimetría offshore a partir de la base de datos EMODnet.

Las observaciones de la posición de la línea de costa se obtienen mediante el algoritmo CoastSat (Vos et al., 2019). A continuación, los treinta años de observaciones, aproximadamente bimensuales de las campañas de Landsat-5, Landsat-8 y Sentinel-2, se corrigen por la marea a partir de la pendiente del frente de playa y se filtran las observaciones erróneas mediante técnicas de filtrado manual y automáticas. Asimismo, se obtiene información del tamaño de sedimento a partir de las campañas del MITERD y se emplea la formulación de del Valle et al. (1993) para inicializar la constante de transporte longitudinal (K_1) en función del tamaño mediano del sedimento ($D50$). Finalmente, se fijan condiciones de contorno impermeables al tránsito de sedimentos en las fronteras del dominio debido a los puertos de Castellón y Sagunto (condiciones de Dirichlet nulas) y se parametrizan las estructuras en el tiempo y en el espacio a partir

de información facilitada por el MITERD e imágenes satelitales.

0.2.3.3.   Resultados

De IH-LANS se extraen predicciones horarias de la posición de la línea de costa en todos los transectos, Figura 0.9. Se aprecia como las predicciones del modelo y las observaciones son similares, con un coeficiente de correlacion (R^2) superior a 0.7 y un error medio cuadrático inferior a 10 m en la fase de validación en todos los perfiles.
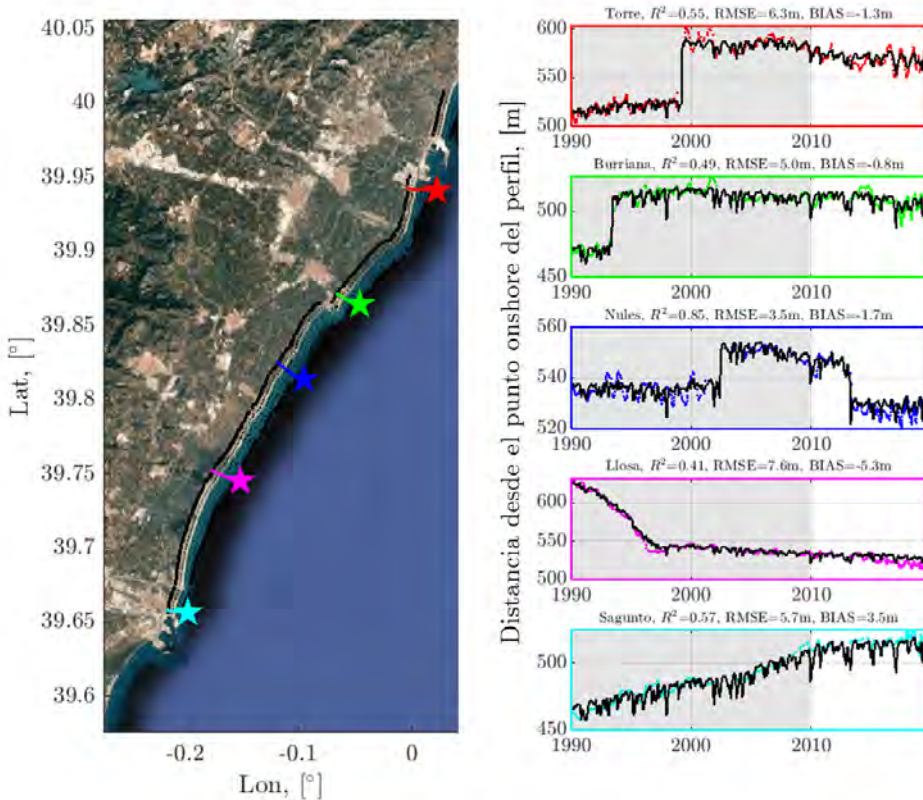
Figura 0.9: Discretización en perfiles (panel izquierdo). Evoluciones horarias modeladas y observaciones (panel derecho). El periodo de calibración se muestra en gris.

Asimismo, se ha hecho un estudio de detalle con transectos espaciados cada 15 metros para evaluar la capacidad del modelo de reproducir formas complejas en torno a estructuras. Se han analizado las playas de Torre (Figura 0.10a) y de Almenara (Figura 0.10b). Como se aprecia en la figura, el modelo es capaz de reproducir la respuesta de la línea de costa ante cambios en las estructuras en ambos casos.
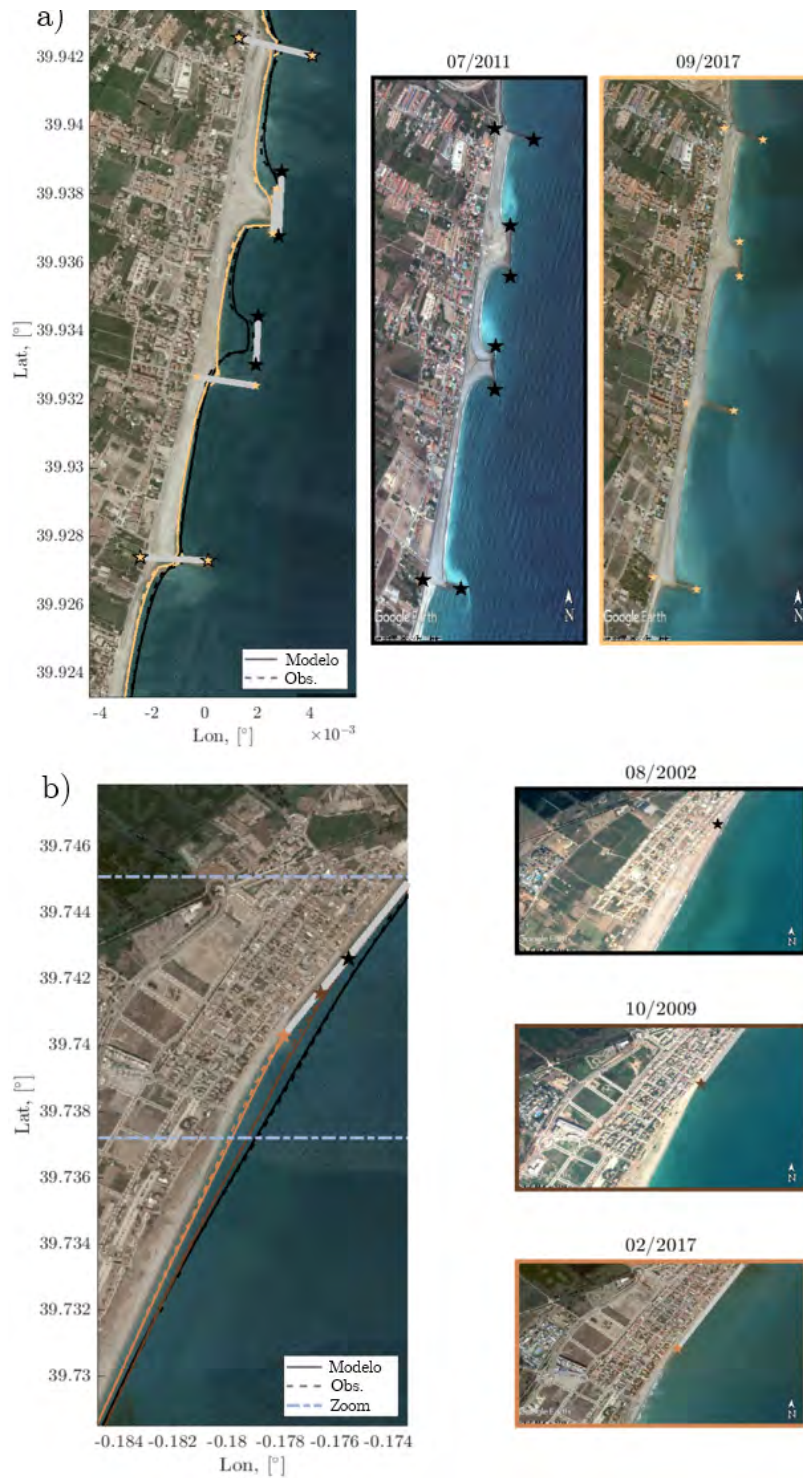
Figura 0.10: Líneas de costa modeladas y observadas en Torre y Almenara (columna izquierda). Evolución de las estructuras antrópicas (columna derecha).

0.3. Aplicación de IH-LANS para predecir la respuesta de la línea de costa

En esta sección, el modelo IH-LANS se aplica para proyectar la evolución de la línea de costa. Para ello, se desarrolla una metodología para obtener proyecciones de línea de costa a escala regional combinando proyecciones multimodelo de oleaje y nivel y modelos de evolución de complejidad reducida. Para considerar la incertidumbre en los forzamientos inducida por el cambio climático, las proyecciones dinámicas regionalizadas y con corrección de sesgo de diferentes combinaciones de modelos climáticos globales y regionales junto con varias trayectorias de aumento de nivel del mar para dos escenarios de concentración, se emplean para forzar el modelo de impacto IH-LANS. La metodología se aplica en el tramo de costa de 40 km entre Castellón y Sagunto en el que se ha calibrado y validado el modelo de evolución en el periodo 1990-2020.

0.3.1. Metodología

Se propone una metodología clasificada como de conjunto dentro del marco propuesto por Toimil et al. (2020a) atendiendo al muestreo de la incertidumbre intrínseca. Para su aplicación, la metodología se compone de tres pasos (Figura 0.11):

1. La recolección de las dinámicas futuras: oleaje y marea meteorológica a partir de modelos climáticos globales y regionales GCM-RCM regionalizados dinámicamente y denotados RCMs, proyecciones deterministas de marea astronómica y trayectorias posibles de ANMM.

2. El cálculo de la evolución de la línea de costa empleando modelos de complejidad reducida, alimentados por las propiedades en rotura del oleaje y calibrados durante el periodo histórico. La propagación a rotura se realiza en dos etapas, en una primera etapa, las dinámicas multimodelo se propagan a la cabeza de los perfiles empleando técnicas estadístico-numéricas. A continuación, las propiedades en rotura se obtienen a partir de una propagación simplificada basada en la conservación del flujo de energía y en la ley de Snell.

3. El post-proceso de los resultados para extraer información relevante de cara a

la gestión del litoral tal como los retrocesos permanentes y las áreas perdidas, la contribución de diferentes procesos a los cambios en la línea de costa o los retrocesos extremos.
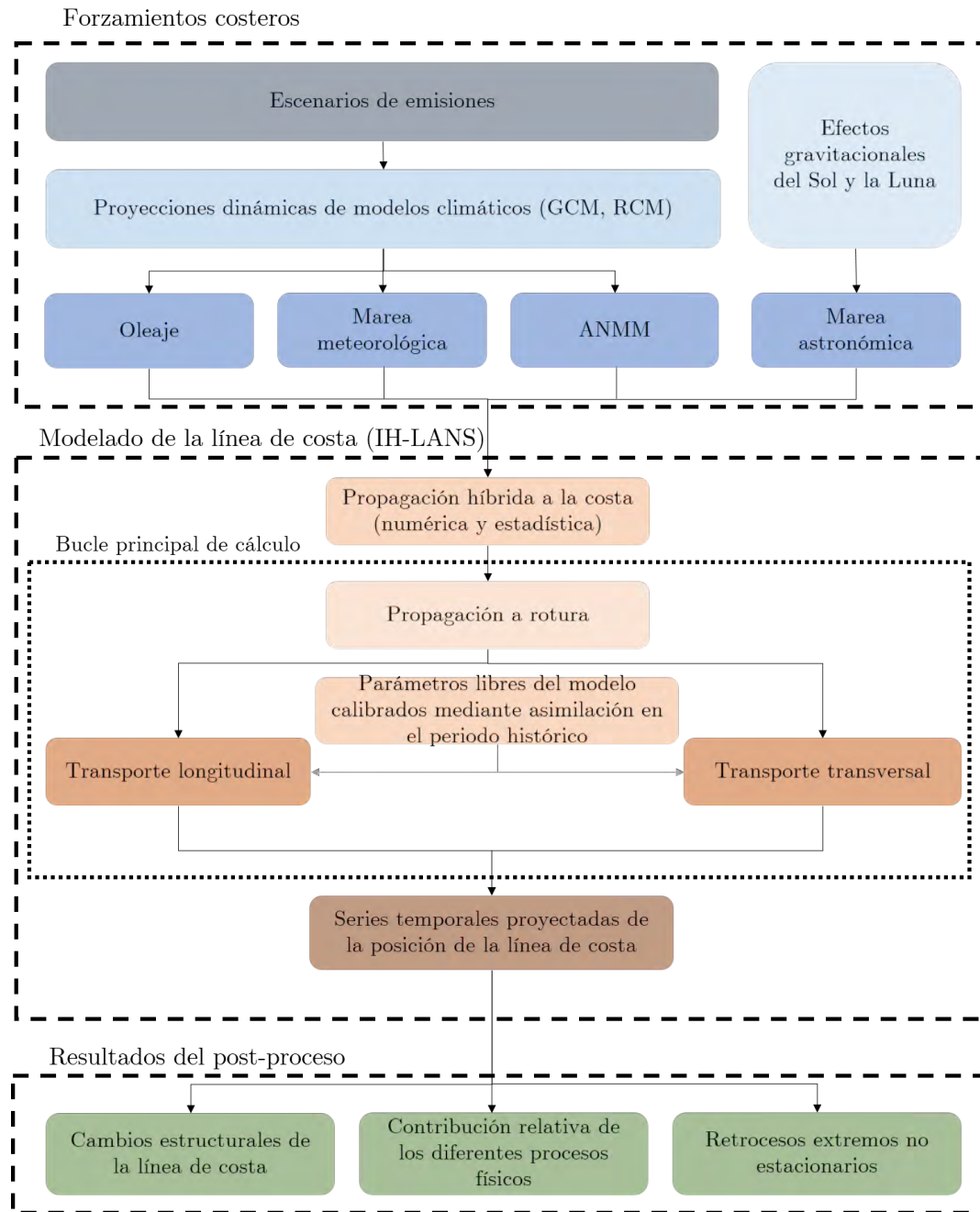
Figura 0.11: Metodología para obtener las proyecciones de evolución de la línea de costa.

0.3.2. Caso de aplicación

La metodología se aplica en el tramo de costa empleado en la calibración y validación del modelo durante el periodo histórico. Se caracteriza por dinámicas costeras suaves (Hs media de 0.75 m y periodos de pico medios en el entorno de 5.1 s) pero que generan un intenso transporte de sedimentos norte-sur. La presencia de grandes puertos que retienen el sedimento genera zonas alternas de erosión y sedimentación que se han tratado de corregir con medidas locales basadas en rellenos y construcción de estructuras (Figura 0.12).
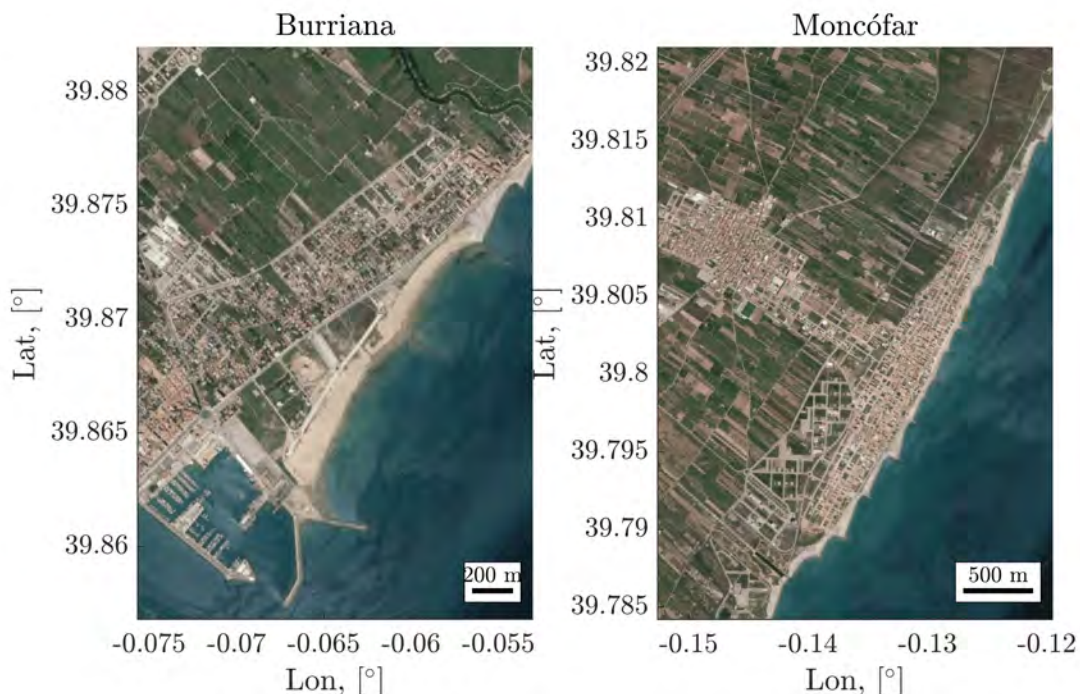
Figura 0.12: Ejemplo de dos de las playas del tramo de estudio.

0.3.2.1. Dinámicas marinas

Las dinámicas marinas que controlan la evolución de la línea de costa se obtienen de diferentes bases de datos. Las proyecciones de oleaje y nivel se han obtenido de regionalizar dinámicamente campos de viento y presión de diferentes RCMs (IHCantabria, 2020) y a continuación, se ha corregido el sesgo calculado entre el histórico de los modelos y la base de datos de reanálisis de referencia (ERA5). Se consideran diferentes trayectorias de ANMM a partir de las simulaciones globales recogidas en el IPCC (Op-

penheimer et al., 2019). La marea astronómica se obtiene a partir de la reconstrucción de armónicos de la base TPXO7.2 (Egbert and Erofeeva, 2002).

Las proyecciones de olas y marea meteorológica se obtienen de 5 RCMs (IPSL, HADG, MEDC, EART y CNRM) para dos escenarios de emisiones (RCP4.5 y RCP8.5). Para ello, los campos atmosféricos se emplean como forzamiento del modelo WaveWatch III (Tolman, 2009) en una malla de 0.08° de resolución. Se obtienen series horarias en los periodos histórico (1985-2005), medio plazo (2026-2045) y largo plazo (2081-2100), Figura 0.13. El hecho de no disponer de series continuas de oleaje para forzar el modelo hasta fin de siglo se resuelve empleando la técnica estadística del *bootstrapping* (Davidson et al., 2017; Kroon et al., 2020). Para ello, se asume que el clima marítimo de cada instante del hueco a la franja de valores más cercana es estacionario.
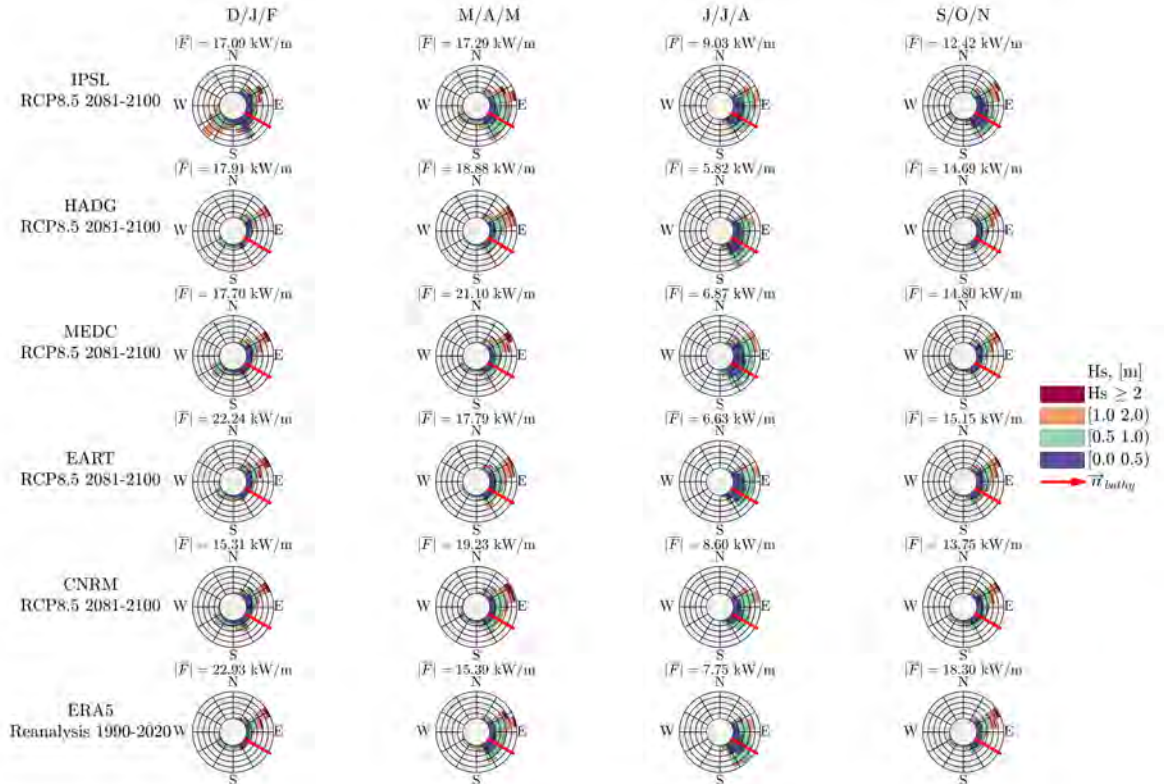
Figura 0.13: Rosas de oleaje (Hs-Dir) de diferentes RCMs en el periodo 2081-2100 (primeras cinco filas) y del reanálisis de ERA5 en el periodo 1990-2020 (fila inferior).

La marea astronómica se reconstruye a partir de la base de datos de TPXO7.2 usando el modelo OTIS (Oregon State University Tidal Prediction Software) en una resolución espacial de 0.25 ° dando lugar a series temporales horarias entre 1985 y 2100.

Las proyecciones de ANMM se obtienen en un grid de 1° de resolución a partir de 21 GCMs (Oppenheimer et al., 2019). La media y la desviación típica del conjunto multimodelo para dos escenarios de emisiones (RCPs 4.5 y 8.5) se emplean para calcular el intervalo probable, definido como la banda de confianza del 90 %, calculada según la metodología del IPCC. Para ello, la media anual se multiplica por ± 1.62 ($\Phi^{-1}(0.95)$) la desviación estándar anual para obtener las trayectorias asociadas a los percentiles del 95 % y del 5 %. Las proyecciones horarias de los tres percentiles de ANMM (P95 %, P50 % y P5 %) se obtienen para los dos RCPs mediante un ajuste cuadrático de los datos anuales.

0.3.2.2. Modelado de la línea de costa

Las series horarias de oleaje en indefinidas y marea meteorológica correspondientes a los 5 RCMs junto con las tres trayectorias de ANMM calculadas para los dos escenarios de concentración, se emplean para obtener las proyecciones de evolución de la línea de costa hasta fin de siglo. Para ello, el clima marino en indefinidas se propaga a la costa empleando una metodología eficiente que aúna técnicas estadísticas y numéricas. A continuación, las propiadades en rotura alimentan el modelo de evolución de la línea de costa IH-LANS, previamente calibrado y validado en el periodo histórico 1990-2020 empleando dinámicas del reanálisis de ERA5. Proyecciones horarias de la línea de costa se obtienen en el periodo 2020 a 2100 considerando el muestreo de la incertidumbre asociada al clima mediante un conjunto de 30 evoluciones posibles, una para cada combinación de RCM, trayectoria de ANMM y RCP.

La propagación híbrida a la costa presenta dificultades por dos motivos. En primer lugar, a pesar de la eficiencia de los métodos híbridos, el coste computacional de propagar cada uno de los RCMs y trayectorias de ANMM para cada RCP desde 2020-2100 no es despreciable. Por otro lado, la variación temporal del ANMM se debe considerar tanto

en la parte estadística como en la numérica, debido a las implicaciones del aumento del calado en la propagación en profundidades reducidas. Para solucionar estos inconvenientes, la metodología original presentada por Camus et al. (2013) y modificada según lo descrito en la sección anterior para considerar una descripción más fidedigna del espectro a partir de particiones espectrales, se altera ligeramente. El problema del coste computacional se remedia generando una única base de interpolación representativa de todos los estados de mar y niveles futuros. Para ello, se realiza una doble selección empleando el algortimo de máxima disimilitud. La primera selección se aplica a cada serie temporal y da lugar a los 500 estados de mar representativos de cada RCM para cada RCP. El ANMM variable entre 2020 y 2100 se resuelve añadiendo a las selecciones, los niveles del mar más extremos para cada RCP, dando lugar a matrices de 1000 estados de mar y niveles, 500 estados de mar y nivel mínimo y 500 estados de mar y nivel máximo para cada combinación de RCM y RCP. A continuación, una segunda selección aplicada a los 10 bloques (5 RCMs y 2 RCPs) de 1000 estados de mar y niveles extremos da lugar a los 500 estados de mar y niveles representativos del conjunto de variables futuras, que se propagan numéricamente. De esta manera, las funciones de interpolación ajustadas a este subconjunto representativo, son capaces de reproducir cualquier estado de mar y nivel intermedio.

Las treinta series horarias de oleaje y nivel propagadas a la cabeza de los transectos de cálculo se emplean para forzar el modelo numérico IH-LANS. Para ello, se obtienen las propiedades en rotura asociadas a cada serie horaria entre 2020 y 2100 empleando las leyes de conservación del flujo de energía, la ley de Snell para la refracción, un criterio de rotura por fondo y correcciones por difracción para tener en cuenta la presencia de estructuras según Kamphius (2000) y Dabees (2000). A continuación, se resuelven los procesos de transporte longitudinal y transversal empleando los parámetros libres calibrados mediante asimilación en el periodo histórico 1990-2020, dando lugar a treinta series horarias de evolución de la línea de costa, una para cada combinación de RCM, percentil de ANMM y RCP, Figura 0.14. Del análisis de las series obtenidas, se aprecia el mayor peso que toma la variabilidad debida al oleaje y a la marea meteorológica en el medio plazo (panel b) de la Figura 0.14). Sin embargo, a fin de siglo, la mayor

dispersión entre los diferentes percentiles de ANMM hacen que la variabilidad en la costa debido al ANMM supere a la debida al RCM, tal y como apunta d'Anna et al. (2022b) y se muestra en el panel f) de la Figura 0.14.
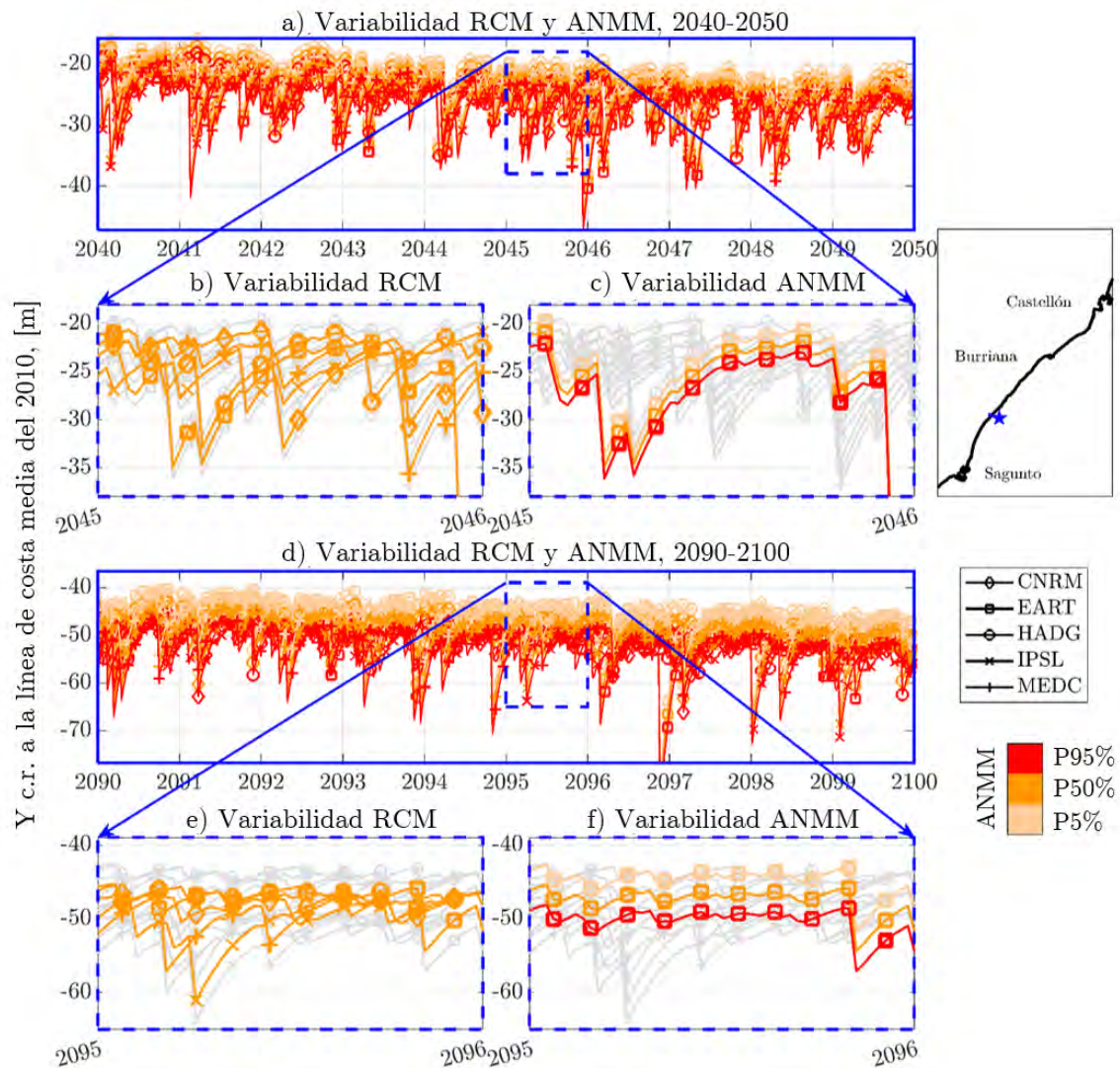
Figura 0.14: Evoluciones de la línea de costa en un trasecto situado en la playa de Llosa considerando diferentes RCMs y trayectorias de ANMM. En los diferentes paneles se resalta la variabilidad debida a los RCMs y a los percentiles de ANMM en el medio y largo plazo.

0.3.2.3. Resultados del modelado

La resolución acoplada de procesos longitudinales y transversales permite resolver conjuntamente varias escalas temporales, desde tormentas hasta cambios decadales. Las series de evolución de la línea de costa proyectadas están influidas por procesos longi-

tudinales de largo plazo, transversales debidos a tormentas y retrocesos de largo plazo debidos al transporte transversal por ANMM. La componente de largo plazo de la línea de costa (denotada estructural de aquí en adelante) se emplea para calcular retrocesos permantentes y áreas de playa perdidas. Los cambios estructurales definen la línea base en la que se producen erosiones episódicas y recuperaciones debido a fluctuaciones de corto plazo. Adicionalmente, el análisis extremal no estacionario permite identificar retrocesos asociados a determinadas probabilidades de ocurrencia y su variabilidad a lo largo del siglo.
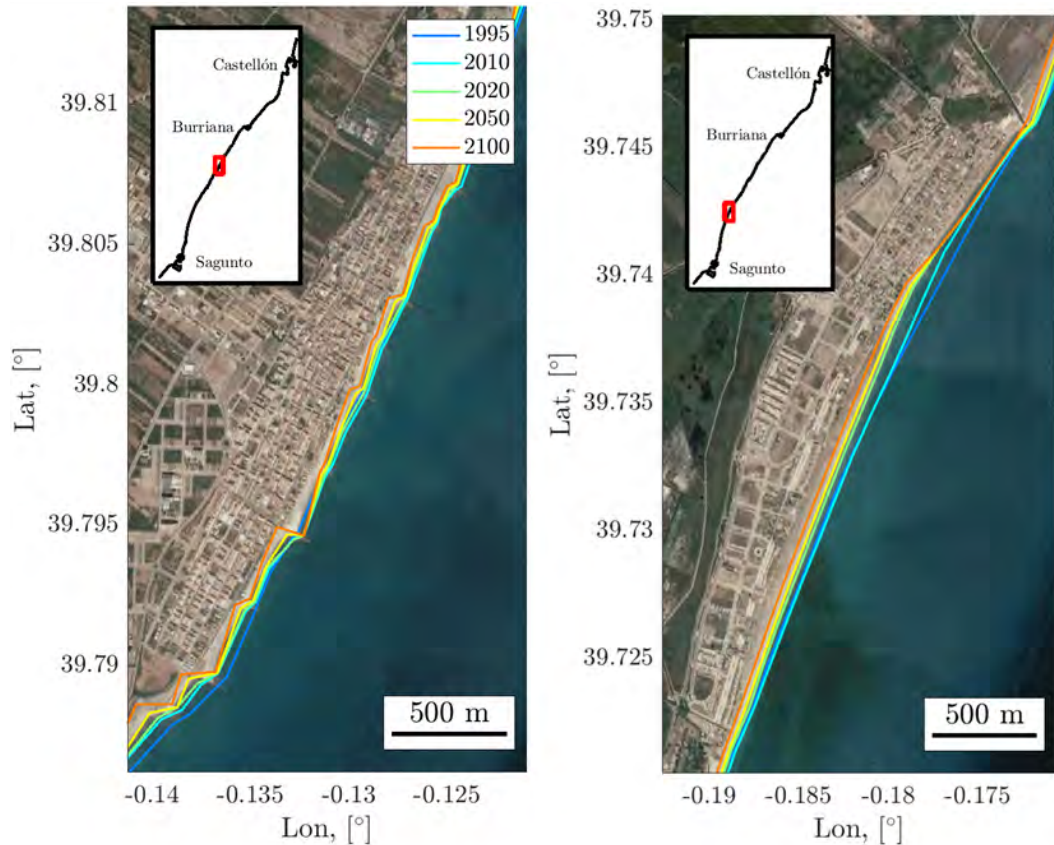
Figura 0.15: Línea de costa estructural en diferentes fechas en las playas de Moncófar (panel izquierdo) y Almenara-Casablanca (panel derecho). Las lineas sólidas (1995 y 2010) se corresponden con las líneas de reanálisis mientras que las líneas de 2050 y 2100 representan la media de los RCMs y de las diferentes trayectorias de ANMM para el RCP8.5.

Sustrayendo las fluctuaciones de corto plazo de las series temporales de evolución de la línea de costa se obtienen los cambios estructurales. Las posiciones estructurales en una

fecha determinada se obtienen promediando la evolución temporal de la linea de costa durante un periodo de dos años. En la Figura 0.15 se muestran las líneas de costa estructurales en 2050 y 2100 promediadas en los diferentes RCMs y percentiles de ANMM para el RCP8.5 en las playas de Moncófar (panel izquierdo) y Almenara (panel derecho).
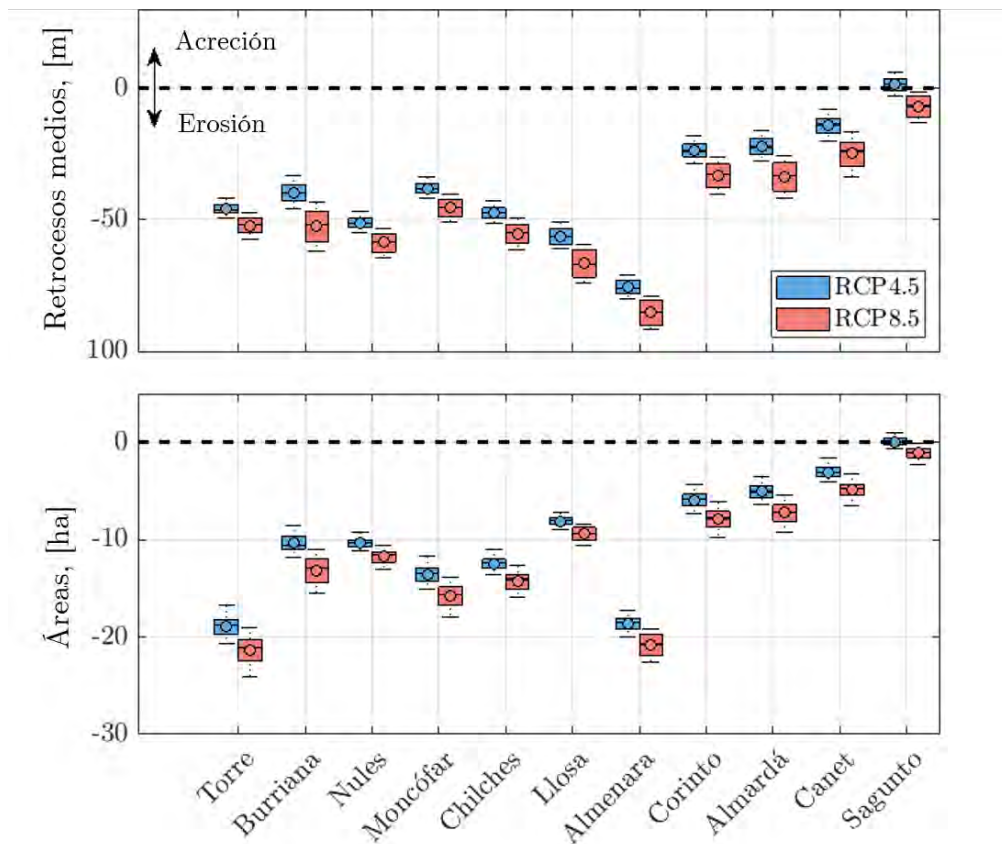
Figura 0.16: Retrocesos medios y áreas erosionadas a final de siglo con respecto a la línea media del 2010 para los RCPs 4.5 y 8.5. Los diagramas de cajas sintetizan los 15 valores correspondientes a los diferentes RCMs y percentiles de ANMM considerados para cada RCP.

Las posiciones estructurales en 2100 para los RCPs 4.5 y 8.5 se emplean para calcular retrocesos permanentes en las diferentes playas (panel superior de la Figura 0.16) y el área de playa seca perdida (panel inferior de la Figura 0.16). Los resultados muestran que, de media, el retroceso a fin de siglo en el tramo de estudio es del orden de 50 metros. Sin embargo, ese valor es superado en las playas de Llosa o Almenara debido a la

retención de sedimento en las playas del norte del tramo (Nules, Moncófar y Chilches). Por otro lado, a pesar de la tendencia a retener sedimento de las playas del sur debido al puerto de Sagunto, todas ellas experimentan un retroceso debido al mayor peso del ANMM en la respuesta de la línea de costa.

Con el fin de evaluar el valor de recreación de la playa durante la temporada estival, se ha calculado la posición media de la línea de costa entre los meses de mayo y septiembre en 2050 y 2100. Los resultados, mostrados en la Figura 0.17, muestran que el área efectiva de playa durante la temporada de baño se reducirá dramáticamente a fin de siglo, lo que tendrá consecuencias negativas para la economía de las zonas costeras.

La gestión y planificación de la costa necesita conocer la naturaleza de los procesos a los que se enfrenta para así plantear medidas de adaptación específicas. Por ello, se ha realizado un análisis de la varianza para evaluar la contribución relativa de los diferentes procesos modelados a los cambios en la línea de costa a fin de siglo, Figura 0.18. Del análisis de los resultados, se aprecia que el transporte longitudinal y el retroceso por ANMM tienen una influencia muy importante en la evolución de la línea de costa a fin de siglo. La contribución relativa del ANMM aumenta en el RCP8.5 con respecto al RCP4.5 de media un 34 % a costa de una menor contribución de los procesos longitudinales y transversales.

Los retrocesos extremos debidos a tormentas se pueden obtener del análisis gracias al modelado conjunto de procesos de corto y largo plazo. Dado que la evolución de la línea de costa es un proceso no estacionario en el que los cambios a largo plazo actúan como una tendencia, los retrocesos extremos de corto plazo se estudian siguiendo el modelo no estacionario de Mentaschi et al. (2016). Los resultados de la aplicación del análisis de extremos no estacionario se muestran en la Figura 0.19. La variación en el tiempo de los retrocesos de corto plazo de 5 y 50 años de periodo de retorno para el RCP8.5 se muestran junto con la evolución de la línea base o estructural en tres perfiles diferentes. Mientras que el retroceso de 5 años de periodo de retorno tiene un amplitud de aproximadamente 15 metros con respecto a la línea base, el de 50 años asciende a

Figura 0.17: Líneas de costa en la temporada estival (mayo-septiembre) en 2050 y 2100 en Torre (panel superior), Moncófar (panel intermedio) y Almenara (panel inferior). Las líneas sólidas representan la mediana y las bandas se corresponden con la banda de confianza del 50 % de las 15 combinaciones de RCM y trayectorias de ANMM para el RCP8.5.
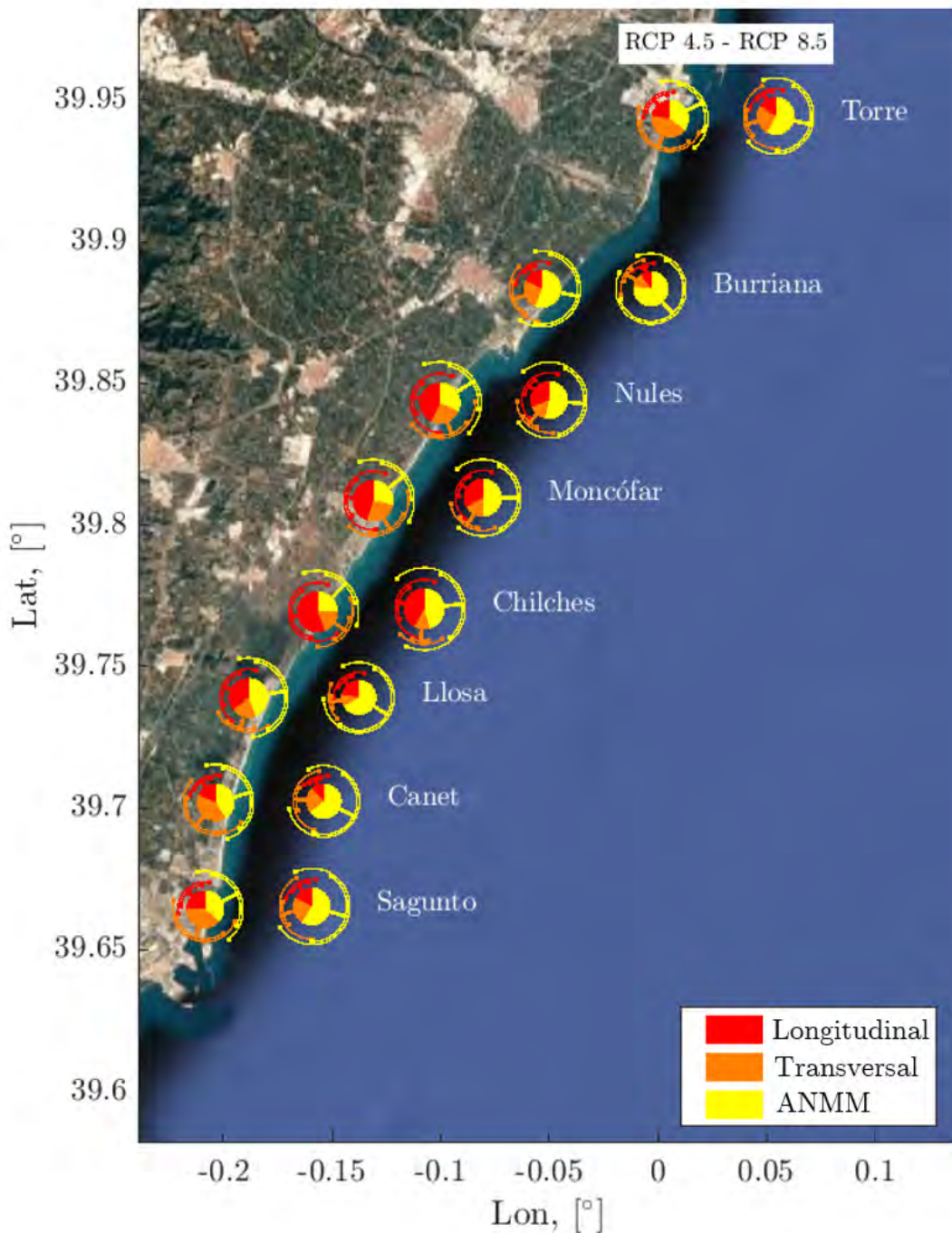
Figura 0.18: Contribución relativa de los diferentes procesos modelados a los cambios en la línea de costa para los RCPs 4.5 y 8.5. Los sectores circulares representan la mediana y los anillos concéntricos los valores máximo y mínimo de las diferentes combinaciones de RCM y trayectorias de ANMM.

más de 20 metros. No se aprecian grandes variaciones en la amplitud de los retrocesos extremos a fin de siglo. Pese a ello, debido al retranqueo de la línea base por procesos de largo plazo, los eventos extremos producirán retrocesos totales cada vez mayores que expondrán a más población y bienes en el frente costero.
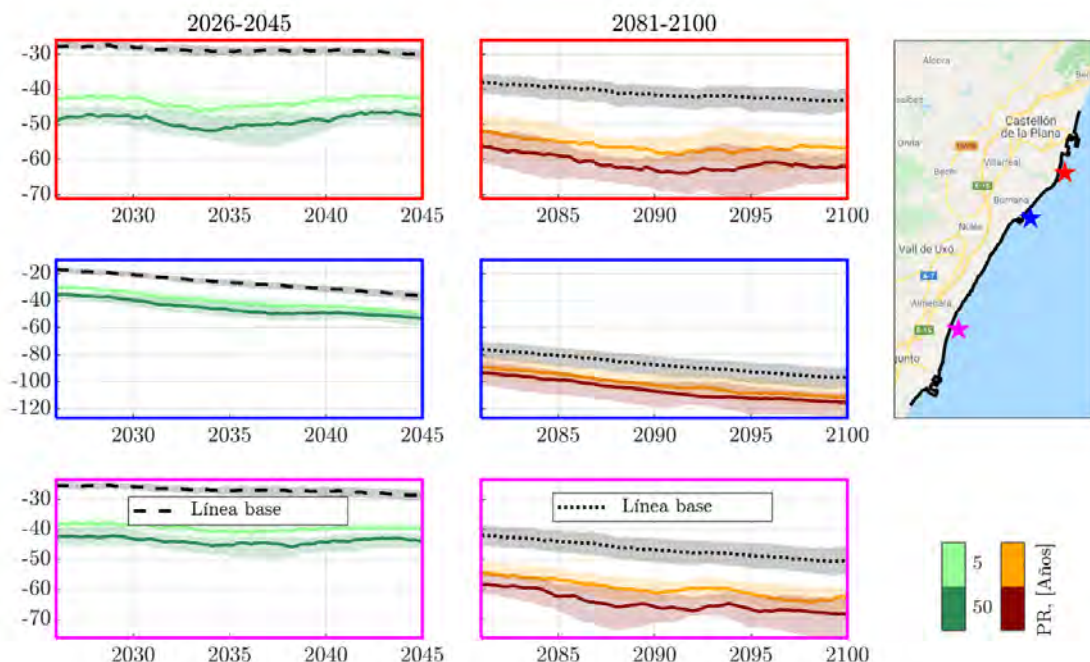
Figura 0.19: Retrocesos no estacionarios calculados en tres transectos para el RCP8.5. La línea negra rayada/punteada representa la línea base estructural en el periodo 2026-2045/2081-2100. Las líneas sólidas representan la mediana y el área sombreada la banda de confianza del 50 % del conjunto de simulaciones.

Con el fin de localizar el el plano la magnitud de los retrocesos extremos, en la Figura 0.20 se muestra la representación espacial de los retrocesos de 5 y 50 años de periodo de retorno junto con las líneas base en los años 2045 y 2100. Se pone de manifiesto que las tormentas reducirán al mínimo el área de playa disponible en 2045. A fin de siglo, las infraestructuras y servicios en primera línea se verán muy perjudicados por fenómenos extremos si no se toman medidas.
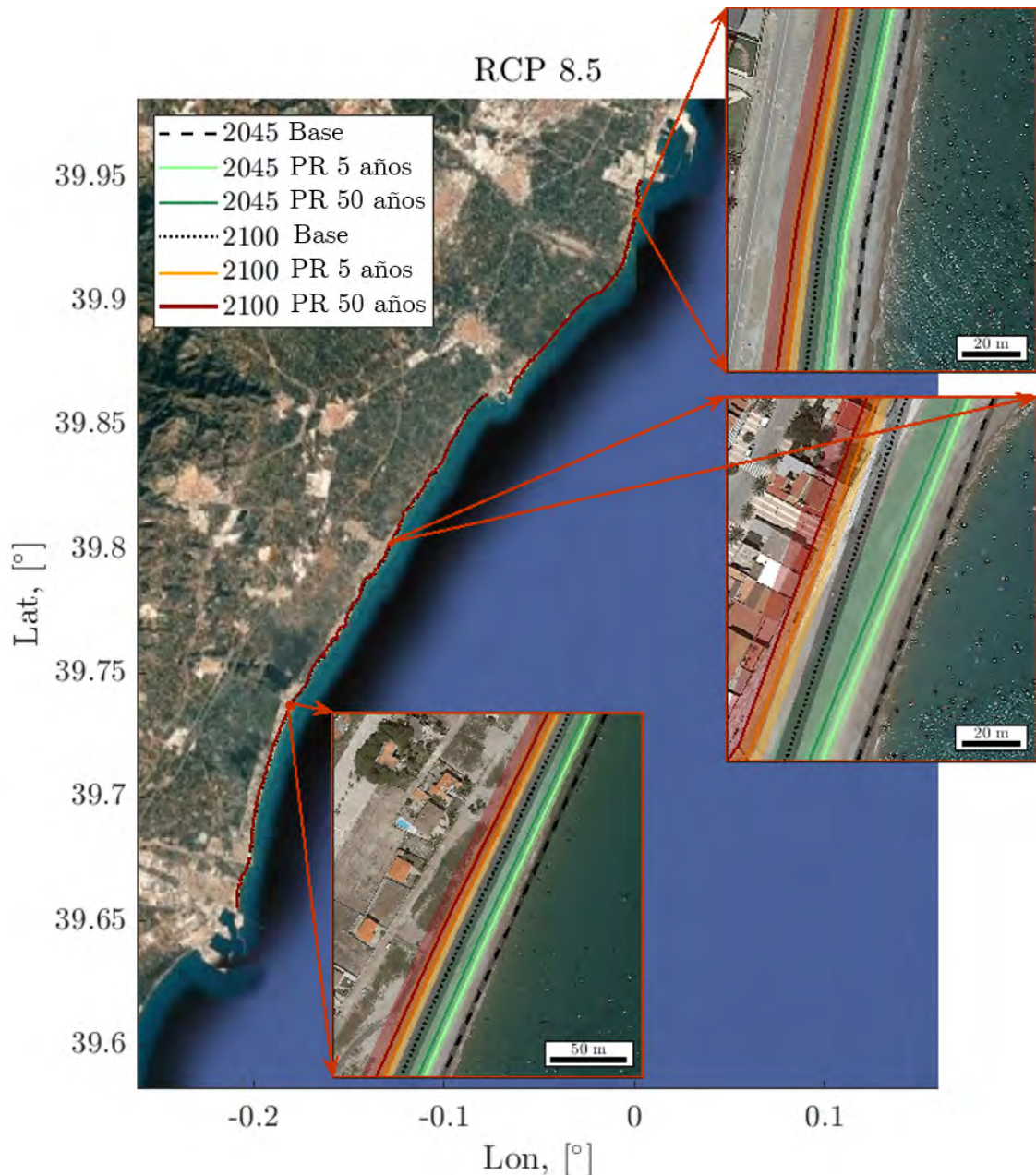
Figura 0.20: Representación espacial de los retrocesos de 5 y 50 años de periodo de retorno en 2050 y 2100 para el RCP8.5. Las líneas sólidas representan la mediana y las bandas se corresponden con el intervalo de confianza del 50 %.

0.4. Aplicación de IH-LANS para predecir la inundación teniendo en cuenta la erosión de la costa

La inundación y la erosión son las amenazas más relevantes de las zonas costeras y, aunque están íntimamente relacionadas, la complejidad inherente a la escala de los procesos hace que se estudien de forma aislada dando lugar a estimaciones potencialmente erróneas. Con el objetivo de progresar en este campo, en esta sección se tratan los siguientes temas: a) el desarrollo de una metodología para traducir los movimientos unidimensionales de la línea de costa obtenidos de modelos de evolución a topobatimetrías bidimensionales para estudios de inundación; b) la cuantificación de los efectos de no considerar el acoplamiento de la erosión y la inundación en estudios de cambio climático y c) la cuantificación de la importancia relativa de la incertidumbre climática en las proyecciones de inundación (Figura 0.21).
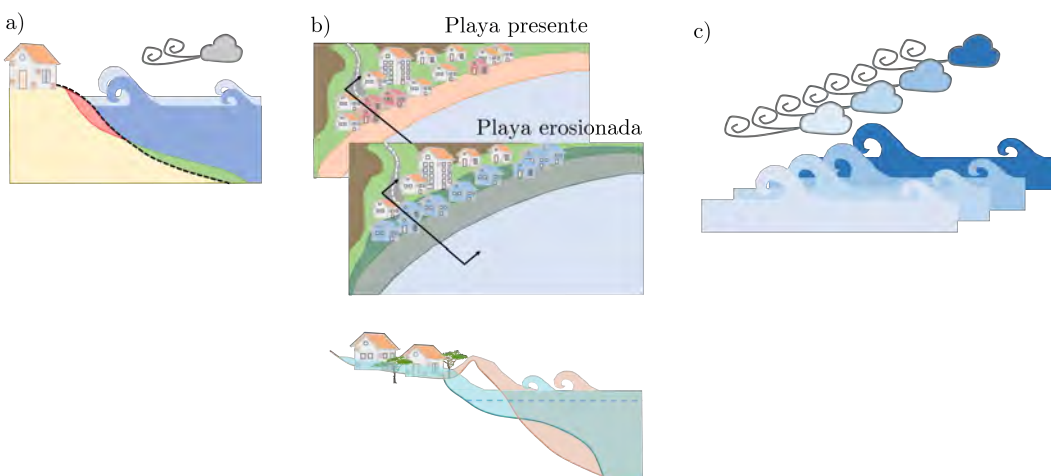
Figura 0.21: Representación gráfica de los temas tratados en esta sección.

Para ello, se ha desarrollado una cadena de cálculo formada por modelos estadísticos y de procesos para generar tormentas sintéticas, propagar los estados de mar extremos a la costa, calcular la hidrodinámica afectada por cambios morfodinámicos de corto y largo plazo y propagar la inundación sobre topobatimetrías que consideran la erosión costera por procesos longitudinales y transversales por erosión de tormenta y ANMM. La incertidumbre climática se muestrea considerando la variabilidad en las tormentas

mediante modelado estadístico, dos escenarios de concentración diferentes, el oleaje obtenido de cinco configuraciones distintas de modelos globales y regionales climáticos y tres trayectorias de ANMM. De los resultados se pone de manifiesto que el no considerar la erosión en las proyecciones de inundación costera puede tener implicaciones negativas para la gestión de la costa, dando lugar a planes de adaptación deficientes y a repartos y cuantificaciones de recursos inapropiados.

0.4.1. Metodología

Para poder incorporar los cambios morfológicos en las proyecciones de inundación, se construye una cadena de cálculo compuesta de modelos estadísticos y de procesos. El dominio numérico debe ser correctamente configurado para satisfacer las necesidades de los modelos de procesos. En primer lugar, se debe generar la malla de cálculo para la propagación de oleaje considerando la localización de los puntos de forzamiento, en los cuales se aplicará el modelo estadístico de generación sintética de tormentas. Dependiendo de la resolución del dominio general, dominios de detalle anidados de mayor resolución pueden ser necesarios. A continuación, se discretiza la línea de costa en un conjunto de perfiles de baja resolución para poder resolver la ecuación de gobierno de la línea de costa mediante IH-LANS y ejecutar el modelo hidro-morfodinámico de tormentas XBeach (Roelvink et al., 2009) para calcular la cota de inundación. Un conjunto de perfiles adicional de alta resolución es necesario para transferir los cambios morfológicos calculados en los perfiles de baja resolución al modelo digital del terreno. Esta discretización fina es necesaria debido a que el espaciamiento de los perfiles de baja resolución ($\mathcal{O}(100m)$) no es compatible con la resolución espacial del modelo digital del terreno empleado en estudios de inundación ($\mathcal{O}(5m)$). Asimismo, la reducción del espaciamiento de los perfiles en los que se ejecuta IH-LANS podría comprometer el cumplimiento de la condición de Courant del transporte longitudinal y aumentaría enormemente el coste de cómputo de la respuesta hidro-morfodinámica calculada con XBeach. Por tanto, la discretización de alta resolución es necesaria así como una interfaz de comunicación entre los perfiles de baja y alta resolución basada en interpolación espacial por distancia.
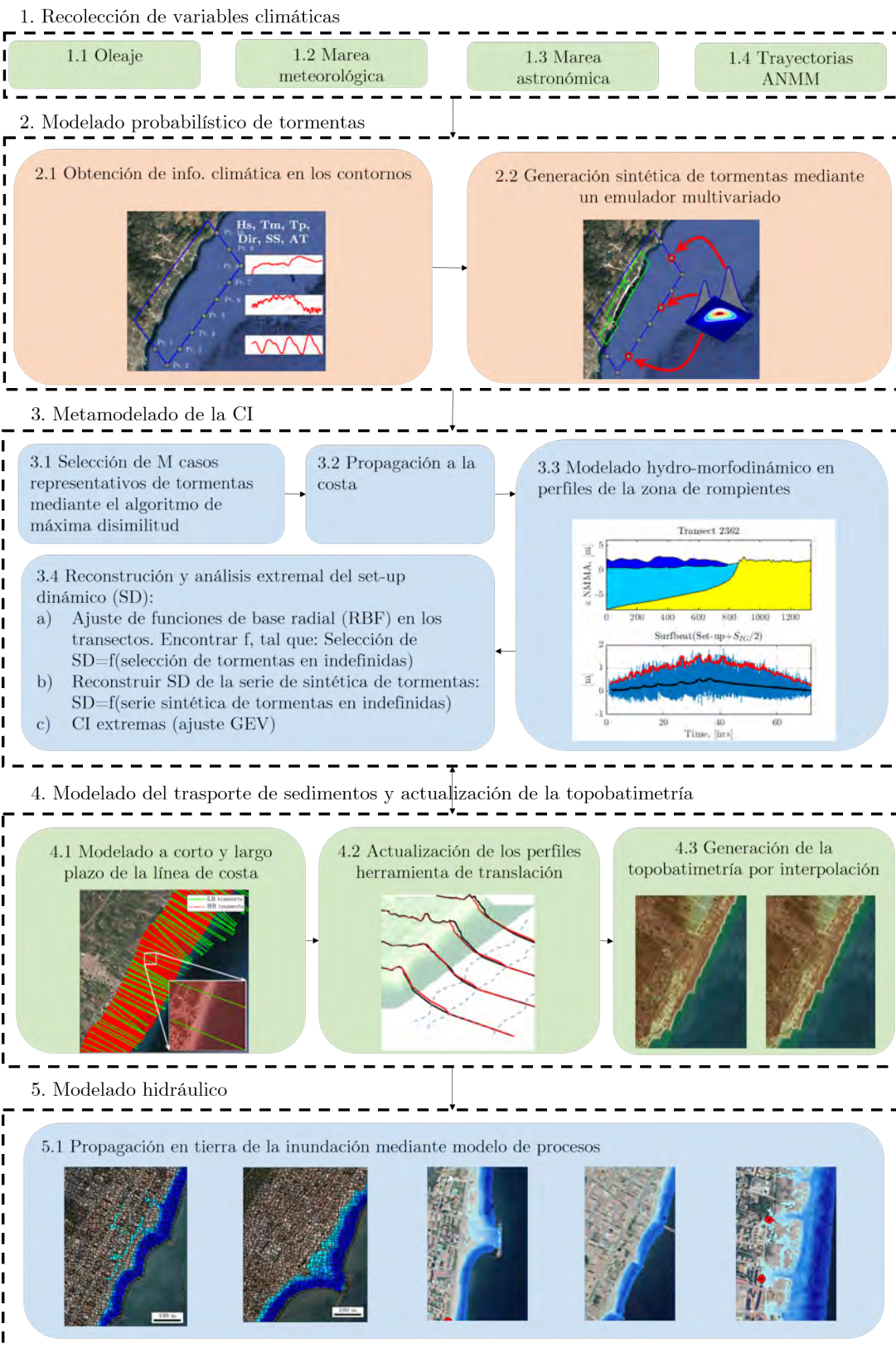
Figura 0.22: Diagrama de flujo de la metodología para obtener proyecciones de inundación considerando la erosión costera.

Una vez se han definido los dominios de cálculo, el primer paso de la metodología que integra erosión e inundación es la recolección de la información climática. Para ello, las proyecciones dinámicas de oleaje y marea meteorológica generadas por IHCantabria (2020), la marea astronómica y las proyecciones de ANMM (Oppenheimer et al., 2019) se recolectan en los puntos de forzamiento offshore del dominio de cálculo. A continuación, para considerar todas las combinaciones de oleaje y nivel representativas de tormentas futuras, se infere un emulador de tormentas que se emplea posteriormente para generar una muestra de tormentas sintéticas. El núcleo del emulador es un módulo estadístico capaz de modelar variables lineales y circulares en varios puntos del dominio y preservando la dependencia espacial, estacionalidad y no estacionariedad (segundo paso en la Figura 0.22).

El tercer paso consiste en el metamodelado de la cota de inundación (CI). En este caso, con el fin de emplear modelos de procesos manteniendo la eficiencia y el coste de cómputo de modelos empíricos tipo Stockdon et al. (2006) o Gomes da Silva et al. (2018) pero resolviendo la física de los fenómenos relevantes, se ha calibrado un metamodelo basado en los transectos de baja resolución. Para ello, de la muestra completa de tormentas sintéticas caracterizadas por parámetros de oleaje y nivel en los puntos de forzamiento, se selecciona un conjunto representativo mediante el algoritmo de máxima disimilitud (Camus et al., 2011). A continuación, el conjunto representativo de tormentas se propaga a la cabeza de los perfiles empleando el modelo espectral SWAN (Booij et al., 1999). En el siguiente paso se fuerza el modelo XBeach en configuración surfbeat en los perfiles de baja resolución y se obtiene la CI de cada tormenta simulada. El modelo estadístico se configura mediante funciones de base radial (RBFs) que se ajustan a la relación entre las propiedades de la tormenta y el set-up dinámico (SD) transecto a transecto. SD se define como la elevación sostenida del oleaje debido a la rotura del oleaje (set-up estático) y una fluctuación de largo periodo debido a la energía infragravitatoria. El último paso del cálculo de la CI consiste en determinar la CI de n años periodo de retorno como $CI_n = (SD + MA + MM)_n + ANMM$, donde $(SD + MA + MM)_n$ es la CI de n años de periodo de retorno por set-up dinámico, marea astronómica y marea meteorológica obtenido a partir de un ajuste de máximos anuales mediante una función

generalizada de extremos (GEV).

El cuarto paso es el modelado del trasporte de sedimentos y la actualización de la topobatimetría. Para ello, las proyecciones de evolución de la línea de costa calculadas con IH-LANS y descritas en la sección anterior, se emplean para generar las topobatimetrías futuras. Las posiciones de corto y largo plazo de la línea de costa se procesan para alimentar el modelo de traslación de perfil ShoreTrans (McCarroll et al., 2021) para generar nubes de puntos a partir de las cuales se interpola la morfología futura considerando la erosión. Los pasos tres y cuatro de la metodología están interconectados (resaltado con una doble flecha en la Figura 0.22), ya que los cambios de largo plazo se emplean para alimentar el modelo hidro-morfodinámico y calcular la CI. Asimismo, XBeach puede ser ejecutado considerando la evolución morfodinámica para así evaluar conjuntamente los cambios de largo y corto plazo en el cálculo de la CI.

El quinto paso consiste en la propagación de la inundación en tierra empleando modelado hidráulico. La CI_n obtenida en cada transecto de baja resolución se emplea para forzar el modelo 2D de inundación RFSM-EDA (Jamieson et al., 2012). RFSM-EDA es un modelo de procesos eficiente que resuelve una versión simplificada de las ecuaciones de Saint-Ventan en una malla computacional no uniforme que se adapta al terreno y considera una rugosidad variable espacialmente.

0.4.1.1. Modelado probabilístico de tormentas

En la literatura, varios estudios han propuesto modelos multivariados para aumentar la población de eventos de tormenta físicamente posibles susceptibles de generar inundación (Heffernan and Tawn, 2004; Wahl et al., 2016; Sayol and Marcos, 2018; Lin-Ye et al., 2016; Lucio et al., 2020). Estos estudios se desmarcan de la hipótesis que los valores máximos de parámetros de oleaje y nivel extremos que contribuyen a la CI y sus combinaciones extremas ya se han observado. De entre los métodos disponibles, los basados en cópulas son ampliamente usados, ya que permiten ajustar las distribuciones marginales de las variables y su estructura de depencia de forma independiente (Sal-

vadori and De Michele, 2004). Sin embargo, uno de los mayores retos en la emulación sintética es la determinación de la estructura de dependencia entre variables lineales (e.g. altura de ola, periodo, duración de la tormenta) y las variables circulares (e.g. dirección del oleaje). Es práctica habitual disociar ambos tipos de variables modelando las variables circulares a partir de métodos de regresión anidados a cópulas que se ajustan a variables lineales (Lin-Ye et al., 2016), linealizar las variables circulares para incluirlas en la cópula (Lucio et al., 2020) o aislar las variables circulares e inferirlas mediante relaciones condicionales a partir de la variables lineales modeladas en la cópula (Wahl et al., 2016).

A pesar de la variedad de métodos para modelar conjuntamente variables lineales y circulares, uno de los mayores inconvenientes de los emuladores de tormentas es que no pueden aplicarse en escalas regionales ya que están diseñados para emular el oleaje y nivel en un único punto del espacio. Debido a las dificultades a la hora de modelar variables lineales y circulares conjuntamente, la generalización de emuladores climáticos a n puntos de forzamiento no es directa. Para superar esta limitación, se propone un modelo que combina un emulador multivariado a escala mensual (EMM) basado en cópulas Gaussianas (Lucio et al., 2020) y un modelo multivariado direccional (MMD) (Mardia et al., 2008) cuya función de densidad es:

$$
\begin{aligned}
f_{H_{s_{iw}}, T_{m_{iw}}, Dir_{iw}, SS_{iss}}&(H_{s_{iw}}, T_{m_{iw}}, Dir_{iw}, SS_{iss}) = \\
&= \underbrace{f(H_{s_{iw}}, T_{m_{iw}}, Dir_j, SS_{iss})}_{EMM} \cdot \underbrace{f(Dir_{iw \neq j}|Dir_j)}_{MMD}
\end{aligned}
\tag{0.6}
$$

dónde H_s es la altura de ola significante; T_m es el periodo medio; Dir es la dirección media; SS es la marea meteorológica; $iw \in [1, 2, ..., n]$ son los puntos directores de oleaje, n es el número total de puntos emulados; iss es el punto de forzamiento de marea meteorológica; y j es el punto de vínculo entre el EMM y el MMD. Asociada a cada tormenta, se extraen el periodo de pico (T_p) y la marea astronómica (MA) mediante regresión heterocedástica y muestreo aleatorio de las series reconstruidas respectivamente (ver Lucio et al. (2020)).

El modelo representa una generalización a n puntos de forzamiento de la relación condicional entre variables lineales y circulares propuesta por Wahl et al. (2016). El acoplamiento entre el EMM y el MMD se materializa mediante una variable circular vínculo en el punto j que se modela dentro del EMM y a partir de la cual se extraen las direcciones en el resto de puntos directores ($iw \neq j$) a partir del MMD. Este enfoque es válido si la dirección de vínculo captura la dependencia entre variables lineales y el resto de direcciones emuladas, lo que permite relajar la dependencia condicional modelada mediante el MMD a una única dirección modelada en el EMM. El emulador captura la estacionalidad de las tormentas gracias a ajustar el EMM a escala mensual.

0.4.1.2. Proyección de la topobatimetría costera

El empleo de modelos de evolución de largo plazo implica, generalmente, que la morfología costera se condensa en una variable de referencia (i.e. la posición de la línea de costa). Esta simplificación permite reducir el coste computacional de los modelos aumentando la escala espacio-temporal de aplicación. Sin embargo, la posición de la línea de costa no se puede emplear directamente como entrada para evaluar el efecto de la erosión en la inundación. Por tanto, se ha desarrollado un método para trasladar los cambios en la línea de costa al modelo digital del terreno que usan como base los modelos de inundación.

El método para generar topobatimetrías futuras a partir de los resultados de los modelos de evolución de la línea de costa se muestra en la Figura 0.23. Tras definir la topobatimetría presente, se extrae la posición de la línea de costa debida a procesos longitudinales Y_l y la debida a procesos transversales Y_c del perfilado de baja resolución. A continuación, se genera un perfilado de alta resolución tomando como base el de baja resolución pero con perfiles más próximos ($\mathcal{O}(5m)$) (Figura 0.23b). La topobatimetría presente se proyecta en los perfiles de alta resolución y los cambios en la línea de costa se transfieren de los perfiles de baja a alta resolución mediante interpolación (Figura 0.23c). La herramienta de traslación de perfiles ShoreTrans (McCarroll et al., 2021) se aplica en los perfiles de alta resolución recibiendo como dato de partida los cambios en la línea de costa y el ANMM y actualiza la geometría del perfil. A conti-

nuación se transforma las cotas de los perfiles del sistema de referencia local del perfil al general, dando lugar a una nube de puntos tridimensional. La nube de puntos se interpola mediante el algoritmo de distancias inversas (IDW) implementado en ArcGIS y se genera la topobatimetría costera futura (Figura 0.23e).
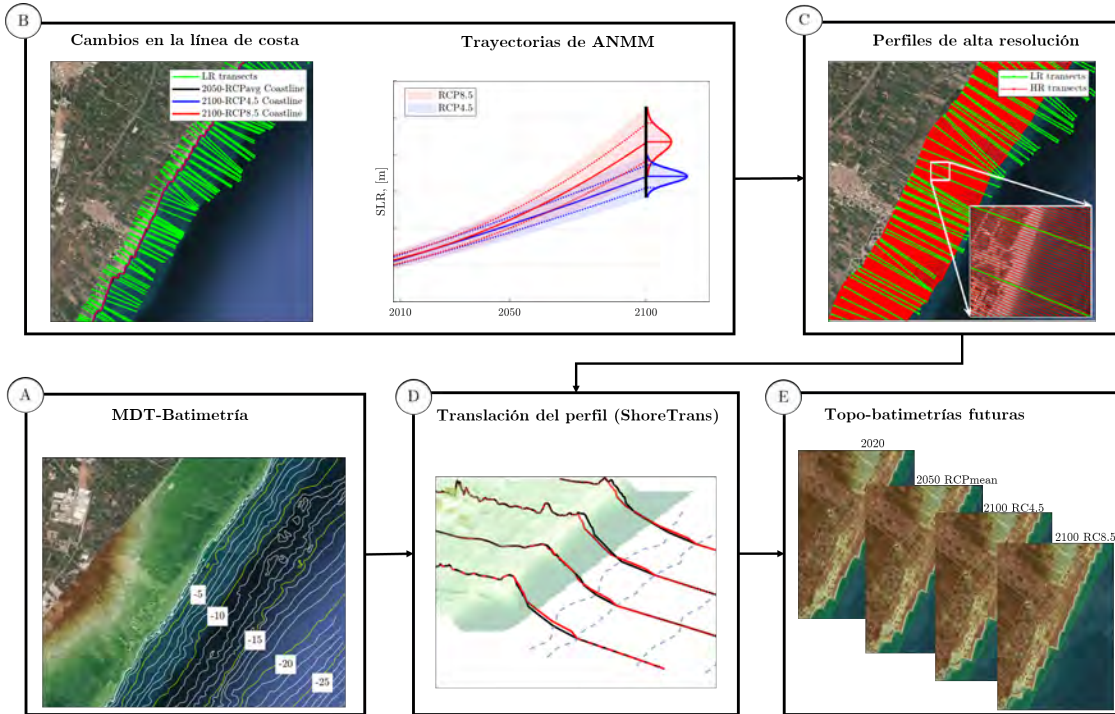
Figura 0.23: Actualización de la topobatimetría costera a partir de cambios en la línea de costa y del ANMM.

Herramienta de traslación del perfil

La piedra angular de la metodología es modelo de traslación del perfil ShoreTrans. ShoreTrans es una herramienta basada en reglas heurísticas que actualiza el perfil costero activo teniendo en cuenta el ANMM según Atkinson et al. (2018), el transporte longitudinal según la teoría clásica de los modelos de una línea y la erosión de tormentas según Kinsela et al. (2017). Los efectos de la rigidización de la costa se tienen en cuenta según los trabajos de Beuzen et al. (2018).

La cinemática del perfil asociada a los diferentes procesos modelados se representa en la Figura 0.24. En primer lugar, el perfil se parametriza para poder aplicar las reglas de

traslación, Figura 0.24a. Los procesos de largo plazo (longitudinales y ANMM) afectan al perfil activo que se extiende desde la berma (y_b, z_b) hasta la profundidad de cierre (y_{dc}, z_{dc}). Por otro lado, los procesos de corto plazo generan una erosión entre la parte superior del frente de playa (y_{tb}, z_{tb}) y la parte inferior (y_{bb}, z_{bb}) ; y una acreción que se extiende desde el punto de inflexión (y_p, z_p) hasta la parte inferior de la barra de tormenta (y_{sb}, z_{sb}). Dependiendo del proceso, el perfil responderá de forma diferente:

- Con respecto al transporte longitudinal, el perfil activo se desplaza sin cambiar de forma hacia el mar en el caso de acreción y hacia tierra en el caso de erosión (Figura 0.24b).

- La erosión de corto plazo da lugar a un retroceso del frente de playa y la deposición de ese material mar adentro formando una barra y dando lugar a un perfil más disipativo (Figura 0.24c). Durante este proceso, el volumen de sedimento en el perfil no cambia, simplemente se redistribuye.

- La cinemática asociada al ANMM consiste en un ascenso del perfil activo siguiendo al aumento del nivel y de un retroceso hacia tierra que garantiza la conservación de sedimento en el perfil (Figura 0.24d). En el caso de un perfil de Dean (Dean, 1991), la traslación hacia tierra del perfil de ShoreTrans coincide con el retroceso estimado mediante la regla de Bruun (Bruun, 1962).

0.4.2. Caso de aplicación

Con el fin de ilustrar la metodología, el proceso de cálculo se aplica en el tramo de costa de 40 kilómetros entre Castellón y Sagunto estudiado anteriormente. Para ello, se parten de las proyecciones de evolución de la línea de costa multimodelo que se obtuvieron tras la ejecución de IH-LANS.

0.4.2.1. Grados de acoplamiento erosión-inundación

Con el fin de analizar la relevancia del acoplamiento de la erosión y la inundación en diferentes escalas, se ha realizado un estudio de la influencia del grado de acoplamiento (CA) erosión-inundación en la cota de inundación y en el área inundada. Se han incluido cuatro CA dependiendo de los procesos considerados. Esos diferentes planteamientos son: 1) full CA, considera los cambios de corto y largo plazo; 2) short-term (ST) CA, só-

a) Parametrización

c) Erosión de corto plazo

b) Transporte longitudinal

d) ANMM
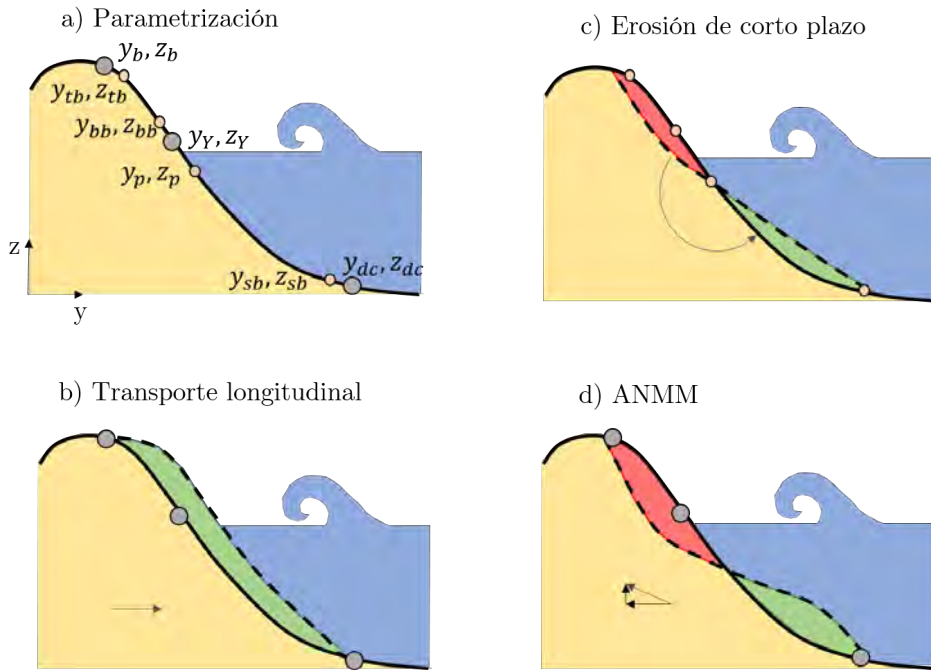
Figura 0.24: Esquema de la cinemática del perfil asociada a los diferentes procesos modelados.

lo tiene en cuenta los cambios a corto plazo debidos a tormentas; 3) long-term (LT) CA, incluye únicamente los cambios de largo plazo por transporte longitudinal y ANMM y 4) no CA, en el que la topobatimetría presente no se actualiza.

Para todos los CAs, la hidrodinámica en la zona de rompientes y la inundación se modelan empleando XBeach y RFSM-EDA respectivamente. El no CA no considera la erosión ni en la CI ni en la propagación de la inundación en tierra. Por otro lado, el full CA considera los cambios de corto y largo plazo en el cálculo hidro-morfodinámico y en la inundación costera. Finalmente los short- y long-term CA limitan la consideración de la erosión en las étapas de cálculo de la CI y de la inundación. En el Cuadro 0.1 se resumen las principales características de los CA considerados.

	CI (XBeach)		Inundación (RFSM-EDA)
CA	Transectos (procesos)	Módulos activados	Topografía (procesos)
Full	ShoreTrans (Longitudinal y ANMM)	Hidro y Morfo	ShoreTrans (Longitudinal, ANMM y corto plazo)
Short-term	Initial (presente)	Hidro y Morfo	ShoreTrans (Corto plazo)
Long-term	ShoreTrans (Longitudinal y ANMM)	Hidro	ShoreTrans (Longitudinal y ANMM)
No	Inicial (presente)	Hidro	Inicial (presente)

Cuadro 0.1: Resumen de las características de modelado de los diferentes CAs.

0.4.2.2. Generación de tormentas sintéticas

Para la generación de eventos sintéticos, se emplea el emulador multivariado regional alimentado con la base de datos de oleaje y nivel empleada en la elaboración de las proyecciones de erosión. La base de datos climática se compone de proyecciones dinámicas multimodelo de oleaje de IHCantabria (2020) en los periodos 1986-2005, 2026-2045 y 2081-2100, series temporales de marea astronómica reconstruidas de la base de datos de TPXO7.2 (Egbert and Erofeeva, 2002) y las trayectorias de ANMM de (Oppenheimer et al., 2019) correspondientes a diferentes percentiles. El emulador de tormentas genera eventos extremos definidos por parámetros de oleaje y nivel en tres puntos directores (puntos 3, 6 y 9), representativos de los diez puntos de forzamiento del dominio de cálculo. En el EMM se simularon las variables [H_{s3}, H_{s6}, H_{s9}, T_{m3}, T_{m6}, T_{m9}, Dir_6, SS_5] mientras que en el MMD se infirieron las variables [Dir_3, Dir_9] condicionadas por Dir_6. En este caso, el punto de vínculo entre el EMM y el MMD fue el punto 6, situado en la parte central del dominio de cálculo.

El modelo estadístico se aplicó en a cada una de las 25 combinaciones de RCM (HADG, IPSL, CNRM, EART, MEDC), RCP(4.5 y 8.5) y periodo de tiempo (1986-2005, 2026-2045, 2081-2100) dando lugar a 100,000 eventos sintéticos por combinación. A modo de ejemplo, en la Figura 0.25 se muestra la habilidad del EMM para reproducir las relaciones estadísticas entre las variables H_{s6}, T_{m6}, SS_5 y Dir_6 en una de las combinaciones. Las observaciones y la emulación se representan en formato matricial. Los paneles A-F ilustran la dispersión entre los datos observados de tormentas y los simulados, los paneles G-J muestran los ajustes de la función generalizada de extremos anual univariada H_{s6}, T_{m6} y SS_5 y la función de densidad empírica polar de Dir_6. Finalmente, los paneles K-P representan la comparación entre las funciones de densidad bivariadas empíricas de las observaciones y de la emulación, y demuestran cualitativamente la bondad del ajuste del modelo.
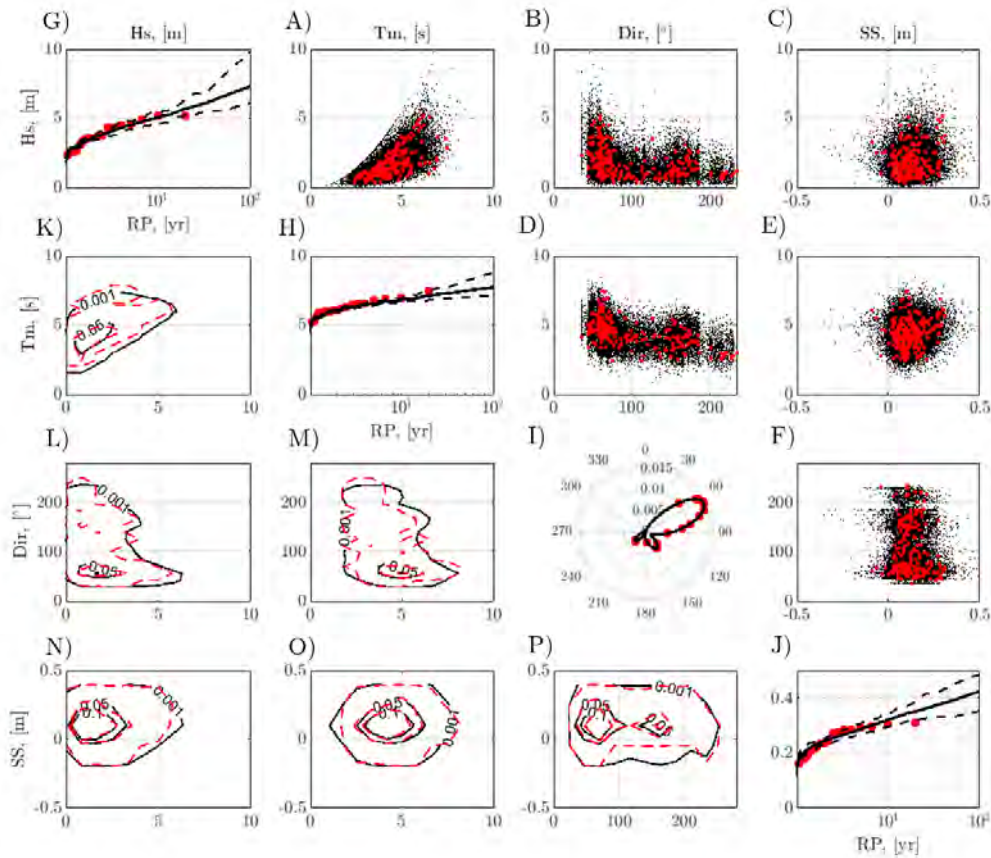
Figura 0.25: Validación del emulador multivariado en uno de los puntos directores (punto 6) coincidente con la dirección de vínculo del modelo multivariado direccional. Las observaciones (rojo) se comparan con los datos simulados (negro).

0.4.2.3. Metamodelado de la cota de inundación

La CI se obtiene como la suma del set-up dinámico (SD), de la marea astronómica (MA), de la marea meteorológica (MM) y del aumento del nivel medio del mar (ANMM). El cálculo de la CI asociada a los 100,000 eventos de las 25 combinaciones de RCM-RCP y Periodo para los diferentes grados de acoplamiento erosión-inundación (full, long-term (LT), short-term (ST) y no) se realiza entrenando un metamodelo basado en funciones de base radial RBF mediante una selección representativa de las tormentas sintéticas y sus respectivas CI calculadas mediante modelos de procesos (SWAN+XBeach).

La consideración del grado de acoplamiento (CA) en el modelado de la CI requiere de dos pasos. En primer lugar, el efecto del long-term CA se considera alterando la

		Topografía		
Escenario	Perfiles base	Procesos ShoreTrans	Módulos XBeach	ID Metamodelo
2005NO	TB2005 perfiles LR	-	Hidro	1
2005ST	TB2005 perfiles LR	-	Hidro y Morfo	2
2045FULL	TB2020 perfiles LR	Longitudinal y ANMM	Hidro y Morfo	3
2045ST	TB2020 perfiles LR	-	Hidro y Morfo	4
2045LT	TB2020 perfiles LR	Longitudinal y ANMM	Hidro	5
2045NO	TB2020 perfiles LR	-	Hidro	6
2100FULL_RCP4.5	TB2020 perfiles LR	Longitudinal y ANMM	Hidro y Morfo	7
2100ST_RCP4.5	TB2020 perfiles LR	-	Hidro y Morfo	4
2100LT_RCP4.5	TB2020 perfiles LR	Longitudinal y ANMM	Hidro	8
2100NO_RCP4.5	TB2020 perfiles LR	-	Hidro	6
2100FULL_RCP8.5	TB2020 perfiles LR	Longitudinal y ANMM	Hidro y Morfo	9
2100ST_RCP8.5	TB2020 perfiles LR	-	Hidro y Morfo	4
2100LT_RCP8.5	TB2020 perfiles LR	Longitudinal y ANMM	Hidro	10
2100NO_RCP8.5	TB2020 perfiles LR	-	Hidro	6

Cuadro 0.2: Características del modelado de los diferentes escenarios necesarios para integrar los diferentes CAs en el cálculo de la CI.

geometría de los perfiles considerando el transporte longitudinal y el ANMM. En segundo lugar, los efectos de corto plazo debidos a tormentas se consideran activando la evolución morfodinámica en la simulación de XBeach. En el Cuadro 0.2, se detallan las características del modelado de los diferentes escenarios necesarios para integrar el acoplamiento erosión-inundación en la CI. Mientras que para los escenarios de no CA se emplean los perfiles iniciales de baja resolución (LR) TB2005 o TB2020 y XBeach se ejecuta únicamente en modo hidrodinámico; en el caso del full CA, los perfiles LR iniciales se modifican con ShoreTrans considerando el transporte longitudinal y el ANMM y XBeach se ejecuta considerando la hidrodinámica y también la morfodinámica.

En la Figura 0.26, se muestra la variabilidad RCM-RCP-ANMM-Periodo de los niveles de retorno de la CI en un perfil de Torre considerando el acoplamiento full CA (completo) erosión-inundación. Mientras que la primera fila de gráficos representa la variabilidad completa identificando los RCMs con marcadores distintos y trayectorias de ANMM con diferentes colores, la segunda fila resalta la variabilidad debida al modelo climático aislando el percentil del 50 % de ANMM y la tercera fila enfatiza la variablidad debida al ANMM aislando los niveles de retorno de la CI del modelo climático EART.
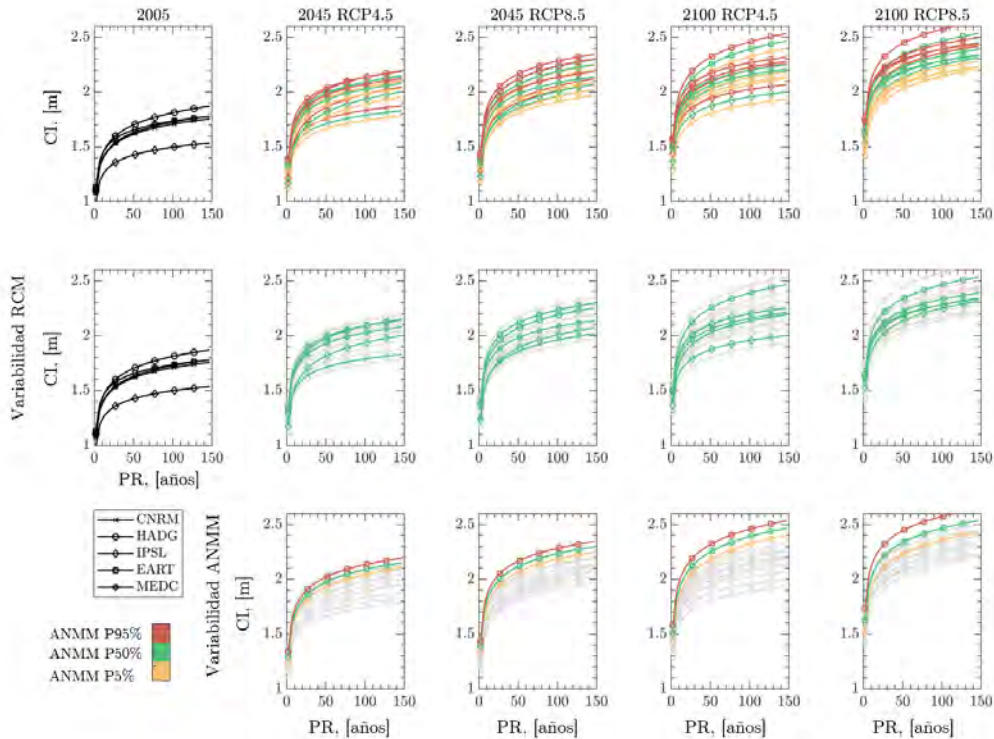
Figura 0.26: Niveles de retorno de la CI para diferentes combinaciones de RCM-RCP-percentil ANMM-Periodo en un transecto de la playa de Torre.

0.4.2.4. Topobatimetrías futuras

Para generar las topobatimetrías futuras se parte de las líneas de costa de 1990 a 2100. En esta aplicación el retroceso debido al ANMM, modelado en las proyecciones de la línea de costa mediante la regla de Bruun, se descarta al emplear ShoreTrans. A partir de la proyecciones multi-proceso, se obtienen los cambios debidos a trasporte longitudinal en los perfiles de baja resolución para cada escenario de RCM-RCP y percentil de ANMM del 50 % en los periodos de referencia (2045 y 2100). A continuación, se calculan los cambios debidos al transporte longitudinal (con respecto a la línea de costa del 2020) y se promedian entre RCMs y RCPs en el año 2045 (C2045) y entre RCMs en el año 2100 dando lugar a C2100_RCP4.5 y C2100_RCP8.5. Debido a la dispersión de los valores de ANMM entre percentiles, y para considerar su incertidumbre, no se realiza el promediado entre RCPs a fin de siglo.
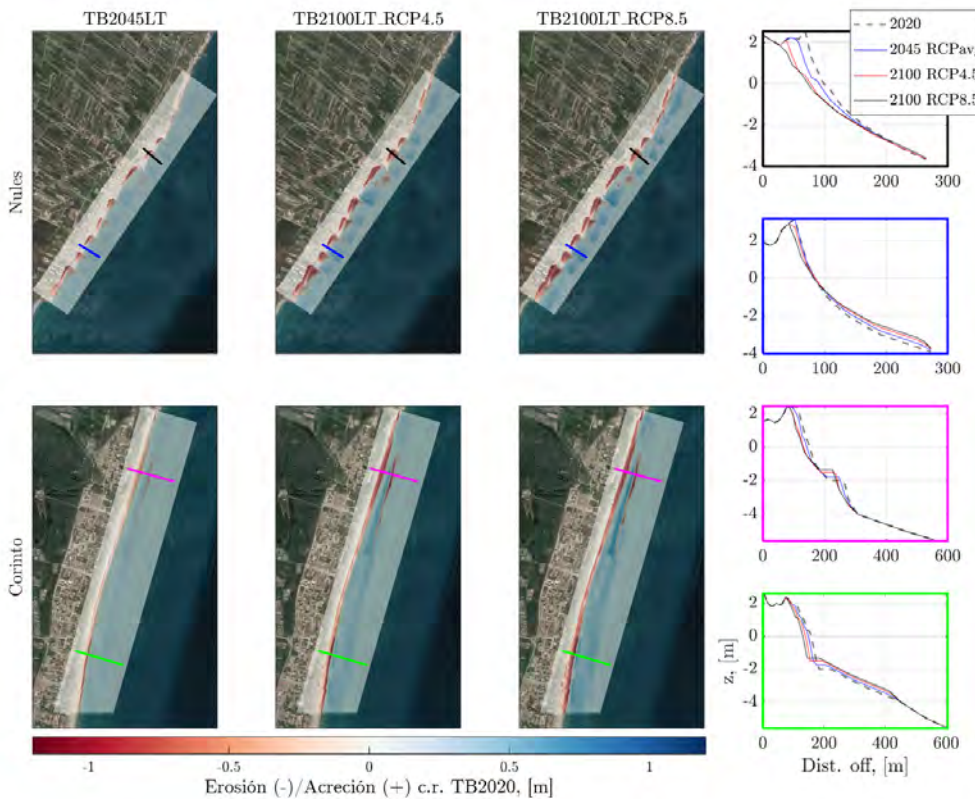
Figura 0.27: Patrones de erosión y acreción de largo plazo en Nules y Corinto de las topobatimetrías TB2045LT, TB2100LT_RCP4.5 y TB2100LT_RCP8.5 con respecto a TB2020.

Los cambios por transporte longitudinal calculados en los 247 perfiles de baja resolución se transfieren a los 4137 perfiles de alta resolución (espaciados 10 metros) mediante interpolación y se calcula el balance de volumen en el perfil multiplicando el retroceso o progreso calculado por el canto del perfil activo. Los cambios de largo plazo se calculan en los perfiles de alta resolución incorporando al transporte longitudinal el efecto del ANMM dando lugar a geometrías actualizadas de perfiles para los casos Z2045, Z2100_RCP4.5 y Z2100_RCP8.5. Los puntos en el perfil están espaciados un metro, con lo que se genera un nube de 10×1 m (longitudinal × transversal). Interpolando la nube en una malla de 5×5 m, se obtienen las topobatimetrías considerando erosión de largo plazo. En la Figura 0.27 se muestran los cambios entre las TB2045LT, TB2100LT_RCP4.5 y TB2100LT_8.5 con respecto a la presente TB2020 en las playas de Nules y Corinto. En Nules seaprecia el giro anti-horario de los compartimentes entre espigones siguiendo el flujo de energía. Del análisis de los transectos se pone de mani-

fiesto cómo el área situada a sotamar del espigón experimenta erosión por transporte longitudinal y ANMM, mientras que el lado a barlomar acrece por transporte longitudinal pero se erosiona por ANMM. El método permite conocer el balance sedimentario del tramo, por ejemplo Corinto gana de media unos 7500 m^3 de sedimento en 2045 por acción del transporte longitudinal mientras que las playas del norte (Torre, Burriana, Nules, Moncófar, Chilches, Llosa y Almenara) lo pierden.
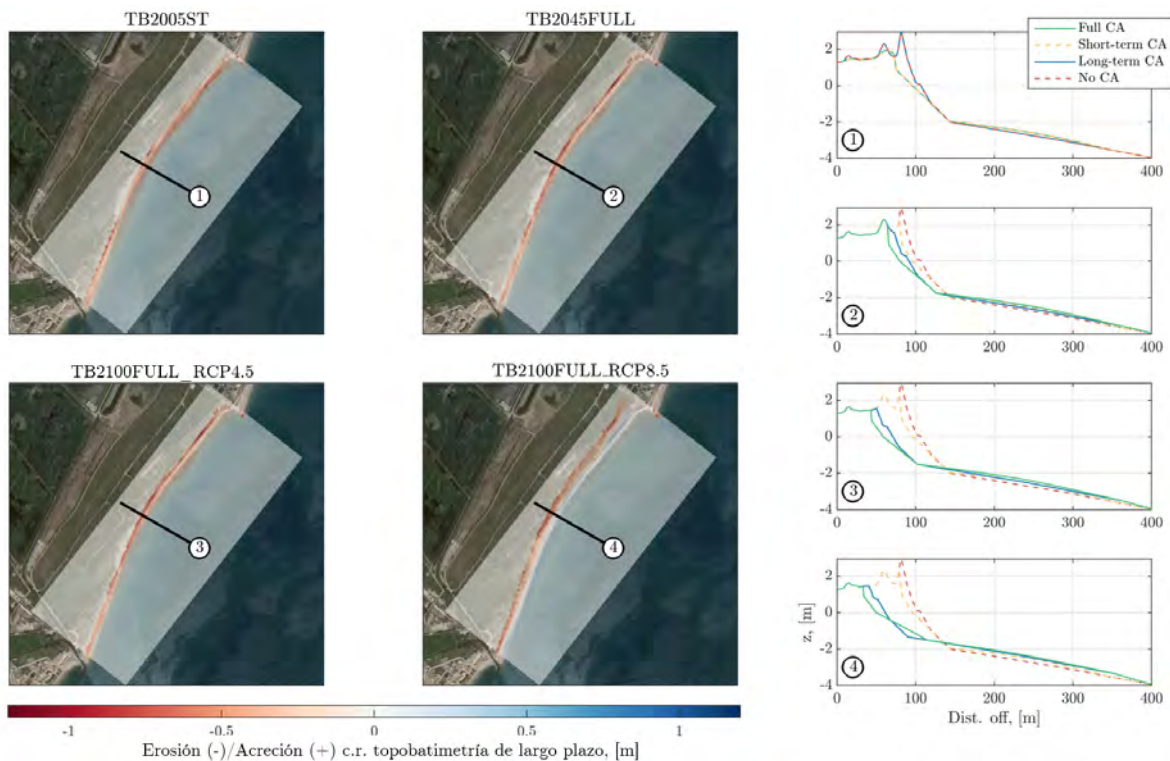
Figura 0.28: Patrones de erosión y acreción de corto plazo en Llosa de la topobatimetría TB2005FULL con respecto a TB2005; y para TB2045FULL, TB2100FULL_RCP4.5 y TB2100FULL_RCP8.5 con respecto a TB2045LT, TB2100LT_RCP4.5 y TB2100LT_RCP8.5 respectivamente.

Empleando las series temporales de evolución de la línea de costa de IH-LANS, se calcularon los retrocesos medios por tormenta promediados por RCM en el periodo 1986-2005, promediados por RCM y RCP en el periodo 2026-2045 y promediados por RCM en el periodo 2081-2100. Los retrocesos se transfieron a los perfiles de alta resolución y se actualizó su geometría según el método de Kinsela et al. (2017) implementado en ShoreTrans. En la Figura 0.28 se muestran los patrones de erosión y acreción en la playa de Llosa de la TB2005FULL con respecto de TB2005 y

de las TB2045FULL, TB2100FULL_RCP4.5 y TB2100FULL_RCP8.5 con respecto
a TB2045LT, TB2100LT_RCP4.5 y TB2100LT_RCP8.5. Al igual que ocurre con la
cinemática asociada al ANMM, la erosión de tormenta resulta en un reajuste de la
distribución del sedimento que se erosiona del frente de playa y se deposita formando
una barra sumergida. Al avanzar en el horizonte temporal y aumentar escenario de
forzamiento radiativo, la topobatimetría de largo plazo retrocede más, y la erosión de
tormenta actúa sobre una costa retranqueada ya de por sí. A modo de síntesis, en el
Cuadro 0.3 se detallan las características de las topobatimetrías generadas en el estudio.

Topobatimetría	Topobatimetría padre	Procesos de ShoreTrans
TB2005	IGN(2009)+MITECO(2009)	-
TB2005ST	TB2005	Erosión corto plazo
TB2020	IGN(2016)+MITECO(2020)	-
TB2020ST	TB2020	Erosión corto plazo
TB2045NO	TB2020	-
TB2045ST	TB2020	Erosión corto plazo
TB2045LT	TB2020	Longitudinal y ANMM
TB2045FULL	TB2045LT	Erosión corto plazo
TB2100NO_RCP4.5	TB2020	-
TB2100ST_RCP4.5	TB2020	Erosión corto plazo
TB2100LT_RCP4.5	TB2020	Longitudinal y ANMM
TB2100FULL_RCP4.5	TB2100LT_RCP4.5	Erosión corto plazo
TB2100NO_RCP8.5	TB2020	-
TB2100ST_RCP8.5	TB2020	Erosión corto plazo
TB2100LT_RCP8.5	TB2020	Longitudinal y ANMM
TB2100FULL_RCP8.5	TB2100LT_RCP8.5	Erosión corto plazo

Cuadro 0.3: Resumen de las características de las diferentes topobatimetrías generadas
en este estudio.

0.4.2.5. Resultados

Los efectos del grado de acoplamiento erosión-inundación se analizan en dos elementos
clave para la peligrosidad por inundaciones: la CI y la extensión del área inundada. La
importancia relativa del grado de acoplamiento erosión-inundación se compara con el
peso de la incertidumbre climática debida a diferentes RCMs y percentiles de ANMM
en la cota de inundación y en el área inundada.

Para cuantificar los efectos de la inundación de corto y largo plazo en la CI, se comparan las CI obtenidas tras aplicar los cuatro CA diferentes. En la Figura 0.29 se comparan los diferentes CA agrupados por horizonte temporal y RCP en Burriana, Chilches, Almenara y Sagunto. En general, se aprecia que a medida que aumenta el ANMM con el horizonte y el escenario de concentración, la CI_{100} también aumenta. El patrón general muestra que el no CA (rojo) da lugar a mayores CI_{100} que el short-term CA mientras que el long-term CA (azul) supera al full CA (verde). Esta observación se explica por el hecho de permitir la evolución morfodinámica en las simulaciones de XBeach de short-term CA y full CA. Los cambios en el perfil durante la tormenta generan un perfil con menor pendiente en el frente de playa y con mayor capacidad para disipar la energía del oleaje, tal y cómo se refleja en la relación de dependencia lineal entre el set-up del oleaje y la pendiente del frente de playa en la mayoría de formulaciones empíricas (Stockdon et al., 2006; Gomes da Silva et al., 2020).

Con respecto al full CA, el short-term, long-term y no CA producen valores de CI_{100} medios un 1 %, 6 % y 5 % superiores en 2045 en Almenara y hasta un 3 %, 4 % y 6 % superiores en 2100. En Chilches el comportamiento es similar y el full CA da lugar las menores estimaciones de CI_{100}. En Burriana, los valores de CI más bajos se alcanzan en el short-term CA. Con respecto al full CA, el corto plazo infraestima los valores de CI_{100} entre un 5-6 % en los diferentes escenarios y horizontes. El enfoque de largo plazo sobreestima la CI_{100} con respecto al full CA entre un 4-5 % y el no CA fluctúa en torno al full CA (± 1 %). En Sagunto, el short-term CA infraestima la CI_{100} con respecto al full CA en un 6 %, el no CA infraestima la CI un 7 % a fin de siglo mientras que el long-term CA fluctúa con respecto al full CA (± 3 %).

La contribución relativa de las distintas componentes (percentiles de ANMM, RCMs y CA) en la CI_{100} se analiza mediante un análisis de la varianza ANOVA (Figura 0.30) en Burriana, Chilches, Almenara y Saugnto en 2005, 2045 y 2100 para los RCPs 4.5 y 8.5. Los resultados son consistentes con los resultados previos. La contribución del ANMM (cian) aumenta al progresar en el tiempo y en el escnario radiativo. La incertidumbre debida a los RCMs gobierna en Burriana, Almenara y Sagunto en 2005 (75-97 % de la
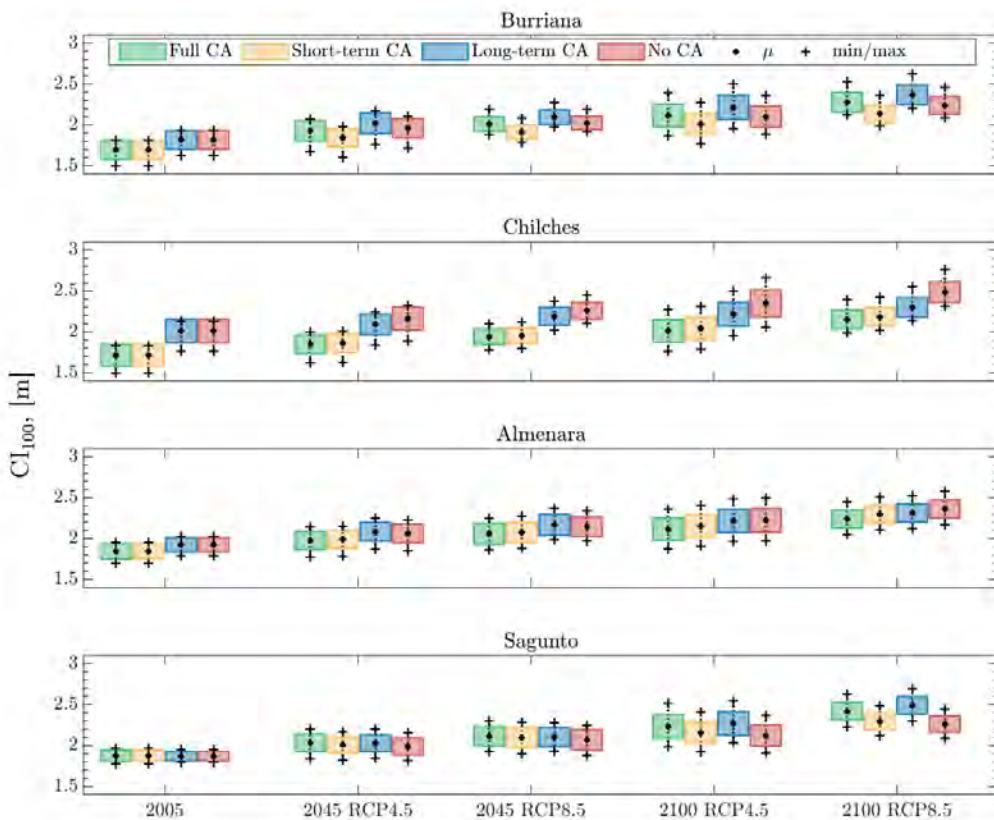
Figura 0.29: Valores la de CI$_{100}$ en Burriana, Chilches, Almenara y Sagunto en 2005, 2045 y 2100 para los RCPs 4.5 y 8.5. El color se refiere al nivel de acoplamiento, los círculos negros son los valores medios, las cruces los valores máximos y las cajas representan los valores medios más/menos la desviación típica.

varianza total de la CI_{100}), en 2045 (52-88 %) y en el 2100 RCP4.5 (65-75 %). La influencia dominante del CA se observa en Chilches (57-68 %), Burriana (23-67 %) y Sagunto. En Sagunto, el peso del CA en la CI_{100} empieza a ser relevante en 2100 RCP4.5 (16 %) y aumenta en el RCP8.5 (46 %) teniendo incluso más peso que el ANMM (35 %). Los resultados ponen de manifiesto la necesidad de considerar el carácter dinámico morfología costera ante eventos episódicos de tormenta en el cálculo de la CI.

La aplicación del modelo de inundación 2D sobre las topobatimetrías actualizadas y considerando las diferentes CI permite obtener los mapas de inundación y la extensión del área inundada asociada a la CI_{100} y denotada AI_{100}. Las Figuras 0.31 y 0.32 muestran algunos ejemplos de los mapas de inundación obtenidos. La Figura 0.31, muestra
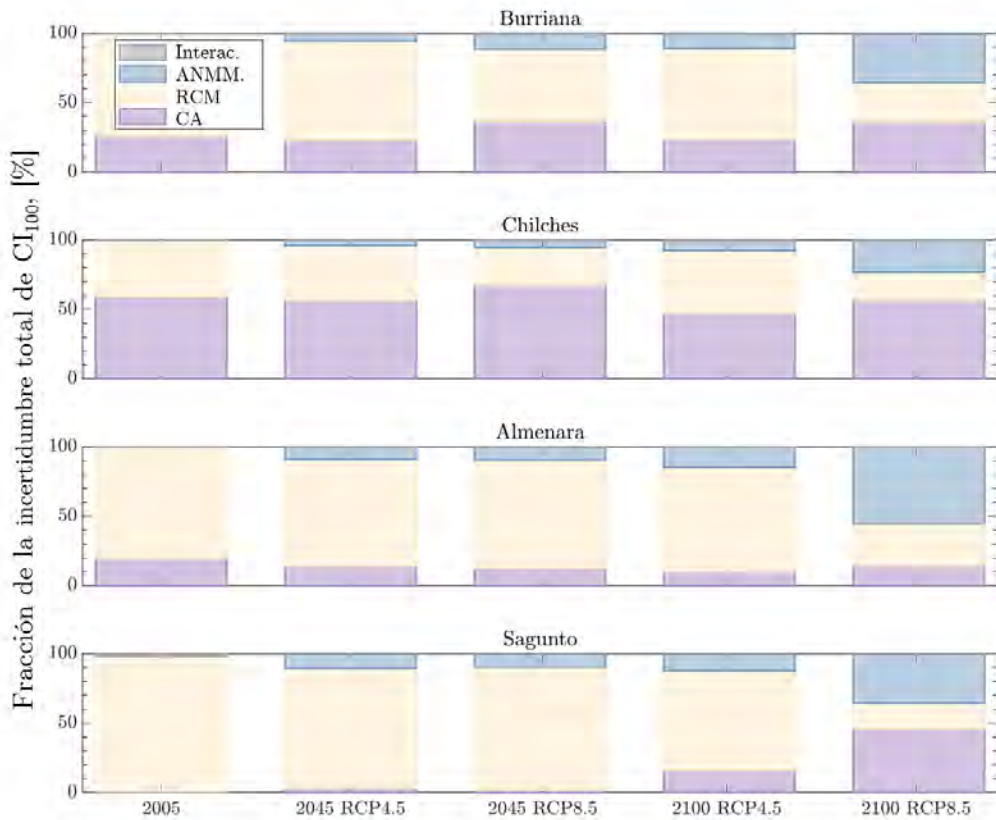
Figura 0.30: Contribución de las diferentes fuentes de incertidumbre y sus interacciones a la incertidumbre total en la CI_{100}.

los mapas de AI_{100} en Moncófar y en Corinto en 2045 para los diferentes RCPs. Los mapas se corresponden con el escenario más desfavorable, ya que muestran la envolvente de los 5 RCMs para el percentil del 95 % de ANMM. La Figura 0.32 muesta la extensión del AI_{100} para el RCP4.5 y el percentil del 95 % de ANMM para los diferentes RCMs considerando los diferentes CA. Desde un punto de vista de la incertidumbre, el full CA y el short-term CA producen el mayor rango de variación entre RCMs (15-27 ha y 26-23 ha respectivamente). El RCM que más área inundada produce es el EART en el caso de full CA (27 ha) y el HADG en el resto de CA (23-25 ha).

Siguiendo el ejemplo de la CI_{100}, el efecto del CA se analiza en AI_{100}. La Figura 0.33 muestra el AI_{100} para diferentes CAs agrupados por horizonte temporal y RCP. El efecto de la erosión de corto plazo es notorio en 2005 y el efecto del CA es más relevante en
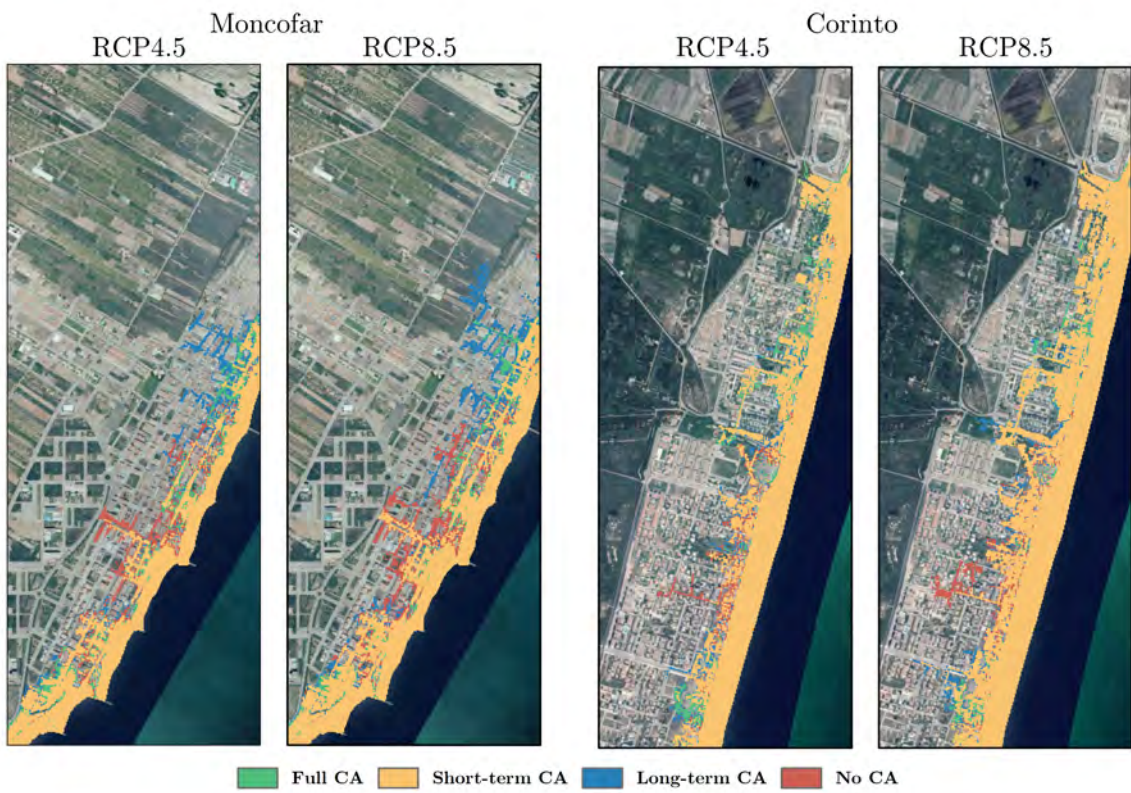
Figura 0.31: AI$_{100}$ en Moncófar y Corinto en 2045 para los RCPs 4.5 y 8.5. El color se refiere al nivel de acoplamiento. Las extensiones de la inundación corresponden con la envolvente de RCMs y el percentil del 95 % de ANMM.

el caso de el AI_{100} que en el caso de la CI_{100}. Por ejemplo, en Chiches y Almenara, el long-term/no CA sobreestiman los valores medios de la CI_{100} aproximadamente entre un 17 % y un 5 % respecto del full CA, pero infraestiman los valores medios de la AI_{100} un 32 % y un 85 % respectivamente, con respecto del full/short-term CA en 2005. En horizontes futuros, los cambios morfológicos de largo plazo contribuyen al AI, dando lugar a valores más altos y dispersos. De acuerdo con la influencia de la morfología en la hidrodinámica, mientras que la CI está influenciada principalmente por el transporte transversal (de corto plazo), el AI está claramente condicionada por el transporte longitudinal, que puede estar apoyado por el retroceso debido al ANMM y la erosión de tormenta, reduciendo el servicio de protección de la playa. Al contrario de lo que ocurría con la CI_{100}, el long-term CA produce valores más altos de AI_{100} en casi todos los casos debido a que los cambios de largo plazo en zonas antropizadas contribuyen a disminuir la capacidad de protección de las playas. En playas como Chilches, dónde hay un paseo
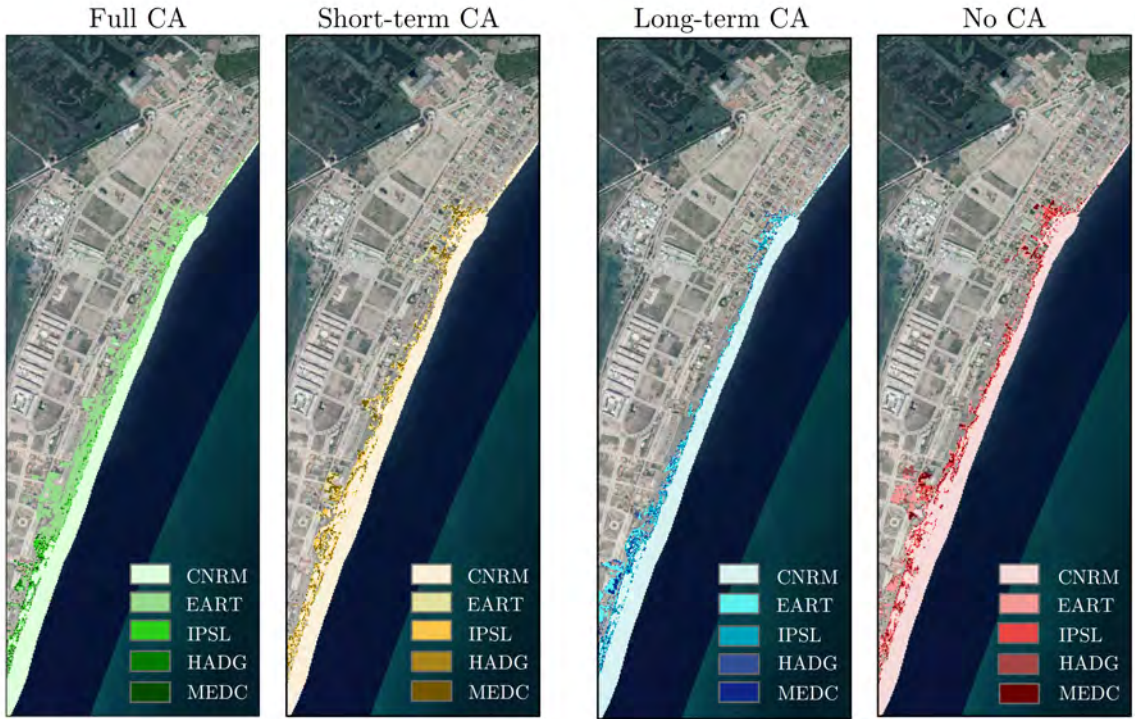
Figura 0.32: AI_{100} en Almenara en 2045 para el RCP4.5 y el percentil del 95 % del ANMM para diferentes RCMs.

que determina la evolución de la playa (especialmente en el largo plazo), valores altos de CI dan lugar a valores altos de rebase y por tanto, de inundación. Por ello, el long-term CA y el no CA dan valores de AI_{100} más altos que el full CA y el short-term CA (36-40 % y 4-19 % respectivamente). En playas mixtas como Almenara o Sagunto, formadas por una parte antropizada y otra natural, la omisión del acoplamiento erosión-inundación con respecto del full CA da lugar a sobreestimaciones de aproximadamente un 18-22 % del AI o infraestimaciones de entre un 15-16 % en 2050 e infraestimaciones de hasta un 22-25 % en 2100. Del análisis se pone de manifiesto la necesidad de considerar el acoplamiento completo de la erosión y la inundación empleando perfiles reales, ya que las singularidades en la forma del perfil dan lugar a comportamientos altamente no lineales de los impactos que serían muy difíciles de predecir de otro modo.
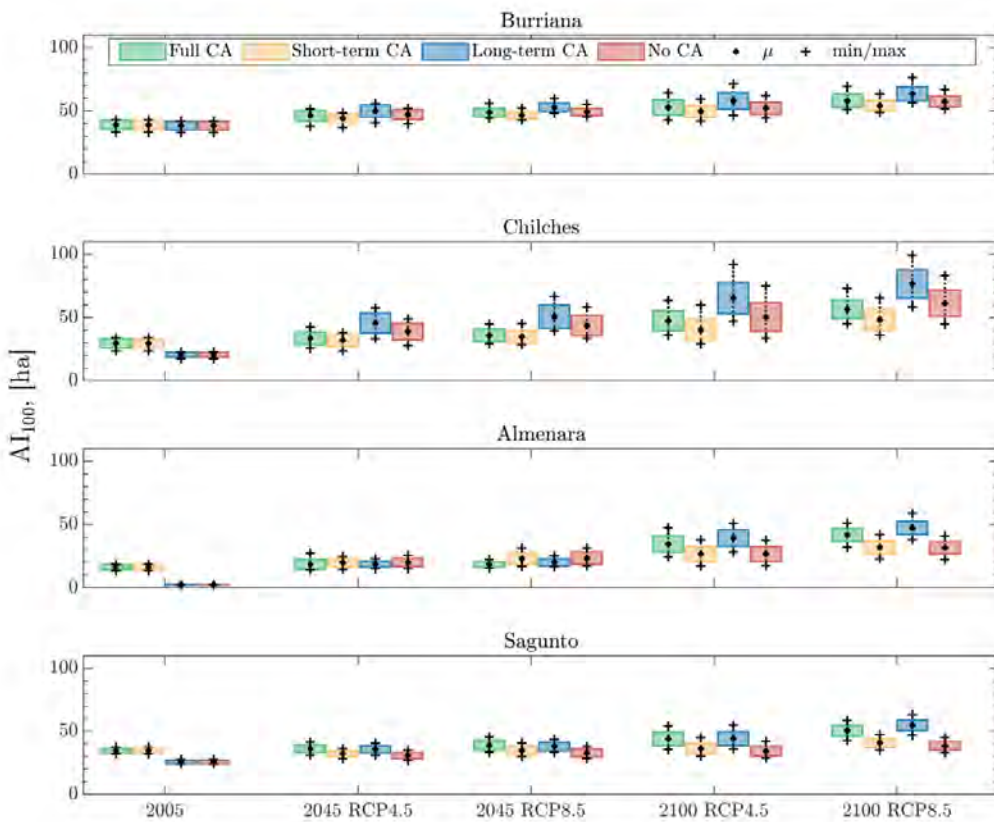
Figura 0.33: Valores de AI_{100} en Burriana, Chilches, Almenara y Sagunto en 2005, 2045 y 2100 para los RCPS 4.5 y 8.5. El color se refiere al nivel de acoplamiento, los círculos negros son los valores medios, las cruces los valores máximos y las cajas representan los valores medios más/menos la desviación típica.

La Figura 0.34 permite visualizar la contribución relativa de los percentiles de ANMM, los RCMs y las CAs a la incertidumbre en el AI_{100} para los RCPs 4.5 y 8.5 en 2005, 2045 y 2100. La contribución del ANMM en Burriana, Chilches, Almenara y Sagunto aumenta a medida que se progresa en el tiempo y en el escenario de emisiones, aunque este efecto es más pequeño en el caso del AI_{100} que en la CI_{100}. El aspecto más destacado es la importancia del CA en todas las playas, siendo más importante que el peso relativo de los diferentes percentiles de ANMM en 2100 para el RCP8.5 dando lugar a una contribución a la incertidumbre total en el AI_{100} del CA del (34 %, 56 %, 65 % y 76 %) frente a los percentiles de ANMM (35 %, 26 %, 20 % y 16 %, en Burriana, Chilches y Almenara respectivamente). Este hecho pone de manifiesto que a pesar de los progresos en la caracterización de la incertidumbre climática (oleaje y niveles), la no consideración

de las interacciones entre la erosión y la inundación de forma adecuada da lugar a predicciones erróneas. Por otro lado, la variabilidad dentro de un mismo CA se debe a la variabilidad heradada de la CI_{100} que se escala en el cálculo del AI_{100} debido a una pequeña variación en la CI_{100} puede generar el rebase de una defensa y un gran impacto en la extensión inundada AI_{100}.
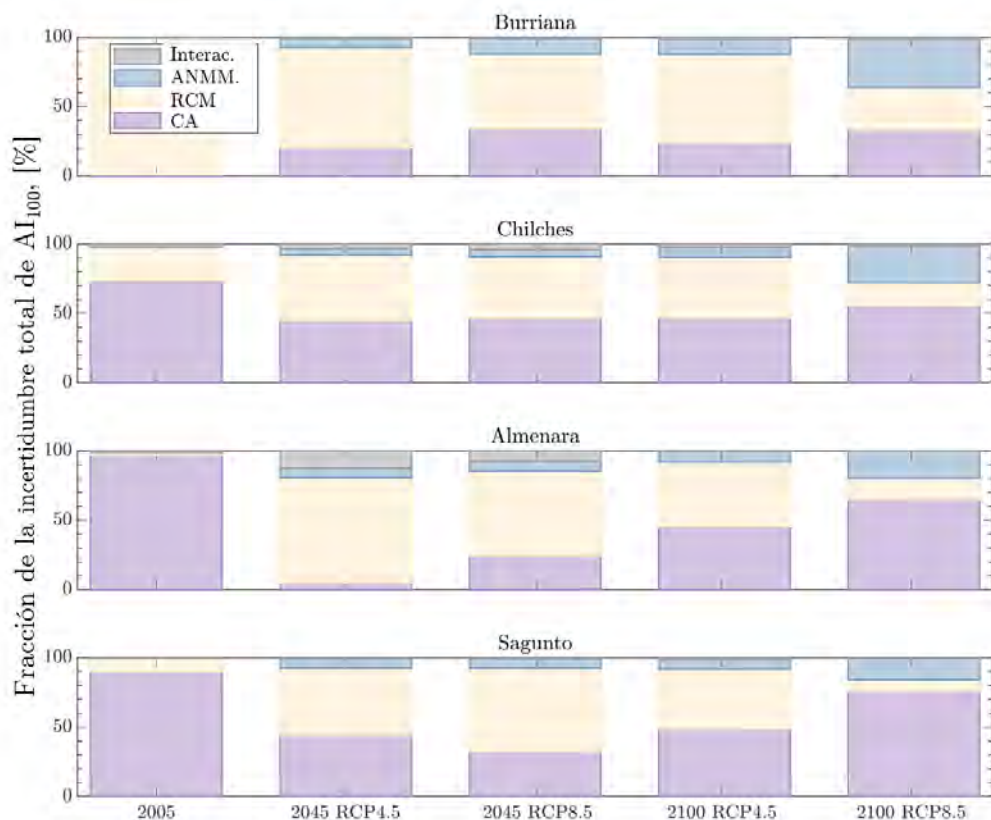
Figura 0.34: Contribución de las diferentes fuentes de incertidumbre y sus interacciones a la incertidumbre total en la AI_{100}.

0.4.2.6. Resumen de los efectos de los diferentes grados de acoplamiento erosión-inundación

Con respecto a los resultados de aplicar los diferentes CA en la CI y AI, se pone de manifiesto la necesidad de abandonar el enfoque estándar de desacoplar los efectos de la erosión y la inundación. Con respecto a la CI, se pueden extraer las siguientes conclusiones:

- En costas naturales los procesos de largo plazo no generan grandes cambios en la CI. El transporte longitudinal no altera la goemetría de la zona de remontes. Los cambios en el perfil por ANMM tampoco alteran la CI con respecto a la situación presente ya que el perfil imita el ANMM y retrocede sin alterar su forma, lo que hace que la geometría de la zona de remonteS no varíe.

- En costas antropizadas, procesos de largo plazo sí influyen en la CI. Los cambios en el perfil debidos al transporte longitudinal y al ANMM en costas rigidizadas por intevenciones generan socavaciones en la base de las estructuras. La combinación del ANMM frente a estructuras desprotegidas hace que la disipación de energía por rozamiento con el fondo disminuya al aumentar el calado y que aumenten los eventos de rebase.

- Los cambios de corto plazo en el perfil debidos a eventos extremos dan valores de CI inferiores que en el caso de asumir un perfil estático debido a que el perfil se hace más disipativo.

- Con respecto al peso relativo de los RCMs, los percentiles de ANMM y las CA en la CI, el peso relativo del percentil de ANMM en los resultados es reducido en el caso de escenarios radiativos medios (RCP4.5 $\approx 10\,\%$) y aumenta en el caso del peor escenario (RCP8.5) a fin de siglo ($\approx$ 20-50 %). La incertidumbre en los RCMs y en las CA influencia significativamente el valor de la CI, pero su contribución relativa depende del sitio y del caso de estudio. De los resultados, el peso relativo del RCM en la CI excede el 50 % en la mayoría de las playas. Sin embargo, sólo cuando el peso de los cambios morfodinámicos de corto plazo es relevante, el CA supera al RCM en cuanto a importancia relativa en la CI.

De forma similar, en el caso del área inundada se infieren los siguientes patrones generales:

- En costas naturales, la consideración de los los procesos de largo plazo genera cambios importantes en el área inundada. Por un lado, los procesos longitudinales pueden dar lugar a déficits de sedimento, desprotegiendo el el frente de las playas y disminuyendo por ende el servicio de protección de éstas frente a inundaciones. De forma similar, el servicio de protección de la duna y la playa se puede reducir debido a los cambios en el perfil por ANMM, al llegar a disminuir la cota de la

berma en algunas configuraciones a la vez que aumenta el NMM.

- En costas antropizadas, la cota de agua crítica a partir de la cual se produce inundación esta controlada por estructuras artificiales que se asumen no erosionables. Por tanto, los efectos morfodinámicos del largo plazo en la inundación se deben fundamentalmente al aumento de la energía que llega al frente constero por disminución de la disipación. De los resultados se extrae que considerar los cambios de largo plazo (long-term and full CA) implica mayores inundaciones que si no se consideran (no and short-term CA).

- La erosión de corto plazo juega un papel fundamental en el área inundada. En playas naturales, la erosión de la duna y de la playa durante eventos extremos puede reducir la cota de la berma desprotegiendo áreas bajas adyacentes. Los procesos de corto plazo generan efectos contrapuestos: mientras que los cambios en el perfil reducen la CI al aumentar la disipación, el frente de la playa e incluso la berma se erosionan aumentando el área potencialmente inundable. Determinar cuál de los dos efectos es más importante no es trivial y requiere modelado específico que depende del caso de estudio, del estado en el que se encuentre la playa y de la cronología de las tormentas. Los efectos de una la tormenta sobre una topobatimetría ya erosionada por otra precedente pueden llegar a generar áreas inundadas muy superiores a las que se producirían en el caso de considerar que la playa está en condiciones normales de erosión.

- Con respecto al peso relativo de la incertidumbre climática y del modelado en el área inundada para un horizonte temporal y RCP dado, la contribución del percentil de ANMM es reducida en escenarios radiativos medios (RCP4.5) pero aumenta a fin de siglo en el RCP8.5 al aumentar la dispersión de los percentiles de ANMM. Sin embargo el peso del ANMM en el AI es inferior que en la CI. La influencia del acoplamiento erosión-inundación en el área inundada es superior al peso del percentil de ANMM y del RCM considerado en todas las playas. La dispersión en el CA se debe principalmente al hecho de considerar o no los cambios de largo plazo. El elevado peso relativo del grado de acoplamiento en la extensión del área inundada pone de manifiesto la necesidad de considerar los efectos de la erosión en las proyecciones de inundación en estudios de cambio climático. La

no consideración de las interacciones multi-escala entre los diferentes impactos desestima todos los esfuerzos en la caracterización del clima marítimo futuro en el cálculo de la inundación.

0.5. Desarrollo de IH-LANSloc para estudios a escala local

En esta sección, las funcionalidades de IH-LANS se extienden para proyectar no sólo la línea de costa sino la evolución de la morfología costera dando lugar a IH-LANSloc (Figura 0.35). La nueva versión está especialmente indicada para su aplicación en estudios a escala local de la evolución a largo plazo de la morfología en zonas costeras naturales o antropizadas. IH-LANSloc comparte los fundamentos de modelado de IH-LANS, pues resuelve la evolución de la línea de costa mediante una ecuación de gobierno enriquecida por observaciones mediante asimilación e integrando los procesos longitudinales y transversales. Gracias a considerar las complejas interacciones entre la propagación del oleaje y una morfología cambiante, se alcanza una mejor representación de los procesos. Esto se consigue gracias al empleo de un modelo avanzado de propagación del oleaje hasta el punto de rotura junto con un modelo de translación del perfil que actualiza la malla de la batimetría en función de los cambios en la línea de costa. IH-LANSloc es capaz de modelar distintas actuaciones antrópicas como rellenos, escolleras, espigones y diques pero también ecosistemas como manglares, praderas marinas o arrecifes de coral. Para testear las capacidades del modelo, se simulan distintos entornos costeros sintéticos en presencia de estructuras y ecosistemas naturales para demostrar la utilidad de IH-LANSloc para la gestión de la costa y la adaptación al cambio climático en entornos complejos.

0.5.1. Estructura y funcionalidades del modelo

Al igual que IH-LANS, IH-LANSloc se fundamenta en tres pilares que son la transformación eficiente del oleaje en dos pasos, un ecuación de evolución de la línea de costa multiproceso que considera procesos longitudinales y transversales y un algoritmo de asimilación para la calibración de los parámetros libres.

IH-LANS

Evolución de la línea de costa
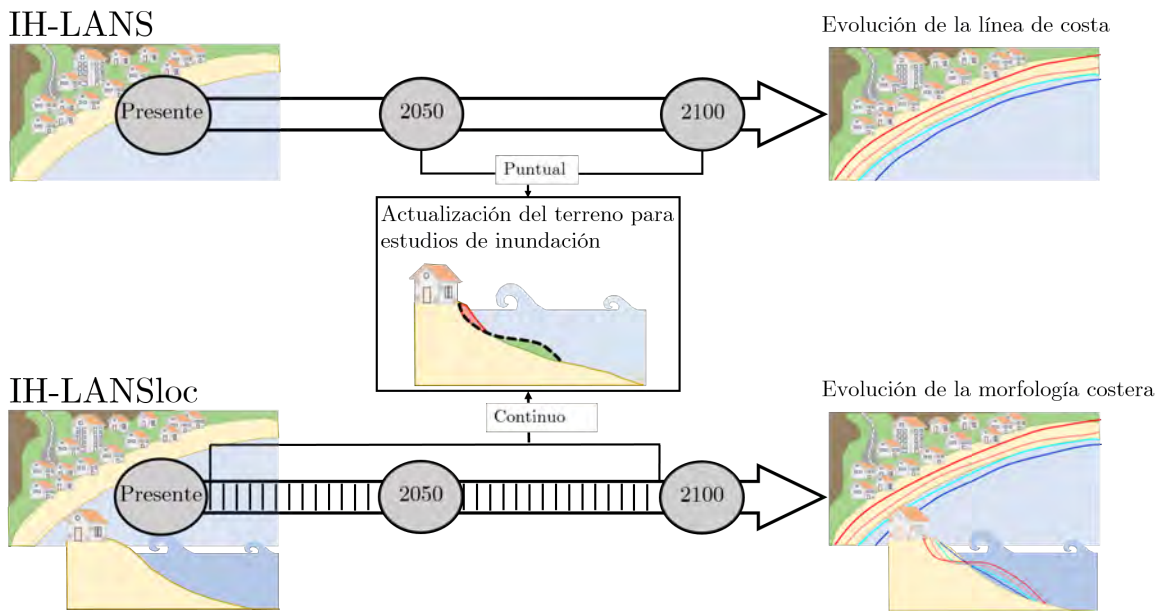
IH-LANSloc

Figura 0.35: Comparación entre IH-LANS y IH-LANSloc en términos de resultados del modelado.

El flujo de cálculo de IH-LANSloc se muestra en la Figura 0.36. Las diferencias con respecto a la versión base se resaltan en amarillo y consisten en la propagación a rotura empleando el modelo SWAN (Booij et al., 1999) y la actualización de la topobatimetría empleando ShoreTrans (McCarroll et al., 2021). El primer paso del cálculo consiste en recolectar todos los datos de partida necesarios en la zona de estudio. A continuación se define el dominio de cálculo para la propagación en dos pasos y la discretización de la línea de costa en perfiles de baja (LR) y alta resolución (HR). Los perfiles LR son los raíles que guían la evolución de la línea de costa y los perfiles HR se emplean para actualizar la malla de la topobatimetría y heredan la información de los perfiles LR mediante interpolación basada en distancias. Esta discretización dual es necesaria debido a que los perfiles LR no tienen suficiente resolución para actualizar el modelo del terreno y reducir el espaciamiento entre perfiles LR comprometería la estabilidad numérica de la ecuación de evolución de la línea de costa.

Datos de partida
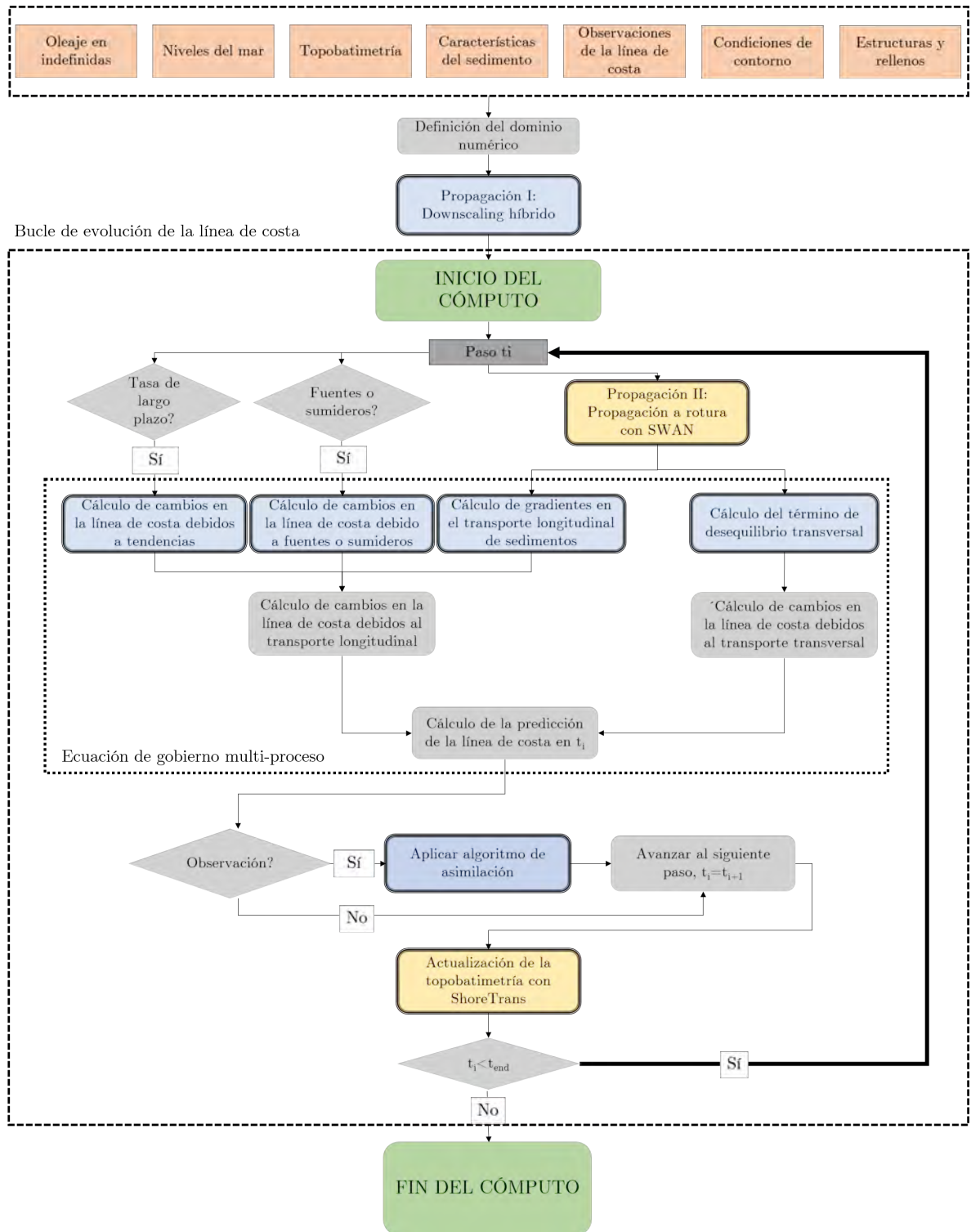
Figura 0.36: Flujo de cálculo de IH-LANSloc.

Las olas se propagan al contorno offshore de la malla dinámica de cálculo mediante el procedimiento estadístico-numérico descrito en Alvarez-Cuesta et al. (2021a) adaptado

de Camus et al. (2013). A continuación, la series de oleaje y nivel se propagan a rotura empleando el modelo SWAN y producen cambios en la línea de costa debidos a procesos longitudinales y transversales. A continuación, los cambios en la línea de costa se transfieren a la morfología bidimensional mediante una herramienta de translación de perfiles que emplea reglas heurísticas cinemáticas adaptadas a los procesos modelados. Para minimizar el tiempo de cómputo, se desarrolla una interfaz de comunicación eficiente entre IH-LANSloc y SWAN basada en interpolación que facilita el intercambio de información desde la malla de SWAN a los perfiles LR y desde los perfiles HR a la malla topobatimétrica de SWAN.

0.5.1.1.   Transformación del oleaje

La propagación del oleaje se realiza en dos pasos. El primer paso consiste en la propagación híbrida empleando herramientas estadísticas y numéricas para trasladar, de forma eficiente, el oleaje en indefinidas de modelos globales a la zona de interés empleando una topobatimetría estática. El segundo paso de la propagación se realiza desde el contorno offshore de la malla dinámica hasta la costa mediante propagación numérica junto con una topobatimetría dinámica, que cambia a lo largo del tiempo considerando la erosión. La diferencia introducida en esta versión del modelo es que se emplea un modelo 2D de propagación en lugar de la simplificación 1D de la refracción mediante la ley de Snell.

El modelo de propagación implementado en IH-LANSloc para el cálculo de las propiedades del oleaje en rotura es SWAN, pero las rutinas de evolución de la línea de costa y de la actualización de la topobatimetría son compatibles con cualquier otro modelo.

SWAN es un modelo espectral de tercera generación que resuelve la ecuación de conservación de la energía considerando fuentes y sumideros, generación por viento, *white capping*, fricción de fondo, interacciones ola-ola, disipación debida a campos de vegetación y rotura por fondo.

0.5.2. Modelado de la línea de costa

Los cambios en la línea de costa son el resultado de la combinación de los cambios debidos a procesos longitudinales y transversales calculados en los perfiles LR según la Ecuación 0.1. Los cambios longitudinales se obtienen a partir de los gradientes longitudinales en el transporte longitudinal mediante la ecuación del CERC (USACE, 1984), la contribución de fuentes y sumideros y la tasa debida a los procesos no resueltos. Adicionalmente, los cambios transversales debidos a oleaje y nivel se consideran mediante la formulación de Miller and Dean (2004). El retroceso debido al ANMM no se modela según la regla de Bruun sino mediante la aproximación de Atkinson et al. (2018) y considerando los perfiles reales. Por otro lado, la cadena de modelado se enriquece mediante asimilación de observaciones empleando el filtro extendido de Kalman.

0.5.2.1. Actualización de la topobatimetría

Los cambios en la línea de costa se transfieren a la topobatimetría empleando Shore-Trans (McCarroll et al., 2021). ShoreTrans es un modelo de translación de perfil y de balance sedimentario guiado por reglas cinemáticas que integra los efectos del ANMM siguiendo el trabajo de Atkinson et al. (2018), el balance sedimentario según la teoría clásica de los modelos de una línea y la erosión de tormenta según Kinsela et al. (2017). Los efectos de la rigidización de la costa debidos a estructuras se consideran según Beuzen et al. (2018). ShoreTrans se aplica a los perfiles HR que heredan los retrocesos debidos a procesos longitudinales y transversales de los perfiles LR y actualiza su geometría incluyendo la respuesta ante el ANMM. La implementación de ShoreTrans se describe en la Sección 0.4.1.2.

0.5.2.2. Acoplamiento bidireccional entre SWAN e IH-LANSloc

Para anidar IH-LANSloc y el modelo 2D de propagación de oleaje de forma eficiente, se requiere una interfaz de comunicación entre ambos modelos. IH-LANSloc necesita las propiedades del oleaje calculadas en la malla de SWAN en los perfiles LR para alimentar la ecuación de gobierno de la línea de costa. Por otro lado, SWAN necesita la topobatimetría actualizada a partir de los perfiles HR. Estos intercambios se realizan en

cada paso de tiempo, por lo que algoritmos ineficientes aumentarían de forma sustancial el tiempo de cálculo. Para evitarlo, se ha implementado en IH-LANSloc una rutina basada en interpolación geométrica. Partiendo de que la discretización de los perfiles en IH-LANSloc no cambia con el tiempo, la posición de los puntos de los transectos con respecto a los puntos de la malla de SWAN no varía, con lo que se requieren únicamente dos matrices de transición (una para cada dirección IH-LANSloc-SWAN).

En la Figura 0.37 se muestra de forma gráfica el principio de interpolación geométrica. En el caso de la comunicación entre la malla de SWAN y los perfiles LR, se genera una matriz $\boldsymbol{WT}$ con tantas filas como puntos haya en los perfiles LR. Para cada punto LR se le atribuyen los tres puntos circundantes de la malla de SWAN y el peso relativo de los puntos circundantes, de tal forma que un campo escalar evaluado en la malla de SWAN se transfiere mediante suma ponderada a los puntos de los perfiles LR. De forma análoga, se establece una matriz de transferencia $\boldsymbol{TW}$ entre los puntos de los perfiles HR y los puntos de la malla de SWAN.
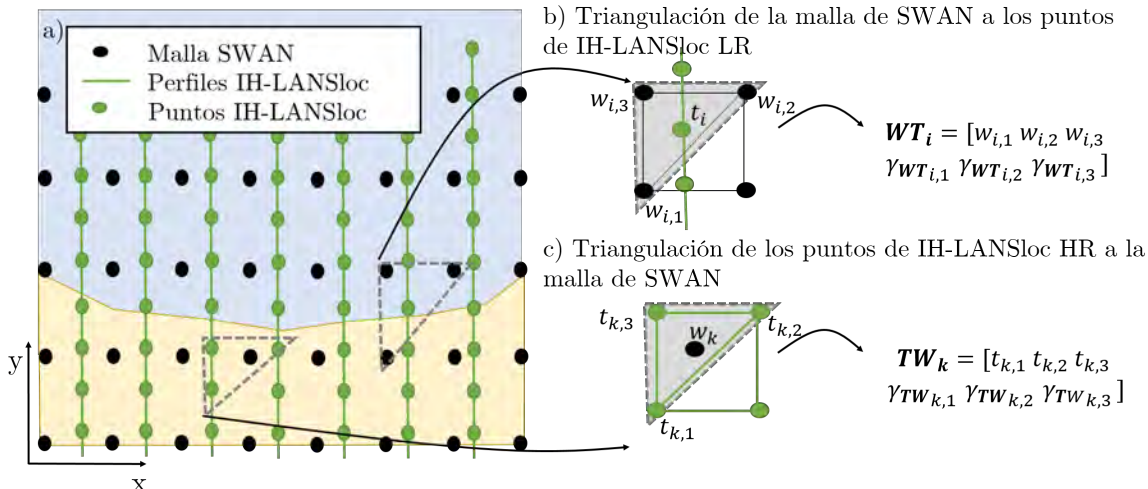
Figura 0.37: Esquema de interpolación para el acoplamiento bidireccional. Para facilitar la visualización, sólo se muestra un conjunto de perfiles y puntos. Sin embargo, el apartado b) emplea los puntos de IH-LANSloc LR mientras que el apartado c) usa los puntos IH-LANSloc HR.

0.5.3. Modelado del efecto de las intervenciones antrópicas y de ecosistemas naturales en la evolución de la línea de costa

El acoplamiento entre IH-LANS y SWAN permite alcanzar una mejor representación de los procesos físicos, facilitando el modelado de la respuesta de la costa ante distintas intervenciones humanas y distintos ecosistemas naturales. Espigones, diques, escolleras, rellenos, salientes rocosos, arrecifes de coral o campos de vegetación se pueden incluir en IH-LANSloc mediante modelado basado en procesos. En el Cuadro 0.4 se sintetizan los distintos elementos costeros que se pueden integrar en el modelo y cómo su impacto en la evolución de la costa se resuelve alterando la propagación del olejae y/o el trasnporte de sedimentos.

Elemento	Propagación del oleaje	Transporte de sedimentos
Espigones	Obstáculo subgrid	Coeficiente de bypass variable
Diques	Obstáculo subgrid	-
Escolleras	-	Condición de contorno realista
Rellenos	Cambio batimetría	Término fuente
Salientes rocosos	Obstáculo subgrid / cambio batimetría	-
Arrecifes de coral	Obstáculo subgrid / cambio batimetría y aumento fricción de fondo	-
Campos de vegetación	Término de disipacióin	-[1]

Cuadro 0.4: Características del modelado de los distintos elementos costeros incluidos en IH-LANSloc.

Con respecto a la alteración en la propagación del oleaje por parte de los distintos elementos costeros, una gran variedad de ellos se puede modelar mediante obstáculos subgrid para los que se define un coeficiente de transmisión K_t directamente o se calcula según la formulación de d'Angremond et al. (1996) para elementos de baja cota de coronación. Asimismo, si el tamaño del elemento es significativo con respecto al tamaño de malla, se puede modelar directamente modificando la topobatimetría. Específicamente, el aumento de fricción por fondo que ejercen los arrecifes de coral se modela según la formulación de Madsen et al. (1988) y la disipación de energía debida a campos de vegetación según Mendez and Losada (2004). Algunos de los elementos costeros como los espigones, las escolleras o los rellenos, también modifican el transporte de sedimentos.

De esta forma se incluye en el modelado el coeficiente de bypass variable en el caso de espigones siguiendo a Hanson and Kraus (1989), las escolleras se consideran mediante una condición de contorno realista que altera el transporte de sedimentos según Hanson and Kraus (1986) y los rellenos se modelan mediante un término fuente en la ecuación 0.1.

0.5.4. Casos sintéticos de estudio

Para testear la capacidad del modelo de reproducir los efectos de diferentes elementos costeros en la respuesta de la costa, se diseñan cuatro configuraciones sintéticas: 1) un caso base sin estructuras ni ecosistemas naturales, 2) un caso incluyendo estructuras, 3) un caso con un arrecife de coral y 4) un caso con campos de vegetación. En todos los casos, la batimetría inicial, el forzamiento de oleaje y nivel y las condiciones de contorno son las mismas y la única diferencia es el elemento costero introducido en el modelo.

La costa inicial modelada en todos los casos es una ensenada parabólica de 3 km de longitud y sigue un perfil de equilibrio de Dean. El clima de oleaje se asume constante en los contornos del dominio y se define por un espectro JONSWAP de $H_s = 2$ m, $T_p = 12$ s, $\theta_m = -40°$, factor de pico $\gamma = 3.3$ y dispersión direccional $s = 30°$. No se producen intercambios de sedimento en el contorno izquierdo (condición nula de Dirichlet) mientras que la línea de costa se mantiene en el derecho (condición nula de Neumann). La malla de SWAN tiene una resolución de 15×15 metros, los perfiles LR están espaciados 100 metros y los perfiles HR 10 metros. La constante de transporte longitudinal se fija igual a $K_1 = 50$ m$^{1/2}$/día.

La configuración inicial de los distintos casos se muestra en la primera columna de la Figura 0.38 y los parámetros del modelado en el Cuadro 0.5. La primera fila de la figura representa el caso base. El efecto de las actuaciones antrópicas se evalúa en el segundo caso. Los espigones se consideran impermeables $K_t = 0$ y el dique parcialmente permeable $K_t = 0.4$. En el tercer caso se modela un arrecife de coral según la parame-

---

[1]Aunque los campos de vegetación pueden actuar como trampas de sedimento, este efecto no se ha implementado en IH-LANSloc en el momento de la redacción del documento.

trización geométrica de Escudero et al. (2021) en cuanto a la anchura de la base del arrecife B_f, la anchura de la cresta B_{rf} y el francobordo h_r. El aumento en la rugosidad del fondo en la zona del arrecife se considera mediante una longitud de rugosidad de fondo $K_N = 0.3$ m (Filipot and Cheung, 2012). El cuarto caso incluye dos campos de vegetación definidos según uno de los ejemplos de Mendez and Losada (2004) en cuanto a coeficiente de arrastre C_D, altura de planta αh, anchura de planta b_v y número de plantas por metro cuadrado N_v.

Caso	Parámetros clave	Referencia
Base	-	-
Estructuras	$K_{t,espigon} = 0$, $K_{t,dique} = 0.4$	-
Arrecife de coral	$B_{rf} = 50$ m, $B_f = 100$ m, $h_r = 3$ m, $K_N = 0.3$ m	Escudero et al. (2021) Filipot and Cheung (2012)
Vegetación	$C_D = 0.2$, $\alpha h = 3$ m, $b_v = 0.1$ m, $N_v = 40$	Mendez and Losada (2004)

Cuadro 0.5: Parámetros clave para incluir el efecto de distintos entornos costeros en la propagación del oleaje.

En la segunda y la tercera columna de la Figura 0.38 se muestra la evolución de la línea de costa en distintos instantes y la morfología final tras 15 años de simulación. Se aprecian claramente las alteraciones en la costa que ejercen los distintos elementos con respecto al caso base y de como la atenuación del oleaje por parte del arrecife de coral y del campo de vegetación se traduce en menores tasas de transporte de sedimentos.

Para evaluar de forma cuantitativa los efectos de los distintos elementos costeros en la respuesta de la costa, se calculan tres indicadores de erosión: la altura media en rotura, el volumen erosionado y el retroceso en el primer transecto de la izquierda. Los resultados se muestran en la Figura 0.39 y evidencian la disminución de la altura de ola en rotura en los casos con estructuras, con arrecife de coral y con vegetación; así como de la reducción en el volumen erosionado y en el retroceso del transecto extremo de los distintos casos con respecto al caso base.
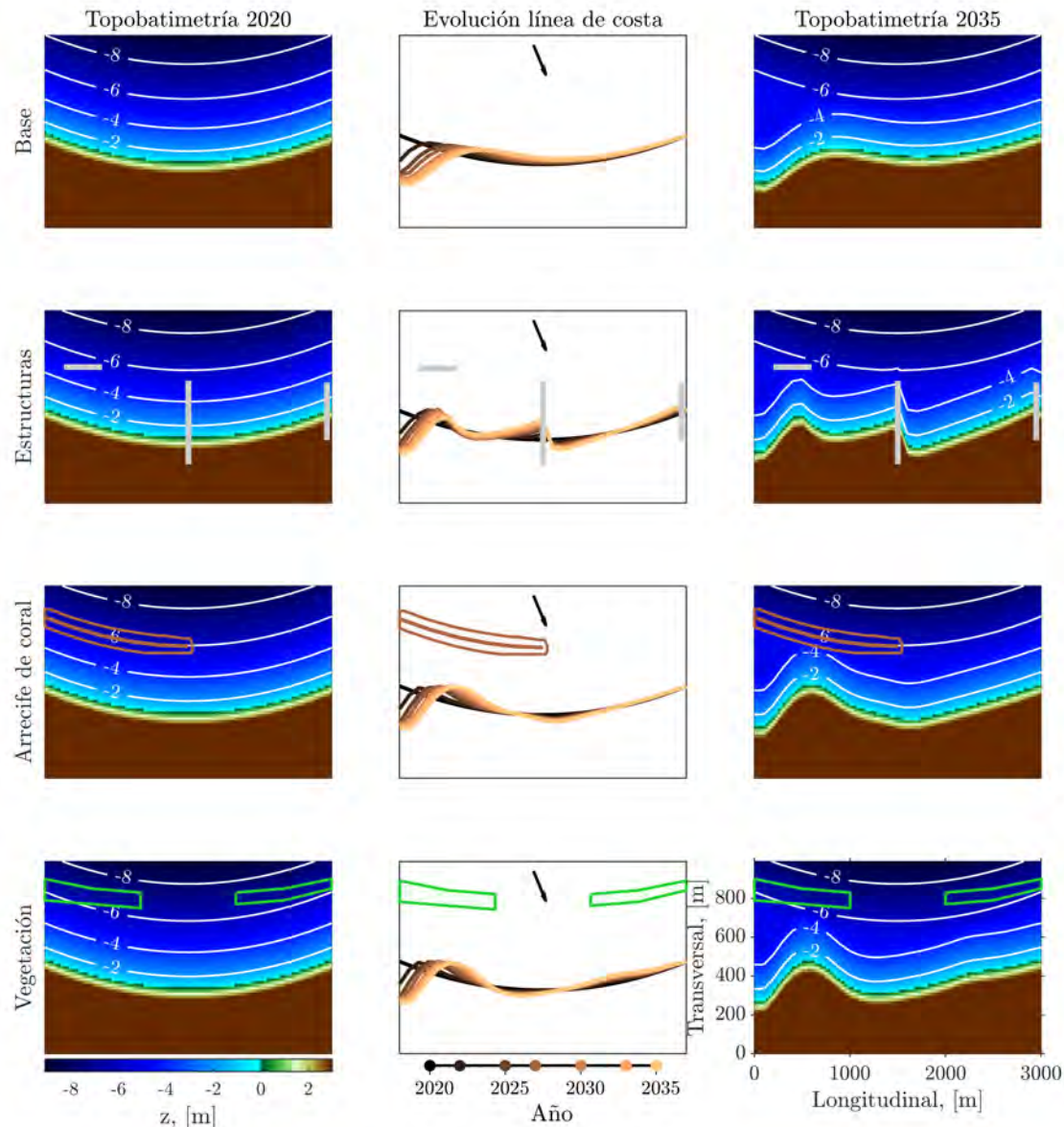
Figura 0.38: Configuración y resultados de los casos sintéticos de estudio.
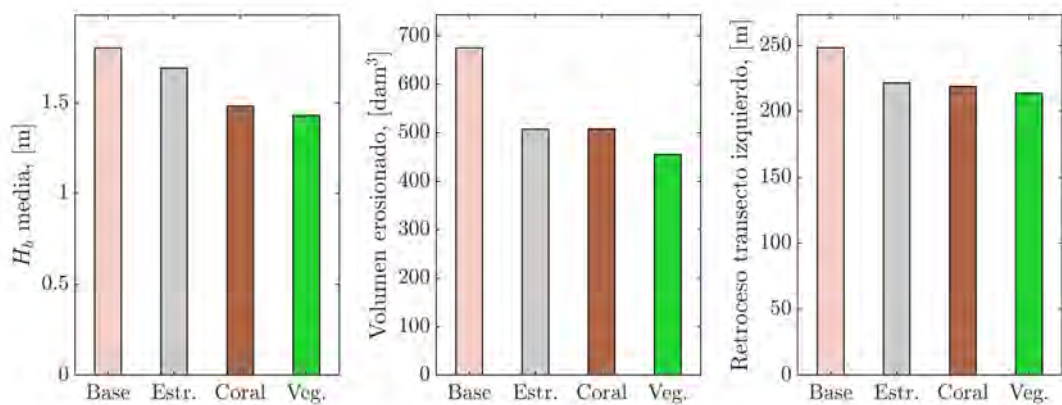
Figura 0.39: Comparación de distintos indicadores de erosión para las distintas configuraciones.

0.6. Conclusiones y futuras líneas

0.6.1. Conclusiones

Se ha desarrollado un marco de análisis de impactos compuesto de diferentes modelos, herramientas y metodologías para mejorar los estudios de riesgo de erosión e inundación y apoyar a la adaptación al cambio climático. La piedra angular del trabajo es la comprensión de los principales procesos morfológicos que dan forma a las zonas costeras en las escalas del cambio climático junto con sus interacciones mediante el desarrollo de un modelo de evolución de la línea de costa. El modelo se emplea para proyectar la línea de costa y generar la morfología costera futura para elaborar proyecciones de inundación costera considerando los efectos de la erosión. El modelo de evolución de la línea de costa se describe en el Capítulo 2 y es capaz de resolver los procesos morfológicos más relevantes, los efectos de las intervenciones humanas y combina las ecuaciones basadas en la física de los procesos con observaciones para lograr una representación más precisa de la respuesta de las zonas costeras. El modelo se emplea para proyectar la evolución de la línea de costa considerando la incertidumbre inherente al cambio climático y generar información importante para la toma de decisiones informada y la adaptación al cambio climático en el Capítulo 3. A continuación, en el Capítulo 4, a partir de las proyecciones de la línea de costa, se ha implementado una nueva metodología para elaborar proyecciones de inundación considerando la erosión. Esto se ha conseguido mediante un aumento de escala de la línea de costa unidimensional producida por el modelo para generar cambios bidimensionales de la topobatimetría empleando un modelo de traslación de perfil. Finalmente, en el Capítulo 5, todos los avances realizados en este trabajo se condensan en un nuevo modelo capaz de proyectar no sólo la línea de costa sino la morfología bidimensional completa, siendo aplicable a la mayoría de las playas de arena del mundo.

De acuerdo con los objetivos inicialmente previstos, se presentan a continuación las principales conclusiones y mejoras alcanzadas:

Objetivo 1 - Desarrollo de un modelo de evolución de la línea de costa

- Se ha desarrollado un nuevo modelo basado en la física y de complejidad reducida capaz de resolver los principales procesos que contribuyen a la evolución de la línea de costa. El modelo resuelve los procesos longitudinales y transversales. La contribución de los procesos longitudinales a los cambios en la línea de costa considera los gradientes longitudinales en el caudal sólido, fuentes y sumideros de sedimento para modelar la descarga de ríos o actividades de dragado y una tendencia que considera los procesos no resueltos. El transporte transversal se resuelve a partir del modelo de equilibrio propuesto por Toimil et al. (2017a) al combinar el modelo transversal de corto plazo de Miller and Dean (2004) junto con la respuesta de largo plazo ante el ANMM según Bruun (1962).

- Las ecuaciones basadas en la física se complementan con observaciones mediante la implementación de un algoritmo de asimilación basado en el filtro extendido de Kalman (Long and Plant, 2012; Vitousek et al., 2017c) para reducir la incertidumbre del modelado y mejorar las estimaciones. Asimismo, se ha propuesto una estrategia de asimilación alternativa para evitar las falsas interacciones entre los procesos longitudinales y transversales en el filtro de Kalman.

- Las intervenciones humanas como espigones, diques escolleras y rellenos se han integrado en el modelo de evolución mediante alteraciones en la propagación del oleaje y en el transporte de sedimentos. Gracias a ello, el modelo se puede emplear en entornos costeros antropizados y para evaluar la respuesta costera ante diversas intervenciones.

Objetivo 2 - Desarrollo de una metodología para obtener proyecciones de evolución de la línea de costa considerando la incertidumbre climática

- Se ha desarrollado una metodología para proyectar la evolución de la línea de costa acoplando técnicas eficientes de regionalización del oleaje con el modelo de evolución. La técnica de regionalización es capaz de reproducir el oleaje en profundidades reducidas a partir de proyecciones de oleaje y nivel globales combinando herramientas estadísticas y numéricas. A continuación, el modelo de evolución se ha ejecutado con las dinámicas propagadas considerando la incertidumbre proveniente de varios escenarios de concentración, el oleaje y la marea meteorológica de

varios modelos globales y regionales climáticos y diferentes percentiles de ANMM.

- A partir de la multitud de series horarias de evolución de la línea de costa, se ha extraído información relevante para la gestión de la costa como los retrocesos permanentes, las áreas de playa perdidas, la contribución de distintos procesos a los cambios en la línea de costa o los retrocesos extremos. Esta información sirve de guía para la identificación de zonas de actuación y para la evaluación de las necesidades y prioridades de adaptación en el contexto del cambio climático.

Objetivo 3 - Desarrollo de una metodología para incluir los efectos de la erosión en las proyecciones de inundación a múltiples escalas

- Se ha formulado un nuevo emulador a escala regional combinando un emulador de variables lineales a escala local con un modelo multivariado de direcciones. Mediante esta mejora, se ha posibilitado la emulación sintética del oleaje y nivel asociado a tormentas en varios puntos de forzamiento para estudios regionales.

- Se ha desarrollado una metodología de acoplamiento multiescala entre la erosión y la inundación. El estudio de la literatura pone de manifiesto que es la primera vez que se ha generado una topobatimetría considerando los cambios en la línea de costa a partir de un modelo de evolución de la línea de costa y una herramienta de traslación del perfil que aplica reglas cinemáticas a los perfiles muestreados según los diferentes procesos modelados.

- Se ha realizado un estudio detallado de los efectos de la erosión en los estudios de inundación analizando la cota de inundación y la extensión del área inundada. Los resultados han revelado que, en el caso estudiado, la no consideración de la erosión en las proyecciones de inundación puede difuminar todos los esfuerzos en desarrollar mejores proyecciones de oleaje y nivel.

Objetivo 4 - Desarrollo de un modelo de evolución de la morfología costera para estudios a escala local

- Se ha desarrollado el primer modelo multiescala de evolución de la costa capaz de resolver la evolución morfológica durante decenas de años haciendo evolucionar la topobatimetría real. El modelo morfológico se ha implementado a partir de

la combinación del modelo de evolución de la línea de costa, la herramienta de traslación del perfil y un modelo avanzado de propagación de oleaje.

- La respuesta de la costa ante el ANMM se ha modelado considerando reglas cinemáticas heurísticas aplicadas a los perfiles reales y no a sus aproximaciones teóricas, distanciándose de la regla de Bruun (Bruun, 1962). Además, se ha validado mediante ensayos experimentales en Atkinson et al. (2018).

- La integración de un modelo de propagación avanzado ha permitido dotar de gran flexibilidad de aplicación al modelo morfológico, al poder modelar diferentes entornos costeros. Gracias a ello, se puede evaluar la respuesta de la costa ante la presencia de elementos costeros como estructuras, salientes rocosos, arrecifes de coral, manglares o campos de vegetación.

0.6.2. Futuras líneas

Los modelos, herramientas y metodologías desarrolladas en esta investigación constituyen el preludio de un objetivo más ambicioso, un modelo digital de la costa (Losada, 2022). Siguiendo otras iniciativas como el modelo digital de la Tierra (Bauer et al., 2021), un modelo digital de la costa es un sistema de información que expondría a los usuarios a una réplica digital del estado y de la evolución temporal del sistema costero condicionada por las observaciones disponibles y las leyes de la física. Puede emplearse tanto para la monitorización como para el pronóstico de la respuesta de la costa a múltiples escalas, para evaluar el error en los procesos y para complementar el conocimiento incompleto de algunos procesos físicos mediante observaciones y técnicas de aprendizaje de máquinas. Un gemelo digital de la costa sería una herramienta útil para la gestión de zonas costeras y para el desarrollo de elementos clave para la economía azul como el turismo o el transporte marítimo en el contexto del cambio climático. Aunque las metodologías y modelos están listos para ser explotados, para dar vida al gemelo digital de la costa, se necesita realizar un esfuerzo muy importante en el campo de la programación. Específicamente, el desarrollo de una interfaz común que integre todas las metodologías, herramientas y modelos de forma inter-operable y fácil de usar es un reto a nivel de desarrollo informático que sin duda alcanzaría retornos positivos en un futuro cercano.

Con respecto a los objetivos específicos, se han detectado elementos que requieren de una mayor atención en el futuro:

Con respecto al modelo de evolución de la línea de costa

- La discretización en transectos de la línea de costa se debería flexibilizar para tender hacia una discretización basada en vectores en la que la línea de costa evoluciona como un conjunto de puntos (Jiménez and Sánchez-Arcilla, 2004; Kaergaard and Fredsoe, 2013; Hurst et al., 2015; Roelvink et al., 2020). Esto permitiría modelar el crecimiento de puntales, las inestabilidades de la línea de costa por incidencia oblicua del oleaje y las costas con gran curvatura respetando de forma estricta la conservación del sedimento. El principal reto sería la integración del algoritmo de asimilación en la discretización basada en vectores. Para ello, una solución consistiría en hacer un símil, en cada paso de tiempo, entre la discretización basada en vectores y la basada en transectos. Los trasectos variarían en cada paso de tiempo y se intersectarían, de forma iterativa, con las líneas de costa observadas para poder aplicar el algoritmo de asimilación.

- Con el fin de aumentar la aplicabilidad del modelo a diferentes entornos costeros, se deberían incluir procesos adicionales como el retroceso de acantilados (Limber et al., 2018), los efectos debidos a estuarios (Toimil et al., 2017a) o la erosión de la duna (Antolínez et al., 2019).

- La asimilación de observaciones mediante el filtro extendido de Kalman requiere la derivación analítica de la matriz de covarianza para promediar el peso de las observaciones y de los resultados de la ecuación de gobierno de la línea de costa. La matriz de covarianza se propaga de forma analítica a partir de una estimación inicial y del ruido del proceso, que son difíciles de determinar debido a que su sentido físico no es claro. Como alternativa, la la matriz de covarianza se puede obtener a partir de la propagación de un conjunto de estados inicial (Ibaceta et al., 2020; Vitousek et al., 2021). La propagación de un conjunto implica un coste de cómputo extra, pero la matriz de covarianza, que juega un papel fundamental en los resultados de la asimilación, se obtiene de una forma más precisa directamente

a partir de los datos propagados. El filtro conjunto de Kalman se ha aplicado satisfactoriamente en modelos transversales de equilibrio, pero la integración de este método junto con modelos combinados de transporte longitudinal y transversal se debería explorar.

- La componente transversal de la evolución de la línea de costa es extremadamente difícil de calibrar debido a que las fluctuaciones de corto plazo comparten escala temporal con la frecuencia de revisita de las campañas satelitales. Por ello, se deberían integrar datos remotos provenientes de campañas de alta resolución y alta frecuencia de muestreo para mejorar la calibración de eventos extremos de corto plazo.

Con respecto a la metodología para obtener proyecciones de evolución de la línea de costa considerando la incertidumbre en el clima

- La incertidumbre en el clima se ha muestreado pero se ha considerado una única parametrización del modelo obtenida mediante asimilación. Se debería realizar un análisis más exhaustivo de la influencia de diferentes parametrizaciones iniciales (d'Anna et al., 2020). La implementación del filtro conjunto de Kalman permitiría tener en cuenta la incertidumbre debida a la parametrización del modelo.

- La tendencia debida a procesos no resueltos puede dar lugar a resultados erróneos a medida que el tiempo progresa durante el periodo de proyección. Es necesario acotar su valor e incluir en el modelado todos los procesos conocidos que contribuyan a la evolución de la línea de costa. Para reducir su valor, se debería mejorar la representación de los procesos físicos y se requerirían mejores observaciones. A continuación, una vía a explorar consistiría en la idea de relacionar la tendencia debida a procesos no resueltos con los forzamientos climáticos que condicionan la evolución de la línea de costa.

- En este trabajo se han aplicado parametrizaciones estacionarias. Esto se debe a que no existen formulaciones que relacionen los forzamientos climáticos con las parametrizaciones de los modelos de impacto. Sin embargo, algunos autores sostienen que las parametrizaciones no estacionarias dan lugar a mejores resultados (Ibaceta et al., 2020; d'Anna et al., 2022a). Para producir proyecciones de evo-

lución de la línea de costa considerando parametrizaciones no estacionarias, se deberían relacionar los forzamientos climáticos de gran escala y los modelos de impacto. Para ello, el trabajo de Montaño et al. (2021) se podría combinar con un método de proyección estadístico como el propuesto por Camus et al. (2017).

Con respecto a la metodología para incluir los efectos de la erosión en la inundación a múltiples escalas

- La respuesta de la costa ante el aumento del nivel del mar es extremadamente incierta ya que los niveles proyectados pueden dar lugar a comportamientos sin precedentes. La hipótesis de que el perfil asciende la misma magnitud que el nivel del mar y retrocede conservando el volumen sólo se validará si la experiencia así lo demuestra. Hasta entonces, los espejos numéricos de la realidad constituidos por modelos muy precisos (Cheng et al., 2017; García-Maribona et al., 2021) se deberían emplear para explorar este comportamiento y arrojar algo de luz al problema.

- La tormenta de referencia empleada para actualizar la topobatimetría no cubre toda la incertidumbre debida a la erosión por eventos extremos. Un mejor muestreo de la incertidumbre debería considerar la frecuencia y duración de las tormentas para incluir los efectos del agrupamiento de eventos extremos y de la recuperación de las playas a la hora de elaborar proyecciones de inundación considerando la erosión de la costa.

- Para integrar los efectos dinámicos de corto plazo de la erosión y de la inundación de la costa, se debería emplear un modelo bidimensional de procesos tipo XBeach en vez de un modelo de complejidad reducida. De este modo, se considerarían todas las interacciones en el corto plazo entre la erosión y la inundación.

Con respecto al modelo de evolución de la morfología costera para estudios a escala local

- IH-LANSloc se debería validar en casos reales considerando batimetrías complejas y diferentes entornos costeros como costas antropizadas o afectadas por corales o campos de vegetación. Idealmente, la validación se realizaría considerando no

sólo la evolución de la línea de costa sino la evolución del lecho.

- No se considera la reducción en la tasa de transporte de sedimentos debido a campos de vegetación o corales. Se debería mejorar la implementación de los procesos, específicamente en lo relativo a la capacidad de retención de sedimentos por parte de distintos ecosistemas naturales. Para ello, los avances en las técnicas de observación remota sin duda ayudarán a definir formulaciones de transporte más apropiadas.

- El empleo de un modelo avanzado de propagación de oleaje permite obtener una descripción detallada de la rotura. Esta información, que se difumina al emplear parámetros agregados del estado de mar, se debería explotar mediante formulaciones de impacto que dependiesen del espectro completo frecuencia-dirección del oleaje. Sólo la formulación de transporte longitudinal de Van Rijn (2014) considera la dependencia frecuencial mediante el porcentaje de olas de mar de fondo en el estado de mar. Al igual que en el caso anterior, la disponibilidad de observaciones ayudarán a desarrollar y mejorar las formulaciones de impacto actuales.

0.7. Contribuciones científicas

Artículos revisados por pares vinculados directamente con la tesis doctoral:

1. Alvarez-Cuesta, M., Toimil, A., and Losada, I. J. 2021. Modelling long-term shoreline evolution in highly anthropized coastal areas. Part 1: Model description and validation. *Coastal Engineering,* 169(Julio):103960

2. Alvarez-Cuesta, M., Toimil, A., and Losada, I. J. 2021. Modelling long-term shoreline evolution in highly anthropized coastal areas. Part 2: Assessing the response to climate change. *Coastal Engineering,* 168(Julio):103961

3. Toimil, A., Alvarez-Cuesta, M. and Losada, I. J. 2022. Neglecting the coupled effect of coastal flooding and erosion can lead to spurious impact projections and maladaptation. *En revisión en Coastal Engineering.* Enviado en Abril del 2022.

Colaboraciones en artículos revisados por pares relacionadas con el tema de la tesis:

1. Thiéblemont, R., Le Cozannet, G., Rohmer, J., Toimil, A., Alvarez-Cuesta, M., Losada, I. J. 2021. Deep uncertainties in shoreline change projections: an extra-

probabilistic approach applied to sandy beaches. *Natural Hazards and Earth System Sciences,* 2015(Enero):1-24

2. Toimil, A., Camus, P., Losada, I., <u>Alvarez-Cuesta, M.</u>, 2021. Visualising the uncertainty cascade in multi-ensemble probabilistic coastal erosion projections. *Frontiers in Marine Science*, 8(Junio):1-19

Presentaciones orales realizadas durante la formación doctoral:

1. <u>Alvarez-Cuesta, M.,</u> Toimil, A., Losada, I. J. 2020. Una herramienta para el modelado de la evolución de la línea de costa en zonas fuertemente antropizadas en un clima incierto. *IV Congreso Transfronterizo sobre el Cambio Climático y Litoral (UHINAK).* Online.

2. <u>Alvarez-Cuesta, M.,</u> Toimil, A., Losada, I. J. 2021. Forecasting the shoreline evolution at highly anthropized coastal areas. *European Geosciences Union, EGU.* Online.

3. Thiéblemont, R., Le Cozannet, G., Rohmer, J., Toimil, A., <u>Alvarez-Cuesta, M.</u>, Losada, I. J. 2021. Deep uncertainties in shoreline change projections: an extra-probabilistic approach applied to sandy beaches. *European Geosciences Union, EGU.* Online.

4. Toimil, A., <u>Alvarez-Cuesta, M.</u>, Losada, I. J. 2021. On the need for uncertainty consideration in coastal erosion projections to support adaptation planning. *American Geophysical Union (AGU)* . Online.

5. <u>Alvarez-Cuesta, M.,</u> Toimil, A., Losada, I. J. 2022. IH-LANS: Una herramienta para el modelado de la línea de costa. *XVI Jornadas Españolas de Ingeniería de Costas y Puertos.* Vigo, España.

6. <u>Alvarez-Cuesta, M.,</u> Toimil, A., Losada, I. J. 2022. Reduced-complexity modelling as a valuable tool to study the coastal impacts of climate change. *European Geosciences Union, EGU.* Online.

CHAPTER 1

INTRODUCTION

1.1. Motivation and state of the art

Coastal areas play a major socio-economic role worldwide as they are densely popu-
lated, accommodate critical infraestructures and host essential economic exchanges like
tourism, fisheries or maritime transport. Nowadays, 10% of the world's population lives
in a narrow band near the sea below 10 meters of elevation and this rate is expected
to increase in the future (Jones and O'Neill, 2016). Population projections expect that
the number of people living in low elevated coastal zones will increase by 66% in 2060
with respect to 2000, eventually reaching 1,000[1] million people (Neumann et al., 2015).
Coastal zones are also essential from an economic perspective. In 2010, the global ocean
economy accounted for an added value of US$1.5 trillion, with relevant contributions
from offshore oil and gas, maritime and coastal tourism, ports and maritime equipment
and ocean-based industries employments (Melet et al., 2020). In the near future (2030),
ocean economy is expected to grow until US$3 trillion relying on fossil fuels extraction,
port activities and tourism (OECD, 2016). Coastal ecosystems house a wide diversity
of flora and fauna species. They are one of the most productive ecosystems on Earth
regarding fisheries and have an important regulation role and protection value (Duarte

---

[1]Throughout the document, the comma is used as the thousands separator while the dot is employed
as the decimal sign.

et al., 2013; Narayan et al., 2016; Beck et al., 2018; Reguero et al., 2021).

In spite the importance of coastal zones, they are under current threats of erosion and flooding. From 30 years of satellite derived observations, Luijendijk et al. (2018) estimated that 24% of the world's sandy beaches are eroding, while the majority of marine protected areas lie in sediment starved regions. Mentaschi et al. (2016) calculated, based on global satellite data, that land losses between 1984 and 2015 (28,000 km^2) double gained land and concluded that man-made factors were clearly the main drivers of change. On the other hand, more than 100 million people occupy areas below present-day high tide lines (Kulp and Strauss, 2019) and the amount of people exposed to low-probability coastal flooding almost doubles this quantity (Dullaart et al., 2021). Low-lying coastal deltas where continental waters meet the ocean are clearly at risk. Syvitski et al. (2009) highlighted that during the first decade of 21st century, 85% of deltas experienced severe flooding mainly due to anthropogenic factors, resulting in the episodic submergence of 260,000 km^2.

In the upcoming decades, erosion and flooding will continue to harass coastal areas in a more intense way due to climate change (Nicholls and Cazenave, 2010; Ranasinghe, 2016; Collins et al., 2019). Mean sea levels have been increasing during the past century (Hay et al., 2015; Fasullo et al., 2016) and they are expected to increase at unprecedented rates during the upcoming decades due to global warming (Kopp et al., 2014; Jevrejeva et al., 2016; Hermans et al., 2021). In addition to mean sea level, climate change is increasing wave power (Reguero et al., 2019) and altering the mean and extreme wave climate (Hemer et al., 2013; Lobeto et al., 2021a), storm surges (Little et al., 2015; Muis et al., 2020), tropical cyclone activity (Bloemendaal et al., 2022; Gori et al., 2022) and astronomical tides (Idier et al., 2017; Haigh et al., 2020). As a result of the interactions between the different drivers, extreme total water levels at the coast will increase at faster rates than sea level rise (SLR), boosting the number of annual overtopping hours by one order of magnitude with respect to present levels (Almar et al., 2021). Half of the world's sandy beaches are at risk of disappearing at the end of the century (Vousdoukas et al., 2020b). Extreme sea levels integrating SLR, astro-

nomical tides, storm surges and waves would expose most of the worlds coastlines every year to the event that occurs today, on average, once every 100 years (Vousdoukas et al., 2018b) from 2050, even for low (1.5°C) warming levels (Tebaldi et al., 2021). With no adaptation measures, increasing levels of coastal exposure and hazard in Europe will push current expected annual damage from €1.25 billion by several orders of magnitude, ranging from €93 to €961 billion by the end of the century (Vousdoukas et al., 2018a) and the global migration of 1.6-5.6 million people due to coastal recession leading to migration costs up to a US$1 trillion (Hinkel et al., 2013). Similarly flood risk at the world's major coastal cities will reach unprecedented levels from US$6 billion losses per year in 2005 up to US$1 trillion or more by 2050 (Hallegatte et al., 2013).

The answer to the question of how the coastal zone will evolve under climate change is extremely uncertain, as it lies at the intersection of social, atmospheric, ocean and earth sciences, civil engineering and policy making. However, it is acknowledged the transcendental role of engineering in shaping its future (Vitousek et al., 2017b), mainly through adaptation measures (Brown et al., 2014; Vousdoukas et al., 2020a). In order to circumvent the very likely and extreme socio-economic losses, robust projections of erosion and flooding risks are needed to help decision makers choose the best adaptation strategies considering all the uncertainty sources (Toimil et al., 2021a). To this end, reliable impact models are deemed essential to forecast erosion and flooding hazards, to evaluate the risk, identify hotspots and evaluate adaptation measures. An ideal coastal impact model should be capable of resolving the relevant physical processes and their interactions at the temporal scale of climate change (decades), at the spatial scale of adaptation (local to regional) and computationally efficient to handle multiple simulations associated with uncertain drivers (Ranasinghe, 2020; Toimil et al., 2020a). Furthermore, uncertainties arising from the incomplete knowledge of the coastal system should be minimized by enriching the physics-based equations with observational data via assimilation (Splinter and Coco, 2021) or machine learning algorithms (Wang et al., 2022), which will profit from the advances in remote sensing and the availability of open source satellite images of global coverage (Turner et al., 2021).

Some progress have been made regarding erosion modelling thanks to the development of multi-process reduced-complexity models (Vitousek et al., 2017c; Toimil et al., 2017a; Robinet et al., 2018; Antolínez et al., 2019; Tran and Barthélemy, 2020); the use of observations in data-assimilation approaches (Long and Plant, 2012; Vitousek et al., 2017c; Ibaceta et al., 2020); and the consideration of different sources of uncertainty ranging from model parametrisations (d'Anna et al., 2020), sea level rise (d'Anna et al., 2021; Thiéblemont et al., 2019), different chronologies of wave climate (Toimil et al., 2017a; Vitousek et al., 2021; d'Anna et al., 2022a), different future wave climate scenarios (Zacharioudaki and Reeve, 2011; Bamunawala et al., 2020) or a combination of different sources (Toimil et al., 2021a). Similarly, several reduced-complexity flooding models suited for climate change studies have been developed (Bates and De Roo, 2000; Gouldby et al., 2008; Leijnse et al., 2021), data-assimilation approaches have been introduced in the analysis to reduce modelling uncertainties (Muñoz et al., 2022; Nguyen et al., 2022), mathematical models have been tuned up to produce statistically robust forcing conditions (Rueda et al., 2016; Lucio et al., 2020) and metamodelling techniques have been applied to efficiently downscale total water levels to the coast (Anderson et al., 2021). Flooding and erosion have been coupled in the temporal scale of storms in forensic studies (Gharagozlou et al., 2020; van Ormondt et al., 2020) and under climate change (Passeri et al., 2018; Grases et al., 2020). Also, long-term changes have been integrated in some flooding studies using different methodological approaches (Passeri et al., 2016; Lentz et al., 2016; Stripling et al., 2017; Grilli et al., 2017; Erikson et al., 2017). To date, a single model capable of holistically solving erosion and flooding at the relevant scales for climate change in an efficient way does not exist, but some efforts have been made in order to develop modelling frameworks that incorporate climate change-driven dynamic coastal processes to develop long-term projections of coastal impacts. The Coastal Storm Modeling System (CoSMoS, Barnard et al. (2019)) is a great example of it, as it is combines a suite of physics-based numerical models (Vitousek et al., 2017c; Erikson et al., 2017; Limber et al., 2018), to assess future coastal flooding risk considering SLR, dynamic water levels and coastal change. However, climate-related uncertainty is not property sampled as just one climate model is considered and future storms do not consider every statistically plausible combination of drivers that could

trigger a major flooding event. The shoreline modelling combines observations and process equations but the effects of man-made interventions are neglected. Flooding is calculated using a transect-based hydrodynamic model and flooding maps are derived by applying spatial interpolation. Terrain heights are updated considering the shoreline evolution but profile kinematics are oversimplified.

A modelling framework capable of reproducing the coastal response in terms of erosion and flooding, combining: a) the most relevant processes at multiple scales and their interactions, b) the effect of man-made structures and nature-based solutions, c) the uncertainty of future drivers, d) the interactions between coastal flooding and erosion, e) the effects of every plausible storm event via synthetic generation and f) and metamodelling techniques to efficiently downscale total water levels using process-based models; does not exist. In order to overcome current gaps, the present research aims to develop a coastal erosion and flooding assessment framework by integrating: a proper uncertainty sampling of future coastal change drivers, the state of the art in remote sensing, new reduced-complexity physics-based models, rigorous modelling of hard and soft engineering interventions, probabilistic storm emulation techniques and a novel and replicable erosion-enhanced flooding methodology.

1.2. Hypothesis and goals

Risks from coastal flooding and erosion and adaptation to climate change along the coast have become one of the main priorities in the decision makers' agenda worldwide. The IPCC's Special Report on the Ocean and Cryosphere in a Changing Climate (Collins et al., 2019) highlights that the combined effect of increasing hazard due to extreme and long-term processes, increasing exposure of population and assets and increasing vulnerability of coastal communities, will yield unprecedented levels of future risk at the coastal zone. Risk management and adaptation represent a global unparalleled investment challenge full of uncertainties. The need to tackle decision making in this context requires having advanced tools, methodologies and models to develop

robust coastal impact assessments so as to obtain reliable risk projections, which will serve as the basis to choose the best solutions and guarantee the appropriate allocation of funds. Establishing efficient adaptation measures in the coast requires assessing the coastal impacts of climate change with reduced uncertainty. Regarding erosion impact assessment, reliable impact models integrating all the relevant coastal processes and their interactions at the climate change scale and capable of evaluating the effects of different adaptation measures on the coastal response are needed. Furthermore, the uncertainties in future climate requires specific methodologies in order to efficiently translate the climate information to probabilistic estimates of coastal impacts. To this end, a methodology to project the coastal evolution under climate change considering the uncertainties of future drivers and minimizing the calibration uncertainty of the impact model is required. Flooding and erosion are commonly studied independently due to the difficulties arising from their interactions at different time scales, specially in the long term. However, a clear correlation exists between coastal erosion and the subsequent coastal flooding hazard. Thus, multi-scale methodologies for including erosion in flooding projections are needed in order to develop robust risk projections to inform decision making in the context of climate change adaptation. In order to produce reliable risk forecasts to guide decision making and adaptation in the coastal zone in the context of climate change, an assessment framework combining all the advances in impact modelling of erosion and flooding and their interactions is needed.

Based on the aforementioned hypothesis, **the general goal of this research is to develop an impact assessment framework composed of different models, tools and methodologies aimed to improve erosion and flooding risk assessments to support climate change adaptation.** The guiding thread of the work is to better understand how the shoreline responds to different forcings and then, to upscale shoreline changes to predict the shoreface behaviour and produce better flooding projections. Special attention needs to be paid to the temporal scales imposed by climate change. While the long-term evolution of the coastal zone is the target, short-term changes due to extreme events of flooding and erosion need to be accounted for and the relative weight on the coastal impacts of the different temporal scales needs to deciphered so as

94

to guide decision making.

In order to pursue the main objective, the following specific research objectives have been proposed:

Objective 1: Development of a shoreline evolution model. The model needs to solve the main processes governing shoreline change, the effects of man-made interventions and needs to take profit from emerging global-coverage remote-sensed observations through data-assimilation. The model needs to be efficient to sample climate-related uncertainty and modular, to be able to follow and adapt to the latest advances in process modelling and data-assimilation.

Objective 2: Development of a methodology to obtain shoreline evolution projections considering climate-related uncertainty. The methodology needs to account for waves and storm surges from different climate models, emissions scenarios and sea level rise trajectories. It needs to include efficient strategies to downscale every future realization of waves and water levels to the coast and together with the coastal model, they will produce the shoreline evolution time series considering the uncertainty of future drivers in order to support decision making in the coastal zone.

Objective 3: Development of a methodology to include the erosion effect on flooding forecasts at multiple scales. Climate-related uncertainty needs to be accounted for by appropriate statistical modelling and simulation of storms at regional scales for different future scenarios. This needs to be achieved by combining a regional-scale synthetic storm generator, to account for every combination of drivers that is statistically plausible, with process-based assessments of flooding extents and depths using metamodelling techniques. Additionally, the methodology needs to be capable of incorporating the one-dimensional shoreline changes from reduced-complexity models, enabling to evaluate coastal flooding on erosion-updated terrain models and produce robust flooding forecasts.

Objective 4: Development of a nearshore evolution model for local-scale studies. The model needs to solve all the processes governing shoreline change and needs to dynamically update the nearshore topobathymetry. Wave propagation over uneven dynamic bathymetries needs to be accounted for using accurate wave models. Additionally, uncertainty reduction benefits from data-assimilation and the effects of man-made and nature-based solutions on the coastal response needs to be integrated in the nearshore model.

1.3. Methodological framework

The main advances developed in this work consist of a set of models, tools and methodologies built around a guiding principle: achieving the best representation of the multi-scale evolution of the nearshore in the context of climate change. This is highlighted by the closed loop in Figure 1.1.

To this end, a shoreline evolution model is built considering long and short-term processes, the effect of man-made interventions and is enriched by observations using an adapted data-assimilation algorithm. Once the model is validated, a methodology to project the impacts of future climates in terms of shoreline evolution is developed. Efficient downscaling techniques are implemented so as to generate the inputs for the shoreline evolution model and sample the uncertainty of future climates in the shoreline response. Starting from the shoreline evolution time-series, a methodology to transfer the one-dimensional shoreline changes to spatial topobathymetric variations is developed so as to produce erosion-enhanced flooding projections. This is done by applying a recently developed profile updating model that uses the outputs of the shoreline model to generate a cloud of points. By interpolating these points, an erosion-updated topobathymetry is obtained and then used as the underlying terrain for process-based flooding simulations. The thesis research loop goes back to its origin of improving the representation of the nearshore response under climate change by integrating all the knowledge acquired throughout the research process. From this, a novel nearshore evolution model is built by coupling in a bidirectional way the shoreline evolution model,

the topobathymetry updating methodology and an advanced wave propagation model. This nearshore model inherits all the advances introduced in the shoreline model in terms of data assimilation; but improves the process description of wave propagation over complex bathymetries, includes the effects of specific coastal features like mangroves or vegetation patches and is capable of handling high-fidelity spectral descriptions of wave climate. The model produces as output the shoreline evolution and the complete nearshore evolution time series, which can be directly introduced as input in an inundation model.

This research provides a step forward in the assessment of coastal impacts of climate change yielding improved hazard estimates. Combining the modelling outputs with exposure and vulnerability sets the basis for risk analysis and climate change adaptation following the IPCC's general framework (Wong et al., 2014; Oppenheimer et al., 2019; Collins et al., 2019), as described in Figure 1.1.
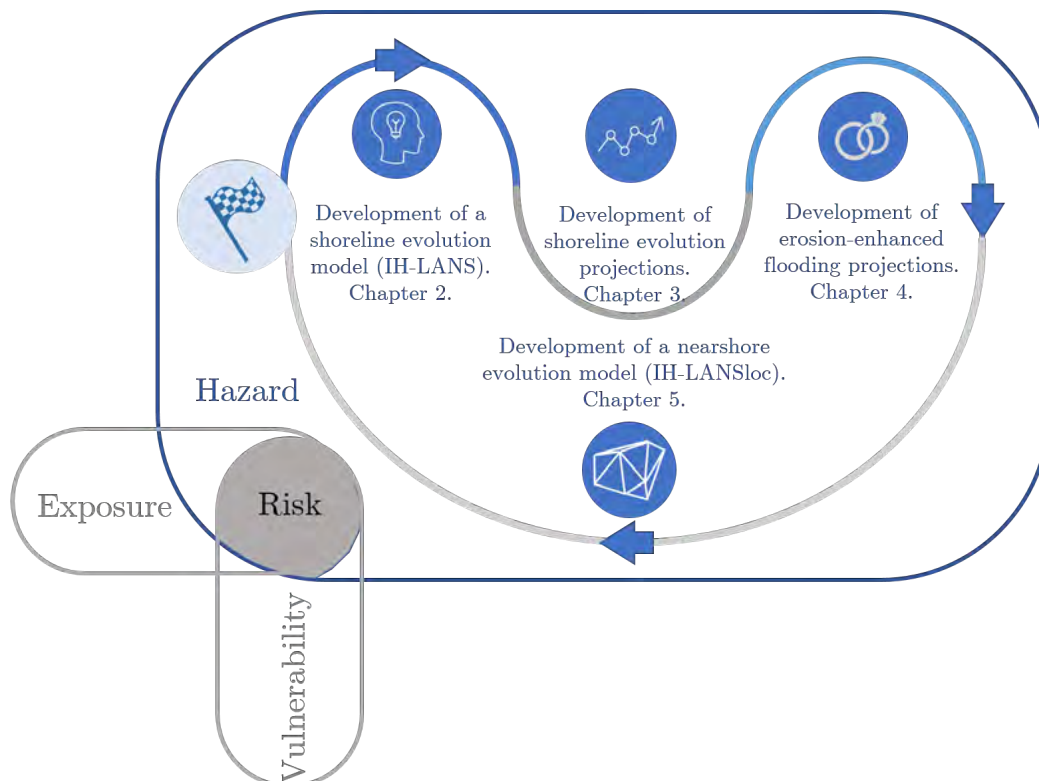
Figure 1.1: Graphical representation of the methodological framework and scope. In blue the elements tackled in this work and in grey the rest of the components of risk.

1.4.　Structure of the dissertation

This PhD thesis is organised in six chapters that try to fulfil the objectives detailed in Section 1.2:

- Chapter 0 presents a summary of the dissertation translated to Spanish.

- Chapter 1 introduces and motivates the research.

- Chapter 2 addresses the development of a new reduced-complexity shoreline evolution model that resolves the main physical processes governing shoreline change.

- The shoreline model developed in Chapter 2 is applied, in Chapter 3, to calculate shoreline projections using future waves and water levels.

- Chapter 4 is devoted to developing erosion-enhanced flooding projections under climate change.

- Chapter 5 is consacrated to the extension of the reduced-complexity shoreline model described in Chapter 2 to two dimensions for local studies of the nearshore evolution.

- Finally, Chapter 6 is dedicated to synthesizing the conclusions of this work and to streamline future research steps.

CHAPTER 2

DEVELOPMENT AND VALIDATION OF IH-LANS

In this Chapter, a new shoreline evolution model, named IH-LANS (Long-term ANthropized coastlines Simulation tool), is presented. IH-LANS is ideally suited for regional-scale analysis of the long-term response of natural and anthropized coasts. In IH-LANS, a hybrid (statistical-numerical) deep-water propagation module and a data-assimilated shoreline evolution model are coupled. Longshore and cross-shore processes are integrated together with the effects of man-made interventions. For every simulation, shoreline changes in response to time-varying wave conditions and water levels are evaluated while reducing calibration uncertainty by means of an extended Kalman filter that allows to assimilate shoreline observations. To test the performance of the model, IH-LANS is applied to a highly anthropized 40 km stretch located along the Spanish Mediterranean coast. The model is run during the period 1990–2020 using high space-time resolution climate data and satellite-derived shorelines in order to calibrate the free parameters and validate model outputs. Shoreline evolution is successfully represented (<10 m of root mean square error, RMSE) while accounting for the effects of

nourishments and the construction and removal of groynes, seawalls and breakwaters over time. The efficiency of the model makes IH-LANS a powerful tool for coastal management and climate change adaptation.

2.1. Introduction

Coastal evolution is the result of complex non-linear interaction between hydrodynamic, geomorphologic and anthropogenic processes at multiple time scales (Stive et al., 2002). Short-term changes at storm to multiannual scales are usually linked to waves, storm surges and extreme river discharge events (Maspataud et al., 2009; Splinter et al., 2014). At the same time, long-term changes are mainly driven by offshore waves that generate gradients in the longshore sediment transport (LST) rates, profile re-accommodation in response to sea level rise or chronic sediment sinks/sources (Jiménez and Sánchez-Arcilla, 2004).

The consequence of the complex interplays between the driving mechanisms at different scales implies that, nowadays, solving coastal evolution hollistically (jointly resolving all the spatio-temporal scales) is untracktable (Toimil et al., 2020b). The most detailed coastal evolution studies combine high-resolution RANS hydrodynamic modelling with sediment transport and bed evolution formulations (Cheng et al., 2017; García-Maribona et al., 2021). However, the enormous computational cost prevents the application of such models to broader scales than the laboratory. A step further in spatio-temporal scale is achieved by simplifying the hydro-morphodynamics using models like XBeach (Roelvink et al., 2009), Delft3D (Lesser et al., 2004) or ROMS (Shchepetkin and McWilliams, 2005), amongst others. These process-based models are succesfully applied at time scales of storms and spatial scales of few kilometers. A reasonable amount of effort has been dedicated to extend the application scale of process-based models via input-reductions techniques (de Vriend et al., 1993), morphological acceleration factors (Ranasinghe et al., 2011) or diffusive techniques to preserve the equilibrium configuration (Falqués et al., 2008). However, even if the computational resources for performing regional centennial process-based simulations of coastal change

were available, propagation of numerical errors and small-scale morphological instabilities could invalidate the results (Ranasinghe, 2016). To overcome these limitations, reduced-complexity physics-based models allow for modelling the coastal evolution at regional and centennial scales by simplifying the physics of the fundamental processes. These models focus on the individual processes that shape the coasts in order to solve particular morphodynamic variables (i.e. the shoreline). Equilibrium shoreline models, which compute shoreline changes in response to a disequilibrium state (Miller and Dean, 2004; Yates et al., 2009; Splinter et al., 2014) are distinguised from models that account for shoreline changes due to LST gradients based on the Pelnard-Considère (1956) equation (the so called one-line models). Additionaly, one-line models can be classified according to the spatial discretization of the governing equation in transect-based models (Tonnon et al., 2018; Kroon et al., 2020), vector-based models (Kaergaard and Fredsoe, 2013; Hurst et al., 2015; Roelvink et al., 2020) and simplified 2D models (Ashton and Murray, 2006; Falqués et al., 2008; Limber et al., 2017).

Recently, in order to achieve a better representation of the shoreline evolution, some authors have coupled several processes in the same model (Vitousek et al., 2017c; Robinet et al., 2018; Antolínez et al., 2019; Tran and Barthélemy, 2020). Due to the increased availability of data through remote sensing techniques (Vos et al., 2019; Sánchez-García et al., 2020), empirical or data-driven models, at various complexity ranges, are being developed (Goldstein et al., 2019; Le Cozannet et al., 2019; Vousdoukas et al., 2020b). The main disadvantages of these models are that the physical processes that drive shoreline change cannot be directly disentangled and the accuracy of the forecast depends on the extrapolation of linear trends from observations. In an attempt to address these shortcomings, a bridge between reduced-complexity and data-driven models was initially built by Long and Plant (2012) and extended by Vitousek et al. (2017c). Even though these models need calibration and thus, they rely on past observed shoreline behaviour, the main physical processes are explicitly modelled. The forecast depends on the extrapolation of the calibrated parameters and, conversely to conventional data-driven approaches, may lead to a non-linear shoreline response. In both research works, a multi-process reduced-complexity physics-based model was enhanced by data via the

automated calibration of free-model parameters through the extended Kalman filter.

Despite the advances in shoreline modelling, the proposed models lack the ability to predict long-term shoreline response to different anthropogenic interventions, which is agreed to be the main shaper of future coastlines (Vitousek et al., 2017b). Most human interventions are directly linked to longshore sediment transport. Thus, the treatment of seawalls and fully developed tombolos in longshore models is detailed in Hanson and Kraus (1986), and realistic bypass boundary conditions for groynes are formulated in Hanson (1989). A step forward in shoreline modelling is attained when including wave diffraction in a longshore model in Suh and Hardaway (1995) and Dabees (2000) to model tombolo formation behind offshore breakwaters. However, in spite of the past efforts to account for structures in longshore models, the current multi-process reduced-complexity models oversimplify structures modelling. For instance, in Robinet et al. (2018), a groyne is analysed but no realistic bypass condition is integrated in the analysis and the treatment of seawalls was not addressed. However, the coupling with a 2D wave model allows for modelling the shoreline evolution behind breakwaters. In Vitousek et al. (2017c), anthropogenic interventions are not explicitly modelled in the process equation but they were included as a trend obtained through data-assimilation. Furthermore, wave-breaking properties, responsible for wave-driven shoreline evolution, are usually uncoupled from morphodynamic changes (Vitousek et al., 2017c) or over-simplified, for instance, by neglecting the spatial variability of wave climate in the study area (Roelvink et al., 2020).

To overcome these limitations, a reduced-complexity physics-based model, IH-LANS, which combines a hybrid (statistical and dynamic) nearshore wave propagation module similar to Camus et al. (2013) and a multi-process data-assimilated shoreline evolution model, is proposed. The shoreline evolution model accounts for longshore and cross-shore processes via the classical transect-based one-line approach (Vitousek and Barnard, 2015) and the equilibrium model described in Toimil et al. (2017a). Man-made interventions such as groynes, breakwaters, seawalls and nourishments are considered both in the breaking wave propagation and in the sediment transport dynamics. Cal-

ibration of free model parameters is done by data-assimilation through the extended Kalman filter (eKf), which has been modified from previous applications to consider two different erosion and accretion constants in the cross-shore transport formulation. Additionaly, one of the concerns regarding multi-process data-assimilated shoreline models is the ability of the assimilation algorithm to attribute the right weight to the longshore and cross-shore parameters. This problem is analysed and an alternative data-assimilation approach to the one originally proposed in Long and Plant (2012) is provided to avoid spurious longshore-cross-shore parameter interactions in the eKf.

The Chapter is structured as follows: Section 2.2 encompasses the details regarding the governing equation calculation flow chart, the downscaling techniques, the different solved processes and the data-assimilation algorithm. In Section 2.3 different synthetic cases are modelled in order to validate the functionalities of the model. Section 2.4 presents the application of IH-LANS to a real case example in a highly anthropized coastal area. Finally, the conclusions regarding the novel reduced-complexity model are presented in Section 2.5.

2.2. Structure and functionalities of the model

The structure of the shoreline evolution model is founded on three key elements that are: 1) an efficient two-step wave transformation module that combines hybrid (statistical-numerical) nearshore propagation and a breaking propagation routine; 2) a multi-process shoreline evolution equation that considers longshore and cross-shore contributions; and 3) a data-assimilation algorithm for the calibration of free parameters.

The calculation flow diagram of IH-LANS is displayed in Figure 2.1. The first step consists of gathering all the necessary inputs at the study area which are: deep-water wave climate and water levels, bathymetry, sediment characteristics, shoreline observations, sediment exchanges at the study area limits and the parametrization of man-made interventions. Then, the numerical domain, which comprises the computational grid for

the nearshore wave propagation of offshore wave climate and the transect-based shore-line discretization, is defined.

Inputs
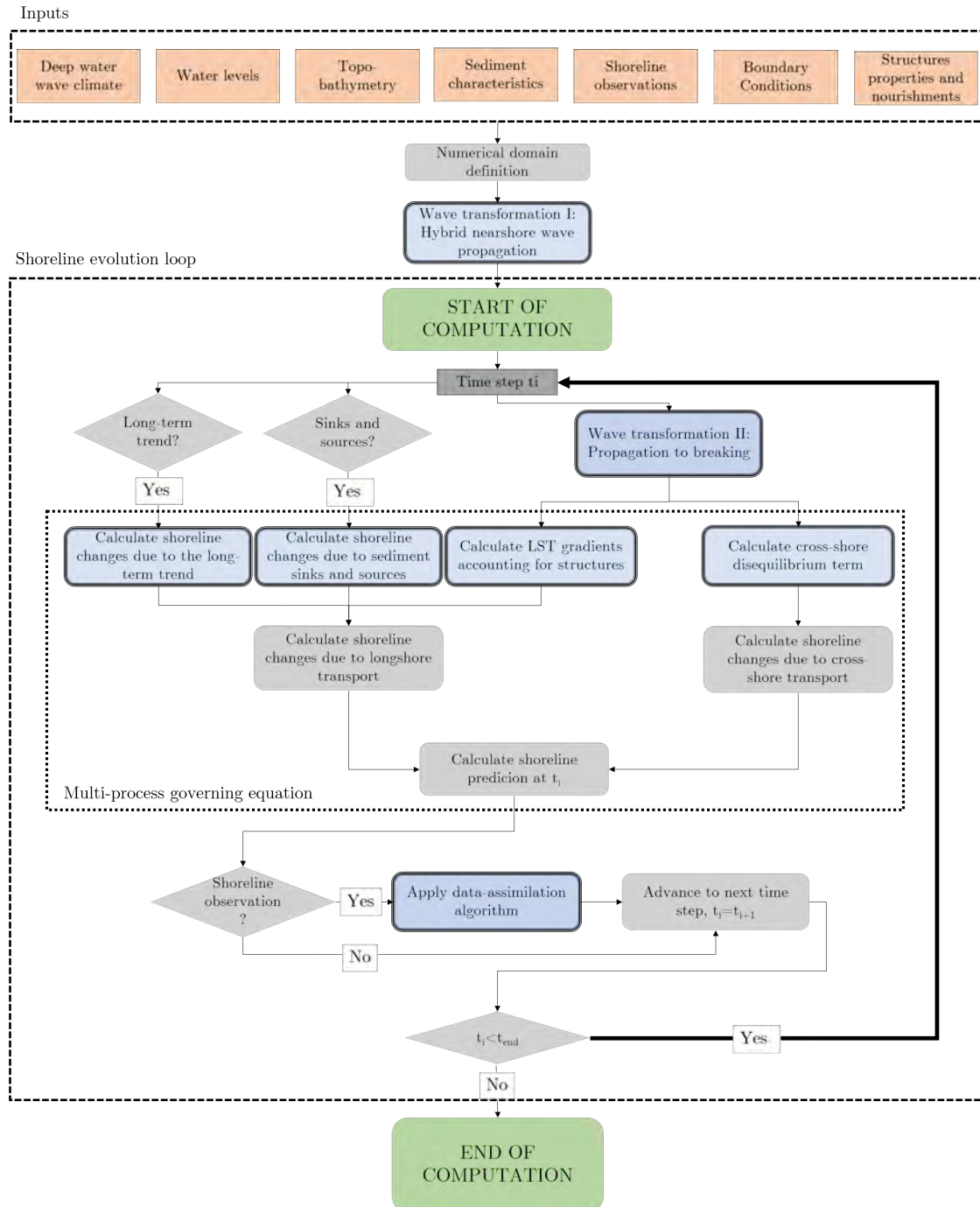
Figure 2.1: IH-LANS calculation flowchart.

Nearshore waves are obtained at a set of pre-defined downscaling points via a hybrid method that combines statistical techniques and numerical propagation. In a later step,

nearshore waves and water levels are further propagated to breaking so as to feed the wave-driven modules of the shoreline evolution equation.

The multi-process shoreline evolution equation accounts for four independent modules (Equation 2.1). Three of these modules, which are the wave-driven LST gradients calculated following the CERC expression (USACE, 1984), sediment sinks and sources and the unresolved processes trend, are responsible for longshore-related shoreline changes. On the other hand, wave and water level -driven cross-shore transport is responsible for cross-shore shoreline changes through the Toimil et al. (2017a) model based on Miller and Dean (2004).

Knowing the rails (transects) that guide shoreline evolution allows for obtaining the observed shoreline positions at each transect from detected continuous shorelines before solving the shoreline evolution governing equation. Therefore, for the ease of coupling longshore and cross-shore processes to the data-assimilation scheme, a transect-based discretization (fixed reference system) is applied to solve the following equation:

$$
\underbrace{\frac{\partial Y}{\partial t}}_{\text{Total shoreline change}} = \underbrace{\frac{\partial Y_l}{\partial t}}_{\text{Longshore shoreline changes}} + \underbrace{\frac{\partial Y_c}{\partial t}}_{\text{Cross-shore shoreline changes}}
$$

$$
\frac{\partial Y_l}{\partial t} = \underbrace{-\frac{1}{B+d_c}\frac{\partial Q}{\partial x}}_{\text{LST gradients}} + \underbrace{\frac{1}{B+d_c}q}_{\text{Sinks and sources of sediment}} + \underbrace{vlt}_{\text{Unresolved processes}} \qquad (2.1)
$$

$$
\frac{\partial Y_c}{\partial t} = \underbrace{K_c^{+/-}[Y_c^{eq} - Y_c]}_{\text{Cross-shore changes}}
$$

where Y is the distance, measured along the transect, from an arbitrary reference line (e.g. the onshore profile point) to the shoreline (mean high water contour), and corresponds to the summation of the shoreline position associated with longshore processes (Y_l) and cross-shore processes (Y_c). B is the berm height, d_c refers to the depth of closure, $\frac{\partial Q}{\partial x}$ corresponds to LST gradients, $\frac{q}{B+d_c}$ represents the shoreline change rate due to sediment sinks ($q < 0$) and sources ($q > 0$), vlt is the long term trend which accounts for unresolved processes, $K_c^{+/-}$ refers to the cross-shore rate of accretion/erosion and Y_c^{eq} defines the cross-shore equilibrium position.

Equation 2.1 is solved numerically by means of an explicit forward Euler scheme in a staggered grid defined by the transect-based discretization. Numerical stability, which needs to be verified for the spacetime dependent equation (LST gradients), is ensured if $\Delta t < \frac{(d_c+B)\Delta x^2}{4Q_{max}}$, being Δx the spacing between transects. The stability condition is checked every time-step and if violated, model forcings are linearly interpolated in order to reduce Δt while preserving Δx.

Solving Equation 2.1 at a given time step yields a shoreline prediction that corresponds to the summation of longshore and cross-shore processes including, if any, the effects of man-made interventions like groynes, breakwaters, seawalls and nourishments. In the next step in the calculation flow of IH-LANS, it is verified if a shoreline observation is available for calibration. In the case there is data for assimilation, shoreline prediction and selected model free parameters are updated by means of the extended Kalman filter and the loop moves forward to the next time step.

In the upcoming subsections, the key elements of IH-LANS, represented as boxes outlined with solid lines in Figure 2.1, are explained in detail. First, the two-step wave transformation is addressed. Then, the four modules responsible for the shoreline evolution are tackled starting from the two wave-driven modules. Finally, the data-assimilation technique, based on the extended Kalman filter, is described.

2.2.1. Two-step wave transformation

Deep water wave climate propagation is performed in two different steps. The first one consists of a hybrid nearshore wave propagation which transforms offshore wave conditions to the nearshore. This propagation step does not depend on any wave-driven morphodynamic changes, as wave characteristics are obtained at a depth greater than the active profile. The second step consists of wave propagation to breaking considering shoaling, refraction and diffraction induced by artificial structures. A schematic representation of the two propagation steps is displayed in Figure 2.2.
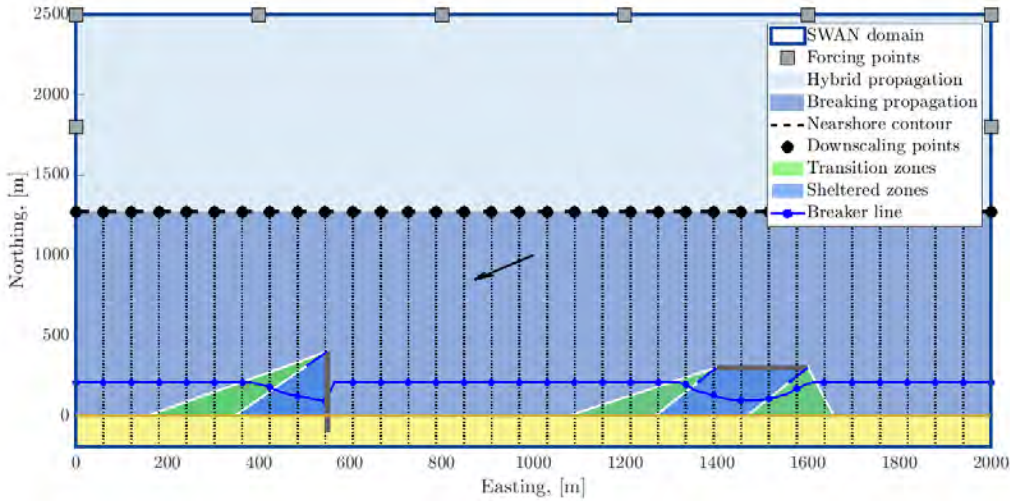
Figure 2.2: Definition sketch of wave propagation techniques employed to obtain the wave properties at the breaking line.

2.2.1.1. Wave transformation I: hybrid nearshore wave propagation

The hybrid nearshore downscaling technique implemented in IH-LANS is adopted from Camus et al. (2013) but slightly modified to account for detailed spectral information (spectral partitions) from global wave models. It comprises four steps. The first step is dedicated to collecting all the wave and water level information and setting the numerical domain, the second step is the statistical selection of the most representative sample of the offshore sea state population, the third step is devoted to dynamically downscaling the selected offshore sample and the final step is focused on fitting multivariate interpolation functions and reconstructing the complete nearshore wave climate. A representation of the nearshore downscaling technique is shown in Figure 2.3. The first step consists of setting up the numerical domain (grid and topo-bathymetry) and collecting wave climate dynamics (significant wave height H_s, peak period T_p, mean period T_m and wave direction θ) and water levels (astronomical tide AT and storm surge SS) at the grid forcing points. Considering a domain with np wave forcing points and nl representative water level points, the wave and water level data matrix $\boldsymbol{M}_{m \times (nM+nl)}$ is assembled. m is the number of elementary temporal units (i.e. hours, days) of the study period and $nM = np \times nvarW$, being $nvarW$ the number of aggregated spectral wave variables (i.e., H_s, T_m, T_p, θ). The different water level components considered are summed up and form the columns $j > nM$.

1. Data collection & pre-process

1.1 Wave data	1.2 Water level data	1.3 Data matrix assembly

2. Statistical treatment I: selection

2.1 Principal Component Analysis

Data matrix projected in the complete physical space	Normalization PC Calculation Dimensionality reduction	Data matrix projected in the reduced EOF space

2.2 First Maximum Dissimilarity selection

Selected cases in the EOF space

2.3 Physical base traslation

Selected cases in the physical space

3. Dynamic downscaling

3.1 Enhanced forcing spectra reconstruction

Identify spectral partitions associated to the selected cases

Reconstruct spectra at the boundary forcing points

3.2 Propagation

Case M

Case 1

Propagated cases at downscaling points

SWAN model

4. Statistical treatment II: reconstruction

4.1 Multivariate interpolation

Fit Radial Basis Functions (*RBF*): Find f, such that :

Selected downscaled cases = f(Selected offshore cases)

4.2 Complete nearshore wave climate reconstruction at the downscaling points

Downscaled cases = f(offshore cases)

Figure 2.3: Schematic description of the hybrid nearshore wave propagation.

The following step is the first part of the statistical treatment. Problem dimensions increase drastically with the number of forcing points considered. However, as data is expected to be highly correlated, principal component analysis is carried out to reduce

the dimension of the problem while retaining most of the explained variance. Next, the maximum dissimilarity algorithm is applied, in the reduced empirical orthogonal function space, to obtain a representative subset of the multivariate offshore wave-climate population. Transformation of the K selected cases in the reduced projected space to the physical basis yields $\boldsymbol{M}_{K \times (nM+nl)}$.

Next, the dynamical downscaling consists of numerically propagating the selected K cases. If no information about the frequency-direction spectral shape of the representative subset is available, the standard JONSWAP spectrum constructed with aggregated spectral parameters and the usual values of directional spreading ($spr = 20°$) and peak enhancement factor ($\gamma_p = 3.3$) is built at the np boundary points. However, global wave models are capable of providing spectral shape information in the form of a number of sea and swell partitions, each of them characterised by directional spreading (spr), mean direction (Dir), peak period (T_p) and wave height (H_s). From the spectral partitions, concomitant with the selected K aggregated spectral wave properties, a more realistic spectral shape is built. To achieve this, it is assumed that each spectral partition has a JONSWAP shape that follows the directional distribution function of (Mitsuyasu et al., 1975). Then, the numerical propagation of the selected cases using the third generation SWAN model (Booij et al., 1999), yields the wave properties at the selected $idow$ downscaling points, $\boldsymbol{DM}^{idow}_{K \times nvarW}$.

The forth step is the second part of the statistical treatment, and consists of performing the multivariate interpolation by linking the offshore wave properties $\boldsymbol{M}_{K \times (nM+nl)}$ to the downscaled ones $\boldsymbol{DM}^{idow}_{K \times nvarW}$ via radial basis functions (RBFs) fitted to each of the wave variables. Fitted RBFs are then applied to reconstruct the complete nearshore wave climate. This procedure allows for considering wave transformation processes over a non-uniform offshore bathymetry at a reasonable computational cost.

2.2.1.2. Wave transformation II: propagation to breaking

The wave-driven shoreline evolution modules (LST gradients and cross-shore sediment transport) depend on wave breaking parameters. Obtaining the breaking line proper-

ties requires solving highly non-linear processes acting on top of the active bathymetry. For local scale studies, it is possible to couple detailed nearshore wave models accounting for all relevant processes (shoaling, spatial refraction, diffraction, bottom friction and breaking) with the shoreline evolution equation. In this case, an additional step is required to update the active bathymetry depending on the shoreline movement as in Robinet et al. (2018). In order to perform regional scale studies, the present implementation in IH-LANS is simplified by considering linear shoaling, one-dimensional refraction, empirical laws of diffraction and depth-induced breaking. For that purpose, wave energy conservation is applied on the wave rays, Snell's law is used to model refraction, a constant depth-induced breaking index (γ) of 0.55 is considered and the empirical laws of diffraction of Kamphius (2000) and Dabees (2000) are used to correct properties at breaking in the presence of groynes and detached breakwaters. Morphological changes are linked to wave propagation via the shoreline orientation, which controls refraction through the Snell's law. Thus, profile translation is indirectly accounted for by the time-varying shoreline orientation. For a detailed description of the breaking propagation routine implemented in the model, the reader is referred to Appendix A.

2.2.2. LST gradients module

Shoreline change due to LST gradients is modulated by the depth of closure, which is calculated according to Hallermeier (1980), and the berm height. LST is evaluated as follows:

$$Q = K_e Q_0 \tag{2.2}$$

where Q is the net sediment transport, K_e is the sediment bypass reduction coefficient to account for the effect of sediment traps (if no structure is present it is set equal to one whereas it takes the value of zero if sediment bypass is completely blocked) and Q_0 is the LST according to the CERC equation (USACE, 1984).

The CERC equation considers the longshore component of wave energy the main driving mechanism of longshore transport while accounting for alongshore gradients in wave height (Ozasa and Brampton, 1980). However, formulations like the ones proposed by

(Kamphius, 1993; Mil-Homens et al., 2013; Van Rijn, 2014) can also be implemented. The CERC formula reads:

$$Q_0 = K \underbrace{\frac{\rho\sqrt{g/\gamma}}{16(\rho_s - \rho)(1 - p)}}_{K_1} H_{s_{bd}}^{5/2} \left[sin(2\alpha_{bd}) - \frac{c}{\tan\beta_s}\frac{dH_{s_{bd}}}{dx} \right] \quad (2.3)$$

where K is a calibration constant, ρ is sea water density ($1025\ kg/m^3$), ρ_s is the density of sediment ($2650\ kg/m^3$), p is the porosity (usually 0.4), $tan\beta_s$ is the slope in the surfzone, α_{bd} is the angle between the shoreline and the breaking wave crests, c is a constant which is set equal to one as recommended by (Hanson and Kraus, 1989) and $H_{s_{bd}}$ is the breaking wave height. The surfzone slope $tan\beta_s$ varies on time, and is calculated based on the incident wave conditions and the equilibrium Dean's profile: $tan\beta_s = \frac{h_b(\gamma A)^{1.5}}{H_{s_{bd}}^{1.5}} = \sqrt{\frac{\gamma A^3}{H_{s_{bd}}}}$, being A the profile scale parameter (Dean, 1991).

Upon calibration, the CERC sediment transport formulation is a good estimator of the bulk longshore transport rate for different sediment grain sizes ranging from sand (del Valle et al., 1993) to gravel (Van Wellen et al., 2000).

Equation 2.3 is valid when sediment is available to transport and no barriers prevent the sediment flow. This may not be the case if groynes, seawalls or breakwaters are present. The calculation of LST rates in presence of these structures is addressed in the upcoming subsections.

2.2.2.1. Modelling the effects of groynes

Impermeable shore-perpendicular structures block longshore sediment transport. In order to cope with this phenomenon, the simplest implementation consists of simulating a complete sediment block, until shoreline reaches the tip of the salient in the upstream side. However, cross-shore distribution of longshore sediment transport occurs in a band limited by the shoreline and by a seaward limit that exceeds the breaking line (Falqués et al., 2008; Bergillos et al., 2017). Due to this fact, sediment bypass is expected to occur if the effective sediment transport band exceeds the offshore limit of the groyne.

In the present work, K_e is modelled as a function of the sediment transport bandwidth, the shape of the cross-shore distribution of LST $q_c(\eta)$ and the distance from the tip of the structure to the shoreline updrift L_e, Figure 2.4a. Following Kristensen et al. (2016), sediment transport is expected to occur, on average, in a band 25% larger than the surf zone width W_b^*. Also, a consistent assumption with regards to the modelling framework is to assume a uniform cross-shore distribution of the LST (Hanson and Kraus, 1989). Thus, K_e is reduced to:

$$K_e = \int_{L_e}^{1.25W_b^*} q(\eta)d\eta = 1 - \frac{L_e}{1.25W_b^*}, \quad K_e \in [0,1] \tag{2.4}$$

where η is the cross-shore position with respect to the shoreline in the upstream side of the structure.

Coupled modelling of diffraction and sediment bypass may cause numerical instabilities in the downstream part of the structure if bypassed sediment is transferred directly to the leeward transect in the influence zone. This is due to the circulation pattern generated by diffracted waves at the vicinity of the structure, which hampers the downdrift flow of sediment. To overcome this problem, a more realistic distribution of bypassed sediment is applied by equally allocating the sediment volume in the sheltered zone.

2.2.2.2. Modelling the effects of seawalls

Seawalls limit the available sediment flow rates by preventing shoreline retreat. A simple approach to integrate this behaviour in the model would be to null the LST constant K_1 when shoreline reaches the barrier. By doing so, the seawall boundary condition is satisfied, but sediment is artificially added to the system. To overcome this problem, LST is modified to fulfil the condition imposed by the structure as in Hanson and Kraus (1986).

If at the time step $t + dt$ the shoreline moves landward a seawall $Y_{li,s}$ reaching Y_{li}^{t+dt} at transect i, the LST rate exiting the numerical cell needs to be corrected to meet

the seawall condition $Y_{li}^{*,t+dt} = Y_{li,s}$ (see Figure 2.4b). Considering the explicit numerical implementation of IH-LANS, the seawall correction for the three different cases is detailed in Equation 2.5.

$$
\begin{cases}
\text{if } Q_{i,i+1}^t > 0 \text{ and } Q_{i-1,i}^t > 0, & Q_{i,i+1}^{t*} = \frac{(Y_{li}^t - Y_{li,s})(B+d_c)dx}{dt} + Q_{i-1,i}^t \\[2mm]
\text{if } Q_{i,i+1}^t < 0 \text{ and } Q_{i-1,i}^t < 0, & Q_{i-1,i}^{t*} = \frac{(Y_{li,s} - Y_{li}^t)(B+d_c)dx}{dt} + Q_{i,i+1}^t \\[2mm]
\text{if } Q_{i,i+1}^t > 0 \text{ and } Q_{i-1,i}^t < 0, & \begin{cases} Q_{i,i+1}^{t*} = Q_{i,i+1}^t \frac{(Y_{li}^t - Y_{li,s})(B+d_c)dx}{dt} \frac{1}{Q_{i,i+1}^t - Q_{i-1,i}^t} \\[2mm] Q_{i-1,i}^{t*} = Q_{i-1,i}^t \frac{(Y_{li}^t - Y_{li,s})(B+d_c)dx}{dt} \frac{1}{Q_{i,i+1}^t - Q_{i-1,i}^t} \end{cases}
\end{cases}
$$

$$(2.5)$$

where Q and Q^* refer to the uncorrected and corrected LST rates.

Note that changing the LST at transect i can make transects at the leeward sediment flow direction violate the seawall condition. Thus, once a transect exceeds the seawall's landward limit, the correction needs to be applied in an iterative scheme following the erosive wave direction. By doing this, the fulfilment of the seawall boundary condition is ensured.
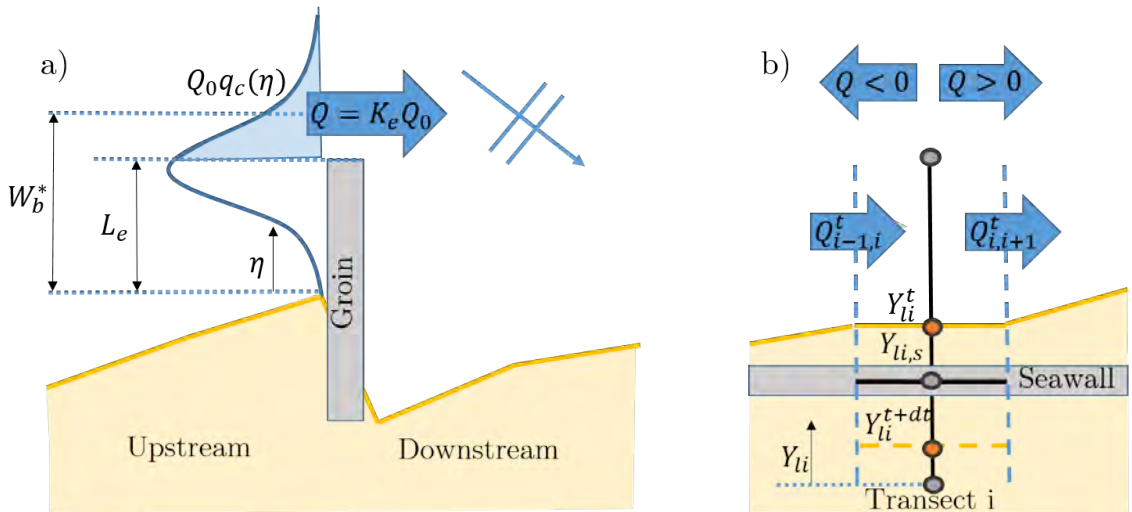
Figure 2.4: Sketch defining two structures that alter the sediment transport rate. a) sediment bypass calculation principle. b) sediment flow readjustment when the shoreline reaches a seawall.

2.2.2.3. Modelling the effects of breakwaters

Offshore shore-parallel structures generate shoreline changes whose triggering mechanism (diffraction or LST changes) depend on the morphological development of the shape that forms behind them. In the salient phase, diffraction patterns controls shoreline evolution due to gradients in wave height and direction. If a tombolo is formed, shoreline change is controlled by diffraction while LST rates are also altered in order to prevent the shoreline from surpassing the structure. This is achieved by a similar but reversed redistribution procedure to the one detailed for the seawall.

2.2.3. Cross–shore transport module

In this study, the cross-shore formulation proposed by Toimil et al. (2017a) which is based upon the Miller and Dean (2004) model, is implemented. It translates changes in wave climate and water levels to shoreline response assuming volume conservation in an equilibrium profile. As the majority of equilibrium cross-shore models, the mathematical representation of the process is based on a kinetic equation in which the disequilibrium with a reference state (i.e., shoreline position) drives shoreline change. The equilibrium shoreline position Y_c^{eq} is calculated as follows:

$$Y_c^{eq} = \Delta y_0 + R_{SLR} + \Delta y_{eq} \tag{2.6}$$

where Δy_0 is an empirical parameter that assures that short-term fluctuations oscillate around a baseline position. In order to sum up the contribution of the different modules in the governing equation, cross-shore baseline location is set equal to zero if R_{SLR} is null. R_{SLR} corresponds to the Bruun-type shoreline retreat due to sea level rise, (Bruun, 1962) and $\Delta y_{eq}(t)$ is the equilibrium position which depends on waves, storm surges, astronomical tide and wave set-up:

$$\Delta y_{eq} = -W_{bd}^* \left(\frac{0.106 H_{s_{bd}} + SS + AT}{B + d_{bd}} \right) \tag{2.7}$$

being d_{bd} the depth at breaking, W_{bd}^* the surfzone width, which according to the Dean's equilibrium profile is $W_{bd}^* = \left(\frac{H_{s_{bd}}}{\gamma A} \right)^{1.5}$. SS and AT are respectively the storm surge and

the astronomical tide.

2.2.4.   Sediment sinks and sources

In order to integrate these processes in the analysis, a distinction needs to be made between punctual and permanent exchanges. In the case of episodic exchanges (e.g. nourishments or dredges), the shoreline evolution rate $\frac{q}{B+d_c}$ $[m/dt]$ is calculated from the total exchanged volume V $[m^3]$, the duration (initial and final date) and the polygon that defines the area of influence of the process. Permanent or persistent exchanges such as solid river discharges or permanent sediment bypasses need to be specified though a constant or time-dependent shoreline evolution rate.

2.2.5.   Long-term shoreline trend

The long-term shoreline trend (vlt) accounts for all unresolved processes of any kind that contribute to shoreline evolution. As in Vitousek et al. (2017c), this empirical term is obtained through data-assimilation. At the beginning of the simulation, vlt is set equal to zero but it changes when data is available to assimilate, and the observation cannot be modelled through the processes explicitly modelled in Equation 2.1. This term is especially useful in the case of stationary sinks or sources whose contribution to shoreline change is initially unknown.

2.2.6.   Data-assimilation

Data-assimilation by means of Kalman filters uses disperse observations to automatically update forecast model predictions and model parameters. The model prediction and free-model parameters, at a given time step, define the state vector $\boldsymbol{\Psi}$, which corresponds to the minimum input necessary for advancing to the next state. Each updated state vector is computed recursively from the previous estimate and the available observation. This is achieved by weighting the model's estimate and the observation via the Kalman gain $\boldsymbol{G}$, estimated by propagating the initial error covariance matrix $\boldsymbol{P_0} = \boldsymbol{diag}(\epsilon(\boldsymbol{\Psi})^2)$ where $\epsilon(x)$ represents the uncertainties in X, the covariance of process noise $\boldsymbol{Q} = \boldsymbol{diag}(\delta(\boldsymbol{\Psi})^2)$ being $\delta(X)$ the inherent noise in the model and the

measurement error R.

Initial values of $\epsilon(X)$ are usually based on the possible range of physically plausible values of X while the values of $\delta(X)$ ensure filter stability and control forecast variance (Long and Plant, 2012). The value of the measurement error R is related to the accuracy of the observations.

The data-assimilation algorithm based on the eKf allows for time-varying or stationary parametrizations based on the value of the process noise matrix $\boldsymbol{Q}$. Once parameters have converged to a certain optimal set, the amplitude of the propagated covariance matrix $\boldsymbol{P}$ is substantially reduced, converging to the process noise $\boldsymbol{Q}$. Thus, setting small $\boldsymbol{Q}$ values would imply stationary parametrizations while bigger noise values would lead to a propagated $\boldsymbol{P}$ with enough flexibility to accommodate parameter variations through time as in Ibaceta et al. (2020). However, the linkage between driver changes and model parameter variations is still unclear for the validation period, when observations are not available, hampering the implementation of time-varying parametrizations when forecasting the shoreline evolution. Thus, in the absence of a robust methodology to account for time-varying and climate-dependent formulations for all the modelled processes, the stationary hypothesis in model parameters has been herein adopted.

Two variants of the data-assimilation algorithm are implemented in the model depending on the coupling of the longshore and cross-shore processes in the eKf. The first implementation is the independent (uncoupled) approach and the second is the joint (coupled) approach, which is similar to the work presented by Long and Plant (2012) and Vitousek et al. (2017c). A complete explanation of the data-assimilation algorithms is provided in Appendix B and a comparison between both data-assimilation approaches is addressed in Section 2.3.7

2.2.7. Coupling longshore and cross-shore processes

The longshore, short-term cross-shore and SLR coupling presented in this application is an intermediate approach between the uncoupled method of Vitousek et al. (2017c)

and the fully coupled approach presented in Antolínez et al. (2019) or in Jaramillo et al. (2020). In the case of the uncoupled approach, the short-term cross-shore evolution is calculated just considering future waves, yielding a temporal evolution of erosion and accretion events, which is then linearly added to the SLR retreat and the longshore effects. The disequilibrium term in the cross-shore formulation is calculated between the short-term cross-shore position and the equilibrium position, which is obtained without considering LST gradients or SLR effects. In the case of the fully coupled approach, the observed shoreline position Y is directly the output of the equilibrium model. In this case, the disequilibrium term is calculated considering the equilibrium position (accounting for LST gradients and SLR effects) and the total observed shoreline position. A review of the different longshore and cross-shore coupling approaches in current reduced-complexity models and their formulation is synthesised in Table 2.1

	Uncoupled, (Vitousek et al., 2017c)	Coupled, (Antolínez et al. (2019), Jaramillo et al. (2020))	Partially coupled, (Current)
Total shoreline	$Y = Y_l + Y_{c,st} + R_{SLR}$	Y	$Y = Y_l + Y_c$
Eq. formulation	$\frac{\partial Y_{c,st}}{\partial t} = K^{+/-}(Y_{eq} - Y_{c,st})$	$\frac{\partial Y}{\partial t} = K^{+/-}(Y_{eq} - Y)$	$\frac{\partial Y_c}{\partial t} = K^{+/-}(Y_{eq} - Y_c)$
Eq. shoreline position	$Y_{eq} = \Delta y_0 + \Delta y_{eq}$	$Y_{eq} = \Delta y_0 + \Delta y_{eq} + Y_l - R_{SLR}$	$Y_{eq} = \Delta y_0 + \Delta y_{eq} - R_{SLR}$

Table 2.1: Summary of the multi-process coupling approaches in reduced-complexity models.

The results from different coupling strategies are shown in Figure 2.5. The test was performed by generating a longshore shoreline position (Y_l) that represents the time-aggregated gradients in the longshore transport, a time series of shoreline retreat due to SLR (R_{SLR}) and a time-series of cross-shore position following the Miller and Dean (2004) model in which the equilibrium position just depends on incident waves, astronomical tide and storm surge $Y_{c,st}$, (top panels in Figure 2.5). As shown, the different coupling strategies yield similar results. Only slight differences are noticed due to the one-step lagged response when coupling the different approaches in the equilibrium formulation solved using a forward temporal discretization. These differences are negligible considering the erosive trend induced by SLR.
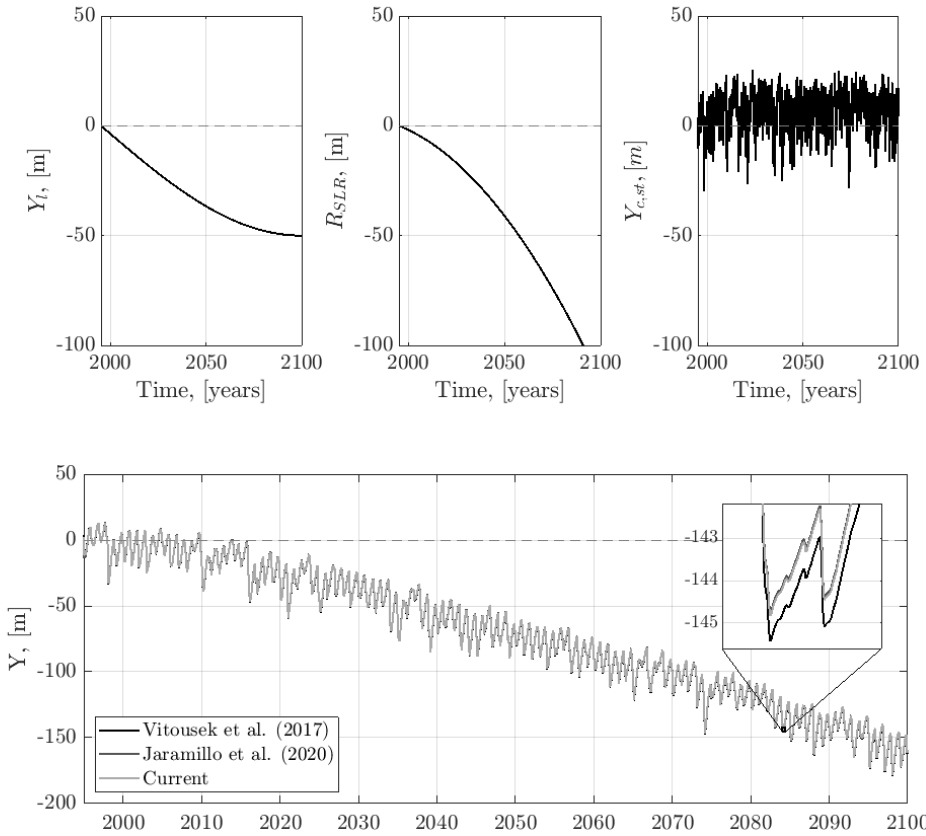
Figure 2.5: Comparison of the longshore and cross-shore coupling approaches.

2.3. Synthetic cases

Seven synthetic cases are selected to validate the correct implementation of the propagation routines, the numerical implementation of the shoreline governing equation (cross-shore and longshore processes) and the data-assimilation algorithm. The experiments presented hereinafter cover the following functionalities: 1) shoreline evolution near a groyne considering diffraction and a realistic sediment bypass boundary condition, 2) seawall's effect implementation, 3) salient formation behind detached breakwaters, 4) time-varying sediment sources, 5) data-assimilated shoreline evolution behind a detached breakwater subjected to oblique waves, 6) data-assimilation considering two different cross-shore constants and 7) data-assimilation combining longshore an cross-shore processes. Unless otherwise specified, simulated wave climate is assumed to be

constant and it is imposed at the downscaling points located at the offshore boundary of the domain. Also, in the groyne test, the bathymetry orientation is held constant and equal to the initial value in order to compare the results with the analytical formulation.

Table 2.2 shows the activated modules and model parameters used for the tests. It is worth mentioning that when the cross-shore transport module is deactivated, the state vector $\boldsymbol{\Psi}_0$ (see Appendix B) simplifies to $\boldsymbol{\Psi}_0 = [Y_l, K_1, vlt]$ with respect to full-model's state vector. In the case data-assimilation is activated together with the longshore transport module, error covariance $\boldsymbol{P}_0^-/\boldsymbol{P}_0^+$ and process noise $\boldsymbol{Q}_0^-/\boldsymbol{Q}_0^+$ matrices are also simplified as they reduce to single matrices:

$$\boldsymbol{P}_0 = \boldsymbol{diag}([\epsilon(Y_l), \epsilon(K1), \epsilon(vlt)]^2)$$
$$\boldsymbol{Q}_0 = \boldsymbol{diag}([\delta(Y_l), \delta(K_1), \delta(vlt)]^2)$$

Similarly, if cross-shore transport is modelled solely, the state vector is $\boldsymbol{\Psi}_0 = [Y_c^-, Y_c^+, K_c^-, K_c^+]$. If data-assimilation is applied together with the cross-shore transport equation, error covariance matrices are:

$$\boldsymbol{P}_0^- = \boldsymbol{diag}([\epsilon(Y_c^-), 0, \epsilon(K_c^-), 0]^2)$$
$$\boldsymbol{P}_0^+ = \boldsymbol{diag}([0, \epsilon(Y_c^+), 0, \epsilon(K_c^+), 0]^2)$$

while process noise matrices are:

$$\boldsymbol{Q}_0^- = \boldsymbol{diag}([\delta(Y_c^-), 0, \delta(K_c^-), 0]^2)$$
$$\boldsymbol{Q}_0^+ = \boldsymbol{diag}([0, \delta(Y_c^+), 0, \delta(K_c^+), 0]^2)$$

The parameter uncertainty $\epsilon(X)$ is chosen to define an initial search space that contains the expected optimal set of parameters. However, setting larger uncertainty values and initial parameter estimates far from the optimal set, will hamper the convergence of the algorithm. Thus, the parameter uncertainty is chosen in such a way that it is on the same order of magnitude as the initial parameter estimates (Evensen, 2003), as shown in Table 1. On the other hand, following the hypothesis of time-invariant parametrization, the value of the inherent noise $\delta(X)$ is chosen low enough to assure filter stability

while converging to hypothetic stationary optimal set of parameters. Optimal values of the inherent noise were obtained to be some orders of magnitude lower than the initial variable estimate. The values of the measurement error R are linked to the expected standard deviation of the observation error distribution. Thus, values of 0 and 10 m are considered. In the case of the test case combining longshore and cross-shore processes and the independent data-assimilation approach, the total measurement error R is distributed between the error in the longshore position $R_l = 0.2R$ and the error in the cross-shore shoreline position $R_c = 0.8R$. The uneven error distribution is due to the averaging effect of the running-mean filter, which makes that errors are expected to be bigger in the cross-shore position while balancing in the longshore position. However, further research needs to be done in the case of applying other unravelling algorithms.

The skill of the data-assimilation algorithm in the synthetic cases is tested by creating a reference shoreline with a certain set of free-model parameters. Then, by changing the free model parameters, a perturbed simulation is created and no data-assimilation is performed (hereinafter named w/o data-assimilation). Data-assimilation is applied next by setting as starting point the free-model parameters of the w/o data-assimilation simulation but using observations from the reference simulation. The sampling frequency is chosen to be 15 days, consistent with the standard revisit time of publicly-available satellite scenes. Two data-assimilation simulations are performed by varying the error introduced in the observation. In this way, a data-assimilated simulation is performed with clear (0 $RMSE$) observations and another one with noisy (10 $RMSE$) observations which matches the reported errors of satellite-derived shorelines (Vos et al., 2019). The error was simulated by adding to each observation, a random number from a normal distribution $\Phi(0, \epsilon(Y_{obs})^2)$, where $\epsilon(Y_{obs}) = RMSE$ of the observations. The simulation time is divided in calibration and test periods. To quantify the efficiency of the assimilation algorithm, different error measures are provided for the test period of the shoreline position ($NMSE$ following the definition in Miller and Dean (2004), $RMSE$, R^2) and of the free model parameters (relative error), by comparing the reference simulation with the data-assimilated one.

Experiment	Activated modules	State vector, $\mathbf{\Psi}_0$	Error covariance, $\mathbf{P}_0^-/\mathbf{P}_0^+$	Process noise, $\mathbf{Q}_0^-/\mathbf{Q}_0^+$	Measurement error, R
Groyne	LT	[0; 200; 0]	-	-	-
Seawall	LT	[0; 200; 0]	-	-	-
Breakwater (salient)	LT	[0; 800; 0]	-	-	-
Nourishment	LT	[0; 200; 0]	-	-	-
Longshore DA	LT, DA	[0; 200; 0]	[1; 200; 1E-6]²	[0.2; 1E-1; 1E-9]²	0/10
Cross-shore DA	CT, DA	[0; 0; 0.5E-2; 1E-3]	[1; 0;1E-2; 0]²/ [0; 1; 0; 1E-3]²	[0.2; 0; 1E-2; 0]²/ [0; 0.2; 0; 1E-4]²	0/10
Longshore and Cross-shore DA	LT, CT, DA	[0; 40; 0; 0; 0; 1E-2; 2E-3]	[1/4; 40;1E-6; 1; 0; 1E-2; 0]²/ [1/4; 40; 1E-6; 0; 1; 0; 1E-3]²	[1E-5; 1E-1; 1E-6; 0.2; 0; 1E-2; 0]²/ [1E-5; 1E-2; 1E-6; 0; 0.2; 0; 1E-4]²	0/10

Table 2.2: Activated modules and model parameters for the different experiments. The abbreviations CT, LT and DA correspond to cross-shore transport, longshore transport and data-assimilation respectively. Error covariance matrices, process noise and measurement error are provided only when the data-assimilation module is activated.

2.3.1. Groyne test

In this example, shoreline evolution near a groyne is modelled and compared with the Pelnard-Considère (1956) solution. After one month, both analytical (black dashed line) and numerical solutions (black solid line) match well in the updrift side of the structure (Figure 2.6). The differences are mainly due to the low angle approximation in the analytical solution. In the lee of the structure, differences are more evident due to the diffraction shadowing effect accounted for in the numerical solution. As time passes, the sediment transport band surpasses the breakwater tip (top-right panel in Figure 2.6) and the difference between the analytical and the numerical solutions becomes more noticeable, which is justified as the analytical result assumes that no bypass takes place.
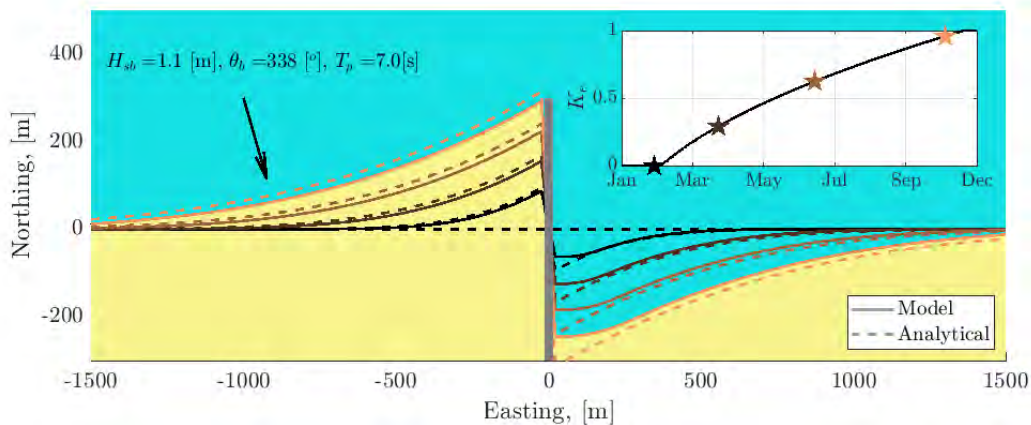
Figure 2.6: Shoreline evolution near a groyne. Modelled shoreline evolution (solid lines) is displayed versus the analytical solution (dashed lines) at different dates. The top right panel shows the modelled evolution of the sediment bypass coefficient K_e.

2.3.2. Seawall test

With the purpose of validating the model's ability to reproduce the seawall constraint, a parabolic planform beach backed with a seawall with no sediment exchanges at the borders is modelled, Figure 2.7. The seawall is placed 50 m behind the initial shoreline (dotted black line). An oblique wave climate that makes the beach rotate clock-wise is applied next. Erosion is propagated to the left until the beach reaches a new equilibrium configuration while mobilizing just the available sediment at the seaward side of the seawall. Shoreline evolution without the seawall is also displayed for comparison (dashed lines). In this latter case, the volume of sediment that needs to be mobilized to reach the new equilibrium is higher.
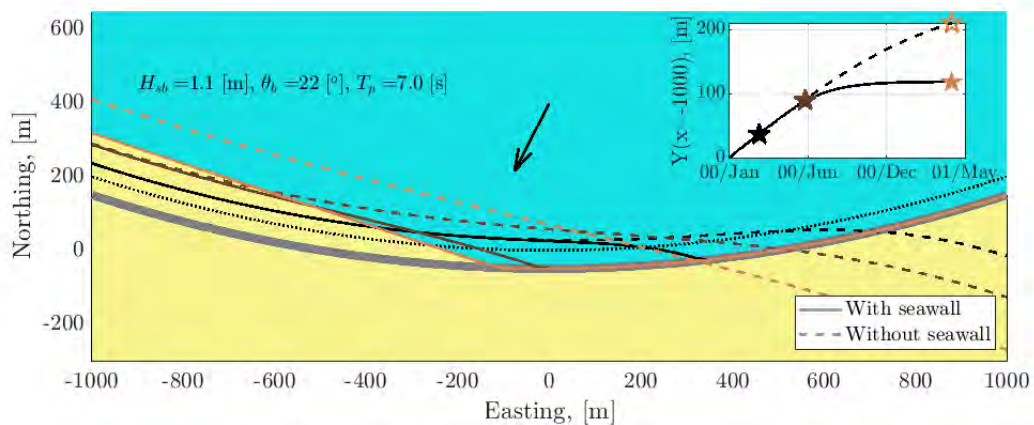
Figure 2.7: Rotation of an embayed beach backed by a seawall test. The initial coastline is the dotted black line and is parallel to the seawall (displayed in gray). The top right panel represents the evolution of the left side of the beach with respect to the initial position for both the seawall backed beach (continuous line) and the unprotected beach (dashed line).

2.3.3. Salient formation test

This experiment allows for verifying the diffraction routines implemented in the model. For that purpose, an initially straight shoreline protected by a detached breakwater of length (L) at a distance (S) from the undisturbed shoreline is simulated. Normal incidence wave angle is applied until an equilibrium position is reached. Then, the distance from the tip of the salient to the structure x is obtained. Modelled x/L ratios

for various non-dimensional breakwater lengths L/S are compared with the empirical curve of Hsu and Silvester (1990) (see Figure 2.8). The range of L/S varies between 0.6 and 1.25 which extends from the limited response condition to the salient formation. Higher values of L/S will eventually yield tombolo formation depending on the ratio of the surf zone width W_{bd}^* and the distance S. As shown in Figure 2.8, modelled salient lengths agree with field observations.
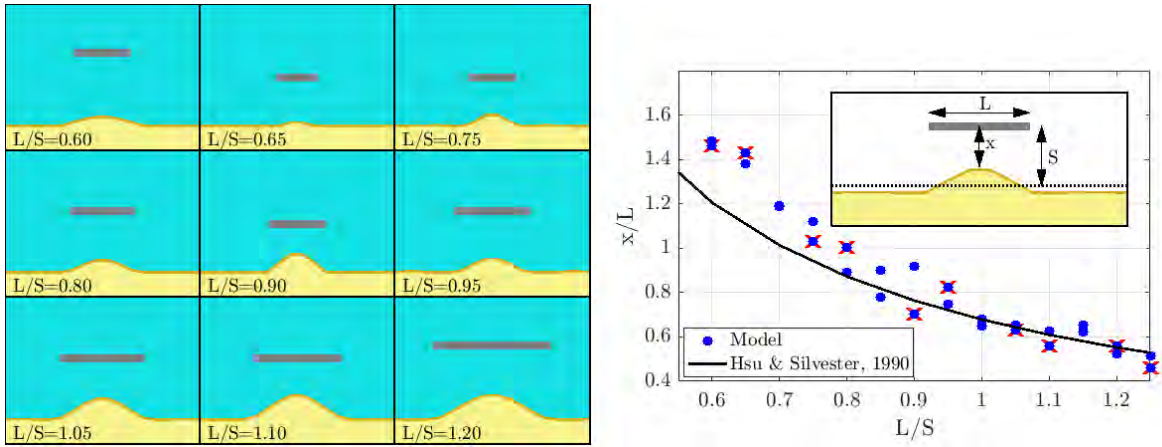
Figure 2.8: Salient development test. On the left panel, in matrix form, modelled equilibrium shoreline positions for different breakwater depth to shoreline distance (L/S) configurations under normal incidence waves. On the right panel, the black continuous line represents the empirical curve of salient formation proposed by (Hsu and Silvester, 1990). Blue dots represent the model simulation while blue dots backed by red crosses correspond to the configurations displayed in the left panel.

2.3.4. Nourishment test

In this example, the ability of the model of reproducing the shoreline evolution after a nourishment of 1.2 Mm^3 distributed in a sinusoidal area is tested (see Figure 2.9). The landfill is centred at the idealised rectilinear coastline, which is in static equilibrium (no sediment exchanges at the boundaries). The nourishment is implemented during 2 months at a constant rate (top-right panel in Figure 2.9), while a normally incident wave climate drives longshore transport that diffuses the poured material until a new equilibrium situation is obtained. By performing this simple example, it is shown that the model is able to reproduce time-varying sediment sources while exhibiting a proper material redistribution though diffusion.
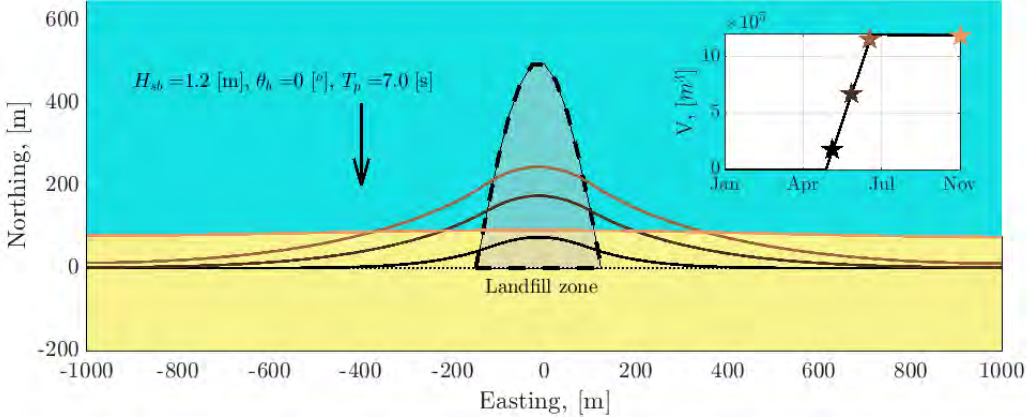
Figure 2.9: Nourishment diffusion test. The initial coastline is the dotted black line and the nourishment area is displayed by the dashed grey polygon. The different dates at which the shoreline is displayed are referenced by the coloured stars in the top right panel.

2.3.5. Longshore data-assimilation test

This synthetic test integrates both the longshore transport and the data-assimilation modules to model a breakwater subjected to oblique wave attack. Observations are obtained from a reference simulation ($K_1 = 400\ m^{0.5}/hr$) during the calibration period. In this case, the same random number from $\Phi(0, \epsilon_{(Y_{obs})}{}^2)$ was added to all the transects at a given observation date, as detection errors are assumed to be consistent throughout the complete scene.

Simulation/Statistic	$Y = Y_l$ $NMSE$; $RMSE$; R^2	K_1 Rel. err.
W/o data-assimilation	0; 1.21; 0.36	-50%
Data-assimilation, $\epsilon(Y_{obs}) = 0\ m$	0; 0.01; 0.99	1.59%
Data-assimilation, $\epsilon(Y_{obs}) = 10\ m$	0; 4.56; 0.50	2.60 %

Table 2.3: Error statistics of the data-assimilated longshore simulation.

Results are shown in Figure 2.10. The upper panel displays the shoreline response at three particular instants of the reference and perturbed simulations. The shaded area in the central and lower panels highlights the data-assimilation period. The central panel shows the shoreline evolution of the central transect for the reference case, the perturbed case without data-assimilation and the perturbed case with data-assimilation

considering clear and noisy observations. The lower panel shows the temporal evolution of the longshore constant. Convergence to the true value is achieved in the synthetic case even in the case of noisy observations after 2.5 years of observations.
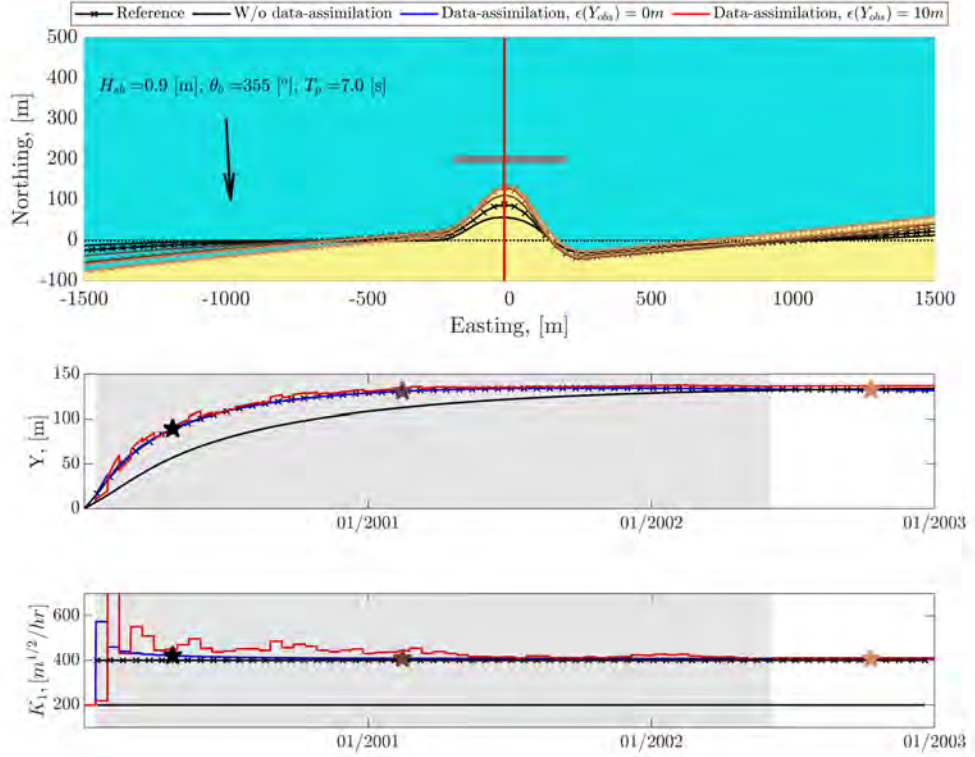
Figure 2.10: Longshore data-assimilation test. The top panel represents the reference shoreline evolution (continuous lines with cross markers) and the perturbed shoreline evolution (continuous lines) at different dates highlighted in the central and lower panels with coloured stars. In the central and lower panel, the blue line is the data-assimilated evolution with clear observations and the red line is the data-assimilated evolution with noisy observations.

In Table 2.3, the statistics of the forecast period are summarised for the shoreline evolution and for the longshore constant. It is worth to mention that the displayed errors in the final shoreline position do not represent a valid reference for analysing the skill of the model in this particular application. This is because a final equilibrium configuration is always attained, even without data-assimilation, and the longshore constant just regulates the speed at which the equilibrium shoreline is reached. However, this is challenging for free-model parameter convergence, as the available time to reach the true value is limited because the perturbed and reference simulations converge. In spite

of this behaviour, the longshore transport constant almost reaches the true value even in the case of noisy observations.

2.3.6. Cross-shore data-assimilation test

This experiment is conducted by considering the cross-shore shoreline evolution, which allows for isolating the modification in the data-assimilation algorithm to distinguish between erosive and accretive events. In order to test the capabilities of the model to assimilate observations, a reference synthetic time-series of shoreline evolution with real waves and water levels is generated considering the constants K_c^+ and K_c^-. In the next step, calibration constants are altered, and the model is run with $K_c^+/5$ and $K_c^-/5$ (values in Table 2.2). Data-assimilation is subsequently performed, starting from the altered constants but taking noisy observations from the reference simulation every 15 days.

The temporal evolution of the shoreline and the different model parameters are displayed in Figure 2.11. The first panel represents the shoreline evolution of the reference, perturbed and data-assimilation simulations. The shaded area highlights the data-assimilation period. The second panel distinguishes between erosion and accretion events from the reference simulation. An erosion event occurs when in the forward numerical solution of cross-shore evolution $Y_c^{t+dt} < Y_c^t$, while an accretion event happens when $Y_c^{t+dt} \geq Y_c^t$. The third and fourth panels represent the temporal evolution of the erosion K^- and accretion K^+ constants.

Simulation/Statistic	$Y = Y_c$ $NMSE$; $RMSE$; R^2	K_c^+ Rel. err.	K_c^- Rel. err.
W/o data-assimilation	0.58; 2.91; 0.16	-80%	-80%
Data-assimilation, $\epsilon(Y_{obs}) = 0\ m$	0; 0.01; 1	-0.05%	0.02%
Data-assimilation, $\epsilon(Y_{obs}) = 10\ m$	0.09; 1.11; 0.95	39.22%	36.77%

Table 2.4: Error statistics of the data-assimilated cross-shore simulation.

In the case of observations with no added noise, convergence is achieved and the optimal values of the erosion and accretion constants are attained with relative errors smaller

than 0.5%, as displayed in Table 2.4. However, in the case of noisy observations, a sub-optimal combination of constants is attained (37% and 39% relative error for K_c^- and K_c^+ respectively). Despite the differences in the constants with respect to the reference simulation, the shoreline evolution assimilated with noisy observations shows good agreement in the test period with the reference one ($NMSE = 0.09$, $RMSE = 1.11$ m and $R^2 = 0.95$).
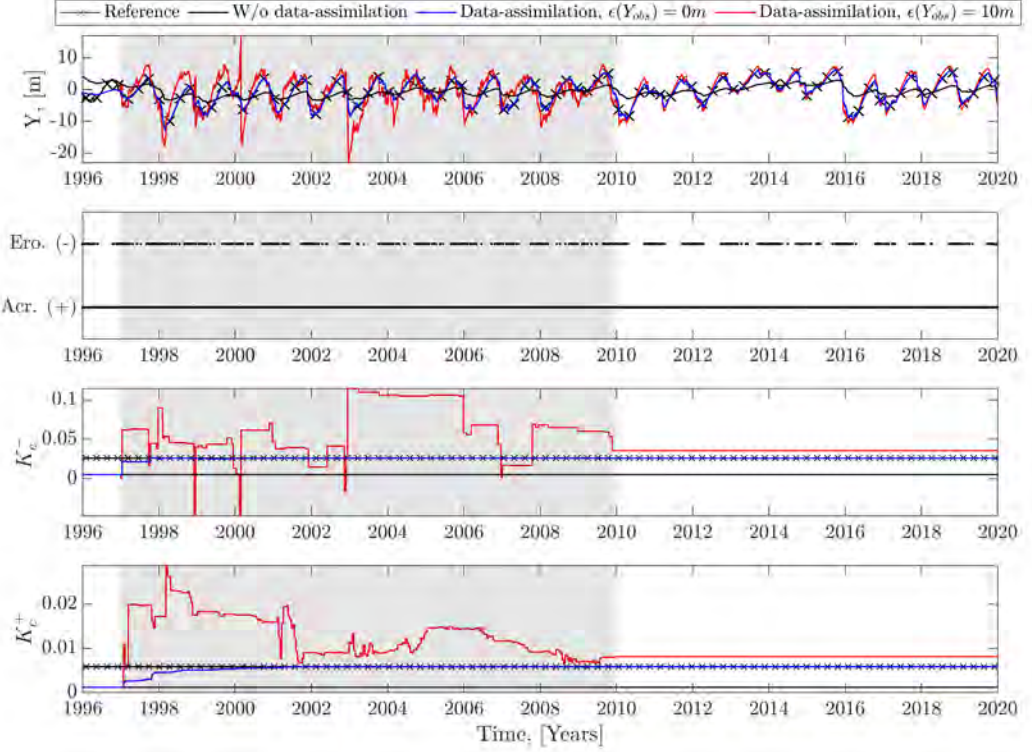
Figure 2.11: Data-assimilation test considering two different constants for erosion and accretion events. In the first, third and fourth panels, the black line with cross markers represents the reference simulation, the black line is the perturbed simulation, the blue line is the data-assimilated simulation with clear observations and the red simulation is the data-assimilated simulation with noisy observations. The second panel represents with points the number of erosion and accretion events.

In this synthetic example, the model convergence is relatively fast, in approximately 3 years of calibration with clear observations, model parameters tend to the reference values. However, in the case of the data-assimilation evolution with 10 RMSE noisy observations, convergence to the optimal parameter set is compromised, specially in the case of the erosion constant K_c^-. The accretive constant K_c^+ fluctuates more while the

temporal evolution of the erosion constant K_c^- shows less jumps. This fact is explained by the temporal scales associated with cross-shore erosion and accretion processes, which are different, being the last ones slower (Stive et al., 2002). Thus, as erosion processes are faster, less events are available to assimilate (second top panel in Figure 2.11) and convergence of K_c^- takes place slower. In order to facilitate the convergence of the erosive constant K_c^-, the added noise $\delta(K_c^-)$ is set to be in the same order of magnitude of $\epsilon(K_c^-)$. By doing so, the corresponding term in the propagated covariance matrix associated with erosive events $\boldsymbol{P}_c^-$ increases, enabling the algorithm to adapt faster when an erosive observation is detected. Divergence due to excessive added noise and search-space over-sizing is not likely to occur due to the reduced number of times in which $\boldsymbol{P}_c^-$ is computed, which is less than 1% of the time. By performing this experiment, the model's ability of assimilating observations considering two distinct erosion and accretion cross-shore rates is successfully validated.

2.3.7. Combined longshore and cross-shore data-assimilation test

In this test, the shoreline evolution of an 8 km embayed parabolic beach is simulated. The beach is subjected to a normally incident time-varying wave climate which drives longshore and cross-shore processes together. As in the previous cases, a reference solution is simulated with a set of parameters, then, with a different set of parameters, a perturbed simulation is obtained without considering data-assimilation.

Two data-assimilation strategies are contemplated depending on the coupling of the longshore and cross-shore processes in the filter, the independent and the joint approaches. The novel independent approach has the advantage that fictitious interactions between longshore and cross-shore parameters are avoided in the eKf. However, it requires an unravelling methodology to isolate the longshore $Y_{obs,l}$ and the cross-shore $Y_{obs,c}$ component from the total observed shoreline Y_{obs}. Here, a filter based on the running mean is employed to extract longshore shoreline position from the total observed shoreline. This is sustained by the fact that the longshore component acts

as a trend due to the larger time scale compared to cross-shore fluctuations (Miller and Dean, 2004; Splinter et al., 2014). The time window is set so as the residue is stationary, which is verified following Mentaschi et al. (2016). In this synthetic case, a time-window of three years gives satisfactory results. However, more sophisticated unravelling techniques, like those based on Empirical Mode Decomposition (Montaño et al., 2021), may also be applied. The joint approach (Long and Plant, 2012; Vitousek et al., 2017c) finds the optimum set of free-model parameters that produce the total observed shoreline. In this case, the search-space needs to be close enough to avoid spurious interactions between free-model parameters that yield the observed shoreline position but converging to a sub-optimal set of free-model parameters. In order to compare the results, the parameters of the error covariance and process noise of both data-assimilation approaches are the same, see Table 2.2.

Six different simulations, shown in Figure 2.12, are analysed. The first panel represents the shoreline response of the left half of the embayment at different dates, for the reference simulation (continuous lines with cross markers) and the perturbed simulation (continuous lines). The dates at which the instantaneous shoreline are drawn are referenced on the second-left panel by coloured stars. The second-left panel represents the total shoreline evolution $Y = Y_l + Y_c$ of the six simulations at the central transect. In this case, two clusters of trajectories are distinguished, the simulation without data-assimilation with a smaller trend and cross-shore oscillations and a trajectory formed by the reference and the four different data-assimilated simulations overlaid. By looking at the final shoreline position, the independent and joint data-assimilation approaches seem to provide satisfactory results in the forecast period for clear and noisy observations. Error statistics of the total shoreline evolution with respect to the reference simulation during the forecast period are in the first column of Table 2.5. In all the simulations with data-assimilation, the $NMSE$ is nearly zero due to the weight of the normalising constant, affected by the longshore trend. The $RMSE$ values of Y are smaller for the independent data-assimilation approach (0.70 and 2.35 m) for clear and noisy observations against the joint data-assimilation approach (3.92 and 5.49 m).
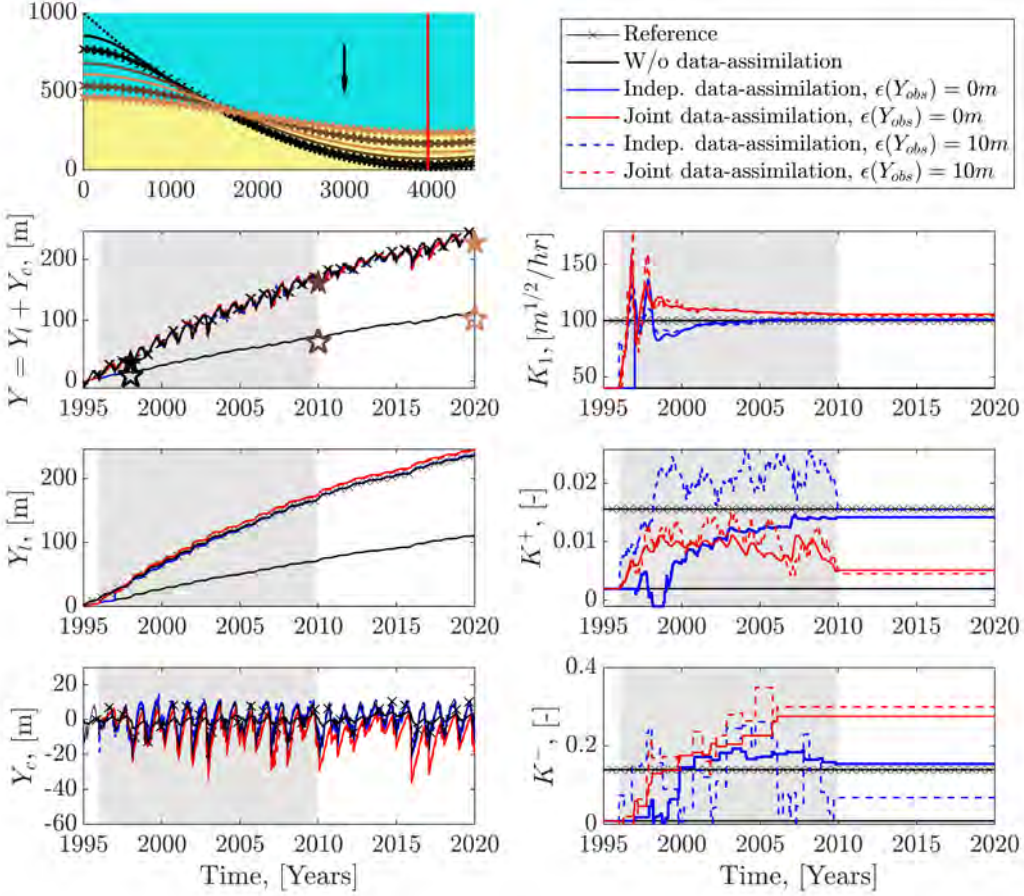
Figure 2.12: Data-assimilation test combining longshore and cross-shore processes. The first-left panel shows the shoreline response for the reference (continuous lines with cross markers) and perturbed (continuous lines) of the left half of the embayed beach at different dates (highlighted with coloured stars in the second-left panel). The rest of the panels show the temporal evolution of the shoreline position and the free-model parameters for the different simulations at the central transect.

The third-left panel shows the temporal evolution of the longshore position Y_l, in this case, we distinguish three different clusters of trajectories. The first trajectory in the figure corresponds to the simulation without data-assimilation, the second one relates to the reference simulation together with independent data-assimilation approach with clear and noisy observations and the third one, separated from the reference trajectory, is associated with the joint data-assimilation approach. Thus, the $RMSE$ of the independent data-assimilation approach (0.19 and 0.29 m) are much more reduced than those of the joint approach (8.37 and 6.72 m) for clear and noisy observations respec-

tively, see Table 2.5.

Further conclusions can be drawn by looking at the evolution of the longshore constant K_1 in the second-right panel in Figure 2.12. The K_1 in the independent data-assimilation approach converges to the reference value with a relative error of 0.1% and 0.24% for clear and noisy observations respectively. However, the joint data-assimilated K_1 is 5.75% and 4.33% bigger than the reference, which explains the errors in the forecasted Y_l by the joint approach.

The fourth-left panel shows the cross-shore evolution Y_c, in which the difference between the more pronounced response of the reference solution contrasts the evolution of the perturbed simulation without data-assimilation. The evolution of the independent data-assimilation approach provides a shoreline response which is much closer to the reference solution than the joint data-assimilation approach, which seems to have a negative bias. The error measures in Table 2.5 highlight this fact, being the $NMSE$ and the $RMSE$ much greater in the joint approach, even bigger than those of the perturbed simulation with no data-assimilation.

This behaviour is explained by the temporal evolution of the cross-shore constants displayed in the third and fourth-right panels in Figure 2.12. The final values of K_c^- and K_c^+ for the joint data-assimilation approach are 70%–115% off the reference value. On the other hand, the independent approach produces K_c^- and K_c^+ values which are closer to the reference solution. As in Section 2.3.6, with clear observations, the cross-shore values of the independent data-assimilation converge to nearly the reference values whereas if noisy observations are present, they tend to a sub-optimal combination. Again, the erosive constant K_c^- is much more difficult to calibrate due to the scarcity of erosion events, which are further reduced when using 15-day revisit shoreline observations.

By looking at the shoreline response, the joint data-assimilation analysis provides satisfactory estimates of the total shoreline evolution Y. However, this is attained by

longshore Y_l and cross-shore contributions Y_c that are biased with respect to the reference simulation, but their counteracting effects add-up to the reference values. The independent assimilation gives satisfactory results but depends on the unravelling algorithm.

Regarding the sensitivity to the observation error $\epsilon(Y_{obs})$, relevant conclusions can be drawn. First, the impact of the 10 m $RSME$ noisy observations does not excessively undermine the calibration of longshore transport models. This is shown in the third panel in Figure 2.10 and the second-right panel in Figure 2.12. Second, the cross-shore model calibration is much more sensitive to the added noise in the observations. When adding noise to the observations, convergence rates are considerably slower and the algorithm fails to add the reference weight to erosion and accretion processes. However, in the case of independent assimilation, the algorithm converges to subset that reproduces, reasonably well, the observed cross-shore evolution.

Two reasons may explain this behaviour, the magnitude of the error regarding the total variance of the process (longshore or cross-shore) and the temporal scale of the individual processes. First, in the case of longshore dominated coasts, the variance of the longshore changes is much higher than the noise of the observations, which is not the case of short-term cross-shore fluctuations. Second, while longshore transport occurs at multiannual or decadal scale, when the magnitude of the added zero-mean Gaussian noise cancels out, cross-shore transport occurs at a much shorter time scale, similar to the frequency of remote sensing observations, which increases the sensitivity to observations inaccuracies as the error does not balance out.

Simulation/Statistic	$Y = Y_l + Y_c$ $NMSE$; $RMSE$; R^2	Y_l $NMSE$; $RMSE$; R^2	Y_c $NMSE$; $RMSE$; R^2	K_1 Rel. err.	K_c^+ Rel. err.	K_c^- Rel. err.
W/o data-assimilation	0.30; 113.98; 0.50	0.30; 114.05; 0.50	0.76; 6.15; 0.1	-60%	-87.5%	-93.75%
Indep. data-assimilation, $\epsilon(Y_{obs} = 0\ m)$	0; 0.70; 0.99	0; 0.19; 0.99	0.11; 0.70; 0.99	0.10%	-8.74%	10.77%
Joint data-assimilation, $\epsilon(Y_{obs} = 0\ m)$	0; 3.92; 0.97	0.01; 8.37; 0.86	2.07; 10.14; 0.59	5.75%	-67.15%	97.81%
Indep. data-assimilation, $\epsilon(Y_{obs}) = 10\ m$	0; 2.35; 0.98	0; 0.29; 0.99	0.11; 2.31; 0.88	0.24%	-0.44%	-50.89%
Joint data-assimilation, $\epsilon(Y_{obs}) = 10\ m$	0; 5.49; 0.94	0; 6.72; 0.90	2.44; 11.01; 0.57	4.33%	-70.87%	115.10%

Table 2.5: Error statistics of the data-assimilated longshore and cross-shore simulation.

2.4. Case study application

With the purpose of validating the model, IH-LANS is run in a real anthropized coastal stretch. After collecting all the inputs (offshore dynamics, bathymetry, sediment characteristics, shoreline observations, sediment flow boundary condition and structures parametrization), the numerical domain for the nearshore wave propagation and the shoreline transect-based discretization are defined. Then, as described in Figure 2.1, the multi-process shoreline evolution governing equation is fed with breaking wave properties propagated from offshore following the two step procedure. The model is executed during the hindcast period (1990–2020) and model predictions were calibrated and validated with satellite-derived shorelines following the independent data-assimilation approach.

2.4.1. Study area

The study area is a 40 km coastal stretch in the Mediterranean Sea, between Castellón and Valencia (Spain), Figure 2.13. Mean wave climate is characterized by mild waves but with an oblique mean angle of incidence (105° in nautical convention) with respect to the mean offshore normal of the bathymetry (120° in nautical convention), Figure 2.14. This drives an intense southerly LST.
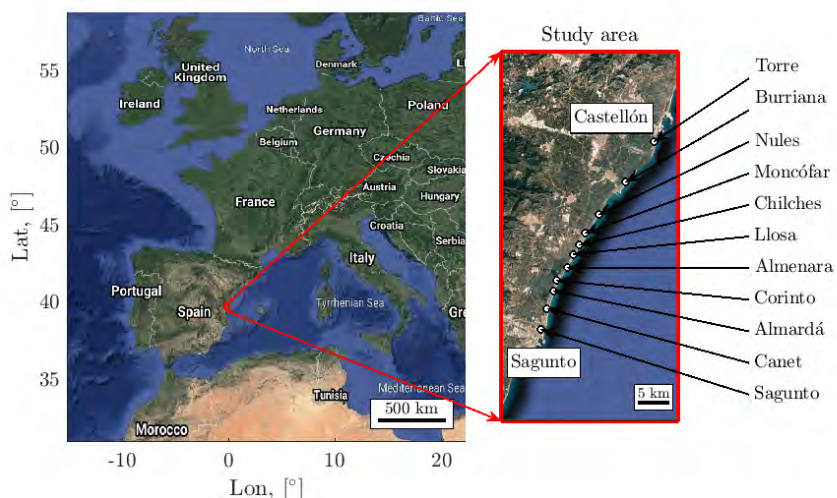
Figure 2.13: Location of the study area and the main beaches.

At the beginning of the 20th century, beaches in the area were in dynamic equilibrium as no gradients in the sediment transport occurred. Then, the construction of the ports of Castellón, Burriana and Sagunto completely altered the sediment dynamics by generating two littoral cells (Castellón-Burriana and Burriana-Sagunto). The coastal stretch was no longer in equilibrium due to the southerly LST and the lack of incoming sediment due to the blockage exerted by the ports. Therefore, two parts are distinguished in each littoral cell, the northern part which suffers erosion and the southern one which receives the sediment from the North. In order to preserve beach width, several anthropogenic interventions were carried out (Table 2.6). The most important ones were based on groyne fields to partition the coast in small units and nourishments.
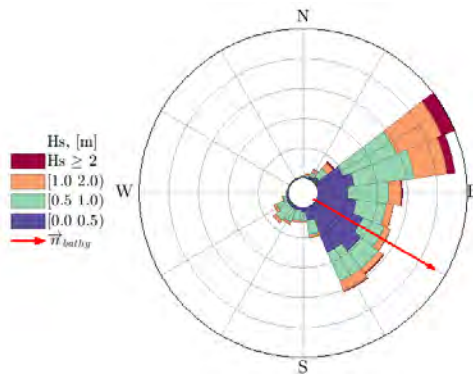
Figure 2.14: Wave rose at an offshore point in front of the coast of Castellón. The red arrow represents the mean offshore normal of the bathymetry.

2.4.2. Numerical domain definition

In order to apply IH-LANS, the computational domain for the hybrid downscaling and the transect-based discretization for the shoreline evolution module need to be defined. The numerical domain for nearshore downscaling is formed by one global 500×500 m grid one-way nested to three high resolution 50×50 m grids, Figure 2.15. Ten forcing points are located at the outer boundaries of the SWAN coarse domain. The water level is supposed to be uniform throughout the domain and is guided by a reanalysis point centred in the study area. The coastline is discretized in shore-normal transects that are automatically generated every 200 m, which is consistent with other large-scale studies Vitousek et al. (2017c). Then, transect spacing and position are manually

tuned in order to capture relevant morphological features such as artificial structures. A nested high-resolution analysis is also performed at Torre and Almenara beaches in which transects are generated every 15 m.
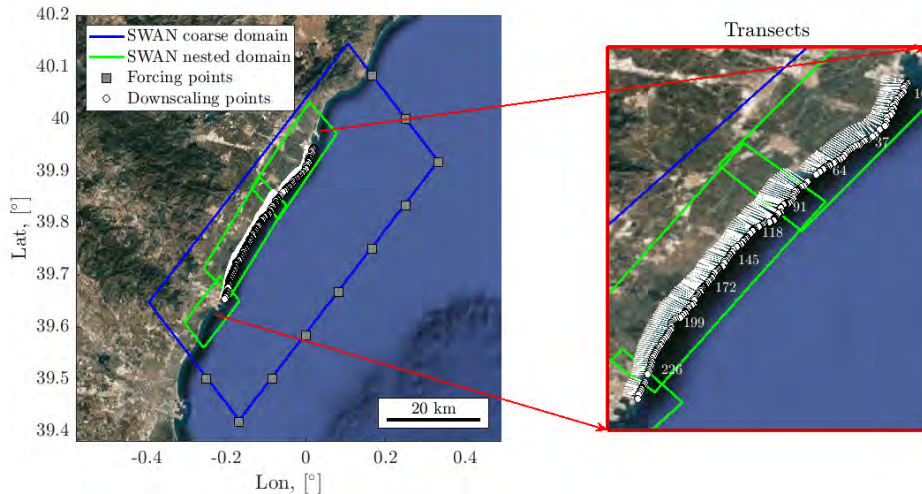
Figure 2.15: Numerical domain definition for the nearshore hybrid downscaling and shoreline transect-based discretization.

2.4.3. Inputs

Hourly offshore waves and storm surge from 1990 to 2020 are obtained from a reanalysis database generated by dynamical downscaling of ERA5 atmospheric fields using process-based models at a 0.08° grid. The astronomical tide is obtained by reconstructing the harmonic constants from the TPXO7.2 global model at a horizontal spatial resolution of 0.25°. The topobathymetry is formed by the topography, collected from the Spanish Geographical Institute (IGN), the nearshore bathymetry from multi-beam echo sounder field campaigns financed by the Spanish Ministry for the Ecological Transition and the Demographic Challenge (MITERD) in 2009 and the offshore bathymetry from the European Marine Observation and Data network (EMODnet) database. Additionally, the spatially varying sediment characteristics of the study area are collected from a MITERD database that summarizes field campaigns carried out in the period 2009–2010.

Observations are obtained from satellite-derived shorelines with the Coast-Sat algorithm, (Vos et al., 2019). Thirty years of bi-monthly to monthly observations are obtained from Landsat-5, Landsat-8 and Sentinel-2 campaigns providing valuable information for model calibration and validation. Shoreline observations are then intersected with the computational transects and tidally corrected to obtain time series of (mean high water line) MHL positions. In order to automatically eliminate outliers due to geo-referencing and detection errors, observations out of the $\mu_t \pm 1.5\sigma_t$ range were deleted, where μ_t and σ_t are the temporal mean and standard deviation of time window t = 6 months. Then, from the "outliers-free" observations, an unravelling algorithm based on a 5-years running mean is used to extract the longshore and the cross-shore components.

The ports of Castellón and Sagunto extend to a depth greater than the depth of closure, therefore null Dirichlet boundary conditions are imposed at the exterior transects. Coastal structures are parametrized from georeferenced images so as to be included in the modelling approach. Nourishments and other interventions executed during the study period and summarised in Table 2.6 are tracked through satellite imagery or by data provided by the MITERD.

Beaches are assumed to be uniformly erodible material but sediment spatial heterogeneity was considered at the transect level. A reference median grain size $D50_{ref}$ is attributed to every transect from a cloud of punctual $D50$ measurements provided by the MITERD. In order to integrate the spatial cloud of measurements in the transect-based shoreline model, a Voronoi spatial discretization was performed. Then, as a transect can extend regions in which sediment characteristics ($D50$) vary, an averaged ($D50_{ref}$) was obtained for each transect, following Aragonés et al. (2016). The Voronoi discretization and the transect $D50_{ref}$ are displayed in Figure 2.16. Bedrock or other non-erodible strata underneath the first sediment layer are not considered, as this information is currently not available. The sediment characteristics are then employed to estimate the initial longshore transport constant and the shape of the equilibrium Dean's profile which controls the cross-shore evolution. This potential profile shape is adopted for all the transects, from fine sand to gravel, as validated in other studies

Beach	Type of intervention	Date
Torre	Nourishment Groyne construction and nourishment Groyne removal/construction and nourishment Breakwater removal, groyne construction and nourishment	1993 1999-2000 2006-2007 2014-2015
Burriana	Groyne construction and nourishment	1993
Nules	Groyne construction and nourishment Nourishment	2001-2002 2013-2014
Moncófar	Nourishment Nourishment	1998-2002 2011-2012
Chilches	Nourisment	2011-2012
Almenara	Seawall construction and nourishment Nourishment Nourishment Seawall reinforcement Seawall enlargement Seawall enlargement Seawall enlargement Seawall enlargement Seawall enlargement Seawall reinforcement	1996-1998 2001 2004 2005 2008 2010 2012 2013 2015 2016
Corinto	Nourishment	1995-1998
Almardá	Nourishment	2007-2010
Canet	Nourishment	1995-1998
Sagunto	Sediment bypass Sediment bypass	1993-1997 1995-1998

Table 2.6: Man-made interventions in the study period (1990-2020).

(Aragonés et al., 2016; Athanasiou et al., 2019; Karunarathna et al., 2016; Vousdoukas et al., 2020b).

In order for the data-assimilation algorithm to converge, the initial parameter guess and search space needs to be constraint enough to the expected true set of parameters. Thus, the initial longshore constant K_1 was obtained, via the del Valle et al. (1993) formulation from $D50_{ref}$. Then, the initial cross-shore parameters were manually obtained by trial and error until a reasonable match was obtained. The same criteria explained in Section 2.3 for the synthetic cases is considered for the selection of the variable uncertainty and process noise. The initiation values of the eKf are detailed in Table 2.7.
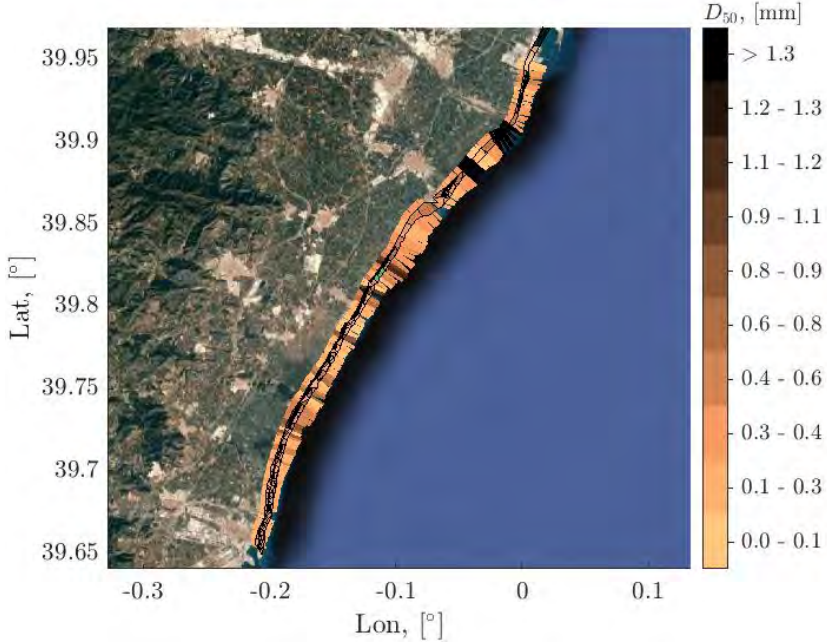
Figure 2.16: Voronoi polygons from the cloud of sediment measurements and transect $D50_{ref}$.

Variable, Var	Initial Value	Variable uncertainty, $\epsilon(Var)$	Process noise, $\delta(Var)$
Y_l	Y_0	4	0.2
K_1	25-250	25-250	1E-2 - 15E-2
vlt	0	5E-5	5E-6
Y_c^-	0	1	0.2
Y_c^+	0	1	0.2
K_c^-	1E-2 - 10E-2	0.5E-2 - 5E-2	1E-4 - 10E-4
K_c^+	1E-4 - 10E-4	0.5E-4 - 5E-4	1E-6 - 10E-6

Table 2.7: Input parameters for the data-assimilation algorithm in the real case. The measurement error R is 10 m, where $R_l = 2\ m$ and $R_c = 8\ m$.

2.4.4. Model application

Once the inputs are defined and the numerical set-up of the model established, hourly wave properties distributed along the 10 m depth contour are obtained from the nearshore downscaling of offshore wave climate. Then, following the main shoreline evolution loop in Figure 2.1, the breaking line properties are obtained and drive the LST gradients module and the cross-shore transport module. Shoreline evolution is evaluated considering full model's equation (Equation 2.1). Additionally, free model parameters are calibrated using the extended Kalman filter during the period 1990–2010, leaving the remaining ten years for validation.

Hourly estimates of the shoreline position are calculated at each transect, Figure 2.17. Note that the predicted shoreline matches well the observations, with a correlation coefficient (R^2) that exceeds 0.7 and a root mean square error ($RMSE$) less than 10 m. The cross-shore behaviour captures seasonal trends but does not properly reproduce extreme events. This fact, also demonstrated by Montaño et al. (2020) for equilibrium-type models, adds to the difficulties of calibrating cross-shore models with 15-day sampled noisy satellite-derived observations discussed in Section 2.3.7.
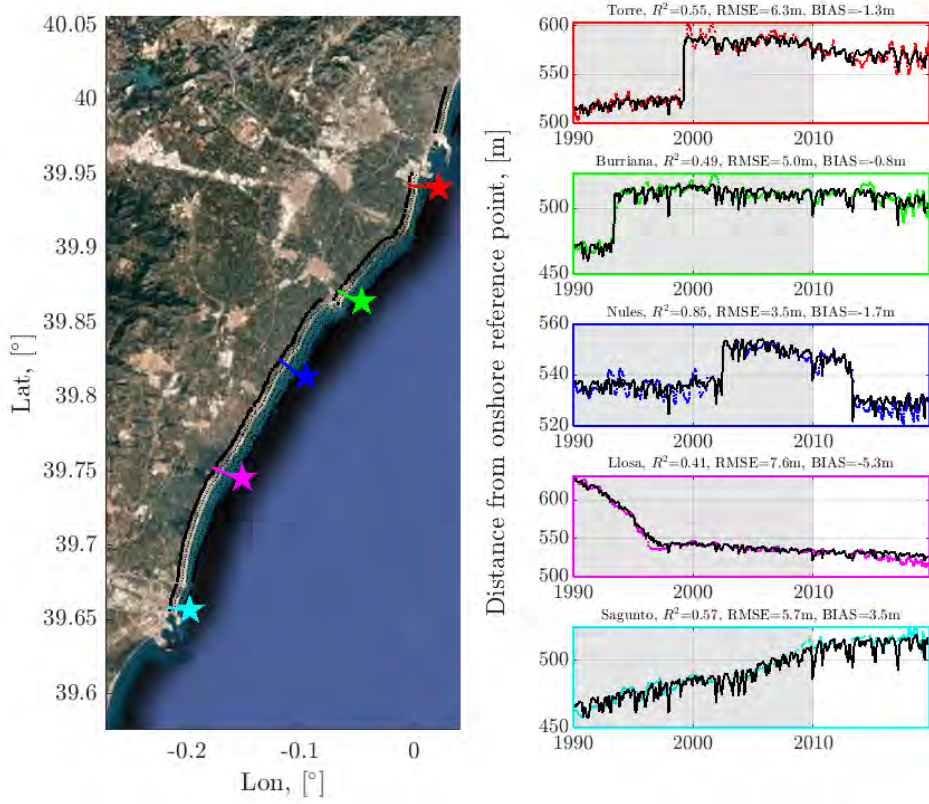
Figure 2.17: Transect-based discretization (left panel). The panels on the right represent the hourly modelled shoreline evolution (black line) and the observations (coloured dots) at different transects. The calibration period is shaded in grey and colour of the dots coincide with the corresponding transect on the left panel.

Contrary to the synthetic test-cases in which the reference shoreline position was known, the only way to quantify the performance of the model in the real case is from the potentially noisy satellite-derived shorelines. Due to the lack of long-term high-quality

in-situ observations, the error measures provided just quantify the difference between the observed satellite-derived shoreline and the model results. Thus, the real error is a non-linear combination of the model error and the observations' error, being the last one impossible to determine with the current means.

Table 2.8 shows different error metrics R^2, $RMSE$ and $BIAS$ averaged between the beach transects with and without data-assimilation. As no rigorous calibration was performed to define the initial set of parameters, the without data-assimilation error measures are provided for the full analysis period. On the other hand, regarding the results of the data assimilation approach, the error measures are provided just for the validation period. The results are, in general, satisfying, as even without data-assimilation $RMSE$ are less than 20 m except in Llosa. In this particular case, the reason is due to the drastic change in trend in 1998 due to the complete erosion of a soft sand bank until 1998 that triggers a change in the LST rate which is not accounted for if data-assimilation is not performed. Shoreline evolution in the southern beaches (Sagunto and Canet) is poorly reproduced without data-assimilation. In this case, the large human pressure in the area and the effects of the big adjacent ports may explain these inconsistencies in the first-pass estimation of the free-model constants.

Beach	$RMSE$, $[m]$	$BIAS$, $[m]$	R^2
Torre	3.80/<u>8.05</u>	0.62/<u>3.40</u>	0.90/<u>0.73</u>
Burriana	4.56/<u>10.99</u>	1.10/<u>6.59</u>	0.88/<u>0.66</u>
Nules	4.01/<u>5.99</u>	0.31/<u>2.31</u>	0.80/<u>0.65</u>
Moncófar	4.72/<u>10.46</u>	0.60/<u>5.74</u>	0.74/<u>0.58</u>
Chilches	4.18/<u>12.31</u>	0.84/<u>9.06</u>	0.73/<u>0.50</u>
Llosa	4.75/<u>22.13</u>	0.80/<u>16.87</u>	0.89/<u>0.55</u>
Almenara	4.60/<u>15.04</u>	1.12/<u>2.92</u>	0.83/<u>0.41</u>
Corinto	5.81/<u>7.56</u>	0.56/<u>2.01</u>	0.68/<u>0.59</u>
Almardá	5.37/<u>8.49</u>	1.21/<u>5.17</u>	0.46/<u>0.39</u>
Canet	5.61/<u>14.49</u>	1.08/<u>9.70</u>	0.87/<u>0.83</u>
Sagunto	4.10/<u>13.24</u>	0.74/<u>10.73</u>	0.89/<u>0.67</u>

Table 2.8: Mean error statistics at different beaches with and without data-assimilation. The non-underlined results are obtained with data-assimilation whereas the underlined values are obtained if no data-assimilation is performed.

2.4.5. High-resolution analysis

When the goal of the study is to evaluate shoreline evolution near artificial structures, the spacing between transects needs to be reduced with respect to regional scale applications. To illustrate model's ability to produce an accurate and detailed description of shoreline evolution under anthropogenic pressure, a high resolution study is performed at the beaches of Torre and Almenara. In both cases, the transect spacing is lowered to 15 m and the sediment flow boundary conditions are inherited from the full domain calculation.
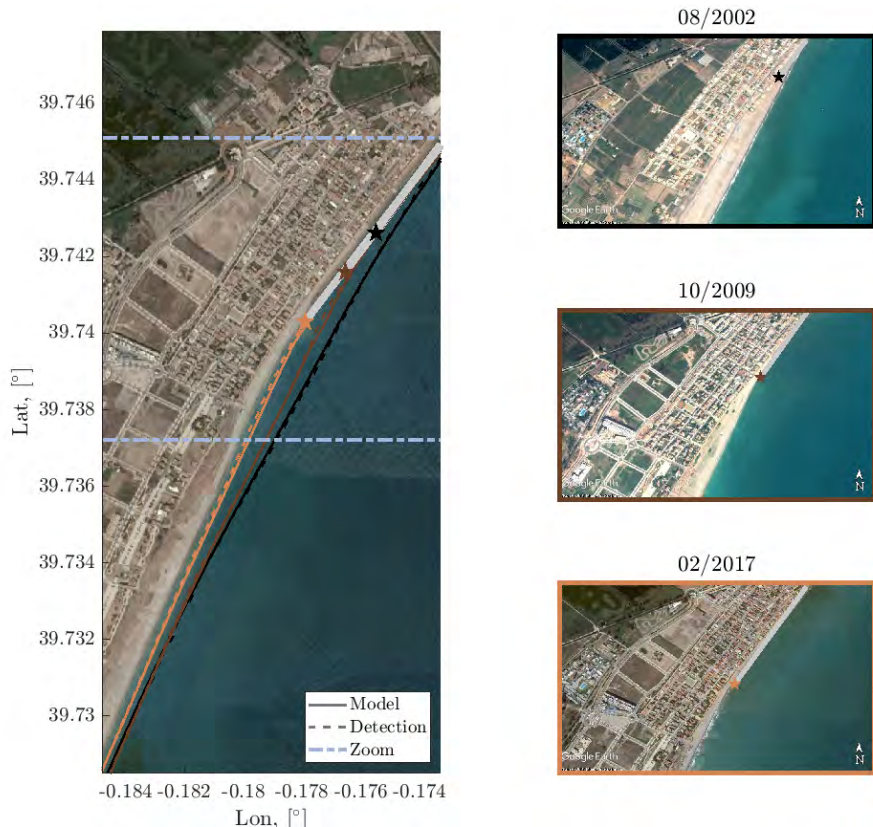
Figure 2.18: Shoreline evolution at Torre beach. Left panel shows the modelled (continuous lines) and detected shorelines (dashed lines) overlaid upon a recent Google Earth map. The coloured shorelines on the left panel match the Google Earth figures on the right that were taken at different dates. The different structures are displayed with stars.

Torre beach is located at the lee of the Castellón port and it is compartmentalized by groynes in order to prevent sediment from leaving the system from the South. Several

anthropogenic interventions like structure construction and nourishments have been executed since 1990. From then on, several man-made interventions are being recorded in the area (see Table 2.6). Figure 2.18 shows the modelled and detected shorelines in Torre beach between 2011 and 2017, highlighting the model ability of reproducing the shoreline evolution when human actions play a major role on the coastal response.
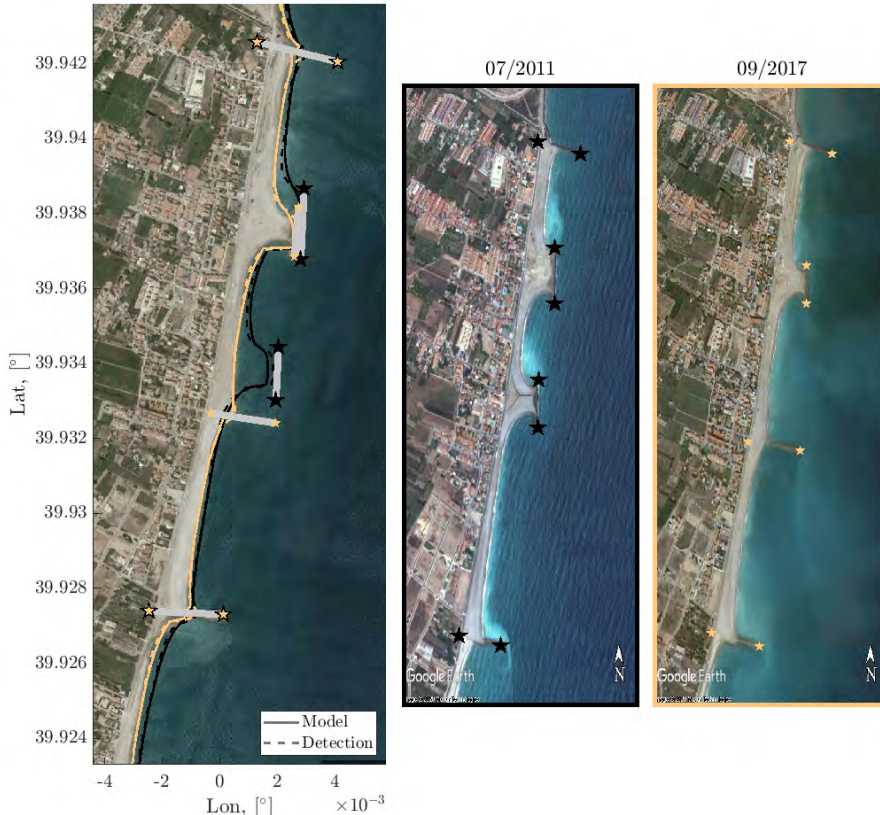
Figure 2.19: Shoreline evolution at Almenara beach. Left panel shows the modelled (continuous lines) and detected shorelines (dashed lines) overlaid upon a recent Google Earth map. The coloured shorelines on the left panel match the Google Earth figures on the right, which were taken at different dates. The evolution of the seawall's tip is also represented by the different coloured stars.

The next high-resolution study case is Almenara beach, located halfway in between the littoral cell defined by the ports of Burriana and Sagunto. In this zone, mean wave direction is particularly deviated with respect to the mean normal to the shoreline. Due to this fact, the sediment propagates towards the South. In order to protect the first-line infrastructure and houses, a seawall is constructed in the upper part of the beach. The structure is progressively advanced as detailed in Table 2.6. Figure 2.19

displays the agreement between the modelled shoreline evolution and the observations at different dates.

2.5. Conclusions

An efficient coastline change model named IH-LANS has been presented and validated in synthetic and real cases. The model integrates a hybrid (statistical and dynamical) deep water wave propagation module, suited for the nearshore downscaling of global wave reanalysis and future wave projections databases, and a reduced-complexity physics-based shoreline evolution model. The shoreline evolution model has a breaking wave propagation module that solves shoaling, refraction and diffraction in order to calculate coastline changes due to longshore and cross-shore processes at short-to-long term temporal, local-to-regional spatial scales. Groynes, breakwaters, seawalls and nourishments are modelled by considering their effects in wave breaking propagation and sediment transport. Additionally, in order to facilitate the calibration of free model parameters, IH-LANS is enriched by observations via a data-assimilation technique based on the extended Kalman filter. Different synthetic tests have proven different model functionalities. A detailed analysis of the data-assimilation algorithm when combining longshore and cross-shore processes is performed. Also, an approach is proposed to facilitate the convergence of the algorithm to the optimal set of parameters when longshore and cross-shore processes are modelled together. A real case in a highly anthropized Spanish coastal stretch in the Mediterranean Sea, is analysed. In the later example, the model is forced with high space-time resolution wave climate database and satellite-derived shoreline observations for calibration to produce hourly shoreline estimates. Model predictions showed good agreement with the observations ($RMSE <$ 10 m and $R^2 > 0.7$).

The modularity of the model allows for implementing different and/or additional process formulations and data-assimilation strategies to account for stationary or non-stationary parametrizations. Here, the stationary hypothesis in the model parameters is applied. However, the temporal consistency of free-model parameters may become

invalid due to changes in sediment supply, geologic conditions or climate patters. This limitation could be superseded by climate-dependent (Montaño et al., 2021) and time-varying parametrizations (Ibaceta et al., 2020). To this end, progress in remote sensing techniques, in multi-process modelling and in the link between climate patterns and shoreline response is required.

The efficiency of the model make it a powerful tool for the development of shoreline projections considering different sources of uncertainty and assessing different adaptation strategies (Toimil et al., 2021b). In the next Chapter, an ensemble of end-of-century shoreline projections are obtained considering the uncertainty in the projections of waves and water levels. Constraints like the computational demand of multiple centennial simulations and the integration of mean sea level rise effects in wave propagation and shoreline change, are thoroughly addressed.

CHAPTER 3

APPLICATION OF IH-LANS TO FORECAST THE SHORELINE EVOLUTION

In this Chapter, the application of IH-LANS to project the shoreline evolution at a highly anthropized coastal area is described. To this end, a methodology to obtain ensemble shoreline change projections at the regional scale by combining multimodel projections of wave climate and water levels and the reduced-complexity shoreline evolution model IH-LANS is developed. In order to account for climate change uncertainty, dynamically downscaled and bias corrected projected waves and storm surge series from different combinations of global and regional climate models and three potential mean SLR trajectories for two representative concentration pathways, are used to force the erosion impact model IH-LANS . The methodology is applied to a 40 km highly anthropized coastal stretch in the Mediterranean coast of Spain. Thirty hourly time series of shoreline evolution between 2020 and 2100 are obtained, each of them linked to one future realisation of waves and water levels. From the shoreline time series

---

[1]This Chapter is based on Alvarez-Cuesta, M., Toimil, A., and Losada, I. J. 2021b. Modelling long-term shoreline evolution in highly anthropized coastal areas. Part 2 : Assessing the response to climate change. *Coastal Engineering*, 168(July):103961.

analysis, long and short-term processes are unraveled, yielding the permanent retreats and the beach area losses, the contribution of individual physical processes (longshore, short-term cross-shore, and SLR) to shoreline change and the non-stationary extreme retreats. The methodology presented hereinafter is intended to be a useful tool for evaluating potential climate change risks while enabling the evaluation and prioritisation of adaptation measures.

3.1. Introduction

Modelling long-term shoreline evolution implies many challenges such as the interaction of processes acting at multiple time-scales and the uncertain changes that climate change will induce in the triggering mechanisms (Toimil et al., 2020a). Mean and storm wave conditions, storm surge, astronomical tide, sea level rise and sand supply changes are the main drivers of shoreline change (Ranasinghe, 2016). However, the majority of the studies concerning shoreline projections focus on the effects of mean SLR while neglecting or considering the rest of the drivers to be stationary (Athanasiou et al., 2020; Le Cozannet et al., 2019; Thiéblemont et al., 2019, 2021; Vousdoukas et al., 2020b).

Few studies have incorporated climate change-induced changes in other drivers than SLR for shoreline evolution assessments. In a pioneering work, Zacharioudaki and Reeve (2011) forced a one-line model with two combinations of global and regional climate models (GCM-RCM) and two emissions scenarios at an idealized embayed beach. They provided seasonal and monthly statistics for the time slice 2071–2100 with respect to the 1961–1990 period. Later, Vitousek et al. (2017c) obtained the shoreline projections in the 2010–2100 period at the Southern California coast. They forced a reduced-complexity shoreline evolution model with one GCM-RCM realization of future wave climate for one RCP. In the global study presented by Vousdoukas et al. (2020b), projected long and short-term shoreline behaviour was modelled independently. They resolved the long-term evolution by a modified version of the Bruun's rule (Bruun, 1962) and by extrapolating the past observed behaviour from satellite-derived shorelines. The storm response was modelled considering future waves and storm surge from six dy-

namically downscaled GCMs that fed the model proposed by Kriebel and Dean (1993). Recently, Bamunawala et al. (2020) used four GCMs for all the RCPs (2.6, 4.5, 6.0 and 8.5) to feed a catchment-estuary-coastal model with projected temperatures and run-off at three inlet interrupted coasts in the USA, United Kingdom and Sri Lanka in the period 2020–2100. Even though changes in fluvial supply were rigorously accounted for, they did not consider the ambient shoreline change due to changes in wave climate and water levels. On the other hand, the influence of free-model parameters, SLR and different wave chronologies of a single future wave climate scenario have been studied by d'Anna et al. (2020, 2021, 2022b) at a cross-shore dominated beach in France.

While previous works focused on the modelling strategy (Vitousek et al., 2017c), other studies simplified the shoreline model in favour of sampling the uncertainty of some of the drivers (Zacharioudaki and Reeve, 2011; Le Cozannet et al., 2019; Vousdoukas et al., 2020b; d'Anna et al., 2021, 2022a). However, the combination of the latest advances in multi-process physics-based shoreline modelling and the multi-model projections of waves and water levels has not been addressed to produce future impact estimates. To this end, an attempt to produce robust shoreline projections is presented by combining 1) an advanced physics-based model calibrated with automated techniques and satellite-derived observations and 2) the treatment (uncertainty sampling and efficient downscaling) of projected waves and water levels from different climate models.

With the purpose of illustrating the methodology, shoreline projections of a combination of five GCM-RCMs and three SLR trajectories for two RCPs are obtained at a highly anthropized coastal stretch along the Mediterranean Sea. First, the offshore GCM-RCM dynamically-downscaled and bias-corrected waves and water levels are collected. Then, the nearshore wave climate is calculated through a hybrid downscaling technique that accounts for propagation over a time-varying water level while reducing the computational burden of the multiple simulations. The reduced-complexity shoreline evolution model presented in Chapter 2 is subsequently forced with continuous time-series of nearshore waves and water levels and produces thirty shoreline evolutions, one for each combination of GCM-RCM and SLR trajectory for the two emissions scenarios.

When modelling long-term coastal evolution, the shoreline response to SLR is one of the major sources of uncertainty (Le Cozannet et al., 2019), mainly due to the lack of long-term observations to validate the different formulations. The most simple approach to quantify SLR-induced shoreline retreat relies on the Bruun's rule (Bruun, 1962). It is based on simple but physical and widespread accepted concepts like the equilibrium profile and volume conservation. In spite of its limitations (Cooper and Pilkey, 2004; Ranasinghe et al., 2012), it is the most used model to quantify profile's response to SLR. Furthermore, conversely to other formulations, the Bruun's rule has been successfully validated under laboratory conditions in Atkinson et al. (2018). Thus, the Bruun's rule is implemented in the cross-shore model.

The integration of longshore and cross-shore processes allows for obtaining post-processed outputs at multiple time-scales. Thus, valuable information for coastal planning is obtained through the ensemble of projected shoreline time series. Unravelling the long-term shoreline changes enables to calculate permanent retreats and beach area losses, which are key for the identification of critical erosion hotspots. Additionally, mean shoreline positions during the summer season, essential for estimating the risk of loss of beach recreation (Toimil et al., 2018; López-Dóriga et al., 2019), are obtained. On the other hand, the design of erosion adaptation strategies highly depends upon the main shoreline change triggering mechanisms. While SLR impacts can be reduced through targeted nourishments (Atkinson and Baldock, 2020), extreme storm retreats may require seasonal recharges to preserve beach width during the bathing season (Cooke et al., 2012) and long-term erosion due to harbour constructions needs more complicated interventions (Tsoukala et al., 2015). Thus, the relative contribution of different coastal change processes is obtained in order to help coastal managers decide the most efficient adaptation strategy. On the other hand, while most studies use dedicated models for evaluating the storm response at particular time-slices, simplifying or even neglecting the long-term evolution (Grases et al., 2020; Anderson et al., 2021); the proposed modelling strategy allows for calculating the time evolution of extreme retreats considering the long-term shoreline evolution.

148

This Chapter is organised as follows: Section 3.2 describes the general methodology, which includes the input collection and pre-process, the nearshore hybrid wave propagation and the shoreline evolution model runs. Section 3.3 focuses on the application of the methodology to the study area. After a brief description of the projected waves and water levels, raw projected shoreline evolution results are obtained. Next, post-processed outcomes at long and short–term scales are displayed to show the potential of this modelling approach for climate change risk assessment and adaptation applications. Finally, Section 3.4 is devoted to providing some conclusions.

3.2. Overview of the methodology

In order to calculate the shoreline projections accounting for all relevant forcings with a proper intrinsic uncertainty sampling, a methodology classified as ensemble approach according to the categorisation established by Toimil et al. (2020a) is proposed. As shown in Figure 3.1, the methodology is structured in three steps, which are the collection of future shoreline change drivers, the calculation of the shoreline evolution by means of a reduced-complexity physics-based model, and a final post-process stage to extract relevant information for coastal managers.

Once the target coastal stretch has been selected, the numerical domain for the nearshore wave propagation needs to be defined in accordance with the offshore dynamics grid. Bias-corrected offshore waves and storm surge from different GCM-RCM realisations (for simplicity, referred to as RCM realisations hereinafter) for various RCPs are collected at the boundary points of the domain. Astronomical tide predictions and plausible SLR trajectories associated with the different RCPs are also obtained.

Climate change-induced coastal drivers
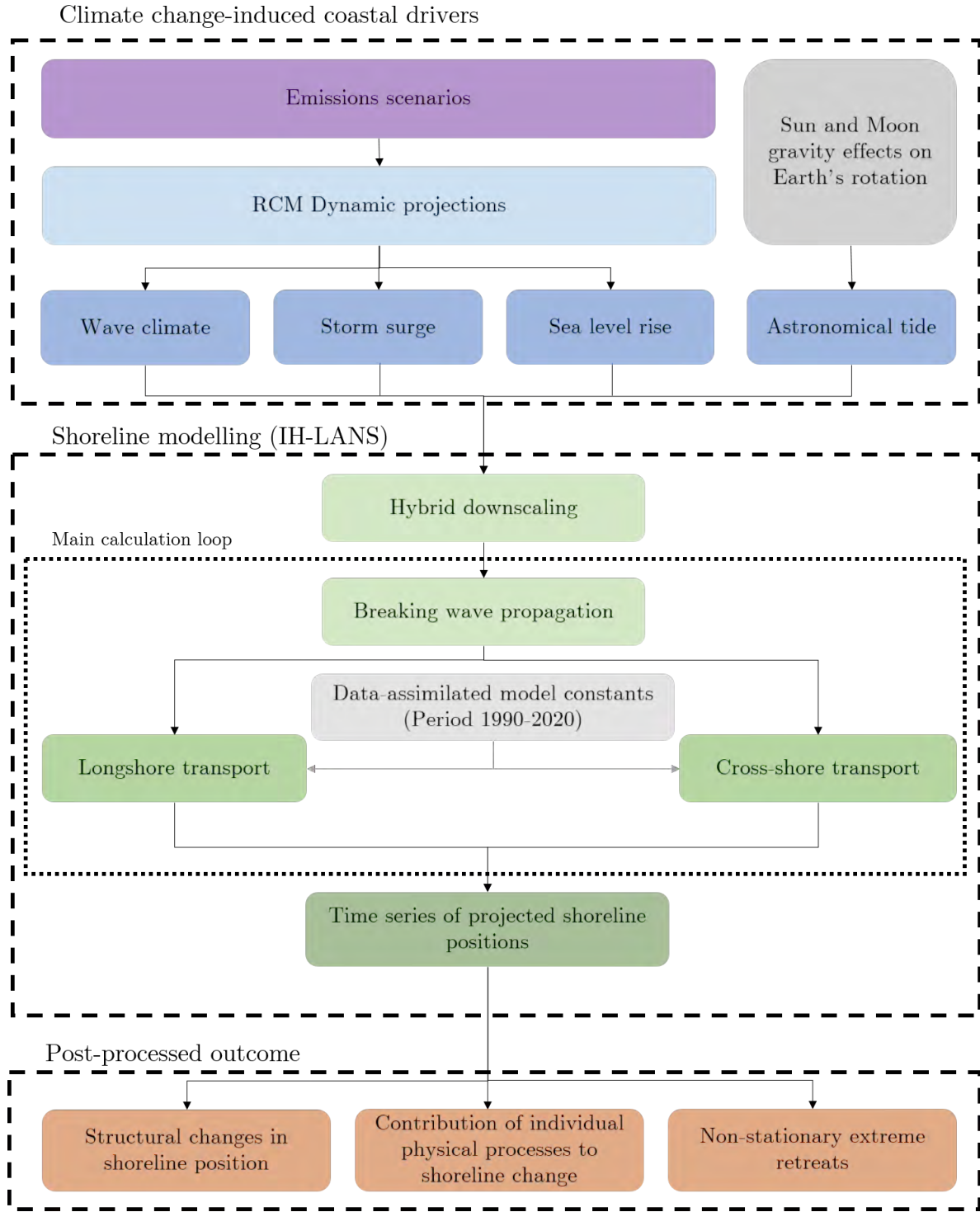
Figure 3.1: Flowchart of the methodology to calculate shoreline evolution projections.

The second step consists of the shoreline evolution modelling using a reduced-complexity model. Projected offshore wave dynamics are propagated to breaking in two different stages. First, a hybrid (statistical and numerical) nearshore wave propagation is

performed accounting for time-varying water levels while reducing the computational expense of individually propagating the multiple realisations of future climate. Then, breaking wave characteristics are solved in the main shoreline evolution loop and drive longshore and cross-shore processes (Alvarez-Cuesta et al., 2021a). Free parameters modulating the different shoreline change processes are inherited from the calibration performed in the reanalysis period, carried out with ERA5 downscaled waves and storm surge. This step is performed multiple times to obtain projected shoreline evolutions for each of the combinations of RCM and SLR trajectories associated with the RCPs considered.

In the third step, future shoreline evolution realisations are postprocessed to untangle the different resolved processes and time scales so as to provide relevant outputs for climate change risk assessment and adaptation.

3.3. Case study application

The field application is performed at a highly anthropized 40 km coastal zone located on the Mediterranean Sea, in between Castellón and Valencia (Spain). Sediment size is spatially variable. While beaches in the southern part of the coastal stretch are formed by fine sediments (D50 around 0.2 mm), beaches in the northern part (Castellón region) show, on average, coarser sediments (D50 around 0.4 mm). Wave climate in the study area is characterised by a mean significant wave height of 0.75 m whose peak period is around 5.1 s. Mean wave direction of incoming waves is 105° in nautical convention, which triggers an intense southerly longshore sediment transport (LST) as the mean offshore normal of the bathymetry is around 120°. Gradients in the LST generated by harbour construction generate erosion problems in the lee of big structures. To overcome these problems, several anthropogenic interventions, mainly based on groynes construction and removal, as well as nourishments, have been implemented over the last three decades, Figure 3.2.
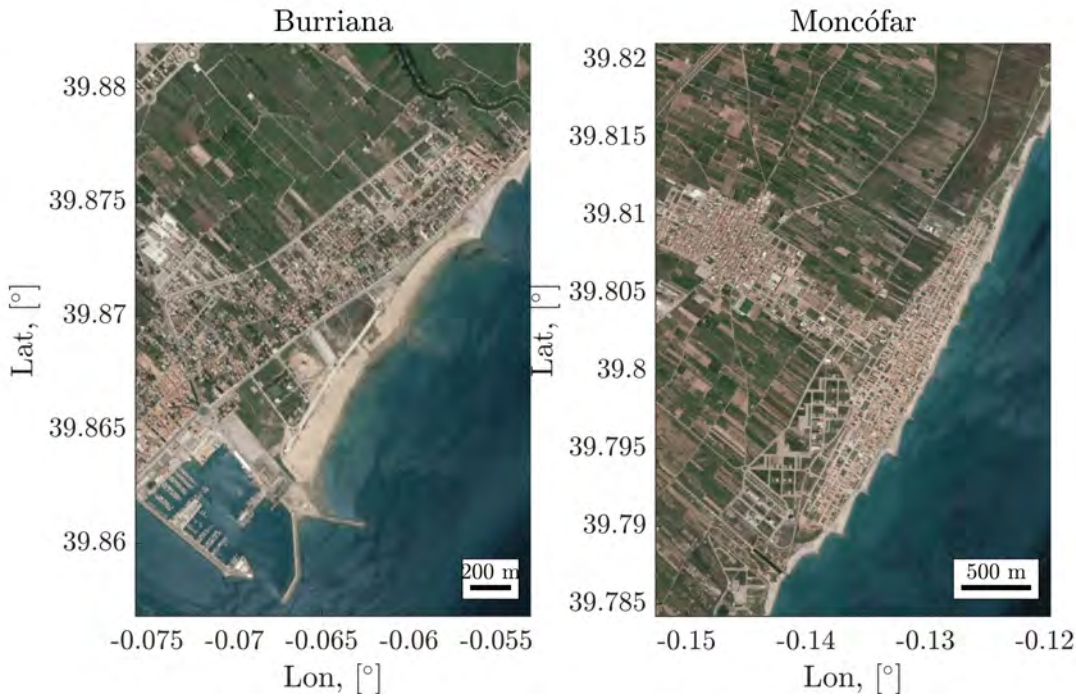
Figure 3.2: Example of two anthropized beaches in the study area.

3.3.1. Climate change-induced coastal drivers

The different drivers governing shoreline change are obtained from several databases due to their diverse nature. Waves and storm surge, which are primarily forced by wind fields and pressure gradients, are obtained from dynamically downscaled and bias-corrected RCM projections developed by IHCantabria (2020). SLR depends on multiple factors such as ocean temperature increase and subsequent thermal Antarctic, changes in the gravitational field of the Earth due to changes in land-ice distribution and shifting surface winds amongst others. Different SLR trajectories are obtained from the global climate model simulations performed within the fifth phase of the Couple Model Intercomparison Project (CMIP5) that are used in the last Intergovernmental Panel on Climate Change (IPCC) report (Oppenheimer et al., 2019). The astronomical tide, which is assumed to be deterministic, is reconstructed in a hourly basis from the harmonic constituents of the global TPXO7.2 database (Egbert and Erofeeva, 2002).

3.3.1.1.   Projections of waves and storm surge

Future time series of waves and storm surge are obtained from the dynamical downscaling of five RCMs for two emissions scenarios (RCP4.5 and RCP8.5), see Table 3.1. RCM atmospheric fields are employed to force process-based numerical models to produce future waves and storm surges at three time periods: historical (1985–2005), midterm (2026–2045) and long term (2081–2100). In the case of waves, the third generation spectral model WaveWatchIII (Tolman, 2009) is used to obtain the hourly spectral description of wave climate at a horizontal spatial resolution of 0.08°. Projected storm surges are derived using the ocean circulation numerical model ROMS (Shchepetkin and McWilliams, 2005) in a domain of 0.08° × 0.06° horizontal resolution at an hourly basis. Then, following the ideal sequence of steps involved in climate-change driven erosion assessments (Toimil et al., 2020a), RCM-derived waves and storm surges are bias-corrected before being used for coastal impact assessments.

GCM-RCM ID	GCM	Institution	Resolution	RCM
IPSL	IPSL-CM5A-MR	Institut Pierre-Simon Laplace	1.25°×1.25°	RCA4
HADG	HadGEM2-ES	Met Office Hadley Centre	1.25°×1.90°	RCA4
EART	EC-EARTH	EC-EARTH consortium	1.125°×1.125°	RCA4
CNRM	CNRM-CM5	Cen. Nat. de Recherches Météorologiques	1.40°×1.40°	RCA4
MEDC	CNRM-CM5	Cen. Nat. de Recherches Météorologiques	1.52°×1.43°	ALADIN52

Table 3.1: Some details of the GCM-RCM models considered in the analysis. The temporal resolution of all GCMs and RCMs is 6 and 3 h respectively. All RCMs have a spatial resolution of 0.11°×0.11°

A first-pass estimation of the impacts of climate change in wave-driven LST is performed by evaluating the mean offshore wave power and mean wave direction with respect to the mean bathymetry orientation. Figure 3.3 shows a comparison of the projected quarterly wave roses and wave power for the RCP8.5 of the RCMs compared to the ERA5 reanalysis at an offshore point in front of the Castellón coast. Projections show a slight reduction in mean annual wave power in the future with respect to the present of 1–2 kW/m. The distribution of future wave power changes during the year and projected wave power is more evenly distributed throughout the seasons. Regarding wave roses, the reanalysis highlights how the mean wave direction forms an angle with the normal to the bathymetry that explains the intense southerly LST and this situation prevails in the future. No clear changes are found in future wave direction except

in the case of IPSL RCM, in which the direction variance is higher. From the analysis of wave roses, no significant changes in future wave dynamics are expected to occur.

The fact of having projections of waves and storm surge for isolated time periods hampers the development of continuous shoreline projections throughout the century. Initial conditions are required for cross-shore and longshore processes, and need to be specified at the beginning of each of the time periods when dynamic projections are available. Thus, in order to avoid the extrapolation of observed shoreline behaviour to define the model initial conditions, the gaps of the time series are filled so as to obtain continuous time series from the end of the reanalysis period (2020) to the end of the century. To do that, a monthly bootstrapping technique is applied as in Davidson et al. (2017) and Kroon et al. (2020), which holds under the assumption that wave climate and storm surges, from every instant of the gap to the closest resolved time-slice, are stationary.
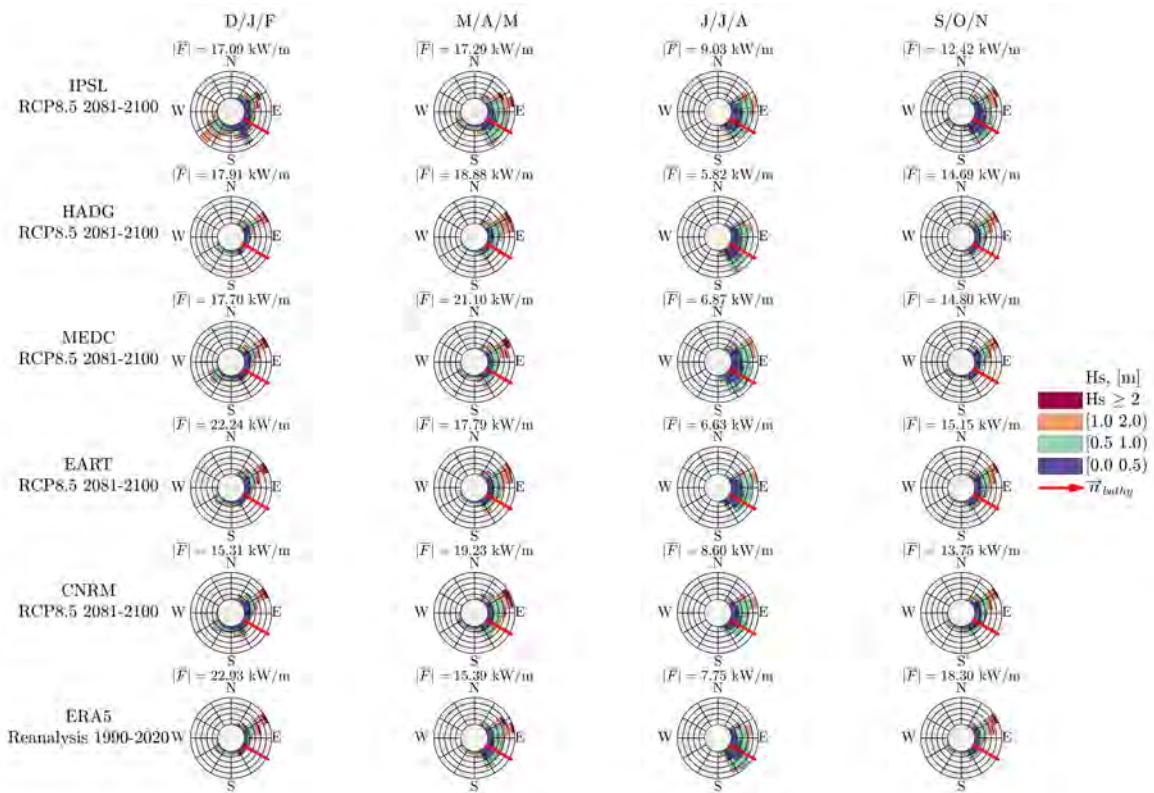
Figure 3.3: Projected RCM seasonal wave roses (Hs-Dir) for the RCP8.5 in the period 2081–2100 (top five rows) and the ERA5 reanalysis in the 1990–2020 period (last row).

3.3.1.2. Astronomical tide

Astronomical tide is obtained from the reconstruction of harmonic constituents from the TPXO7.2 global model using the Oregon State University Tidal Prediction Software (OTIS) at a horizontal spatial resolution of 0.25°. Continuous hourly time series extracted from 1985 to 2100 show the mixed diurnal-semidiurnal cycle of approximately 20 cm of tidal range.

3.3.1.3. Sea level rise

Regional SLR projections are obtained at a 1° horizontal resolution grid and include the contribution from sterodynamic effects, melting of mountain glaciers and ice sheets, land water and glacial isostatic adjustments from 21 GCMs (Oppenheimer et al., 2019). Mean and standard deviation of the multi-model ensemble for the two emissions scenarios considered (RCP4.5 and RCP8.5) are used to compute the likely range, defined as the 90% confidence band) following the IPCC methodology. To do that, the yearly mean is multiplied by ± 1.62 ($\Phi^{-1}(0.95)$) the yearly standard deviation to obtain the trajectories of the 95% and 5% percentiles. Hourly time series for the three percentiles (P95%, P50% and P5%) are obtained for the two RCPs by linearly interpolating the yearly time series fitted to a parabola.

3.3.2. Shoreline modelling

Bias-corrected hourly time series of waves and storm surge from five RCMs together with three SLR trajectories associated with the median and the 90% confidence band percentiles for the two emissions scenarios considered (RCP4.5 and RCP8.5), are used to drive shoreline change projections over the 21st century. For that purpose, offshore wave climate is propagated nearshore using an efficient hybrid (statistical and numerical) technique. Then, breaking wave properties are employed to feed the reduced-complexity shoreline evolution model IH-LANS that accounts for longshore and cross-shore processes and whose free parameters were calibrated and validated during the period 1990–2020 using waves and storm surge from the ERA5 reanalysis database (see Chapter 2). Hourly projected shoreline time series are obtained from 2020 to 2100. Cli-

mate change-related uncertainty is sampled through an ensemble approach accounting for thirty possible future shoreline evolutions, one for each combination of RCM, SLR trajectory and emissions scenario.

3.3.2.1. Hybrid downscaling of wave climate

The hybrid nearshore propagation of future waves and water level trajectories is challenging in two ways. First, in spite of the efficiency of hybrid downscaling, the computational cost and memory demand of propagating each of the RCM realizations and SLR trajectories for the different emissions scenarios until the end of the century is non-negligible. Second, time-varying water depth due to SLR needs to be accounted for in the statistical and numerical steps of the hybrid downscaling methodology.

To overcome these burdens, the original methodology presented in Camus et al. (2013) and modified following Chapter 2 to account for detailed spectral information from global wave databases, is tuned up. The computational demand problem is addressed by creating a single interpolation subset (selected offshore waves and water levels and the corresponding numerically propagated nearshore wave properties) representative of all future wave and water level realizations. SLR is accounted for by adding to the wave climate data matrices the most extreme sea levels of the corresponding RCP. Then, the selection algorithm identifies the most disjoint cases in terms of waves and water levels. In this way, the multivariate interpolation functions, fitted to the selected interpolation subset, are capable of reproducing any intermediate waves and water level scenario.

A schematic flow diagram of the present hybrid downscaling methodology is showed in Figure 3.4 Once the numerical domain for the hybrid downscaling is defined based on forcing databases and the shoreline discretization, the first step consists on collecting all the data. Considering a domain with np wave forcing points and nl representative water level points, the following matrices are assembled:

$$\underbrace{\boldsymbol{W}_{m \times nM}^{iM,iRCP}, \underbrace{\boldsymbol{SS}_{m \times nl}^{iM,iRCP}, \boldsymbol{AT}_{m \times nl}, \boldsymbol{SLR}_{m \times nl}^{iPrc,iRCP}}_{\text{water level data}}}_{\text{wave data}} \tag{3.1}$$

where iM corresponds to the RCM, $iRCP$ to the emissions scenario, m is the number of elementary temporal units in the forecast period (2020–2100), $iPrc$ is the number of SLR trajectories and $nM = np \times nvarW$, being $nvarW$ the number of aggregated spectral wave variables (i.e. Hs, Tm, Tp, θ). In this particular application $np = 10$, $nl = 1$, $iM \in \{IPSL, HADG, EART, CNRM, MEDC\}$, $iRCP \in \{RCP4.5, RCP8.5\}$ and $iPrc \in \{P5\%, P50\%, P95\%\}$.

Next, wave and water level data is aggregated for every combination of RCM and RCP and condensing SLR trajectories by considering the maximum and the minimum values:

$$
\boldsymbol{M}_{2m \times (nM+nl)}^{iM,iRCP} = \begin{bmatrix} \boldsymbol{W}_{m \times nM}^{iM,iRCP} & \boldsymbol{SS}_{m \times nl}^{iM,iRCP} + \boldsymbol{AT}_{m \times nl} + min(\boldsymbol{SLR}_{m \times nl}^{min(iPrc,iRCP)}) \\ \boldsymbol{W}_{m \times nM}^{iM,iRCP} & \boldsymbol{SS}_{m \times nl}^{iM,iRCP} + \boldsymbol{AT}_{m \times nl} + max(\boldsymbol{SLR}_{m \times nl}^{max(iPrc,iRCP)}) \end{bmatrix}
$$
(3.2)

In order to account for the effects of SLR, the matrix $\boldsymbol{M}$ doubles the number of rows of the antecedent matrices, $\boldsymbol{W}$, $\boldsymbol{SS}$, $\boldsymbol{AT}$, $\boldsymbol{SLR}$. In this case, the only difference between the rows $i \leq m$ and the rows $i > m$ are the columns $j \geq nM$ is related to the water level. The water level considered in the rows $i \leq m$ accounts for the minimum SLR of the smallest percentile's trajectory while the values $i > m$ account for the maximum SLR of the largest percentile's trajectory value, in both cases summed up to the other water level components. In this way, the data matrix $\boldsymbol{M}$ contains the most disjoint elements in terms of waves and water levels. Ten $\boldsymbol{M}$ matrices are obtained, one each for each RCM and RCP combination.

The next step is the first statistical treatment. In this process, the $\boldsymbol{M}$ matrices are projected in a reduced empirical orthogonal function (EOF) space so as to decrease the number of dimensions while maximizing the explained variance via principal component analysis (PCA). Selection of the K most different cases (out of 2m) is performed in the reduced EOF space via the maximum dissimilarity algorithm (MDA) and backtranslated to the physical space yielding the matrix $\boldsymbol{M}_{K \times (nM+nl)}^{iM,iRCP}$. Then, the selected K cases of every RCM-RCP combination are merged and form the matrix $\boldsymbol{MG}_{(nc \times K) \times (nM+nl)}$, where nc is the number of RCM-RCP combinations. In this application, a value of $K = 500$ cases was considered following Camus et al. (2013), $2m \approx 1.4M$ and $nc = 10$.

The second MDA selection is performed on the matrix $\boldsymbol{MG}_{(nc \times K) \times (nM+nl)}$ and yields $\boldsymbol{MG}_{K \times (nM+nl)}$.

1. Data collection & pre-process

| 1.1 Wave data | 1.2 Water level data | 1.3 Data matrix assembly (one for each RCM-RCP combination) |

2. Statistical treatment. Part 1: nested selection

2.1 Principal Component Analysis

| Data matrix projected in the complete physical space | Normalization PC Calculation Dimensionality reduction | Data matrix projected in the reduced EOF space |

2.2 First Maximum Dissimilarity selection

Selected cases in the EOF space for each RCM-RCP combination

2.3 Physical base traslation

Selected cases in the physical space for each RCM-RCP combination

2.4 Global data matrix aggregation (one matrix with selected states from each RCM-RCP combination)

2.5 Second Maximum Dissimilarity selection

3. Dynamic downscaling

3.1 Enhanced forcing spectra reconstruction

Identify spectral partitions selected cases for the boundary forcing points

Reconstruct spectra at the boundary forcing points

3.2 Propagation

Case M

Case 1

Propagated cases at downscaling points

SWAN model

4. Statistical treatment. Part 2: reconstruction

4.1 Multivariate interpolation

Fit Radial Basis Functions (RBF): Find f, such that :

Selected downscaled cases = f(Selected offshore cases)

4.2 Complete nearshore wave climate reconstruction at the downscaling points for every (RCM and SLR)–RCP combination

Downscaled cases = f(offshore cases)

Figure 3.4: Flowchart of the hybrid downscaling of future wave climate.

Once the two nested MDA selections have been performed, the next step is the numerical downscaling of the $\boldsymbol{MG}_{K\times(nM+nl)}$ selected cases that yields the propagated wave properties at the selected idow downscaling points $\boldsymbol{DMG}_{K\times nvarW}^{idow}$ distributed through the 10 m depth contour. This step is performed by enhancing the SWAN model (Booij et al., 1999) wave forcing boundary condition with high-fidelity spectral information as detailed in Chapter 2.

The multivariate interpolation subset formed by offshore wave conditions $\boldsymbol{MG}_{K\times(nM+nl)}$ and the corresponding propagated cases at each downscaling point $idow$ $\boldsymbol{DMG}_{K\times nvarW}^{idow}$ is used to fit radial basis functions (RBFs) for each of the wave variables $[Hs, Tm, Tp, \theta]$. Finally, nearshore wave climate associated with every combination of RCM and SLR percentile for each RCP is reconstructed at the downscaling points by applying the fitted RBFs to the predictor matrices $\boldsymbol{N}$:

$$\boldsymbol{N}_{m\times(nM+nl)}^{iM,iRCP,iPrc} = [\boldsymbol{W}_{m\times nM}^{iM,iRCP}, \boldsymbol{SS}_{m\times nl}^{iM,iRCP} + \boldsymbol{AT}_{m\times nl} + \boldsymbol{SLR}_{m\times nl}^{iPrc,iRCP}] \qquad (3.3)$$

Note that contrary to matrix $\boldsymbol{M}$, $\boldsymbol{N}$ columns $j \geq nM$ contain the complete SLR trajectory associated with the corresponding percentile iPrc. In this application thirty matrices N are assembled, corresponding to five RCMs (IPSL, HADG, EART, CNRM, MEDC) and three SLR trajectories (P5%, P50%, P95%) for two emissions scenarios (RCP4.5 and RCP8.5).

3.3.2.2. Projections of shoreline evolution

The shoreline evolution model IH-LANS presented in Chapter 2 is forced with high-resolution downscaled space-time dynamics and produces, at every transect, thirty hourly time-series for each of the RCM and SLR combinations for the considered RCP scenarios. The transect-based numerical model, capable of modelling the effects of different man-made interventions, accounts for longshore and cross-shore processes forced by breaking wave properties. Free model parameters are calibrated and validated during the period (1990–2020) via a data-assimilation algorithm based on the extended Kalman filter. Shoreline projections rely on the calibrated parameters assuming that

they remain stationary in the future. Amongst them, one key data-assimilated parameter is the unresolved processes trend (*vlt*). This initially unknown quantity modelled as a linear trend, is found on the order of 0.2 m/year (Figure 3.5), which compares to the satellite-derived observation trends of more than 4 meters per year in some of the beaches in the area. The difference between the observations trend and the unresolved processes trend is explained explicitly by the model, which accounts for more than 80% of the shoreline response. The remainder is the unresolved processes trend, which is reasonably low and in line with the values reported in Vitousek et al. (2017c). This value arises to compensate the differences between the modelled and the observed shoreline position, which can be due to numerous factors that represent our knowledge uncertainty in the processes and in the system itself. The unresolved processes trend represents the hybrid nature of the proposed approach, which combines a purely data-driven model based on extrapolation as in Le Cozannet et al. (2019) and a physics-based model. However, further work is needed in order to decipher the physical origin and behaviour of the unresolved processes.
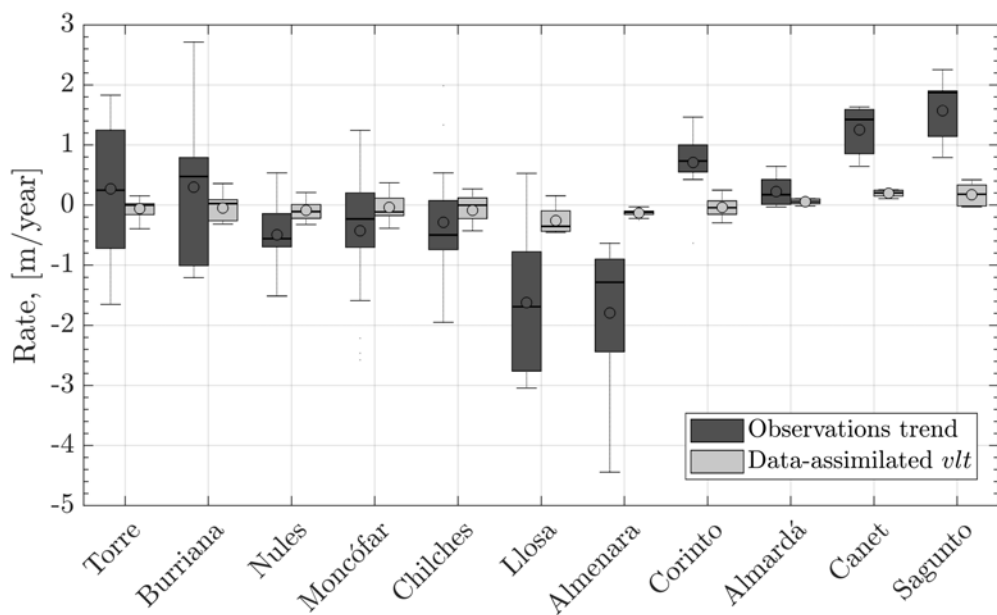
Figure 3.5: Initial observations trend compared to the data-assimilated unresolved processes trend. The difference between these values represent the shoreline change modelled explicitly in IH-LANS.

In spite of the efforts to account for climate non-stationarity in shoreline modelling (Ibaceta et al., 2020; Montaño et al., 2021), when observations are not available, there are currently no methods to infer reliable time-varying model parametrizations from changes in the drivers. Thus, the stationarity hypothesis has been adopted when forecasting the shoreline evolution.

The main shoreline evolution loop starts by calculating the breaking wave properties at every transect. This is done by considering the linear wave theory and the Snell's law of refraction. If diffracting structures are present, the breaking line properties are updated following the work of Kamphius (2000) and Dabees (2000). Then, the sum of longshore and cross-shore-related shoreline changes drives shoreline evolution (equation 3.4). Longshore shoreline changes are evaluated as the sum of three modules, which are LST gradients, sediment sinks and sources and the unresolved processes trend. In this application, LST gradients are forced by breaking wave projections, no sediment sinks and sources are considered in order to define a do-nothing management strategy and the unresolved processes trend is obtained through data-assimilation during the calibration and validation period.

In order to couple longshore, short-term cross-shore fluctuations and long-term cross-shore evolution, the approach consists of modelling the total (observed) shoreline Y as the sum of the longshore shoreline position Y_l and the cross-shore shoreline position Y_c, as shown in equation 3.4. The cross-shore shoreline position is calculated following Toimil et al. (2017a) based on Miller and Dean (2004) model. The cross-shore evolution accounts for short term effects due to storms and seasonal wave-climate variations, and long-term shoreline response to SLR. This is achieved by including in the cross-shore equilibrium position Y_{eq} the shoreline retreat due to an increase in water level (R_{SLR}) evaluated according the Bruun's response (Bruun, 1962), $R_{SLR} = \frac{SLR}{tan\beta_n}$ where $tan\beta_n$ is the nearshore slope, which is calculated assuming an equilibrium Dean profile type following Dean (1991). The disequilibrium term in the cross-shore formulation is calculated based on the cross-shore shoreline position and the equilibrium shoreline position, both accounting for short-term effects and SLR retreat. Thus, the restoring

force in the equilibrium formulation does not diverge on time.

$$
\underbrace{\frac{\partial Y}{\partial t}}_{\text{Total shoreline change}} = \underbrace{\frac{\partial Y_l}{\partial t}}_{\text{Longshore shoreline changes}} + \underbrace{\frac{\partial Y_c}{\partial t}}_{\text{Cross-shore shoreline changes}}
$$

$$
\frac{\partial Y_l}{\partial t} = \underbrace{-\frac{1}{B+d_c}\frac{\partial Q}{\partial x}}_{\text{LST gradients}} + \underbrace{\frac{1}{B+d_c}q}_{\text{Sinks and sources of sediment}} + \underbrace{vlt}_{\text{Unresolved processes}} \qquad (3.4)
$$

$$
\frac{\partial Y_c}{\partial t} = \underbrace{K_c^{+/-}[Y_c^{eq} - Y_c]}_{\text{Cross-shore changes}}
$$

The longshore, short-term cross-shore and SLR coupling presented in this application is an intermediate approach between the uncoupled method of Vitousek et al. (2017c) and the fully coupled approach presented in Antolínez et al. (2019) or in Jaramillo et al. (2020). In the case of the uncoupled approach, the short-term cross-shore evolution is calculated just considering future waves, yielding a temporal evolution of erosion and accretion events, which is then linearly added to the SLR retreat and the longshore effects. The disequilibrium term in the cross-shore formulation is calculated between the short-term cross-shore position and the equilibrium position, which is obtained without considering LST gradients or SLR effects. In the case of the fully coupled approach, the observed shoreline position Y is directly the output of the equilibrium model. In this case, the disequilibrium term is calculated considering the equilibrium position (accounting for LST gradients and SLR effects) and the total observed shoreline position.

In spite of the different coupling strategies, all of them yield similar results. Only slight differences are noticed due to the one-step lagged response when coupling the different approaches in the equilibrium formulation solved using time-stepping schemes. These differences are negligible considering the erosive trend induced by SLR. On the other hand, for transects backed with rigid walls without accommodation space, the nearshore slope $tan\beta_n$ is substituted by the structure's slope so as to consider passive flooding due to SLR.

Raw model outputs at one transect for the RCP8.5 (15 time-series) are displayed in

Figure 3.6 while distinguishing the modelled RCMs with different line markers and the SLR-trajectories, representative of the IPCC likely range (Oppenheimer et al., 2019), with different colours. For instance, the shoreline response of the EART model projected waves and storm surge acting on top of the SLR trajectory of the 95% percentile is represented with a red line and square markers. Panels a) and d) in the figure show the time series at the periods 2040–2050 and 2090–2100. In the panels b) and c) it is represented a zoom in the period 2045–2046 of the 15 time-series in which the RCM variability and the SLR are highlighted. Similarly, panels e) and f) underline the RCM and SLR variability in the period 2095–2096. In panels b) and e) it is stressed the RCM variability by colouring the shoreline responses of the 5 RCMs for the SLR trajectory of the 50% percentile. On the other hand, in panels c) and f) it is emphasized the SLR variability corresponding to the three SLR trajectories for the same RCM (EART). In the period 2040–2050, the greatest source of uncertainty is linked to the RCM variability, as the SLR spread is less than 5 m. By the end of the century, in spite of the increase in variance of the RCM contribution due to episodic events (see for instance the peak of the IPSL model in 2095), the greatest source of uncertainty is due to the SLR trajectory (d'Anna et al., 2022b). This conclusion can be drawn from panel d), in which the shoreline responses are almost clustered by SLR trajectory or even from panels e) and f), where the SLR spread (around 8 m) is higher than the RCM spread (around 5 m).

3.3.3. Post-processed modelling outcomes

Coupling longshore and cross-shore processes allows for jointly resolving several temporal scales ranging from storm events to decadal shoreline changes. Projected shoreline evolution time series combine longshore processes, mainly driven by long-term LST gradients, and cross-shore processes due to short-term storm response and long-term SLR retreat. The long-term component of shoreline evolution (hereinafter referred to as structural) is used to calculate permanent retreats and beach area loses. Structural changes define the baseline condition at which the instantaneous shorelines oscillate due to alternative erosion and accretion short-term fluctuations. Additionally, non-

stationary extreme value analysis of shoreline change allows for identifying time-varying storm retreats at given occurrence probabilities throughout the century. In the upcoming subsections, valuable information for coastal managers is obtained by unravelling the modelled time scales.
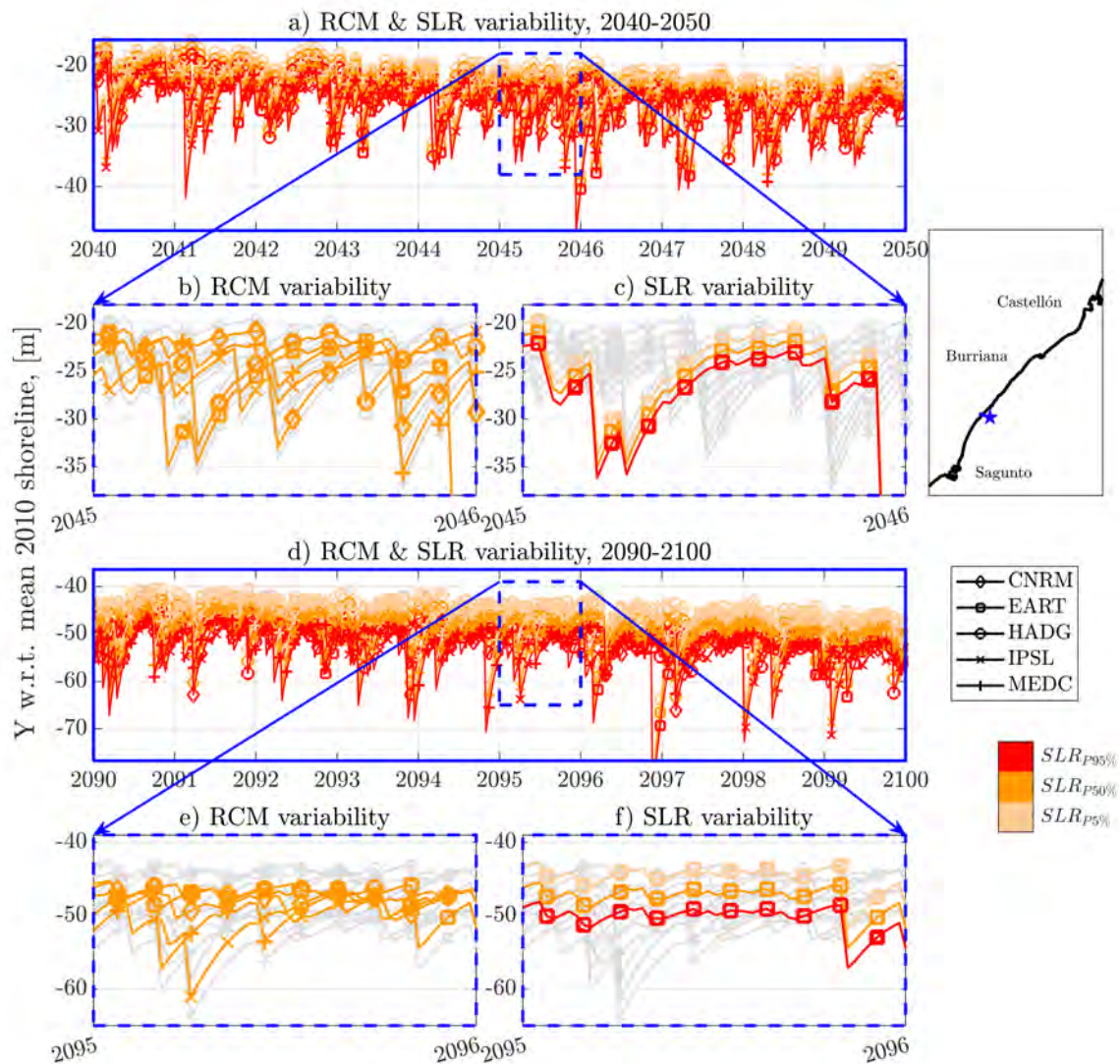
Figure 3.6: Shoreline evolutions at one transect located in Llosa beach calculated considering the different RCM configurations and SLR trajectories.

3.3.3.1. Structural changes in shoreline position

Short-term fluctuations are subtracted from shoreline change in order to obtain structural changes. Thus, the structural shoreline position at given dates is estimated by averaging previous modelled shorelines over a period of two years. Figure 3.7 shows the structural shoreline positions at two beaches in the study area, Mocófar (left panel) and Almenara (right panel). For the sake of comparison, three structural reanalysis shorelines (1995, 2010 and 2020) and two projected structural shorelines (2050 and 2100) for the scenario RCP8.5 are displayed. Projected structural shorelines are calculated by averaging the structural shoreline positions of the five RCMs and the three SLR trajectories. Results show that in 2050 and 2100, a coastal realignment between the cells bounded by groynes in Moncófar beach will be produced, which will tend to rotate counterclockwise sense to adapt to the incoming wave energy flux. Even though the compartmentalised coastline prevents sand migration, the rotation of the coastal segments together with shoreline retreat due to SLR are major threats for the first-line infrastructure in the absence of corrective interventions. In Almenara beach, current erosion problems (detailed in Chapter 2) will persist, as they will propagate southwards until the shoreline reaches an orientation almost perpendicular to the incoming wave energy flux.

Structural shoreline positions at 2100 for the scenarios RCP4.5 and RCP8.5 are used to calculate mean permanent beach retreats (top panel in Figure 3.8) and the area loss (lower panel in Figure 3.8) by taking the 2010 baseline shoreline as a reference. Mean beach retreats are obtained by averaging the projected retreats over the corresponding transects. The area loss is calculated from the projected beach area measured from the structural shoreline until the back-end of the beach accommodation space, which is usually limited by man-made features. Results show that, on average, end-of century mean retreat is around 50 m. However, this value is exceeded in beaches like Llosa or Almenara, where the sediment trapping infrastructures built to contain erosion on the northern beaches (Nules, Moncófar and Chilches) have a negative impact on the downdrift areas. Southern beaches exhibit smaller retreats, as sediment coming from

the North is blocked by the port of Sagunto. In spite of the accretive behaviour of these beaches, longshore processes will be overcome by SLR at the end of the century. In terms of loss of beach area only Llosa beach is likely to disappear by the end of the century. Due to coastal segmentation in small units bounded by hard structures, beaches like Torre, Nules, Moncófar or Chilches are likely not to disappear at the end of the century. However, as previously highlighted, exposure of nearby communities and assets will substantially increase due to shoreline reorientation and SLR retreat. Relative loss of beach area in Burriana, Corinto, Almardá, Canet and Sagunto is projected to be smaller due to the relatively large accommodation space created by the sediment retained by the downdrift structures.
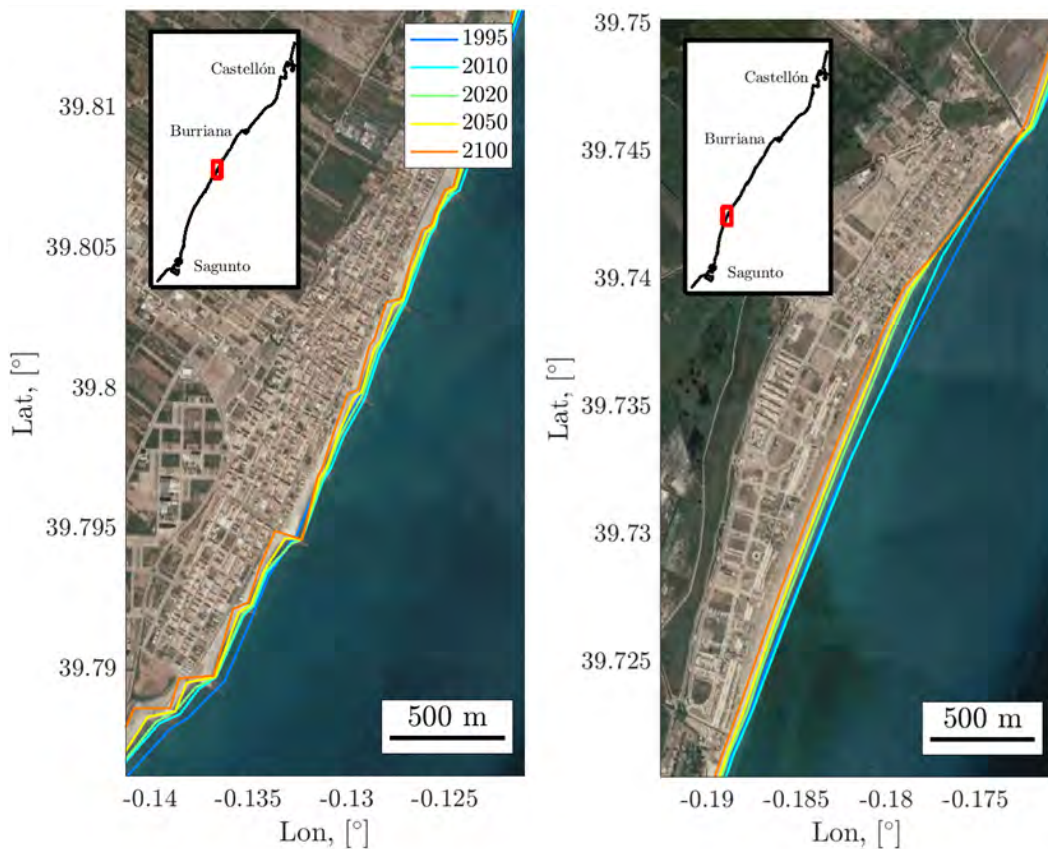
Figure 3.7: Structural shoreline positions at different dates in the beaches of Moncófar (left panel) and Almenara-Casablanca (right panel). Solid lines (1995 and 2010) correspond to the reanalysed shoreline position while 2050 and 2100 projections represent the mean of the RCM and SLR percentile shorelines for the RCP 8.5.
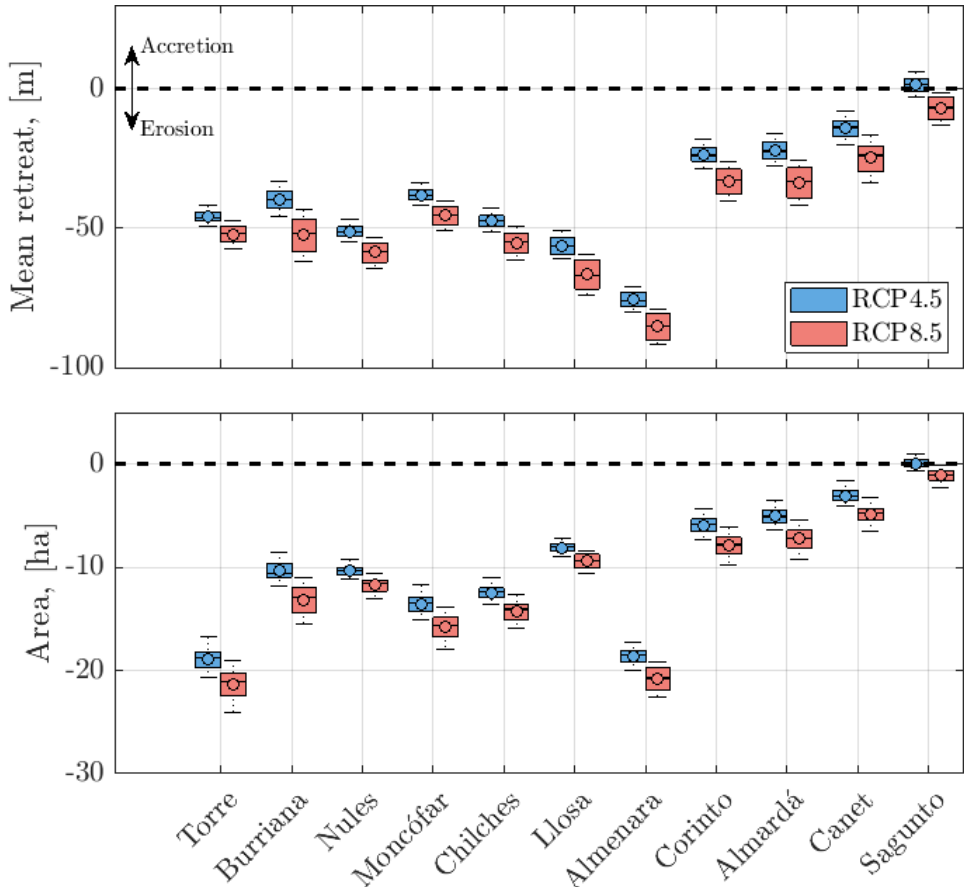
Figure 3.8: End-of-century structural shoreline retreats and relative beach area losses with respect to the 2010 baseline shoreline for the RCPs 4.5 and 8.5. Box whiskers synthetize 15 values corresponding to the different RCM and SLR percentile combination for each RCP.

3.3.3.2. Interannual changes in shoreline position

A key variable to assess the value of beach recreation services is the effective beach width during the tourist season. Thus, tourist season (May to September) shoreline positions in 2050 and 2100 are calculated by averaging tourist shoreline position during the two preceding years. Results shown in Figure 3.9 highlight that the effective beach width during the tourist season will be dramatically reduced by the end of the century. This fact will certainly have a negative impact on the recreation value of beaches and provides useful information for further analysis. A specific assessment should account for the fact that models project an increase in mean and extreme temperature and an important reduction in precipitation that may shift or extend the tourist season beyond its present length.

Figure 3.9: Tourist season shorelines (May, June, July, August, September) for 2050 and 2100 in Torre (top panel), Moncófar (middle panel) and Almenara (lower panel). Solid lines represent the median and the bands correspond to the 50% confidence interval of the 15 RCM and SLR percentile configuration for the RCP8.5.

3.3.3.3. Contribution of individual processes to shoreline change

With the purpose of identifying the contribution of different modelled components to shoreline change, a variance analysis is carried out in which the process explained variance relative to the total shoreline variance is quantified similarly to other studies in the literature (Vitousek et al., 2017c; Vousdoukas et al., 2020b). Figure 3.10 shows the fraction of total shoreline variance explained by each of the individual modelled processes (longshore, short-term cross-shore and SLR) in the period 2020–2100 for the RCPs 4.5 and 8.5 and the associated uncertainty. It is noticeable that longshore processes and SLR are the main contributors to shoreline change (Table 3.2). The relative contribution of SLR increases under the RCP8.5 with respect to the RCP4.5. In this sense, average longshore transport contribution in the study area reduces 45 % and cross-shore transport contribution decreases 70% in favour of the SLR contribution, which increases by 34% in the RCP8.5 with respect to RCP4.5.

[%]	RCP4.5			RCP8.5		
	Longshore	**Cross-shore**	**SLR**	**Longshore**	**Cross-shore**	**SLR**
Torre	22, (18-26)	42, (34-48)	35, (26-43)	16, (11-26)	26, (14-44)	58, (41-69)
Burriana	18, (8-26)	26, (19-35)	57, (49-63)	10, (3-14)	13, (7-24)	77, (62-89)
Nules	43, (20-58)	25, (18-40)	32, (23-44)	31, (12-42)	16, (10-26)	54, (38-77)
Moncófar	45, (24-58)	27, (19-41)	28, (21-39)	33, (15-44)	17, (11-28)	50, (34-72)
Chilches	56, (36-67)	27, (14-31)	28, (21-39)	42, (22-53)	12, (8-21)	46, (31-69)
Llosa	36, (24-45)	20, (14-28)	44, (38-52)	22, (12-29)	11, (6-20)	67, (52-81)
Almenara	7, (6-8)	32, (24-40)	61, (54-69)	4, (3-5)	16, (8-30)	81, (66-89)
Corinto	8, (7-10)	46, (37-55)	46, (38-54)	5, (4-7)	26, (14-46)	69, (49-81)
Almardá	4, (3-5)	43, (33-53)	54, (44-63)	2, (2-3)	22, (12-41)	76, (56-87)
Canet	19, (13-23)	40, (32-51)	41, (35-48)	12, (8-16)	23, (13-42)	64, (46-79)
Sagunto	25, (20-30)	39, (31-48)	36, (29-43)	17, (13-23)	24, (13-43)	59, (41-73)

Table 3.2: Relative contribution of different processes to shoreline change for the RCPs 4.5 and 8.5. The first value represent the median while the values in brackets are the minimum and maximum value of the different RCMs and SLR trajectories.

This information is key for coastal planning, as the different coastal processes require different adaptation measures. While short-term cross-shore sediment transport may require episodic interventions after storms and/or early warning systems, longshore transport may be tackled through long-term sediment management strategies, the restoration of natural ecosystems or grey engineering solutions. On the other hand, SLR-induced

sediment transport can be managed in anthropized environments by means of nature based solutions like nourishments, the suppression of man-made coastal invasions or the construction of coastal defences.
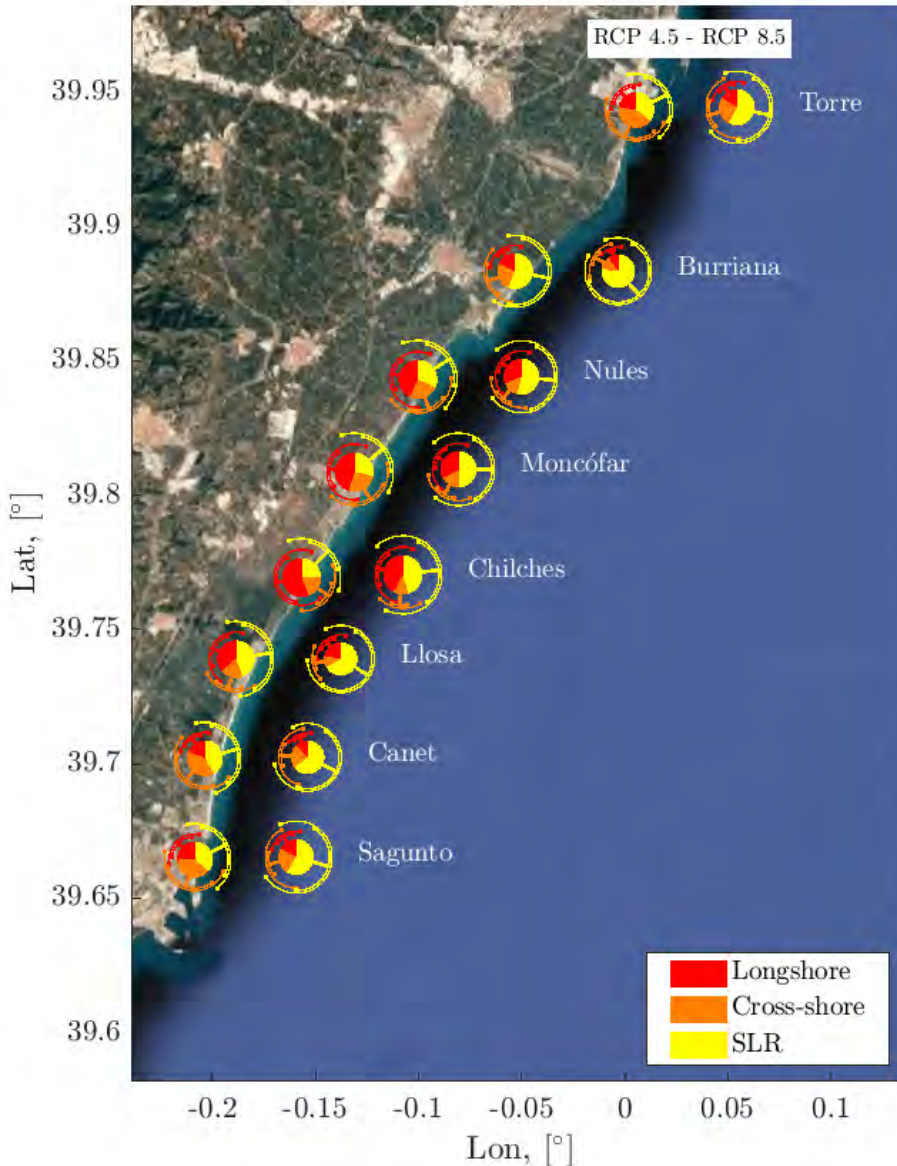
Figure 3.10: Relative contribution of different modelled processes to the total shoreline variance for the RCPs 4.5 and 8.5 in the main beaches. Circular sectors represent the median considering the different RCM and SLR percentile combinations for each emissions scenario. RCM and SLR percentile uncertainty is represented by two concentric circular arcs to each sector, which display the maximum and minimum relative contribution of each process to the total shoreline variance.

3.3.3.4. Non-stationary extreme-value analysis of shoreline retreat

In this case, advantage is taken from IH-LANS capability of jointly modeling long and short–term behaviour to analyse storm extreme retreats. Future shoreline evolution is a non-stationary process as structural changes behave as a trend. Therefore, storm retreats are analysed following the non-stationary methodology described in Mentaschi et al. (2016) and depicted in Figure 3.11. Basically, the methodology consists of transforming shoreline time series $Y(t)$ into a normalised stationary variable $x(t)$ so as to apply stationary extreme value analysis. A shoreline time-series is transformed as follows:

$$x(t) = \frac{Y(t) - T(t)}{C(t)} \tag{3.5}$$
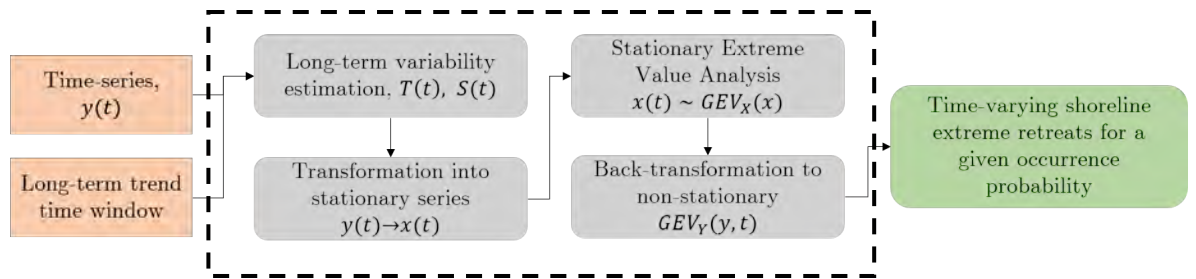
Figure 3.11: Transformed stationary methodology to perform non-stationary Extreme Value Analysis of shoreline change. Adapted from Mentaschi et al. (2016).

where $T(t)$ is the long-term slowly-varying trend of the series and $C(t)$ is the long-term slowly varying amplitude of an interval representing the amplitude of the distribution of $Y(t)$. The trend $T(t)$ represents the baseline (structural) shoreline position due to long-term changes, and accounts for longshore processes (Y_l) and cross-shore SLR-retreat (R_{SLR}). Due to the coupling strategy between longshore and cross-shore processes, discussed in subsubsection 3.3.2.2, the baseline $T(t)$ differs from the equilibrium shoreline position of the cross-shore model Y_{eq}.

Thus, $T(t)$ is calculated via a 5-year running mean and $C(t)$ is estimated through a smoothed 5-year running standard deviation. Annual maxima from the stationary time series are sampled next and fitted to a GEV (Generalized Extreme Value distribution). Then, by inverting expression 3.5, the non-stationary extreme value distribution of annual shoreline maxima is obtained.

Application of the non-stationary extreme value distribution is shown in Figure 3.12. Time-varying 5 and 50–year return period storm retreat for the RCP8.5 are displayed together with the baseline shoreline $T(t)$ with respect to the 2010 shoreline at three different transects. For the sake of clarity, instead of representing the 15 trajectories of return periods and baseline shorelines $T(t)$ of each combination of RCM and SLR trajectories, the median values and the 50% confidence band are chosen for visualisation.
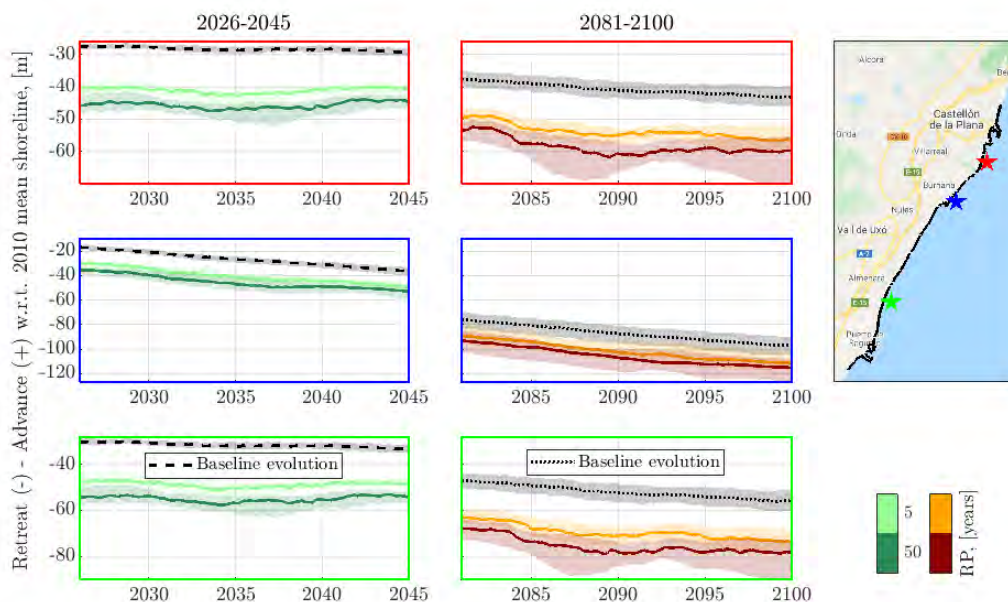
Figure 3.12: Non-stationary extreme retreats calculated at three different transects for the RCP8.5. The black dashed/dotted line corresponds to the median baseline of the period 2026–2045/2081-2100. Solid lines represent the median and the shaded area corresponds to the 50% confidence band of the 15 RCM and SLR percentile configurations for RCP8.5. The top right panel shows, with coloured stars, the location of the different transects.

While in the 2026–2045 period, the median 5-year return period retreat varies between 10 and 20 m, the median 50-year return period retreat ranges from 15 to 30 m with respect to the median baseline shoreline in the study area. In the period 2081–2100, median extreme retreats, with respect to the median baseline shoreline do not show much variation. However, the 50% percent confidence band increases at the end of the century and the baseline shoreline moves onshore due to the effects of SLR.

In order to geographically allocate the magnitude of future extreme retreats, Figure 3.13 shows the spatial representation of the 5 and 50–year return period shoreline position together with the baseline at 2045 and 2100. It is clearly shown that storm-related retreats may reduce to a minimum the available beach area at 2045. By the end of the century, first-line infrastructure will likely be surpassed by extreme events due to the shoreward migration of the baseline associated with long-term retreats.
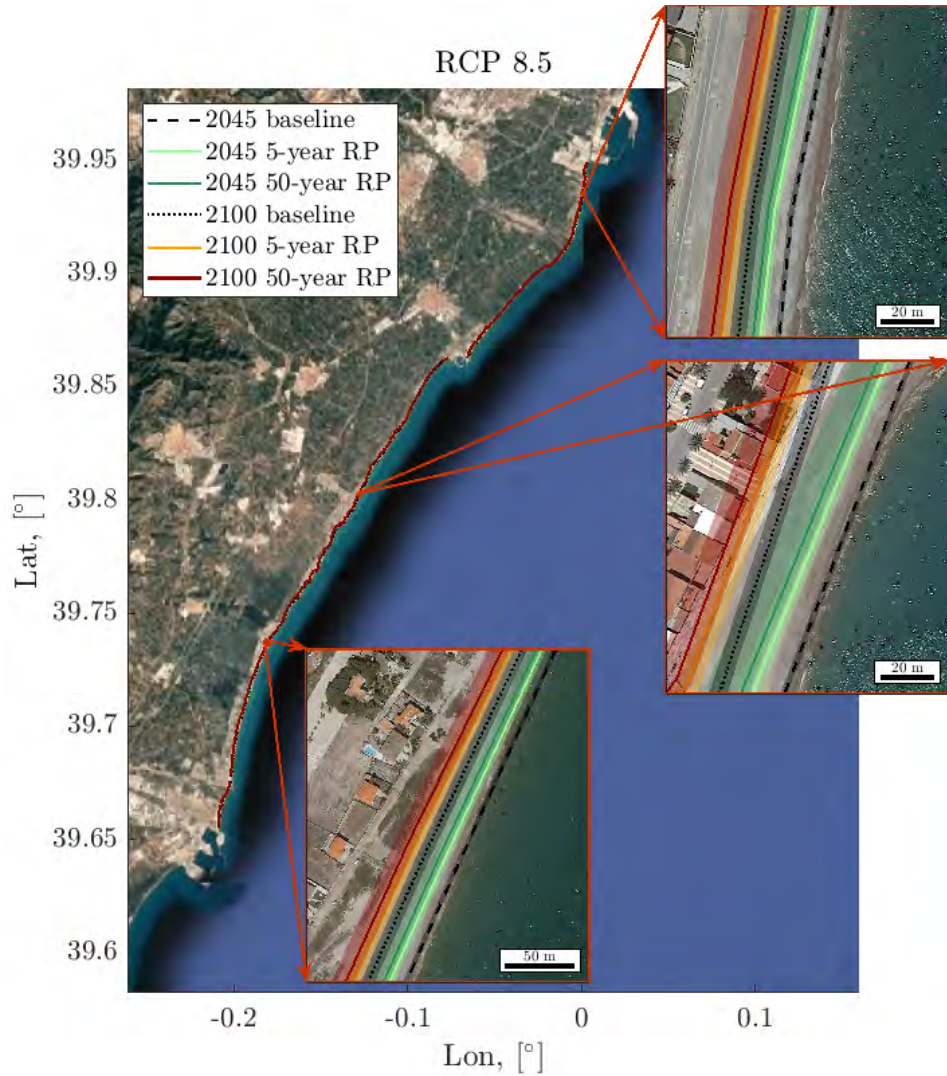
Figure 3.13: Spatial representation of the 5-year and 50-year return period shoreline retreats in 2050 and 2100 for the RCP8.5. Solid lines represent the median and the bands correspond to the 50% confidence interval of the 15 RCM and SLR percentile configuration for the RCP8.5.

3.4. Conclusions

The proposed methodology provides a mean of quantifying the uncertainty in shoreline projections, which is necessary for coastal management and adaptation at long-term time scales. In order to assess climate-related risks in coastal areas, projections of coastal impacts are essential. To this end, the reference dates are the mid-century (2050) and the end-of-century (2100). End-of-century shoreline projections are inherently uncertain for many reasons, including our poor understanding of the system itself, uncertainties regarding climate scenarios or the unknown nature of the future management strategies. However, assessing future (uncertain) scenarios at reference temporal horizons is relevant for identifying hotspots and for benchmarking different coastal adaptation pathways that need to be planned for the long run but soon enough to anticipate future climate change threats.

In an attempt to quantify and/or reduce the uncertainty associated with the shoreline projections, a methodology considering climate change-induced uncertainty in future waves and water levels has been presented. Although just forcing drivers uncertainty is tackled, the methodology can be easily adapted to account for different transport formulations and parametrizations to better characterize the uncertainty cascade, as in Toimil et al. (2021a). Starting from dynamically downscaled and bias-corrected offshore waves from different climate models for various emissions scenarios, an efficient hybrid nearshore propagation technique that accounts for time varying water levels while considering all relevant physical processes is introduced. High-resolution space-time projections of nearshore waves and water levels are used to drive a reduced-complexity shoreline evolution model that solves longshore and cross-shore transport while accounting for the effects of different man-made structures. Thanks to the multiple processes included in the reduced-complexity shoreline evolution model, outcomes at multiple temporal scales are derived. The proposed modelling strategy offers a great promise for analysing the effects of different adaptation actions on shoreline change.

The methodology is applied to a highly anthropized 40 km stretch along the Spanish

Mediterranian coast. Ensemble shoreline projections considering the uncertainty related to two concentration scenarios (RCPs 4.5 and 8.5), five regional climate models and three mean sea level rise trajectories associated with the 5, 50 and 95% percentiles, are obtained. Structural retreats, seasonal variability of the shoreline position, contribution of modelled components to shoreline change and time-varying extreme retreats are calculated. Results show that, in the absence of adaptation or new interventions, by the end of the century, SLR retreat will compensate accretion at the upstream of large ports and all beaches will retreat for the RCP8.5, being SLR and longshore processes the main shoreline change drivers. In spite of the numerous sediment-trapping structures, sediment-starved beaches at the lee of large ports (Castellón and Burriana) will loose between 50 and 100% of their beach surface, retreating between 50 and 100 m with respect to the 2010 baseline shoreline. Non-stationary extreme retreats associated with storms, in an already inland-shifted baseline shoreline, will likely reach most of front line infrastructure (houses and promenades) by the end of the century, if no adaptation actions are undertaken.

In this application, single process parametrizations and stationary free-model parameters are considered. However, drivers uncertainty may be combined with different process formulations and better parametrizations in order to produce more robust and reliable shoreline projections.

CHAPTER 4

APPLICATION OF IH-LANS TO FORECAST EROSION-ENHANCED FLOODING

Flooding and erosion are the most relevant hazards for coastal regions and although they are linked, their inherent complexity has led to them commonly being addressed separately, potentially leading to highly uncertain estimates. In order to make progress in this area, this Chapter addresses three topics: a) the development of a methodology to upscale one-dimensional shoreline changes from reduced-complexity models to two-dimensional topobathymetries for flooding studies; b) the quantification of the effects of neglecting the flooding and erosion coupling on future projections, and c) the analysis of the relative importance of climate-related uncertainty sources on coastal flooding (Figure 4.1). For that purpose, a suite of statistical, process-based and physics-based models is tuned to generate and downscale storms, compute the hydrodynamics affected by short- and long-term profile changes and propagate flooding over erosion-enhanced topobathymetries accounting for longshore, SLR and and storm-driven changes. Cli-

---

[1]This Chapter is based on Toimil, A., Alvarez-Cuesta, M. and Losada, I. J. 2022. Neglecting the coupled effect of coastal flooding and erosion can lead to spurious impact projections and maladaptation. *Under review in Coastal Engineering.* Submitted on April 2022.

mate uncertainty is sampled by considering the storm variability through statistical modelling, two different radiative forcing scenarios, five configurations of global and regional climate models and three sea-level rise trajectories.
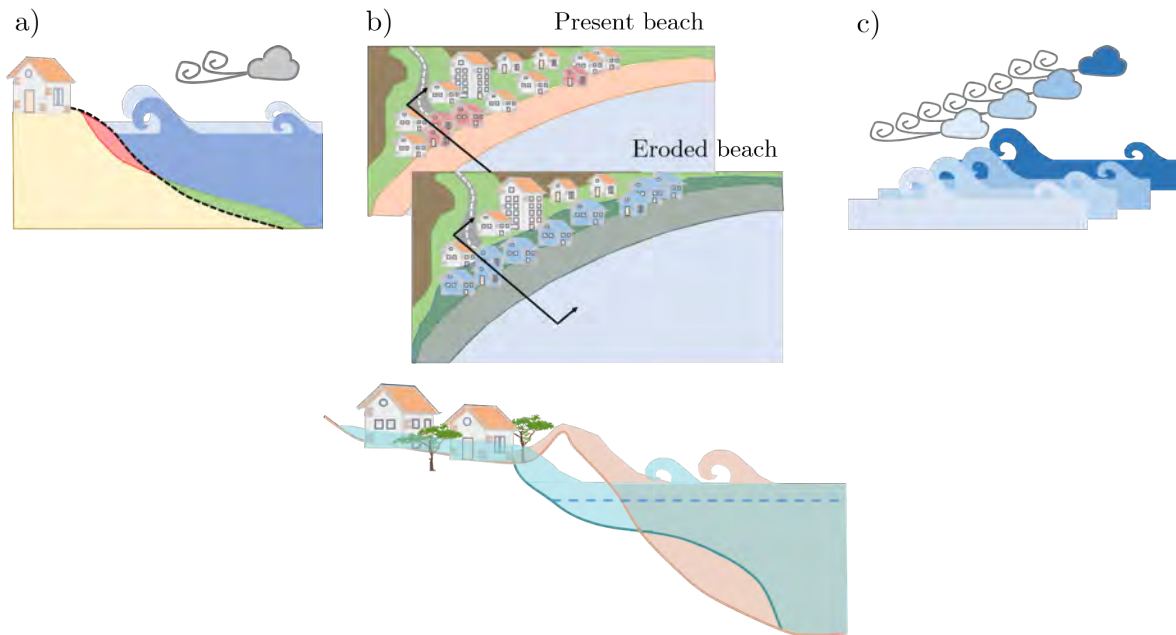
Figure 4.1: Graphical representation of the topics addressed in the Chapter.

4.1. Introduction

The need for jointly modelling coastal flooding and erosion is widely recognised in the literature (e.g. Pollard et al. (2019); Lentz et al. (2016)) as the flooding risk is conditioned by the protection capacity of the natural environment, i.e. the morphological state of beach-dune systems (Leaman et al., 2021). The main challenge when coupling both impacts is related to the temporal scale at which both impacts interact, which is controlled by their driving mechanisms and is prone to be altered by climate change (Toimil et al., 2020a; Ranasinghe, 2016). While flooding events are episodic, morphological changes are related to both episodic and long-term temporal scales. At short time-scales, extreme events due to waves and storm surges are the main drivers of coastal flooding and erosion. These events are expected to increase in frequency mostly due to sea-level rise (Vitousek et al., 2017a) and are likely to change in intensity due to the effects of climate change (Lobeto et al., 2021a; Muis et al., 2020). On medium

time scales (months to years), oblique wave attack triggers longshore transport whose gradients generate chronic erosion and accretion areas in open beaches and beach rotation of pocket beaches (Jaramillo et al., 2021); finally leading to a spatial time-varying change of the flood protection service provided by beaches. On longer time-scales (years to decades), SLR will induce shoreline retreat (Nicholls and Cazenave, 2010; Cazenave and Cozannet, 2014) and profile readjustments (Bruun, 1962) that in some circumstances (lack of accommodation space, dune retreat, encroaching, ...) may lead to a lowering in the natural defence crest elevation (McCarroll et al., 2021); increasing flooding exposure. For these reasons, it seems thus essential to account for the multiscale dynamism of the morphodynamic system when developing accurate flooding projections (Lentz et al., 2016).

Adding up to the temporal scale problem, the spatial scale required for coastal adaptation decisions spans from tens to hundreds of kilometres and modern risk-based planning frameworks require appropriate climate-related uncertainty sampling that implies multiple impact model runs (Ranasinghe, 2016). A model capable of jointly solving the combined effect of flooding and erosion at the spatiotemporal scales of interest while being computationally compatible for probabilistic frameworks has not being developed. Consequently, a modelling chain composed of reduced-complexity physics-based models, statistical models and process-based models is currently the best solution by looking at the compromise amongst physical processes, scales, efficiency and accuracy.

The coupled flooding and erosion problem was first addressed for short temporal scales thanks to the development of process-based models like Delft3D (Lesser et al., 2004) or XBeach (Roelvink et al., 2009) that solve hydrodynamics, sediment transport and bed update. Applications of such models in forensic studies that characterise the impacts of storms are abundant. For instance, McCall et al. (2010) used XBeach to simulate 2DH overwash morphology on a portion of a barrier island in Santa Rosa (Florida) during hurricane Ivan (2014). Gharagozlou et al. (2020) used XBeach nested to ADCIRC (Luettich et al., 1992) to reproduce morphodynamics and inundation in the North Carolina Outer Banks during hurricane Isabel (2003). Their findings revealed the need

for integrating morphodynamics in large scale flooding modelling and strengthening model couplings. On the other hand, van Ormondt et al. (2020) coupled XBeach and Delft3D to model the yearly evolution of a breach on eastern Fire Island (New York) after its formation during hurricane Sandy (2012). The novelty of the coupling is that Delft3D was used to simulate calm conditions while XBeach was employed to simulate the coastal response to extreme events. 2DH hydro-morphodynamic simulations were also used in the context of climate change or to project the coastal response. Passeri et al. (2018) simulated the hydrodynamic and morphodynamic impact of hurricanes Ivan (2004) and Katrina (2005) in Dauphin Island under present and future sea levels without considering long-term morphodynamic changes. Similarly, Grases et al. (2020) studied the short-term hydro-morphodynamic response in a beach of the Ebro Delta (Spain) considering current and future synthetic storms. They simulated the coastal response for the RCP8.5 and the 90% SLR percentile in 2050 and 2100 with a set of future storms generated with the copula-based emulator of Lin-Ye et al. (2017). Recently, Sanuy and Jiménez (2021) proposed a response-based approach to model coastal flooding and erosion using XBeach 2DH related to past-observed storms in the Tordera Delta (Spain). Long-term changes were considered by horizontally translating the profile using observed shoreline trends. While McCall et al. (2010); Gharagozlou et al. (2020); van Ormondt et al. (2020) are examples of forensic studies of short-term hydro-morphodynamic modelling, Sanuy and Jiménez (2021) extended the approach to forecast the coastal response using past storms and medium-term morphodynamic changes from observed shoreline trends and Passeri et al. (2018); Grases et al. (2020) introduced climate change only through the inclusion of SLR but neglecting long-term morphological changes. In all these studies, no multi-scale coupling between coastal erosion and flooding was considered and they lacked appropriate climate-related uncertainty sampling.

Few studies have integrated long-term morphodynamic changes on coastal flooding. Benavente et al. (2006) modelled flooding in Valdelagrana spit and marshes (Spain) using a flood extent model that was underlined by a terrain model updated using rates of shoreline change from aerial photographs. They highlighted the importance of long-

term shoreline retreat trends in the prediction of coastal flooding due to the variation in exposure to sea storms. More recently, Stripling et al. (2017) used a one-line model to adjust the seawall and toe levels and calculate overtopping rates to be used as forcing in a 2D flood model (RFSM, (Gouldby et al., 2008)) to produce storm-induced flood maps. Some studies have also incorporated climate change effects. Dawson et al. (2009) developed a methodology to integrate shoreline changes into flood projections for the 21st century on the East Anglian coast (UK). The authors connected coastal flooding and erosion in an indirect way, by introducing changes in the shoreline position (modelled with SCAPE (Walkden and Hall, 2005) and a one-line model) into the probability of failure of flood defences for several SLR scenarios. More recently, Passeri et al. (2015, 2016) studied the influence of incorporating long-term shoreline changes into hydrodynamic modelling and inundation along the northern Gulf of Mexico under future SLR scenarios. In the first case, they considered the impact of several hurricanes and a single SLR scenario; in the second, they evaluated variations in tidal amplitudes for different SLR scenarios and projected future shoreline changes and dune heights using a Bayesian network model (Gutierrez et al., 2011). In both studies, beach profiles were translated upwards by the amount of SLR and horizontally by the amount of projected erosion and accretion while maintaining shape. Recently, Grilli et al. (2017) assessed coastal flood risks in Charlestown (Rhode Island) associated with the 100-year return period storm, including the effects of SLR and dune erosion. The topography was updated by replacing the current dune profile with an empirical storm profile shifted landwards and upwards to account for episodic dune erosion and long-term shoreline retreat, respectively. Flood maps were obtained by a static inundation method based on GIS interpolation. Finally, within the Coastal Storm Modelling System (CoSMoS) Project, Barnard et al. (2019) presented a modelling approach to estimate climate change-driven changes in coastal flood exposure along the coast of California. GCM-driven projections were used to force a suite of oceanographic, hydrodynamic and geomorphic models to predict coastal waves, water levels, flooding and erosion for different SLR and deterministic storm scenarios over the 21st century. Projected long-term estimates of shoreline change (obtained with the CoSMoS-COAST model, (Vitousek et al., 2017c)) and cliff retreat (Limber et al., 2018) were employed to translate cross-shore profiles

upwards and landwards (Erikson et al., 2017). Flooding extents were mapped by spatially interpolating the water excursion calculated at the transects using 1D XBeach simulations. In spite of the comprehensiveness of the approach, uncertainty sampling was very limted both in terms of the dynamics used (range of SLR trajectories and projections of a single GCM for one RCP) and in terms of their statistical treatment, as storms were directly obtained from one single realisation of the GCM-projected time series. Furthermore, profile kinematics used to update the topobathymetry were applied at real profiles but using translation magnitudes obtained from theoretical profiles.

In this Chapter, a methodology to elaborate erosion-enhanced flooding projections at all the relevant scales at which these impacts interact is proposed. The influence of long-term profile displacements and storm morphodynamics is evaluated on the total water level and on the flooded area. The importance of the erosion-flooding coupling is analysed at all the relevant temporal scales by comparing the full coupling (long- and short-term), the long-term coupling and the short-term coupling alone and the no coupling at any scale. The methodology, which includes a series of process- and physics-based models, integrates the climate-related uncertainty by considering future storm variability from different RCPs and RCMs in combination with different SLR trajectories. Focusing on 2005, 2050 and 2100 as target horizon years, the uncertainty contribution of the climate-related drivers (RCMs and SLR) and the erosion-flooding coupling approach on the total water level and flooded areas total uncertainty is quantified.

4.2. Overview of the methodology

In order to include the nearshore morphological changes into flood projections, a modelling chain composed of statistical and process-based models is constructed. The numerical domain needs to be carefully defined so as to suit the needs of every process-based model. First, the computational grid for the 2D wave propagation model needs to be specified considering the location of the offshore forcing points at which to apply the statistical model for the synthetic storm generation. Nested grids may be required de-

pending on the spatial resolution of the coarse domain. A low-resolution (LR) transect-based discretisation is established in order to run the erosion model IH-LANS described in Chapter 2 and to execute a short-term hydro-morphodynamic model used for the total water level (TWL) calculation, an example is shown in Figure 4.2. An additional high-resolution (HR) transect-based discretisation is also generated to transfer morphological changes calculated in the LR discretisation to the digital terrain model. This finer discretisation is needed because the spacing of the LR transects ($\mathcal{O}(100\,m)$) is not compatible with the spatial resolution of the digital terrain model used for flood modelling ($\mathcal{O}(5\,m)$). Reducing the spacing of the LR transects may hamper the fulfilment of the Courant condition for the longshore module in IH-LANS and will dramatically increase the computational cost of the hydro-morphodynamic TWL simulation with XBeach (Roelvink et al., 2009). Thus, a finer HR discretisation is needed to match the digital terrain model resolution. A communication interface between LR and HR transects is established through a distance-based interpolation.
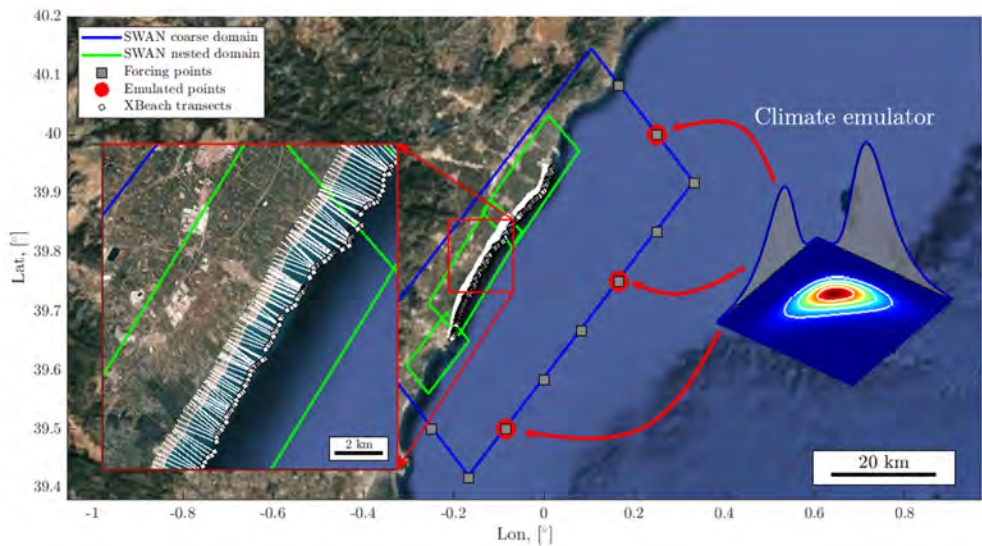
Figure 4.2: Computational domain definition for the erosion-enhanced flooding methodology.

Once the computational domains are defined, the first step of the erosion-enhanced flooding methodology consists of collecting wave and water level data. To this end, dynamically downscaled and bias corrected waves and storm surges (IHCantabria, 2020),

astronomical tides and SLR projections (Oppenheimer et al., 2019) are collected at the offshore boundary of the study area. Then, in order to consider every plausible combination of wave dynamics and water levels that are representative of future storms, a storm emulator is inferred and used to generate a sample of synthetic extreme events. The core of the storm emulator is an statistical module capable of modelling linear and circular variables at several forcing points while preserving the multivariate and spatial dependence structure and seasonal non-stationarity, (second step in Figure 4.3).

The third step consists of the total water level (TWL) modelling. In this case, in order to use process-based models while achieving a similar computational efficiency of empirical approaches for TWL estimation (Stockdon et al., 2006; Gomes da Silva et al., 2018), a transect-based metamodel has been tuned. To this end, from the whole sample of synthetic extreme events characterised by wave and water level data at the boundary forcing points, a representative subset is chosen via the maximum dissimilarity algorithm (Camus et al., 2011). Then, the subset of storms is propagated nearshore using the spectral wave model SWAN (Booij et al., 1999). The wave and water level data is gathered at the offshore points of the LR transects and then used to feed the 1D XBeach model (Roelvink et al., 2009) run in surfbeat mode. Radial basis functions (RBFs) are subsequently fitted to describe the relationship between the offshore wave properties of the selected storms and the corresponding dynamic wave set-up (DWS) at every transect. DWS is defined as the sustained elevation of the water level due to the transference of wave-related momentum to the surfzone (static set-up) plus a long-period oscillating component due to infragravity-wave energy. Once fitted, the RBFs are used to obtain the DWS associated with the complete set of synthetic storms at every transect. The last step of the TWL metamodelling consists of obtaining the n-year return period TWL as $TWL_n = (DWS + AT + SS)_n + SLR$, where $(DWS + AT + SS)_n$ is the n-year return period TWL without SLR from a generalised extreme value distribution (GEV) fit.

The fourth step is the sediment transport modelling and the topobathymetry update. IH-LANS shoreline projections developed in Chapter 3 are used to generate future topobathymetries. The long- and short-term shoreline positions are processed to feed the
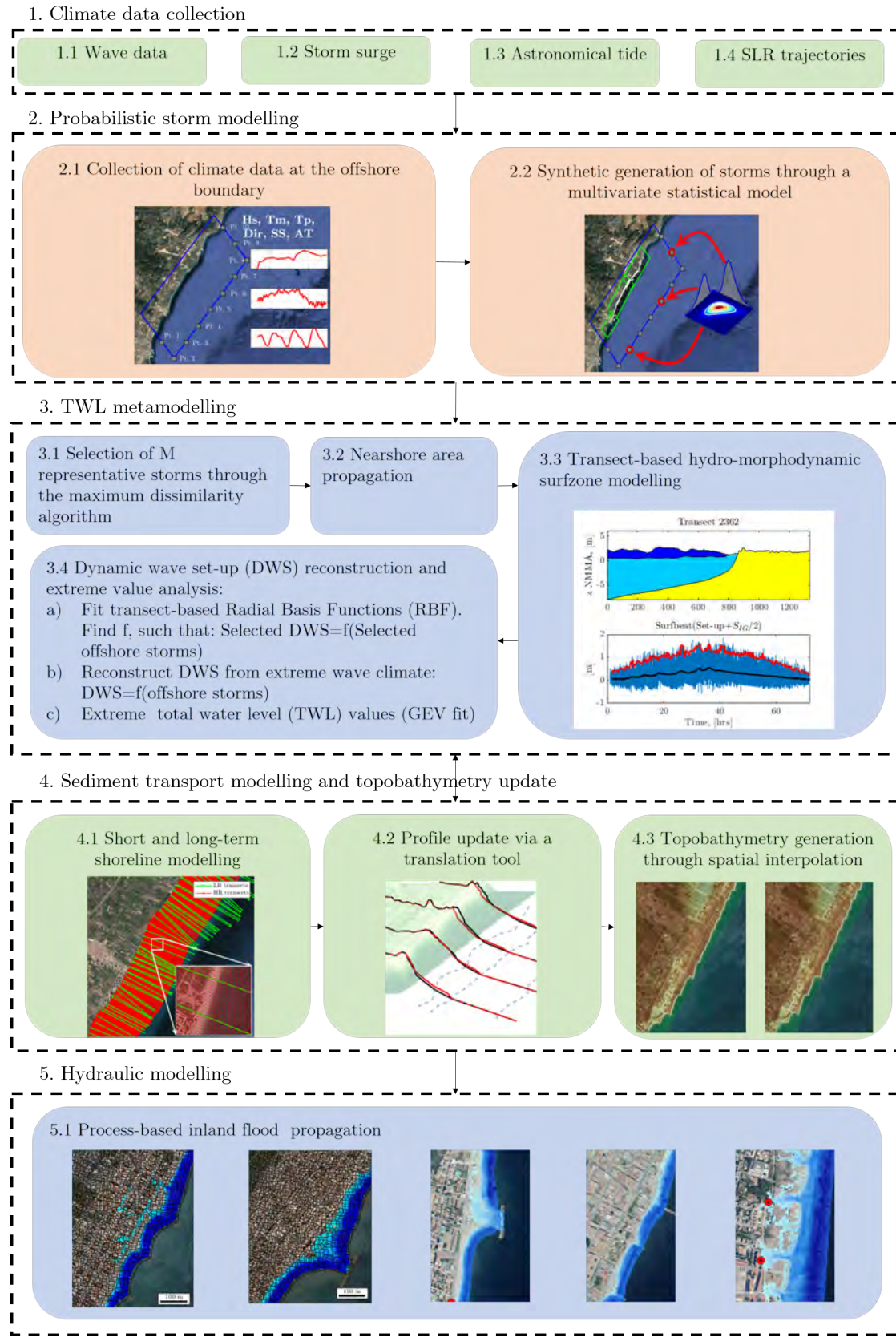
Figure 4.3: Flowchart of the erosion-flooding coupling methodology.

profile translation model ShoreTrans (McCarroll et al., 2021) to generate a cloud of points that yield the nearshore morphology surface by interpolation. It is worth mentioning that steps three and four are linked (highlighted with a double arrow in Figure 4.3), as the long-term updated profiles are used to feed the hydro-morphodynamic model and calculate the TWL. Additionally, XBeach can be run considering the morphodynamic evolution so as to jointly include the long- and short-term morphological changes on the TWL calculation.

The fifth step comprises the hydraulic modelling of flood propagation. TWL_n obtained at every LR transect are used to force the 2D flood model with sub-element topography RFSM-EDA (Jamieson et al., 2012). RFSM-EDA is an efficient process-based model that solves a simplified version of the full Saint-Venant equations in a non-uniform computational mesh that adapts to terrain features and accounts for spatially-varying bed roughness effects.

In the upcoming sections, the main novelties of the erosion-enhanced flooding methodology, which are the probabilistic storm model for regional-scale application and the topobathymetry update from reduced-complexity model outputs are further detailed.

4.2.1. Probabilistic storm modelling

In the literature, several studies have proposed multivariate statistical models to increase the population of physically possible storms (due to waves and storm surges) that could drive coastal flooding (Heffernan and Tawn, 2004; Wahl et al., 2016; Sayol and Marcos, 2018; Lin-Ye et al., 2016; Lucio et al., 2020). These studies stand apart from the widely spread simplifying assumption that the maximum realisations of individual TWL variables or their potential extreme combinations have already been observed. Amongst the different multivariate statistical approaches, copula-based methods are widely used as they allow to fit the marginal distribution and the dependence structure between different variables independently (Salvadori and De Michele, 2004). However, one of the greatest challenges in stochastic climate emulations is the determination of the dependence structure between linear-scale variables (e.g. wave height, wave period,

storm duration) and circular-scale variables (e.g. wave direction). In copula-based models, it is common practice to model circular variables through regression methods from the linear variables included in the copula (Lin-Ye et al., 2016), to perform a linearization of circular variables so as to be included in the copula model (Lucio et al., 2020) or to isolate the circular variables from the copula and infer their value via site-specific formulations from the linear variables in the copula (Wahl et al., 2016).

In spite of the variety of approaches to jointly model linear and circular variables, one major shortcoming of wave-climate emulators is that they cannot be applied to regional-scale applications as they are designed to emulate wave climate and water levels at one singular point in space. Due to the complexities of modelling the dependence structure between linear and circular variables, the generalization of state-of-the-art climate emulators to n forcing points is not straightforward. To overcome this limitation, a model that combines a monthly-scale multivariate emulator (MME) based on Gaussian copulas (Lucio et al., 2020) and a multivariate directional model (MDM) (Mardia et al., 2008) is proposed. The density function of the proposed multivariate model is:

$$
\begin{aligned}
f_{H_{s_{iw}}, T_{m_{iw}}, Dir_{iw}, SS_{iss}}&(H_{s_{iw}}, T_{m_{iw}}, Dir_{iw}, SS_{iss}) = \\
&= \underbrace{f(H_{s_{iw}}, T_{m_{iw}}, Dir_j, SS_{iss})}_{MME} \cdot \underbrace{f(Dir_{iw \neq j}|Dir_j)}_{MDM}
\end{aligned}
\tag{4.1}
$$

where H_s is the significant wave height; T_m is the mean wave period; Dir is the mean wave direction; SS is the storm surge; $iw \in [1, 2, \dots, n]$ are the wave director points; n is the total emulated points; iss is the storm surge forcing point; and j is the tie point between the MME and the MDM. Associated with each deep-water storm, we extract the peak period (T_p) and the astronomical tide (AT) by the application of a heterocedastic regression and by random choice from the harmonic reconstructed time series respectively (see Lucio et al. (2020) for more details).

The model represents a generalisation to n forcing points of the conditional relationship between linear and directional variables proposed by Wahl et al. (2016). The MME and MDM are coupled by means of a circular link variable j modelled in the MME,

from which the directions of the remaining director points ($iw \neq j$) are inferred using the MDM model. Importantly, this approach is valid provided that the link direction captures the dependence between the linear variables and the remaining emulated directions, which allows for limiting the conditional dependence modelled with the MDM to a single direction modelled in the MME. The MME-MDM emulator captures the seasonality of the storms through fitting the MME to the marginal variables monthly.
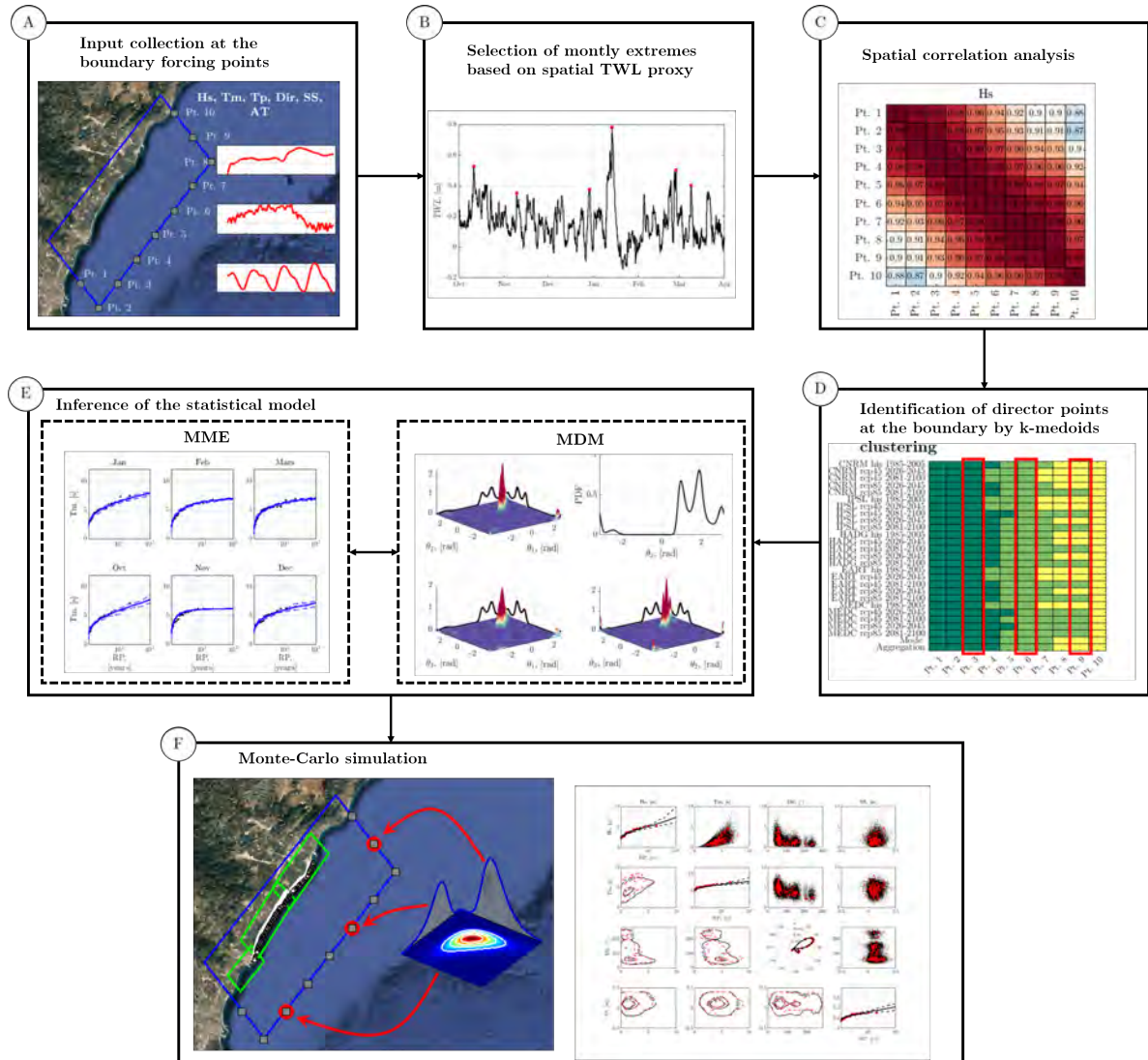
Figure 4.4: Workflow for the synthetic generation of storms.

The statistical model is fitted to every future scenario of wave climate and water levels following the methodology summarised in Figure 4.4. The first step consists of collecting wave conditions and water levels at locations near the outer contour of what is to be

the SWAN propagation grid Figure 4.4A. The second step comprises the design and application of a storm selection criterion Figure 4.4B. A simplified spatially-averaged $\overline{TWL}$ indicator is used and combines AT, SS, wave setup and infragravity swash, which is defined using the semi-empirical formulation of Stockdon et al. (2006):

$$\overline{TWL} = \frac{1}{nt} \sum_i^{nt} \left[AT_i + SS_i + (0.016 + 0.03)\sqrt{H_{0,i}L_{0,i}} \right] \tag{4.2}$$

where nt is the number of forcing points on the contour; H_0 and L_0 are the significant wave height and length in deep water, respectively.

The maximum monthly $\overline{TWL}$ values during the storm-dominated season of the study site and their corresponding forcing variables H_s, T_m, Dir, SS, AT are selected at the forcing points. This time window allows to have a number of extremes events large enough to ensure statistical robustness while representing actual storms. After selecting such maximum monthly $\overline{TWL}$ values, a correlation analysis is performed to check the intra-variable correlation between contour points and identify high-correlated groups (or clusters) (Figure 4.4C). This step allows for reducing the number of statistically emulated points so as to reduce the mathematical complexity of the problem.

The next step is the identification of director points or the points that are representative of a group of adjacent points (cluster points) by applying the K-means technique (Figure 4.4D). The choice of the number of clusters should consider the maritime climate of the area and the bathymetry. Provided that contour points are statistically similar (e.g., owing to little spatial variability in bathymetry and marine climate), the MME-MDM emulator is applied only to a reduced number of director points (2-4) and the multivariate interpolation is applied at the remaining points.

The following step entails the inference of the MME-MDM emulator (Figure 4.4E), which consists of obtaining the fitting parameters that best reproduce the statistical and interdependence relationships of the dynamic simulations of waves and storm surges. For this purpose, the MME is fitted by calculating the univariate distribution function

of each variable independently and the correlation matrix in the probability space $\mathbf{\Sigma}$. The distribution function for month l reads:

$$
\begin{aligned}
F_{(H_{s_{iw}}, T_{m_{iw}}, Dir_j, SS_{iss}, l)}(H_{s_{iw}}, T_{m_{iw}}, Dir_j, SS_{iss}) = \\
= \boldsymbol{C}(F(H_{s_{iw}}), F(T_{m_{iw}}), F(Dir_j), F(SS_{iss}); \mathbf{\Sigma}) = \\
= \boldsymbol{C}_\Sigma(\Phi^{-1}(F(H_{s_{iw}})), \Phi^{-1}(F(T_{m_{iw}})), \Phi^{-1}(F(Dir_j)), \Phi^{-1}(F(SS_{iss})))
\end{aligned}
\tag{4.3}
$$

where $F_{(H_{s_i w}, T_{m_{iw}}, Dir_j, SS_{iss}, l)}(H_{s_{iw}}, T_{m_{iw}}, Dir_j, SS_{iss})$ is the multivariate distribution function that jointly models significant wave height and mean period at director points iw, direction at point j and storm surge at point iss. The multivariate model is expressed by means of the marginal distributions $F(H_{s_{iw}})$, $F(T_{m_{iw}})$, $F(Dir_j)$, $F(SS_{iss})$ and the associated n-dimensional Gaussian copula $\boldsymbol{C}_{\mathbf{\Sigma}}$ inferred through the correlation matrix $\mathbf{\Sigma}$ of the different variables in the probability unit hypercube.

The parameters of the MDM are inferred using a mixture distribution composed of several multivariate mono-modal von Mises distributions following Equation 4.4. Through K-means and a circular distance metric, Dir is classified into as many clusters as mixing components and each cluster is fitted to a multivariate von Mises distribution. The number of mixing components should be set as a function of the predominant wave directions in the study region.

$$
f_{\boldsymbol{\theta}}(\boldsymbol{\theta}) = \sum_{i=1}^{k} p_i T_{\boldsymbol{\theta} i}(\boldsymbol{\theta})
\tag{4.4}
$$

where $\boldsymbol{\theta}$ is the direction vector $[Dir_1, Dir_2, \dots Dir_n]$; k is the number of directional mixing components; p_i is the probability of occurrence of each directional component; and $T_{\boldsymbol{\theta} i}(\boldsymbol{\theta})$ is the mono-modal multivariate von Mises distribution.

The last step is the synthetic generation of monthly extreme events that may cause coastal flooding (Figure 4.4F). Monte-Carlo simulation techniques are applied to emulate 100,000 multivariate storms for every future scenario. Random realisations of the MME ($H_{s_{iw}}$, $T_{m_{iw}}$, Dir_j and SS_{iss}) are subsequently coupled with the MDM through Dir_j, which also allows the remaining Dir_{iw} to be randomly determined based on the

conditional distribution from the MDM. Is then that the related T_p and AT are obtained. For the sake of readability, the mathematical inference of the multivariate model and the details regarding the Monte Carlo simulation are described in Appendix C.

4.2.2. Projecting the nearshore topobathymetry

Reduced-complexity modelling of coastal evolution implies that the complete morphological behaviour of the nearshore area is summarized in a reference variable (i.e. the shoreline position). This simplification allows for reducing the computational cost of reduced-complexity models with respect to process-based morphological models and increasing the temporal scale of the processes that can be studied. In contrast, even if the shoreline position is a relevant morphological magnitude, it cannot be directly used to model erosion-enhanced flooding. To overcome this problem, a novel method to translate the shoreline evolution into a digital terrain model, used as input in flooding models, is proposed.

The proposed method to generate future topobathymetries from reduced-complexity model outputs is depicted in Figure 4.5. After defining the present-day topobathymetry, the longshore shoreline position Y_l and the short-term cross-shore position Y_c are extracted at the LR transects in IH-LANS (Figure 4.5B). Then, a HR discretisation based on the LR transects is defined at a lower spacing $\mathcal{O}(5\,m)$. The present-day topobathymetry is projected to the HR transects and the shoreline changes modelled at the LR transects are transferred to the HR transects through distance-based interpolation (Figure 4.5C). A profile translation tool, named ShoreTrans (McCarroll et al., 2021), is applied to the HR transects to update the transect shape using the shoreline changes and the SLR variations (Figure 4.5D). Transforming the elevation information from the local transect coordinate system to a global coordinate system allows for generating a cloud of 3D points. This cloud of points is interpolated via the inverse distance weighting (IDW) procedure implemented in ArcGIS, yielding the updated nearshore topobathymetry (Figure 4.5E).
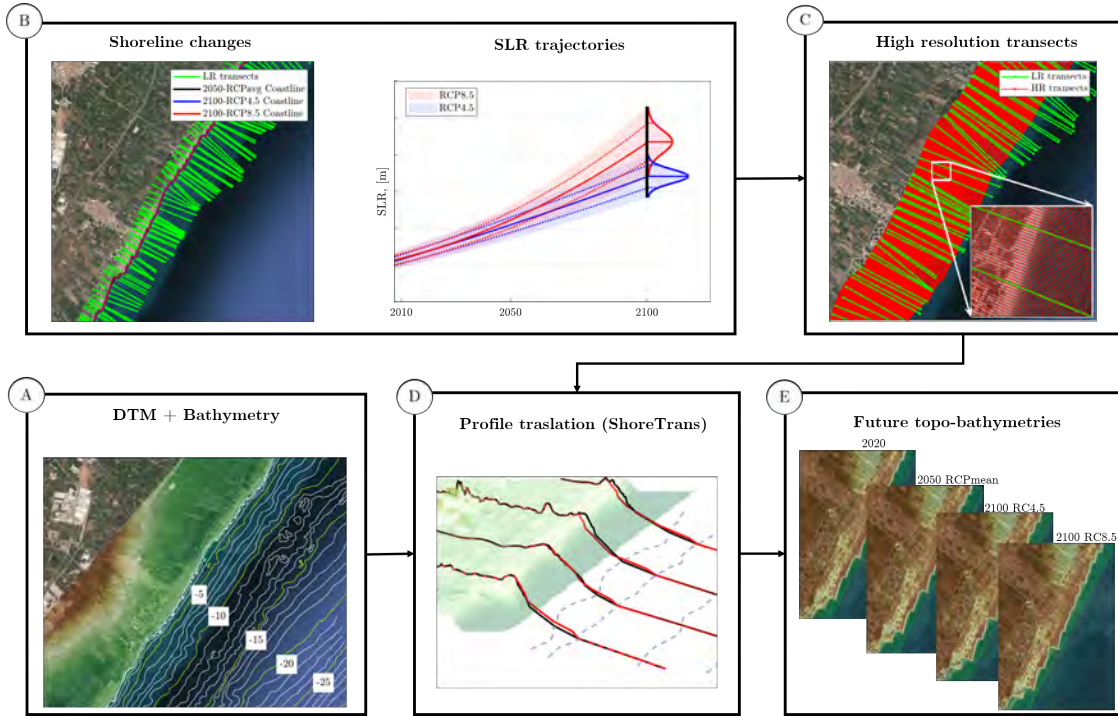
Figure 4.5: Methodology to update the nearshore topobathymetry from the shoreline changes and SLR.

Profile translation tool

For the sake of completeness, the fundamentals of ShoreTrans are herein described. Additional explanations on the capabilities of the profile translation tool can be found in McCarroll et al. (2021). ShoreTrans is a rules-based shoreface translation and sediment budgeting model, that updates surveyed profiles accounting for SLR following Atkinson et al. (2018), variations in sediment supply following the classical one-line theory and storm erosion following Kinsela et al. (2017). The effects of shoreline armouring and non-erodible structures are also taken into account following Beuzen et al. (2018).

Profile kinematics associated with the different modelled shoreline processes are displayed in Figure 4.6. First, the profile is parametrised so as to apply simple translation rules Figure 4.6a. A different parametrisation is made for long-term processes (longshore transport and SLR) and short-term processes (cross-shore transport). For long-term processes, the active depth extends between the berm (y_b, z_b) and the depth of closure (y_{dc}, z_{dc}) while the reference shoreline is located at point y_Y, z_Y. For short-term ero-

sion, profile reference points are the top of the beachface (y_{tb}, z_{tb}), the bottom of the beachface (y_{bb}, z_{bb}), the erosion-accretion inflection point (y_p, z_p) and the bottom of the storm bar (y_{sb}, z_{sb}). Longshore transport kinematics are intended to alter the initial profile by a shoreward (erosion) or seaward (accretion) movement (Figure 4.6b). In case of short-term erosion, the beachface retreats and an erosion wedge is formed until the pivot point (Figure 4.6c). This process is assumed to produce a net zero volume change. Thus, an accretion sinusoidal shape is generated between the pivot point and the bottom of the storm bar. Finally, the active profile is expected to move upwards following SLR. As for the case of short-term erosion, the process is linked to a net zero volume change, so the active profile also moves shoreward until the erosion and accretion volumes match. In case of a Dean's shaped profile (Dean, 1991), the shoreward movement coincides with the Bruun's rule retreat (Bruun, 1962).
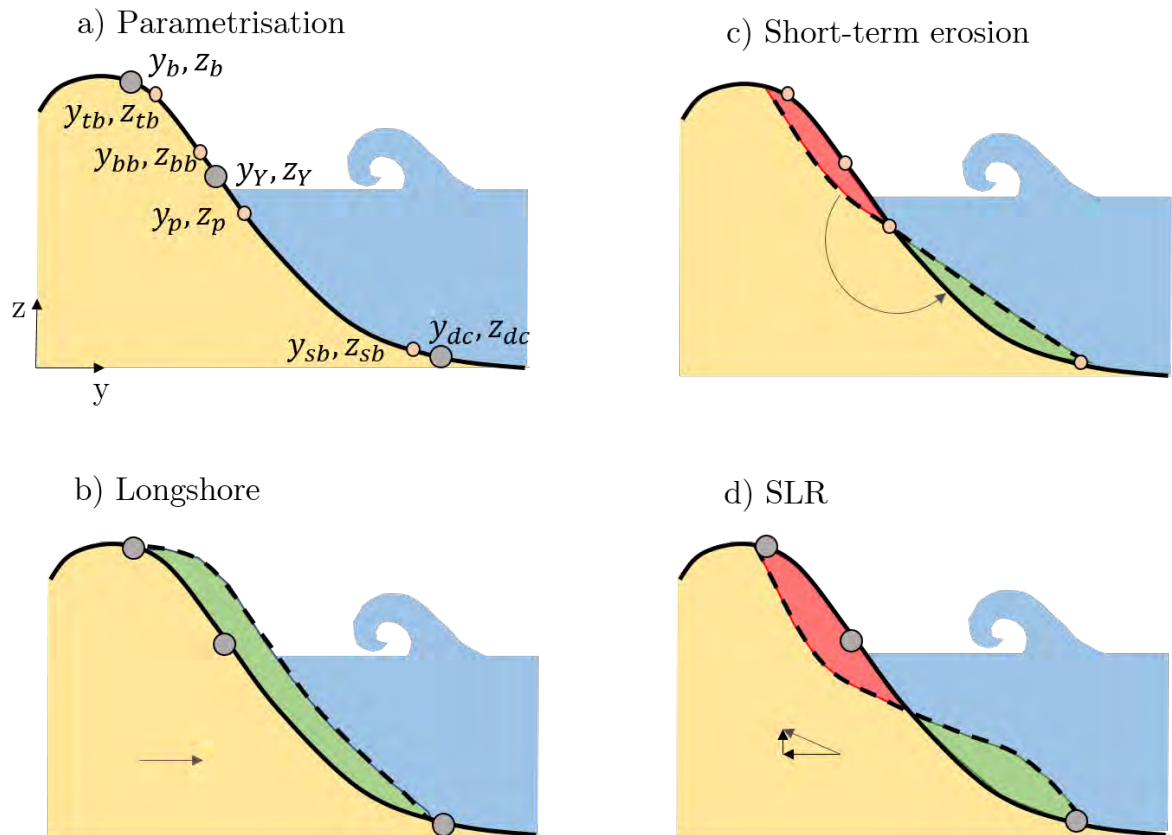
Figure 4.6: Profile kinematics associated with the different processes being modelled (not drawn to scale).

While long-term processes are modelled through a simple active profile traslation (hor-

izontal in case of longshore and horizontal and vertical in case of SLR), profile dis-placemet associated with short-term erosion implies beachface changes and the forma-tion of an erosion bar. Thus, the algorithm to update the profiles is different depending on the temporal scale of the process being modelled.

For long-term processes, the new elevation at time $(t + 1)$ of a profile defined by its in-plane $y(t)$ and $z(t)$ coordinates is:

$$z_{t+1}(y) = z_t(y - \Delta Y) + \Delta SLR, \quad a < y < b \tag{4.5}$$

where ΔY is the unknown horizontal displacement associated with both longshore and SLR changes and ΔSLR is the vertical profile displacement between instants t and $t+1$. The domain is bounded by the active profile, being a the onshore limit $a = y_b + \Delta Y$ and b the offshore limit $b = y_{dc} + \Delta Y$.

In order to solve for ΔY, the function $F(\Delta Y)$ is minimised:

$$F(\Delta Y) = \int_a^b [z_{t+1}(y) - z_t(t)] \, dx + \Delta V \tag{4.6}$$

where ΔV is the net profile volume change due to longshore processes and other sed-iment sinks or sources. The value of ΔV is obtained from the longshore shoreline evolution Y_l in IH-LANS as:

$$\Delta V = (Y_{t+1,l} - Y_{t,l})(B + d_c), \quad [L^3/L] \tag{4.7}$$

By applying this approach, three basic cases can be modelled (Figure 4.6b and/or Figure 4.6d):

$$\begin{cases} \Delta SLR \neq 0; \, \Delta V = 0 & \text{change due to SLR without volume change in the profile} \\ \Delta SLR = 0; \, \Delta V \neq 0 & \text{no change due to SLR and volume change in the profile} \\ \Delta SLR \neq 0; \, \Delta V \neq 0 & \text{change due to SLR and volume change in the profile} \end{cases}$$

In case of a seawall preventing the shoreline displacement, the same procedure is applied without considering the wall. Then, the potential erosion in the shoreward part of the non-erodible structure is transferred to the offshore area adjacent to the wall. It is distributed in a triangular wedge that extents offshore a distance equal to 1/3 of the extent of the active profile from the toe of the structure.

With reference to the short-term erosion, the beachface defined by its upper and lower limits (Figure 4.6a) is translated following the short-term shoreline displacement obtained from IH-LANS. The erosion wedge is closed by linearly joining the bottom of the beachface (y_{bb}, z_{bb}) with the inflection point (y_p, z_p). Finally, as the net volume change for short-term erosion is supposed to be null, an erosion volume is deposited offshore the pivot point until the bottom of the storm bar (y_{sb}, z_{sb}) following a sinusoidal shape.

4.3.   Case study application

For illustration purposes, the methodology is applied at a 40 km Spanish Mediterranean coastal stretch located between Castellón and Valencia (Figure 4.7). A forensic study of the shoreline evolution of the area is detailed in Chapter 2 and the shoreline projections have been developed in Chapter 3 using IH-LANS. As stated before, the stretch has a high degree of anthropization and intense southerly longshore transport. Although man-made interventions have been taken, the erosion and flooding problem persists this day, and climate change exerts a doubly detrimental effect by reducing the natural protection service of beaches while boosting the flooding potential of extreme events.

4.3.1.   Erosion-flooding coupling approaches

In order to analyse the importance of coupling coastal flooding and erosion at different time-scales, an analysis has been performed unravelling the influence of the erosion-flooding coupling approach (CA) on TWL and flooding maps. Four different CAs have been included depending on the processes considered. These approaches are 1) full CA, which considers both short- and long-term shoreface changes; 2) short-term (ST) CA, which accounts only for storm-driven short-term shoreface changes; 3) long-term (LT)

Figure 4.7: Study area and main beaches.

CA, which is limited to considering the long-term shoreface response and 4) no CA, in which the active shoreface remains unchanged.

The flooding modelling strategy determines the way CAs are introduced in the modelling chain. Based on the spatial scale and on the computational demand, several strategies are used to model coastal flooding (Toimil et al., 2016). For regional-scale studies in probabilistic frameworks as the present one, a balanced solution is to uncouple TWL modelling from the inland flood model. TWL is modelled using a hydro-morphodynamic model executed in every LR transect and then, this information is transferred as boundary condition for the flood model. This strategy is chosen instead of performing a complete 2DH simulation of hydro-morphodynamic evolution during extreme events, which would be computationally unfeasible. After calculating the TWL associated with the thousands of synthetic storms via metamodelling techniques, the

100-year return period TWL (European Flood Directive) drives the flood model. However, the morphodynamic changes associated with this TWL are unknown, hampering the topobathymety update for the flood model. In order to include the effects of short-term storm erosion in the topobathymetry, the average storm short-term retreat from the shoreline simulation with IH-LANS is used as input for the profile translation tool.

In all CAs, surf-zone hydrodynamics and coastal flooding are modelled using XBeach and RFSM-EDA respectively. The no CA does not consider erosion effects on either TWL computation or flood propagation over land. Conversely, the full CA does account for surf-zone morphodynamics and long-term shoreface translation in TWL computation and for short- and long-term shoreface changes in the modelling of coastal flooding. Finally, the short- and long-term CA limit erosion consideration to short-term morphodynamics in the TWL stage and short-term shoreface erosion in coastal flooding and to long-term shoreface updates in both TWL and coastal flood modelling stages, respectively. Table 4.1 summarises the main features of the CA considered.

CA	TWL (XBeach) Transects (processes)	Activated modules	Flooding (RFSM-EDA) Topography (processes)
Full	ShoreTrans (Longshore & SLR)	Hydro & Morpho	ShoreTrans (Longshore, SLR & Short-term)
Short-term	Initial (Present)	Hydro & Morpho	ShoreTrans (Short-term)
Long-term	ShoreTrans (Longshore & SLR)	Hydro	ShoreTrans (Longshore & SLR)
No	Initial (Present)	Hydro	Initial (Present)

Table 4.1: Summary of the main characteristics of how the coupling approaches are modelled.

4.3.2. Climate and exposure data

Atmospheric fields from 5 RCMs were dynamically downscaled to generate future hourly time series of waves and storm surges during the time periods 1986-2005, 2026-2045 and 2081-2100 for the RCPs 4.5 and 8.5. The RCMs used (RCA4 and ALADIN52) and their driving GCMs (IPSL-CM5A-MR, HADGEM2-ES, EC-EARTH, CNRM-CM5 and CNRM-CM5) have time resolutions of 3 and 6 h and spatial resolutions of $0.11° \times 0.11°$ and from $1.25°$ to $1.90°$, respectively. For simplicity, we denote the 5 configurations of GCMs-RCMs as IPSL, HADG, EART, CNRM and MEDC hereinafter. The numerical models used were WaveWatch III (Tolman, 2009) for waves and ROMS (Shchepetkin

and McWilliams, 2005) for storm surges.

Astronomical tide is obtained from the reconstruction of harmonic constituents from the TPXO7.2 global model using the Oregon State University Tidal Prediction Software (OTIS) at a horizontal spatial resolution of 0.25°. Continuous hourly time series extracted from 1985 to 2100 show the mixed diurnal-semidiurnal cycle of approximately 20 cm of tidal range.

Regional SLR projections are obtained at a 1° horizontal resolution grid and include the contribution from sterodynamic effects, melting of mountain glaciers and ice sheets, land water and glacial isostatic adjustments from 21 GCMs (Oppenheimer et al., 2019). Mean and standard deviation of the multi-model ensemble for the two emissions scenarios considered (RCPs 4.5 and 8.5) are used to compute the likely range, defined as the 90% confidence band following the IPCC methodology. Hourly time series for the three percentiles (P95%, P50% and P5%) are obtained for the two RCPs by linearly interpolating the yearly time series fitted to a parabola. On average, the RCP8.5 SLR 5%, 50% and 95% percentiles are expected to reach 0.25, 0.30 and 0.36 m by 2050 and 0.75, 0.89 and 1.01 m by 2100, respectively, along the study coast.

Due to the anthropization of the area, two initial topobathymetries are generated by integrating different sources of topographic and bathymetric information. The TB2005 is constructed combining the 2009 digital terrain model of the Spanish Geographic Institute (IGN) with a 5 m resolution, the 2009 nearshore bathymetry of Castellon and Valencia of the Spanish Ministry for Ecological Transition and Demographic Challenge (MITERD); and the deep-water bathymetry of the European Observations and Data Network (EMODnet). To obtain the second topobathymetry (TB2020), the 2016 digital terrain model of the IGN with a horizontal resolution of 5 metres, the updated 2009 nearshore bathymetry to 2020 using the PNOA coastline and satellite images and the EMODnet deep-water bathymetry, are used. In addition, to each cell of the digital terrain models, a Manning's roughness value is assigned, which is inferred from the land uses of the Corinne Land Cover EU database as in Toimil et al. (2017b).

4.3.3. Generation of synthetic storms

The storm model is applied to derive synthetic storms for each, RCP, RCM realisation and time period (1986-2005, 2026-2045 and 2081-2100) yielding 25 combinations. At every future realisation of waves and water level climate, after identifying the storms following the average $\overline{TWL}$ criterion, three representative points were chosen as director points to be emulated in the storm model by applying K-means classification algorithm and a proper linear-circular distance metric (Camus et al., 2011), (Figure 4.8). Points 3, 6 and 9 are chosen as representative cluster centres of the 10 forcing points of the domain. Then, the statistical model is inferred by fitting the marginal distributions and calculating the monthly correlation matrix in the probability space Σ_l of the variables $[H_{s3}, H_{s6}, H_{s9}, T_{m3}, T_{m6}, T_{m9}, Dir_6, SS_5]$. Dir_6 is selected to be the link variable between the MME and the MDM models.
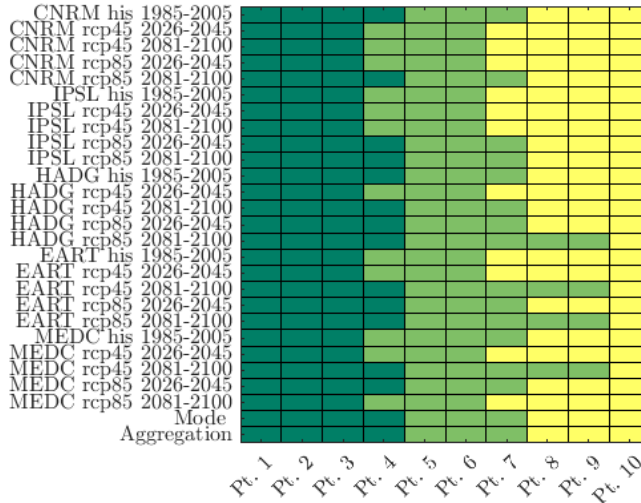
Figure 4.8: Identification of emulation points using K-means.

Next, the number of mixing components of the multivariate von Mises distribution of the MDM model needs to be defined based on the wave rose of the selected storms. Three main directions N-E, S-E and S-W are clearly identified by visual inspection (Figure 4.9a). Fixing the number of mixing components to be three, a K-means algorithm using a circular distance metric (Mardia et al., 2000) is used to identify three clusters in the Dir_3, Dir_6 and Dir_9 space (Figure 4.9b).
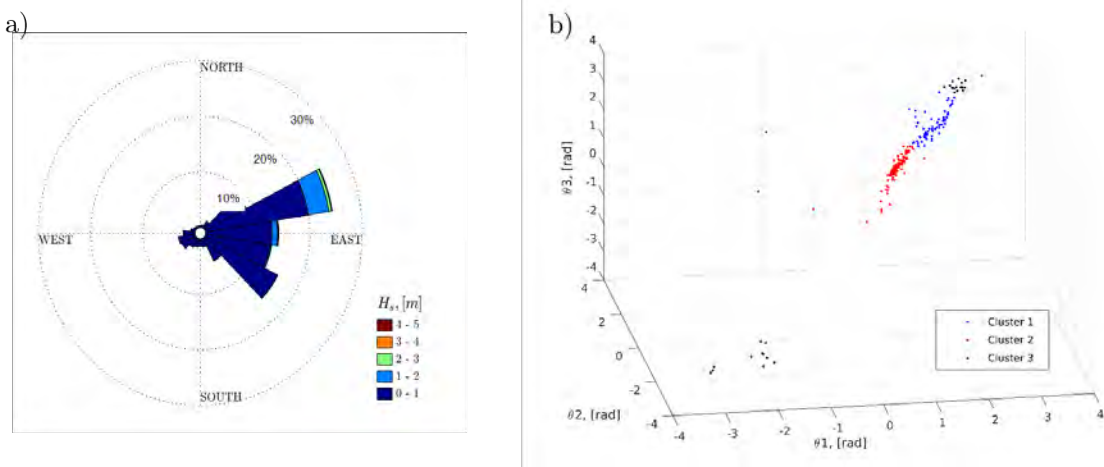
Figure 4.9: Classification of directional components for the MDM model.

Three mono-modal multivariate von Mises distributions $T_{\boldsymbol{\theta}}(\boldsymbol{\theta})$ are fitted to each of the three directional clusters following the maximisation of the pseudo-likelihood function detailed in Appendix C. For every future scenario of wave and water-level dynamics, these distributions are combined with their probability of occurrence (calculated as the number of elements per cluster divided by the total number of elements) yielding the mixing multivariate directional distribution $f_{\boldsymbol{\theta}}(\boldsymbol{\theta})$ that considers all possible incoming storm directions. Figure 4.10 shows the density function of the MDM model for RCP4.5 MEDC 2026-2045 realisation. The most likely directional cluster (probability of 0.64) has a mode centred on $Dir_3 = 63°$, $Dir_6 = 65°$ and $Dir_9 = 70°$.

For the synthetic generation of storms, the marginal distribution of each variable is entered with normal random vectors and then the k random realisation of the vector $[H_{s3}, H_{s6}, H_{s9}, T_{m3}, T_{m6}, T_{m9}, Dir_6, SS_5]_k$ is extracted. All the EMM realisations are linked to the MDM through Dir_6. In every case, Dir_3 and Dir_9 are obtained from the MDM by randomly extracting a realisation of the conditional density trivariate function $f(Dir_3, Dir_9|Dir_6)$. T_p is determined from the calibrated heteroscedastic model, and AT values are derived by selecting a random value of the month and year from the time series of AT reconstructed from harmonics. 100,000 multivariate storms are generated following this procedure for each of the 25 combinations of RCM, RCP and Period.
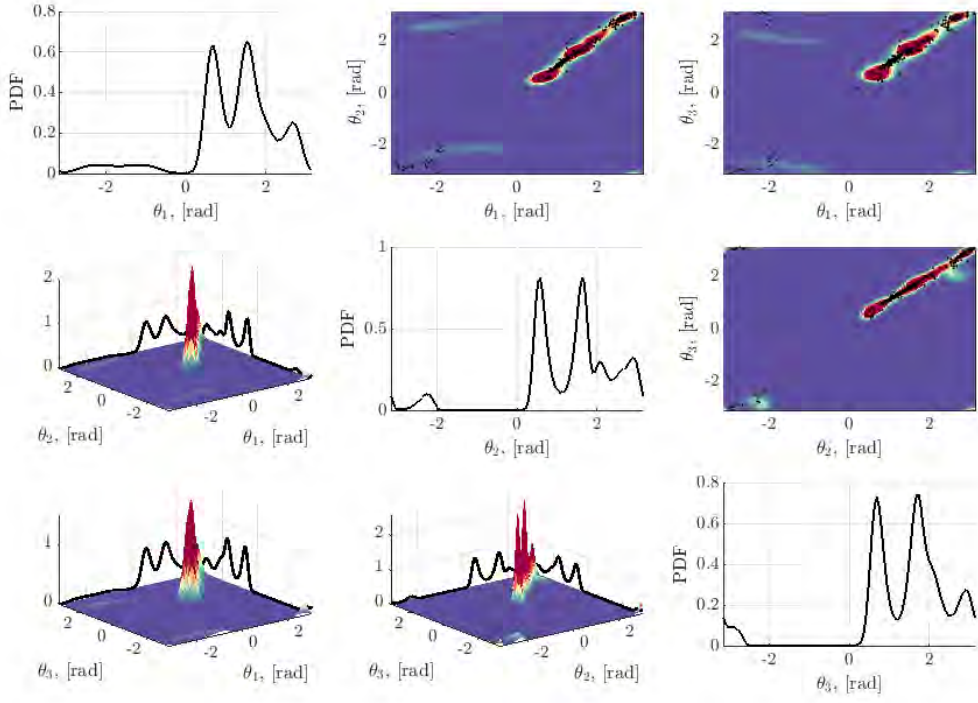
Figure 4.10: Bivariate representation and marginals of the MDM model for the RCP4.5 MEDC 2026-2045 realization.

As an example, Figure 4.11 shows the skill of the MME model in reproducing the statistical relationships between the linear variables H_{s6}, T_{m6} and SS_5 and the circular variable Dir_6. The observations and the emulation are represented in matrix form. Panels A-F illustrate the scatter plots of observed and simulated data; panels G-J show the univariate GEV annual distribution function of H_{s6}, T_{m6} and SS_5 and the empirical polar density function of Dir_6; and panels K-P represent the comparison between the observed and emulated empirical bivariate density functions, where the goodness of fit of the MME is quantitatively validated.

In Figure 4.12, the MME-MDM coupling is validated as the variables H_{s3}, T_{m3} and SS_5 are modelled by the MME model while variable Dir_3 is obtained from the MDM model by the conditional dependence through Dir_6 (modelled in the MME model). The statistical relationship between the variables modelled in the MME model and the directional variables of the MDM is successfully maintained through the conditional linkage. This fact is is observed by looking at panels L, M, I and F and B, D, I and P

in Figure 4.12.
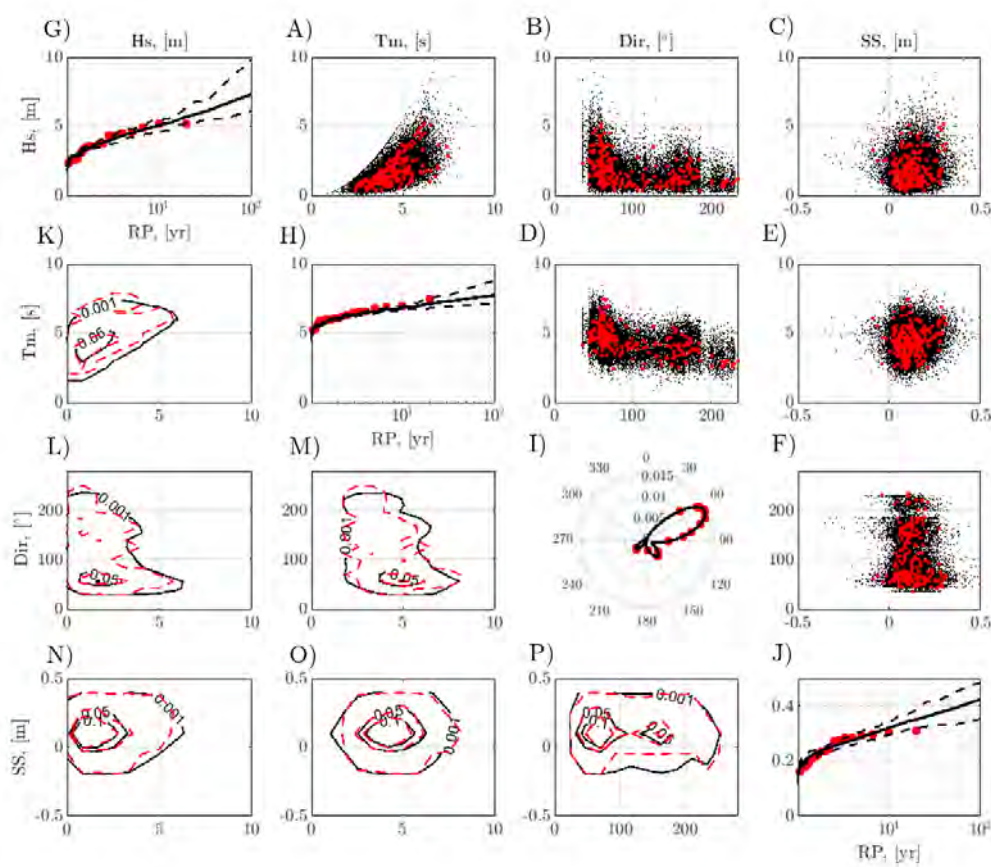
Figure 4.11: Validation of the EMM-MDM emulator in one of the director points (point 6). Observations (red) are compared to the simulated data (black).

4.3.4.   Total water level metamodelling

TWL is obtained as the summation of the wave contribution in terms of the dynamic wave setup (DWS), the astronomical tide (AT), the storm surge (SS) and the sea-level rise (SLR). Calculating the TWL associated with the 100,000 synthetic storms for every RCM (HADG, IPSL, CNRM, EART, MEDC), RCP (4.5 and 8.5), period scenario (1985-2005, 2026-2045 and 2081-2100) and coupling approach (full, long-term, short-term and no) is done by using a combination of statistical and process-based models. To this end, a RBF-based metamodel trained with a reference set of synthetic storms for which the TWL is numerically downscaled is used to infer the TWL associated with

each of the synthetic storms.
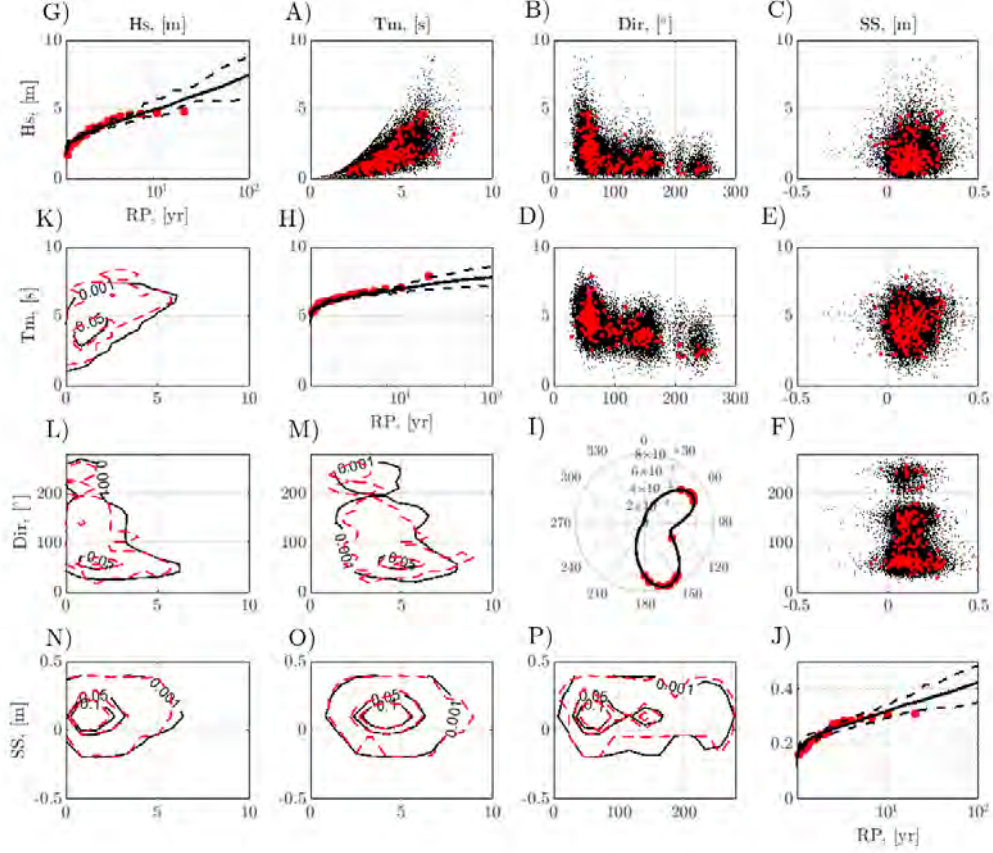
Figure 4.12: Validation of the EMM-MDM emulator in one of the director points (point 3). Observations (red) are compared to the simulated data (black).

The first step is the definition of the computational domain for SWAN, which is composed of one global grid with a spatial resolution of 500 m one-way nested to three high-resolution grids (50×50 m). The global grid must be aligned with the forcing points used for storm modelling, as the wave conditions and the water levels required to generate the storms have to be collected at the outer contour points of the grid. In the second step, the maximum dissimilarity algorithm is applied to select the representative subsets of storms with 500 cases per subset that represent the full sample of storms. The third step is the nearshore propagation of the selected cases using SWAN at the offshore point (10 m depth) of the 247 LR transects. Next, the nearshore waves and water levels at the offshore point of the LR transects (spaced 200 m apart) are used to

force XBeach in 1D surfbeat mode yielding the DWS associated with the selected subset, Figure 4.13. A calibrated XBeach (see Appendix D) is forced with series of hourly JONSWAP spectra that generate a 72-hour synthetic storm (a typical value of storm duration accepted for the Mediterranean Sea region, (Marcos et al., 2009)). The shape of the storm is parametrised based on historic records. Then, the RBF-metamodel is fitted by establishing the relationship at every selected subset between the offshore waves and water levels defining the storm and the computed DWS transect by transect. This dual relationship is then used to obtain statistically the DWS associated with the 100,000 synthetic storms for every RCM, RCP, period and CA scenario.
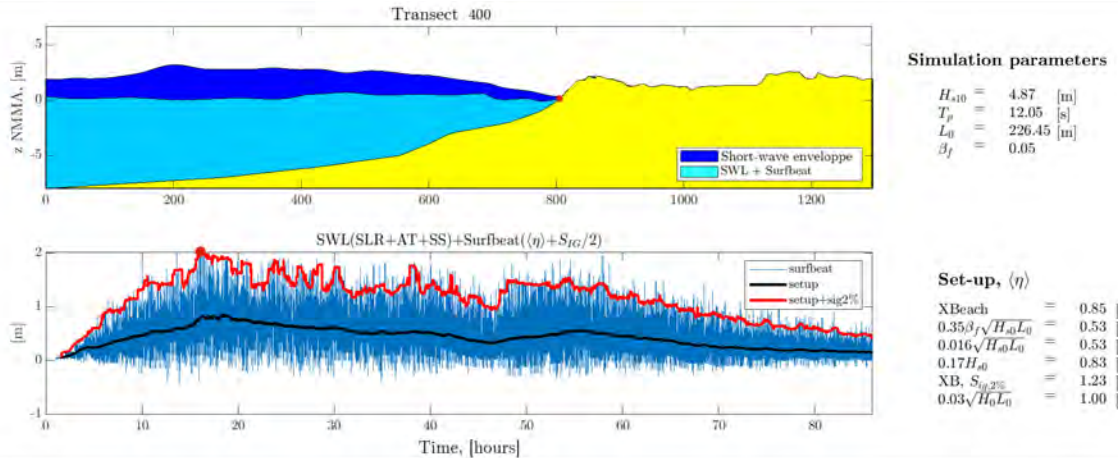
Figure 4.13: DWS estimation using XBeach and comparison with commonly used empirical formulations.

4.3.4.1. Extreme value analysis of TWL

Next, in order to force the flood model RFSM-EDA, the 100-year return-period TWL_{100} value is used. TWL_{100} is obtained as $TWL_{100} = (DWS + AT + SS)_{100} + SLR$, where $(DWS + AT + SS)_{100}$ is the stationary total water level ($TWL_{100} - SLR$) obtained from a generalised extreme value distribution (GEV) fit. Although future storms account for climate change in the distribution of wave conditions and storm surges over time, intra-period variation trends are not significant, so a stationary fit is justified by the augmented Dickey-Fuller test, Figure 4.14.

The null hypothesis of this test is that time-series has a unit root and therefore are not

stationary. A p-value analysis is carried out independently for the RCMs H_s, T_m and SS at the boundary points. Considering a significance level of 5%, if the computed p-value is lower, the non-stationary hypothesis is rejected. As shown in Figure 4.14, the obtained p-values are always lower than the significance level for every RCP-RCM-Period combinations, at all the boundary points for the three tested variables. The time-series are therefore stationary according to the Dickey-Fuller test and the stationary GEV fit is deemed valid.
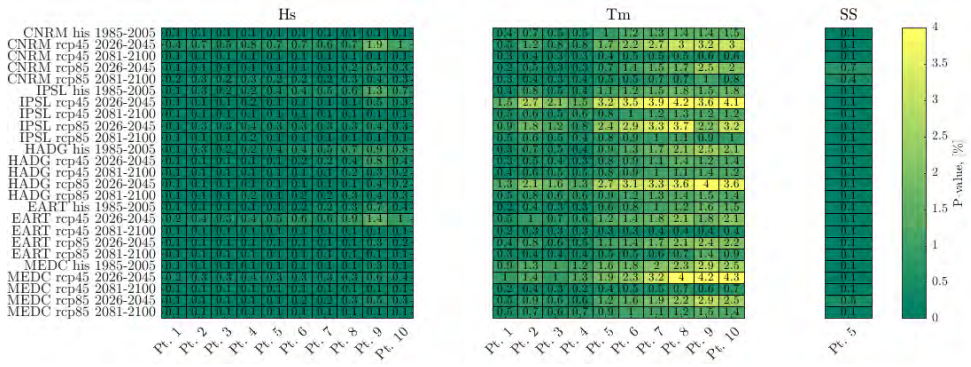
Figure 4.14: Application of the Dickey-Fuller test to verify if the projected wave climate is stationary.

Having such a large population of storms enables the determination of TWL of high return periods that are statistically robust as the multivariate statistical dependencies are preserved. In Figure 4.15, the RCM-RCP-SLR percentile-Period variability is highlighted in the TWL return levels for the full CA in a profile in Torre beach. While the first row in the figure displays the whole RCM-RCP-SLR percentile-Period variability by identifying different RCMs with different markers and SLR trajectories with different colours, the second row highlights the RCM variability by isolating the $P50\%$ of SLR in future scenarios and the third row stresses the SLR variability by isolating the EART RCM return levels. Looking at the SLR variability, the TWL_{100} spread range increases for longer time horizons and higher radiative forcing. If focusing on the 50% SLR percentile, the inter-RCM TWL_{100} spread range moves upwards in 2045 (1.7-2.2 m) and 2100 (1.8-2.4 m) with respect to 2005 (1.4-1.6 m). For the EART model, the variation in the spread range between RCPs is smaller in 2045 ($\approx$ 0.15 m for both RCP4.5 and RCP8.5) than in 2100 ($\approx$ 0.20 m for the RCP4.5 and $\approx$ 0.30 m for the

RCP8.5).
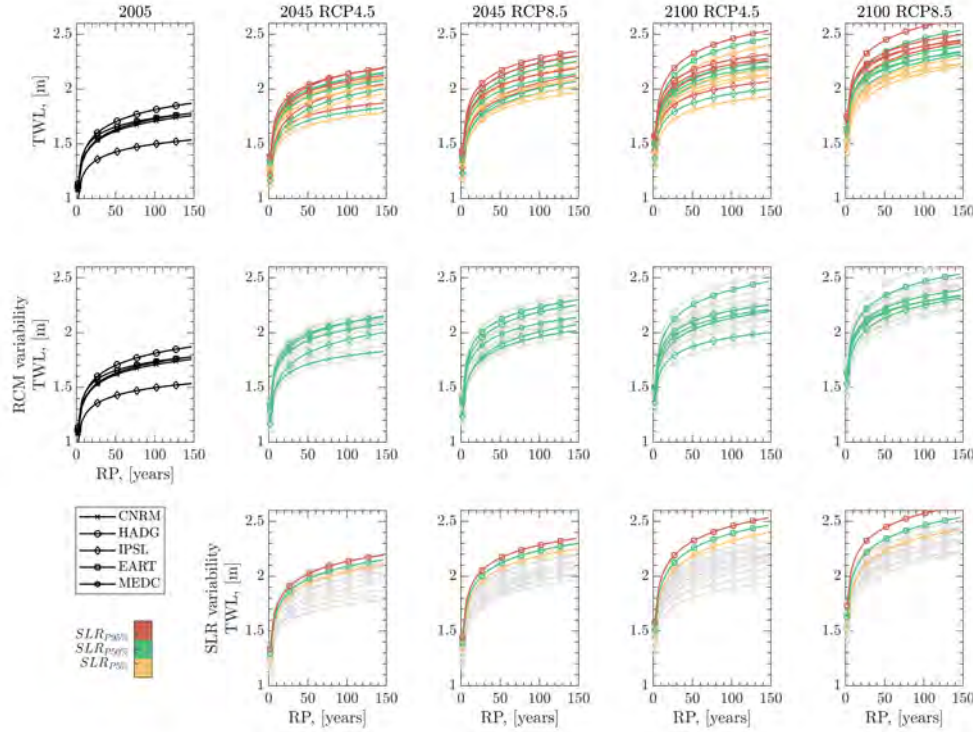
Figure 4.15: TWL return levels for different RCM-RCP-SLR percentile-Period combination for the full CA at one transect in Torre beach.

4.3.4.2. Considering erosion-flooding coupling approaches in TWL metamodelling

Wave-induced coastal erosion has a limited offshore extent (Hallermeier, 1980) which is between 4 and 6 meters in the study area. The offshore point of the LR transects is chosen in such a way that it exceeds the depth of closure, and thus, they reach the -10 metres contour line. Nearshore propagation using SWAN is unaffected by the erosion-flooding coupling approach, as the bathymetry does not change due to wave-induced transport at the communication interface between the SWAN propagation and the starting offshore point of the LR transects used for the XBeach computation. However, considering different erosion-flooding coupling approaches implies accounting for long- and short-term wave-induced alteration of the LR transects, which extent from the -10 meters contour to the shore.

Consideration of the coupling approach in the TWL modelling requires two steps. On one hand, the effect of long-term coupling is considered by altering the geometry of the profiles accounting for longshore transport and SLR. On the other hand, storm-induced short-term effects are modelled by activating morphodynamic evolution in the XBeach simulation. In Table 4.2, the modelling characteristics of the different scenarios needed for integrating the erosion-flooding coupling approaches in the TWL estimation are detailed. While for any no coupling approach scenario, the initial LR TB2005 or TB2020 profiles are used as reference and XBeach is run just in hydrodynamic mode; for the full coupling approach, the initial LR profiles are modified using ShoreTrans considering longshore and SLR effects and XBeach is run considering hydrodynamics and also morphodynamics.

		Topographic BC		
Scenario	Base profiles	ShoreTrans processes	Xbeach act. modules	Metamodel ID
2005NO	TB2005 LR profiles	-	Hydro	1
2005ST	TB2005 LR profiles	-	Hydro & Morpho	2
2045FULL	TB2020 LR profiles	Longshore & SLR	Hydro & Morpho	3
2045ST	TB2020 LR profiles	-	Hydro & Morpho	4
2045LT	TB2020 LR profiles	Longshore & SLR	Hydro	5
2045NO	TB2020 LR profiles	-	Hydro	6
2100FULL_RCP4.5	TB2020 LR profiles	Longshore & SLR	Hydro & Morpho	7
2100ST_RCP4.5	TB2020 LR profiles	-	Hydro & Morpho	4
2100LT_RCP4.5	TB2020 LR profiles	Longshore & SLR	Hydro	8
2100NO_RCP4.5	TB2020 LR profiles	-	Hydro	6
2100FULL_RCP8.5	TB2020 LR profiles	Longshore & SLR	Hydro & Morpho	9
2100ST_RCP8.5	TB2020 LR profiles	-	Hydro & Morpho	4
2100LT_RCP8.5	TB2020 LR profiles	Longshore & SLR	Hydro	10
2100NO_RCP8.5	TB2020 LR profiles	-	Hydro	6

Table 4.2: Modelling characteristics of the different scenarios needed for integrating erosion-flooding coupling approaches in the TWL estimation. Note that the 2005NO and 2005ST scenarios condense 5 RCMs each and every future scenario include 5 RCMs and 3 percentiles of SLR.

In spite of the RCM and eventually SLR variability, the RCM mean ensemble of longshore shoreline changes for the 50% SLR percentile is considered for all the RCMs and SLR trajectories in a given scenario. Also, the SLR variability is reduced regarding LR profile update to the 50% SLR percentile. Additionally, in order to avoid an unrealistic behaviour of the metamodel while considering the different scenario characteristics in Table 4.2, a single RBF-based metamodel was trained for every different combination

of topographic boundary condition and Xbeach activated modules. This yielded a total amount of 10 RBF-based metamodels to reproduce the complete RCM-RCP-SLR percentile-Period-CA set of cases, see the fifth column in Table 4.2.

4.3.5. Future topobathymetries

Shoreline projections developed in Chapter 3, which consist of hourly time-series of shoreline changes from 1990 to 2100 for 2 RCPs and 5 RCMs are employed. These projections were developed using free-model parameters calibrated and validated during the periods 1990-2010 and 2010-2020 respectively using the extended Kalman filter and observations from satellite-derived shorelines using the CoastSat algorithm (Vos et al., 2019). However, for this application, the SLR retreat considered in the shoreline projections of Chapter 3 is discarded, as the more advanced approach described in Section 4.2.2 is used instead of the Bruun's rule. From the multi-process shoreline projections, longshore shoreline changes are extracted at the LR transects for every RCM-RCP scenario for the 50% SLR percentile at the end of the reference periods (2045 and 2100). Then, longshore shoreline changes (with respect to present 2020 shoreline position) are averaged between RCMs and RCPs for the short-term future yielding C2045 and between RCMs in the long-term future yielding C2100_RCP4.5 and C2100_RCP8.5. RCPs in the long-term future are not averaged due to the high variance of SLR .

Longshore shoreline changes calculated at the 247 LR transects are transferred to the 4137 HR transects (spaced 10 m apart) by interpolation and the volume associated with the longshore shoreline change is calculated following the one-line theory by multiplying the shoreline change times the active profile depth, Equation 4.7. Long-term profile changes are computed at the HR transects by incorporating the profile diagonal translation due to SLR yielding the profile geometry for the cases Z2045, Z2100_RCP4.5 and Z2100_RCP8.5. Profile elevation points z_i are spaced one meter apart, so a cloud of 10×1 m (alongshore × cross-shore) is generated. By interpolating this cloud into a 5×5 m grid, long-term changes are incorporated into the digital elevation model used for flood modelling. In Figure 4.16, changes between TB2045LT, TB2100LT_RCP4.5 and TB2100LT_RCP8.5 with respect to TB2020 are displayed in Nules and Corinto. In

Nules, it is clear the counter-clockwise rotation of the compartments between groynes following the wave-energy flux. By looking at the transects (highlighted in black and blue), it is clear how the area at the leeward side of the groynes experiences erosion due to longshore transport and SLR (transect in black) while the windward side experiences accretion due to longshore transport and erosion due to SLR (transect in blue). Additionally, complex profile changes due to irregular bathymetric features is also considered in this approach, as shown in the Corinto transect highlighted in pink.
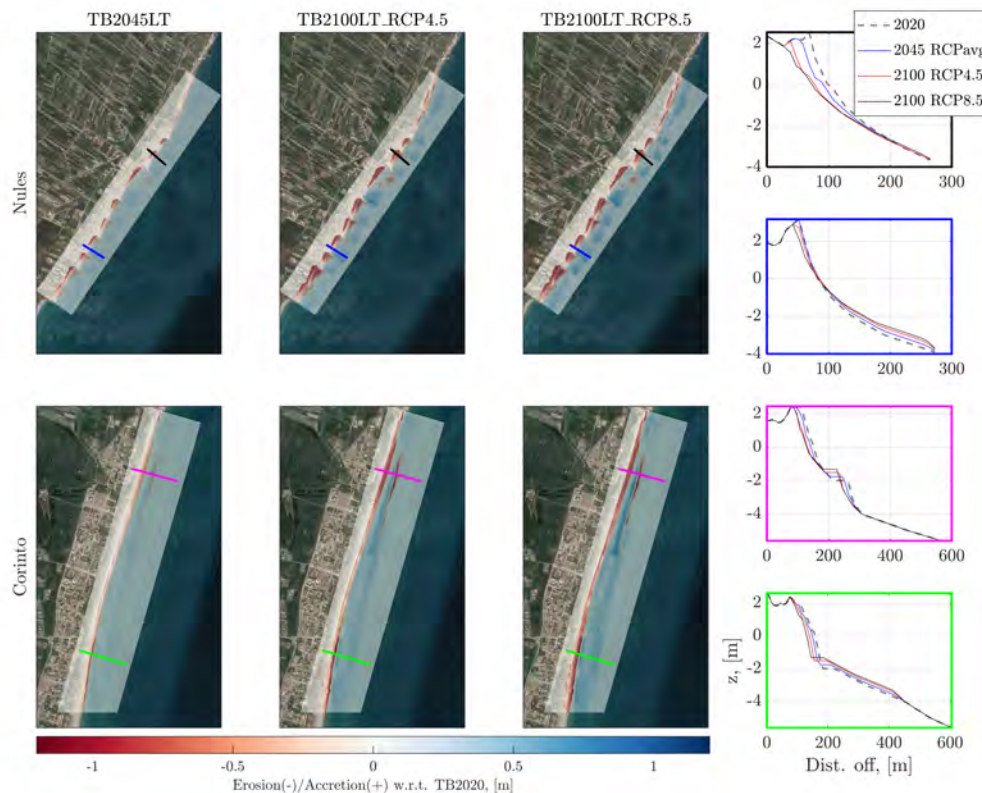
Figure 4.16: Long-term erosion and accretion patterns in Nules and Corinto for TB2045LT, TB2100LT_RCP4.5 and TB2100LT_RCP8.5 with respect to TB2020.

This approach allows to calculate the sediment balance in the study area. As an example, Corinto sediment gains in 2045 ($\approx 7500\ m^3$) triple at the end of the century ($\approx 21000\ m^3$). Overall, longshore drift causes the northern beaches (Torre, Burriana, Nules, Moncófar, Chilches, Llosa and Almenara) to loose sediment, which accumulates in the southern beaches (Corinto, Canet and Sagunto).
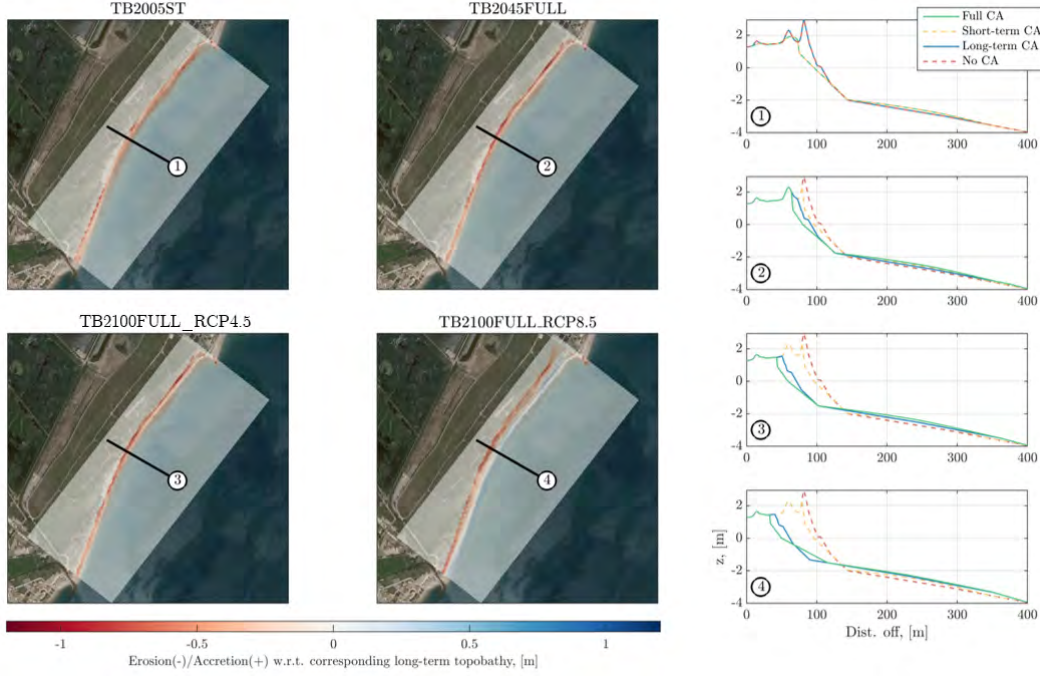
Figure 4.17: Short-term erosion and accretion patterns in Llosa for TB2005FULL with respect to TB2005; TB2045FULL, TB2100FULL_RCP4.5 and TB2100FULL_RCP8.5 with respect to TB2045LT, TB2100LT_RCP4.5 and TB2100LT_RCP8.5 respectively.

Using the time series of shoreline evolution from IH-LANS, average storm erosion retreats along each LR transect are obtained for (RCM-averaged) 1986-2005, (RCM-RCP-averaged) 2026-2045 and (RCM-averaged) 2081-2100. The average storm retreat is obtained by averaging the erosion peaks above the 95% treshold from each RCM-RCP short-term shoreline position simulation. Results show that the beaches with the highest average storm retreat are Canet ($\approx$ 15 m), Corinto ($\approx$ 14 m) and Sagunto ($\approx$ 11 m). The ranking is maintained for each RCM-RCP-SLR simulation. These short-term storm retreats are interpolated to the HR transects. Profile changes are evaluated following the kinematics of the Kinsela et al. (2017) method implemented in ShoreTrans and described in Section 4.2.2. In Figure 4.17, it is presented the storm erosion and accretion patters in Llosa for TB2005FULL with respect to TB2005 and for TB2045FULL, TB2100FULL_RCP4.5 and TB2100FULL _RCP8.5 with respect to TB2045LT, TB2100LT_RCP4.5 and TB2100LT_RCP8.5, respectively. Similarly to SLR kinematics, storm erosion results in a readjustment of sand that is eroded at the beach front and deposited in the lower part of the surveyed profiles, making them

more dissipative. When moving away in time and with increasing radiative forcing, the long-term topobathymetry is further set back, and above that, storm erosion pushes the coastline further backwards (the blue and green solid lines represent the long-term and full CAs, respectively). The storm volumes displaced in Llosa are ≈ 23500 m^3 (RCM-averaged 2005), ≈ 22600 m^3 (RCM-RCP-averaged 2050), ≈ 24700 m^3 (RCM-averaged RCP4.5 2100) and ≈ 19500 m^3 (RCM-averaged RCP8.5 2100).

Topobathymetry	Parent topobathymetry	ShoreTrans processes
TB2005	IGN(2009)+MITECO(2009)	-
TB2005ST	TB2005	Short-term erosion
TB2020	IGN(2016)+MITECO(2020)	-
TB2020ST	TB2020	Short-term erosion
TB2045NO	TB2020	-
TB2045ST	TB2020	Short-term erosion
TB2045LT	TB2020	Longshore & SLR
TB2045FULL	TB2045LT	Short-term erosion
TB2100NO_RCP4.5	TB2020	-
TB2100ST_RCP4.5	TB2020	Short-term erosion
TB2100LT_RCP4.5	TB2020	Longshore & SLR
TB2100FULL_RCP4.5	TB2100LT_RCP4.5	Short-term erosion
TB2100NO_RCP8.5	TB2020	-
TB2100ST_RCP8.5	TB2020	Short-term erosion
TB2100LT_RCP8.5	TB2020	Longshore & SLR
TB2100FULL_RCP8.5	TB2100LT_RCP8.5	Short-term erosion

Table 4.3: Summary of the characteristics of the different topobathymetries generated in this study.

In Table 4.3 the characteristics of all the topobathymetries generated in this study are summarized. The no CA uses the present-day TB2020 for the flood simulations. The short-term (ST) CA uses as basis the present-day TB2020 but incorporates short-term erosion. Considering the long-term (LT) CA requires updating TB2020 accounting for longshore and SLR while the full CA starts from the LT CA topobathymetry and includes short-term erosion due to the reference storm. As a reminder, for the short-term future (2045), RCM and RCP averaged longshore transport for the 50% SLR percentile is considered while the 50% percentile SLR used for profile updating is averaged between RCPs. The reference storm for the short-term future is calculated by averaging the storm retreats of the period 2026-2045. Regarding the long-term future (2100)

topobathymetries, RCM-averaged longshore transport for the 50% SLR percentile is adopted together with the 50% SLR percentile value for the profile updating process. The reference storm is calculated considering the 2081-2100 period for the RCPs 4.5 and 8.5.

4.3.6. Coastal flood modelling

Inland coastal flooding is calculated by forcing the RFSM-EDA model over an updated topobathymetry that depends on the time period, the RCP and the CA being considered. Downscaled TWL used as forcing boundary condition also depend on the RCM, RCP, time period and CA. The complete set of modelled cases considering their main modelling features are displayed in Table 4.4.

Scenario	TWL forcing	Topobathymetry
2005NO	$TWL_{100} - MID_1$	TB2005
2005ST	$TWL_{100} - MID_2$	TB2005ST
2045FULL	$TWL_{100} - MID_3$	TB2045FULL
2045ST	$TWL_{100} - MID_4$	TB2045ST
2045LT	$TWL_{100} - MID_5$	TB2045LT
2045NO	$TWL_{100} - MID_6$	TB2020
2100FULL_RCP4.5	$TWL_{100} - MID_7$	TB2100FULL_RCP4.5
2100ST_RCP4.5	$TWL_{100} - MID_4$	TB2100ST_RCP4.5
2100LT_RCP4.5	$TWL_{100} - MID_8$	TB2100LT_RCP4.5
2100NO_RCP4.5	$TWL_{100} - MID_6$	TB2020
2100FULL_RCP8.5	$TWL_{100} - MID_9$	TB2100FULL_RCP8.5
2100ST_RCP8.5	$TWL_{100} - MID_4$	TB2100ST_RCP8.5
2100LT_RCP8.5	$TWL_{100} - MID_{10}$	TB2100LT_RCP8.5
2100NO_RCP8.5	$TWL_{100} - MID_6$	TB2020

Table 4.4: Modelling characteristics of the different flooding scenarios regarding TWL and topobathymetric boundary conditions. The TWL forcing is defined by the 100-yr TWL return level from the metamodel ID (MID) defined in Table 4.2. Note that the 2005NO and 2005ST scenarios condense 5 RCMs each and every future scenario include 5 RCMs and 3 percentiles of SLR.

The scenarios considered widely sample all relevant sources of uncertainty, from wave climate and water level projections to modelling approaches so as to provide a first site-specific insight of the relative importance of the different elements. As an example,

in Figure 4.18, RCM, RCP and SLR variability on coastal flooding for the full CA is represented at Moncófar and Corinto beaches.

4.3.7. Results

In this section, the effects of the CA are analysed in two key elements defining flood hazard: TWL and flooded area. The relative importance of the erosion-flooding CA is contrasted with the importance of climate-related uncertainty induced by different RCMs and SLR percentiles in the TWL and flooded area. This allows to provide a site-specific, yet unique, analysis of the key factors to be considered for developing robust projections of coastal flooding.

4.3.7.1. Effects of the coupling approaches on TWL estimates

In order to quantify the effects of considering short- and long-term shoreline changes on TWL, TWL estimates are compared by applying the four CA. Figure 4.19 shows TWL_{100} for different CA and grouped by time horizon and RCP in Buriana, Chilches, Almenara and Sagunto. Overall, as SLR increases with the time horizon and radiative scenario, the TWL_{100} value also increases. The general pattern shows that the no CA (red) yield greater TWL_{100} values than the short-term CA (yellow) while the long-term CA (blue) exceeds the full CA (green). This observation is explained by the fact of allowing morphodynamic evolution in the full and short-term CA in the XBeach simulation. Profile changes during storm events generate a flatten profile with increased wave dissipation capabilities. Allowing for short-term morphodynamic changes enables the beach to adapt to higher incoming energy conditions that increase wave dissipation by profile flattening, reducing the foreshore slope and the TWL at the coast. This is also sustained by the linear relationship between the wave set-up and the foreshore slope in commonly used empirical formulations (Stockdon et al., 2006; Gomes da Silva et al., 2020). Site-specific behaviour is also observed and a similar pattern in the TWL_{100} response is observed in Chilches and Almenara and in Burriana and Sagunto respectively. As it can be observed in Figure 4.20, while initial XBeach profiles in Chilches and Almenara show a uniform slope in the swash zone, Burriana and Sagunto profiles exhibit strong slope gradients in the swash area that may influence the water excursion.
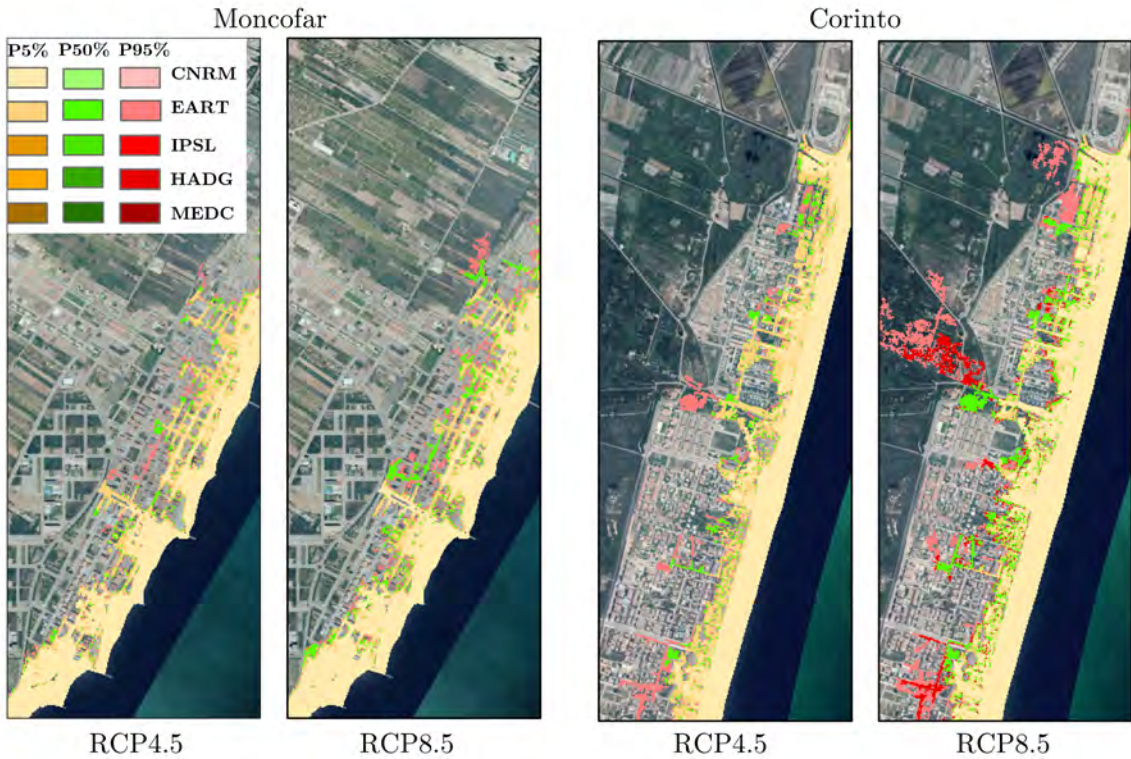
Figure 4.18: End-of-century coastal flooding projections for the full CA at Moncófar and Corinto beaches considering RCM, RCP and SLR variability.

With respect to the full CA, the short-, long-term and no CA provide increased TWL_{100} mean values in Almenara by up to 1%, 6% and 5% in 2045 and by up to 3%, 4% and 6% in 2100. In Chilches 1%, 13% and 18% in 2045 and 2%, 11% and 16% in 2100. The pattern in Burriana and Sagunto is different due to the swash zone geometry (Figure 4.20). In Burriana, the lowest TWL are reached with the short-term CA. As such, with respect to the full CA, the short-term underestimate TWL_{100} mean values by around $5-6\%$ for the different scenarios and time-horizons. The long-term CA overestimates TWL_{100} with respect to the full CA by $4-5\%$ and the no CA mean values fluctuate around the refeernce full CA ($\pm 1\%$). In Sagunto, with respect to the full CA, the short-term CA underestimates TWL_{100} mean values by up to 6%. The no CA also underestimates TWL by up to 7% at the end of the century while the long-term CA fluctuates with respect to the full CA ($\pm 3\%$). The relative contribution of SLR percentiles, RCMs and CAs to TWL_{100} total uncertainty is also quantified
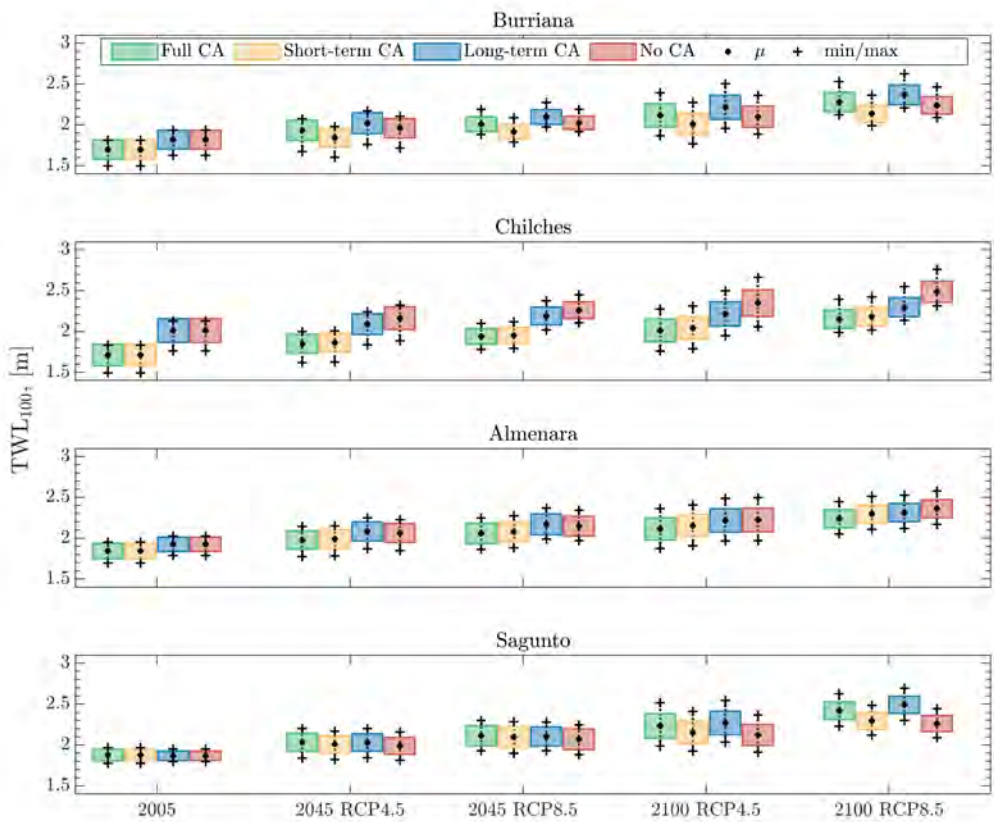
Figure 4.19: TWL_{100} value range in Burriana, Chilches, Almenara and Sagunto in 2005, 2045 and 2100 for the RCP4.5 and RCP8.5, where colour code refers to CA, black circles are mean values, crosses are maximum values and box limits represent mean values plus minus the standard deviation.

using a three-factor ANOVA-based decomposition (Figure 4.21) in Burriana, Chilches, Almenara and Sagunto in 2005, 2045 and 2100 for the RCPs 4.5 and 8.5. Findings are consistent with the results obtained in previous analyses. A strong dominating influence of the CA is observed in Chilches (57-68%), Burriana (23-36%) and Sagunto. In Sagunto, the CA weight on TWL_{100} uncertainty starts to be noticeable in 2100 for the RCP4.5 (16%) and increases for the RCP8.5 (46%), having even more weight than SLR (35%). The relative difference between the boxplots of a given time horizon-RCP scenario, the greater the weight of the CA on TWL_{100} value. Pairwise and triple interactions between SLR, RCM and CA are negligible (<2%), which is mainly due to the fact of aggregating TWL_{100} by time-horizon and RCP. SLR contribution (cyan) increases as time and radiative forcing progresses (from 11%, 5%, 9% and 11% in 2045 to
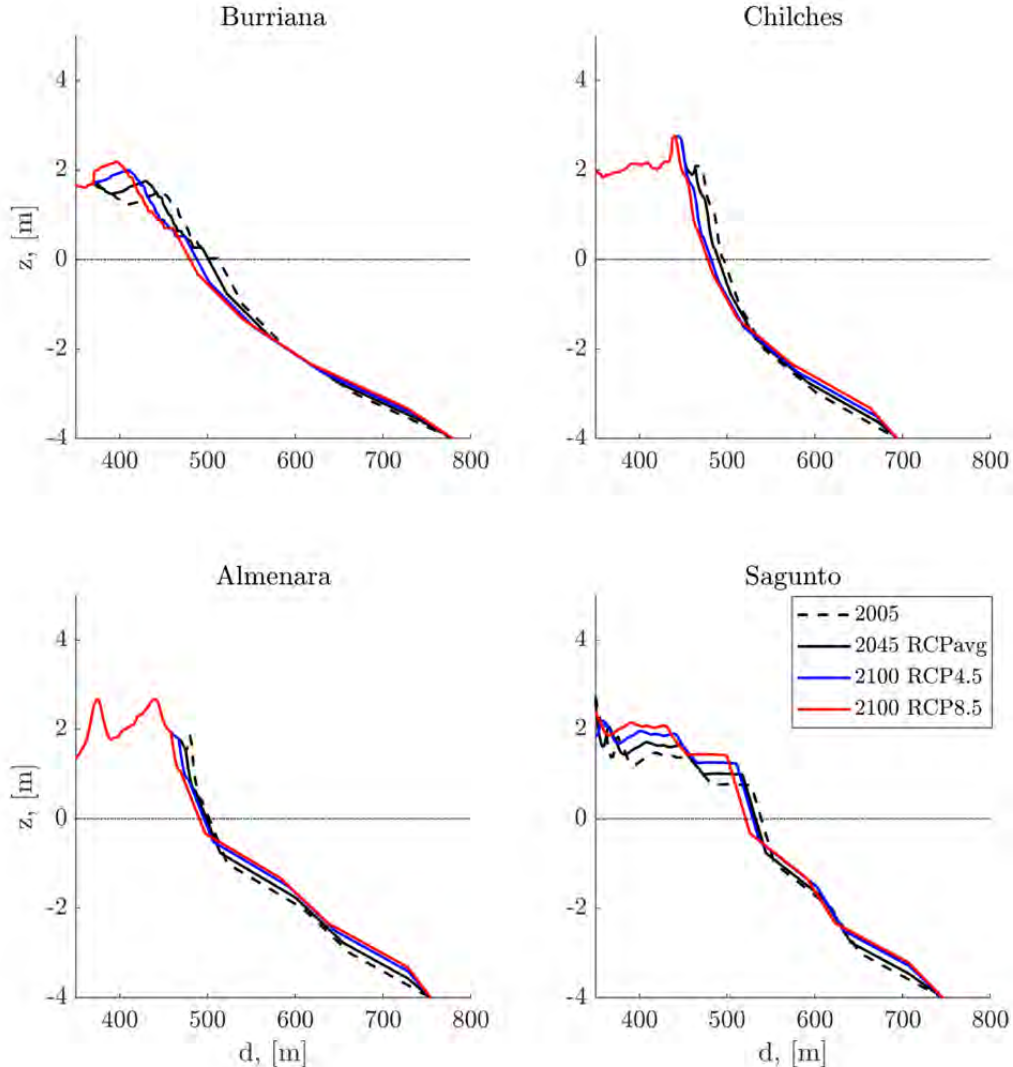
Figure 4.20: Initial XBeach profiles for the different TWL scenarios in Burriana, Chilches, Almenara and Sagunto.

up to 35%, 23%, 55% and 35% in 2100 for Burriana, Chilches, Almenara and Sagunto, respectively). RCM uncertainty governs in Burriana, Almenara and Sagunto in 2005 (75-97% of the total TWL_{100} variance), in 2045 (52-88%) and in 2100 RCP4.5 (65-75% of the total variance).

4.3.7.2. Effects of the coupling approaches on coastal flooding

Following the application of the 2D flood model, coastal flood maps driven by the TWL_{100} and the projected topobathymetries following the full, short-term, long-term
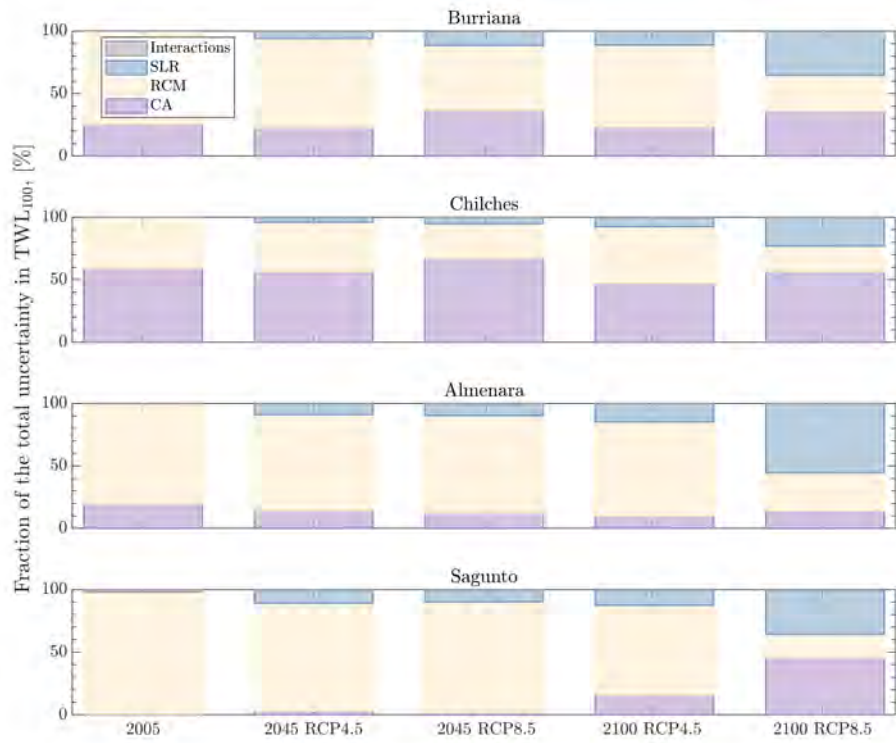
Figure 4.21: Contribution of each uncertainty source and their interactions to the total TWL_{100} uncertainty.

and no CA, are obtained. For brevity, flooded area (FA) ralated to TWL_{100} is referred to as FA_{100}.

Results reveal that in 2100, the top 5 beaches with the largest FA are Corinto (64.64 ha), Moncófar (58.27 ha), Burriana (57.99 ha), Chilches (56.04 ha) and Llosa (52.78 ha) following the full CA. If no CA is applied, the rank changes to Chilches (56.04 ha), Corinto (59.46 ha), Moncofar (57.2 ha), Burriana (57.2 ha) and Canet (48.5 ha) (results averaged across RCMs and RCP8.5 for the 50% SLR percentile). This highlights that neglecting erosion-flooding CA in adaptation planing could lead to erroneous prioritisation of hotspots and subsequent fund allocation, as these beaches are urban and with high degree of social and economic exposure. Figure 4.22 and Figure 4.23 provide some examples of the flood maps obtained. Figure 4.22 show FA_{100} maps in Moncófar and Corinto in 2045 factorised by CA for the RCP4.5 and RCP8.5. These maps correspond to the most unfavourable scenario, as the envelope of outcomes of the 5 RCMs and

the 95% SLR percentile are displayed. In Moncófar, the full CA FA_{100} for the worst RCM-RCP-SLR percentile reaches 44.92 ha (40% of this area is built) in 2045. If the long-term or no CA were applied instead, such FA could be overestimated by 40% and 22% in 2045. The short-term CA provides FA_{100} underestimated by 23% in 2045 with respect to the full CA. The fact that the full CA provides lower FA_{100} values than those of the long-term CA is due to the reduction in TWL_{100} as profile adapts and the low short-term storm erosion values in this beach.
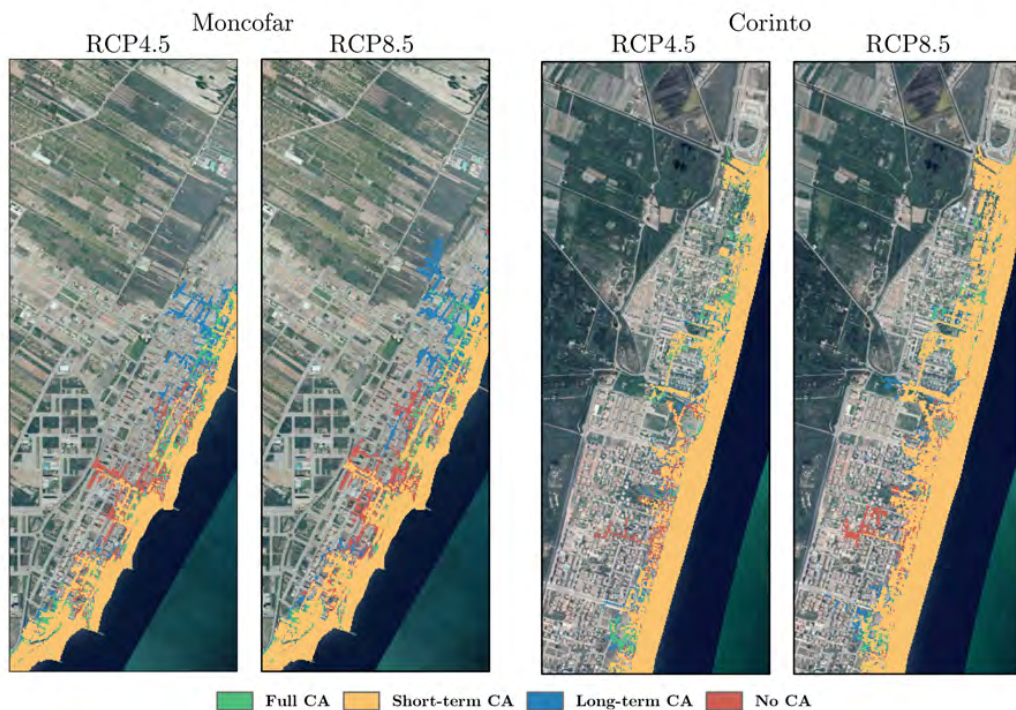
Figure 4.22: FA_{100} in Moncófar and Corinto in 2045 for the RCP4.5 and the RCP8.5, where the colour code refers to the CA. Flood extents correspond to the envelope of RCMs and the 95% SLR percentile.

Figure 4.23 shows FA_{100} maps associated with each CA in Almenara in 2045 for RCP4.5 and the 95% SLR percentile for the different RCMs. From an uncertainty sampling point of view, the full CA and the short-term CA provide the widest and narrowest range of inter-RCM variation (15-27 ha and 16-23 ha respectively). The worst RCM in terms of flooding varies between CAs, with the EART model providing the largest FA_{100} in the full CA (27 ha) and the HADG model for the short-term, long-term and no-CAs (25,

23 and 25 ha respectively).
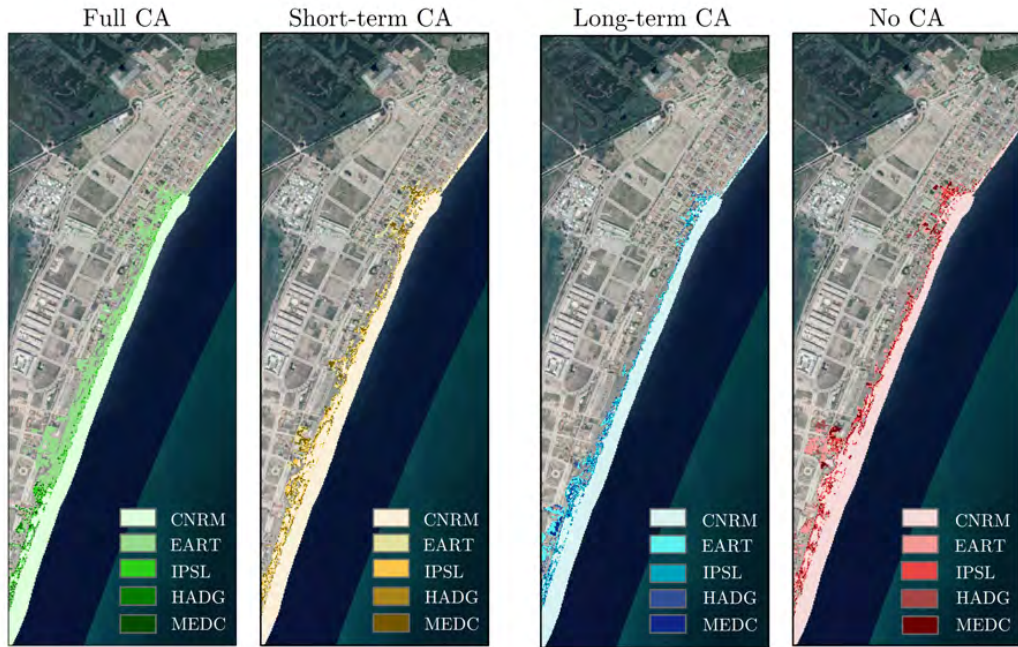
Figure 4.23: FA_{100} in Almenara in 2045 for the RCP4.5 and the 95% SLR percentile factorised by RCM (colour intensity).

As in the case of the TWL_{100}, the effect of CA is analysed on FA_{100}. Following the same examples of Burriana, Chilches Almenara and Sagunto, Figure 4.24 shows the FA_{100} for the different CAs and grouped by time horizon and RCP. In 2005, the influence of the CA in FA_{100} is greater than in TWL_{100}. For instance, in Chilches and Almenara, long-term/no CA can provide overestimated TWL_{100} mean values of approximately 17% and 5% respectively, but underestimated FA_{100} mean values of 32% and 85% respectively, with respect to the full/short-term CA in 2005. On the other hand, in Burriana, the presence of groynes reduces the impact of storm erosion on FA_{100}. As time horizons move away, long-term morphological changes due to SLR and longshore transport increasingly contribute to FA, leading to greater values and larger spread ranges. Regarding the influence of morphology on hydrodynamics, while TWL is mainly affected by cross-shore transport (both short and long term), FA is highly influenced by longshore-driven shoreline changes, which if they imply retreat, can in

turn be enhanced by the long-term SLR profile displacement and storm erosion, reducing protection services provided by the beaches. In contrast to TWL_{100}, the long-term CA provides the highest FA_{100} values in almost every case because it is linked to high TWL_{100} values and long-term shoreline changes, which are great contributors to flooding. On beaches such as Chilches, where there is a promenade that determines the evolution of the beach (especially in the long term), the higher the TWL is, the more overtopping and therefore the more coastal flooding there is. As such, the long-term and no CAs provide projected FA_{100} mean values higher than those of the full CA by 36%-40% and 4%-19%, respectively. For mixed beaches such as Almenara or Sagunto, where only one part has a high degree of anthropisation and the rest is natural, the omission of flooding-erosion interplays can lead with respect to the full CA to either FA_{100} overestimates by approximately 18%-22% (mean values) or underestimates by approximately 15%-16% (mean values) in 2050 and underestimates of up to 22%-25% (mean values) in 2100. Singularities (in both the swash zone and the land over which flood spreads) make it critical to consider the joint impact of erosion and flooding using surveyed profiles, as generalisations (e.g., standard correction factors) do not necessarily apply.

Figure 4.25 allows the visualisation of the relative contributions of SLR percentiles, RCMs and CAs to FA_{100} total uncertainty for the RCPs 4.5 and 8.5 in 2005, 2045 and 2100. The SLR contribution in Buriana, Chilches, Almenara and Sagunto increases for more distant time horizons and higher RCPs, although this effect is smaller for FA_{100} (10-35%, 7-26%, 8-20% and 7-16% respectively in 2100) than for TWL_{100} (11-35%, 7-23%, 14-55% and 12-35% respectively in 2100). The most striking ascpect is the dominating influence of the CA in all these beaches, which is stronger that that of SLR percentiles in 2100 for RCP8.5 (34%, 56%, 65% and 76% of CA versus 35%, 26%, 20% and 16% of SLR, for Burriana, Chilches, Almenara and Sagunto, respectively). This highlights that no matter the effort made to improve waves, storm surges and SLR projections, inaccuracies will occur if no appropriate flooding-erosion coupling is considered. Inter-CA variability at the stage of inland flood modelling is partly inherited by TWL modelling but mostly attributed to the land part of the topobathymetries

modified to account for long-term shoreline changes and storm erosion. It is also worth mentioning the contribution of RCM-CA interactions to FA_{100} uncertainty in Chilches and Almenara in 2045 (up to 4% and 12%, respectively). This interplay has its origin in TWL, as RCP-driven waves are scaled for each CA by foreshore slopes. Differences are small for TWL_{100} but become larger in FA terms due to terrain heights (e.g., if water depth exceeds the height of a defence, flood extent can increase considerably if the area behind the structure has a low elevation level).
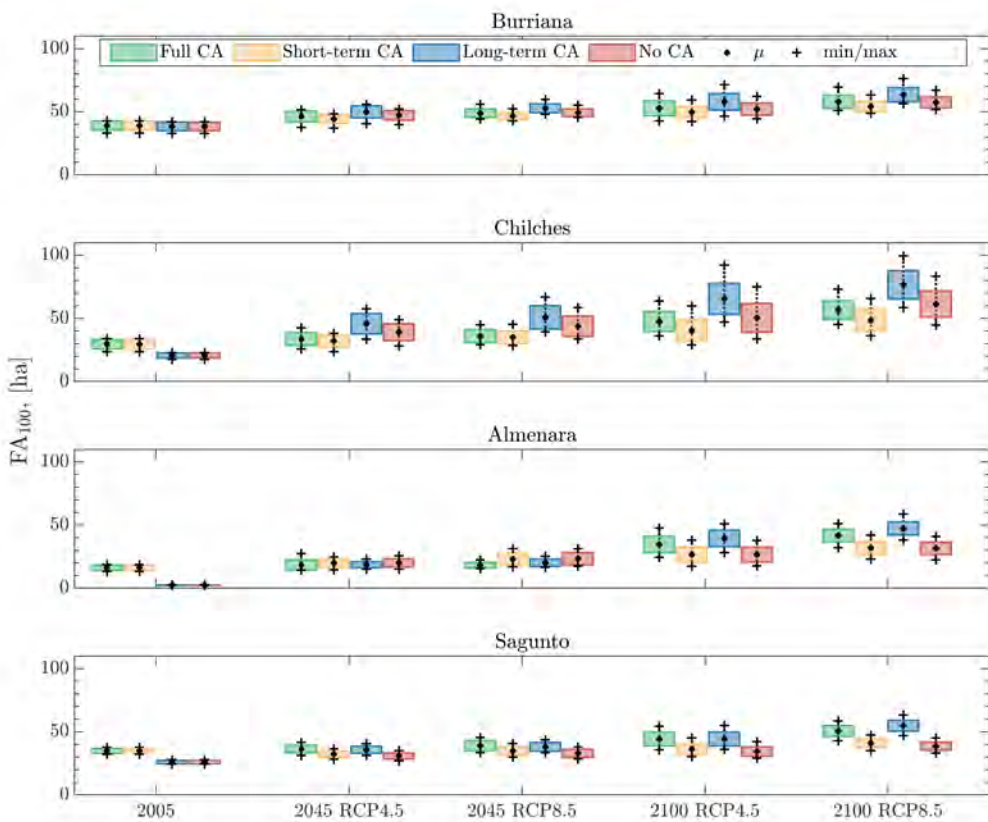
Figure 4.24: FA_{100} value range in Burriana, Chilches, Almenara and Sagunto in 2005, 2045 and 2100 for the RCP4.5 and RCP8.5, where colour code refers to CA, black circles are mean values, crosses are maximum values and box limits represent mean values plus minus the standard deviation.
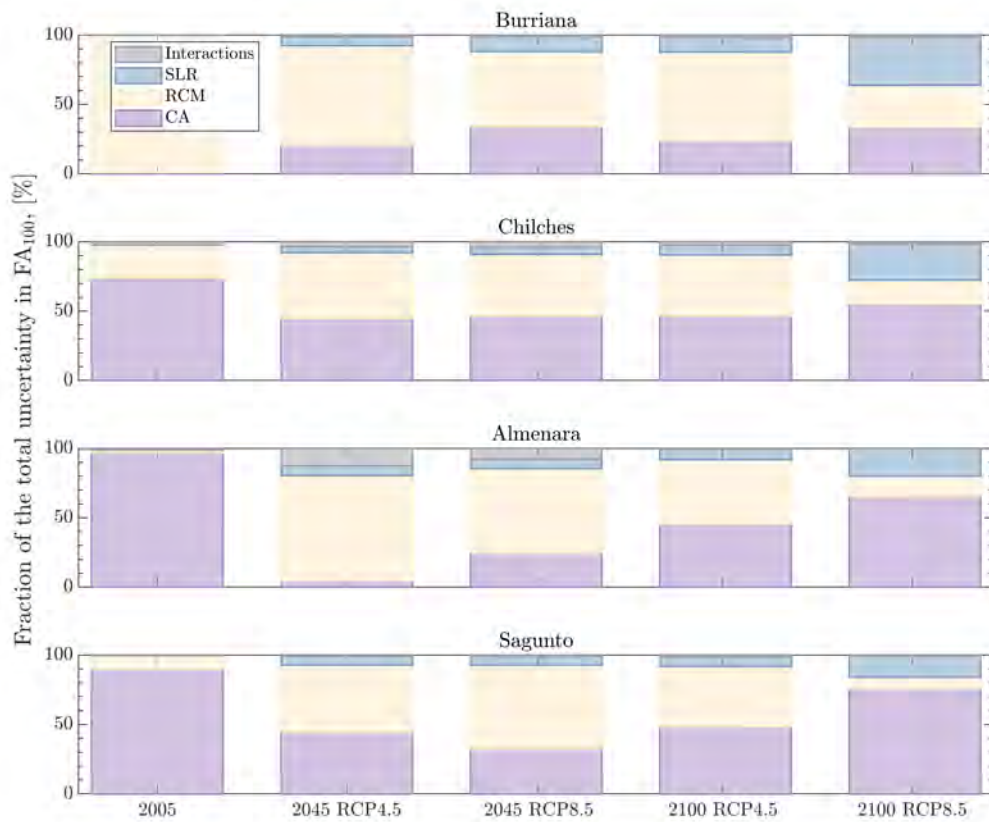
Figure 4.25: Contribution of each uncertainty source and their interactions to total FA_{100} uncertainty.

4.3.8. Summary of the effects of the different erosion couplings on coastal flooding

From the computed effects of the different CAs on TWL and flooded areas, the need to abandon the standard approach of neglecting erosion effects on coastal flooding is stressed. Disregarding erosion-flooding interplays while delineating risk-informed adaptation strategies may imply an erroneous tracking of hotspots and misplaced allocation of funds.

From the analysis presented here, the following specific conclusions are extracted for the TWL:

- In natural coastal areas long-term processes do not trigger major changes on

TWL. Longshore transport does not alter the profile shape and thus, the dissipation properties of a natural profile remain unchanged when subjected to longshore transport. Regarding SLR-induced profile changes, the effects of considering profile kinematics associated with SLR do not alter TWL. Assuming that the profile mimics the upward movement of SLR while retreating to assure volume conservation, the shape of the profile does not change. As the active profile moves upwards following SLR, the swash zone morphology facing the waves acting on top of the raised sea-level is the same as if no SLR occurs.

- In man-made coastal areas, long-term processes may trigger major changes on TWL. Profile changes due to longshore transport and SLR in squeezed areas protected by man-made interventions generate local scour at the base of the defences. The combination of rising sea levels in front of undermined structures triggers a reduction of wave energy dissipation and a subsequent increase of the overtopping power of extreme events.

- Regarding short-term profile changes, coupling hydrodynamics and morphodynamics during extreme events gives lower TWL values than assuming a static profile. When subjected to energetic events, the cross-shore sediment transport from the beachface to the outer bar results in a more dissipative profile adapted to the incoming wave conditions. Thus, in most of the cases, the no and the long-term CA yield greater TWL values than the short-term and the full CA that consider short-term profile adaptation.

- With reference to the weight of the RCM, SLR percentile and CA on the TWL at a given horizon and radiative forcing scenario, the relative influence of the SLR percentile is small ($\approx$10%) for medium-low radiative scenarios (RCP4.5 and lower). However, SLR percentile weight on TWL increases in case of a high radiative scenario at the end of the century ($\approx 20 - 50\%$). RCM and CA significantly influence the value of the TWL but untangling their relative contribution is site- and case-specific. From the results, RCM contribution to TWL_{100} total uncertainty exceeds 50% in most of the beaches. However, just when the effect on TWL of accounting for short-term morphodynamic changes (full CA and short-term CA), significantly differs from the cases where this is not accounted for (no

CA and long-term CA), the CA exceeds the RCM influence on TWL.

Similarly, for the flooded area, the following findings are extracted:

- In natural coasts, long-term processes may trigger major changes on the flooded area. On one hand, longshore processes can generate sediment-starved regions, undermining the beachfront and reducing the protection capacity of beaches against flooding. Similarly, the dune and beach protection service will be reduced due to SLR-induced profile changes and waves propagating on top or raising seas. This is certainly the case when the dune crest elevation is maintained or even reduced while SLR increases.

- In engineered coasts, the critical flood elevation is controlled by an artificial structure which is assumed to be non erodible. Thus, the effects of long-term morphological changes on coastal flooding are mainly due to the increase in wave energy reaching the coast as SLR increases and as the scour at the toe of the structure progresses. From the results, considering long-term profile changes (long-term and full CA) lead to higher flooded areas than when these processes are not considered (no and short-term CA).

- Short-term erosion plays a fundamental role on flooded area. In natural beaches, dune and beach erosion during extreme events may lower the dune crest elevation leaving unprotected low-lying areas. This process yields an opposing effect: while short-term profile adaptation reduces the energy reaching the coast, the beachface and even the dune crest are also eroded and the potential flooded area increases. Determining which of the counteracting effects is dominant is not trivial and requires site and case-specific modelling as it depends on the beach state and on the storm chronology. From the results, short-term profile changes (short-term and full CA) yield lower flooded area estimates in most of the beaches than when these processes are neglected (no and long-term CA). Thus, in this particular case, the reduction on the TWL due to wave dissipation is more significant than the short-term erosion of the dune and beach system for the flooded area. The fact of being an anthropized area protected by non erodible man-made defences and the choice of the reference storm is undoubtedly conditioning this result. When modelling short-term effects in beaches in good condition, flooded area may be

reduced with respect to the standard approach due to the reduction in TWL. However, short-term effects acting on eroded beaches after storm sequences may yield a substantial increase in flooded area with respect to the standard approach. This fact highlights the need for further research in order to define and extrapolate general behavioural rules to other sites.

- With reference to the weight of the RCM, SLR percentile and CA on the flooded area at a given time-horizon and radiative forcing scenario, the relative influence of the SLR percentile is small for the medium radiative scenario (RCP4.5) and increases at the end of the century for the high radiative scenario (RCP8.5) as SLR percentiles diverge. However, SLR percentile weight on FA is smaller than in the case of the CA. The CA influence on FA exceeds the weight of the SLR percentile and the RCM in most of the beaches. The spread range in the CA in mostly attributed to considering or not long-term effects. The relevant weight of the CA on flooded area strengthen the need to consider erosion-enhanced flooding for climate change studies. Neglecting the multi-scale interactions between these processes diminish all the efforts to improve waves, storm surges and SLR projections on flooding characterisation.

4.4. Conclusions

Reliable coastal flood projections are essential for coastal management and climate change adaptation. However, their development remains a challenge in several ways. Coastal flooding does not occur in isolation but is the result of the interaction of complex hydrodynamic and morphodynamic processes at different time scales (hours to decades), which makes it difficult to analyse. In addition, decision-making in this context takes place at the regional level and requires sufficient consideration of uncertainty. Such uncertainty, which needs to be adequately sampled, arises from the choice of radiative forcing scenarios, climate models and mean sea-level rise trajectories and the flood projection modelling itself.

A methodology to develop erosion-enhanced flooding projections is presented. The

methodology is novel as it combines a set of elements in a new way that allows to consider coastal flooding and erosion coupled at the relevant scales and the consideration of uncertainty. It is composed of a suite of statistical, process-based and physics-based models where the main update with respect to the published literature is the development of a regional-scale storm emulator and the procedure for the spatial upscaling of shoreline evolution projections to generate future topobathymetries via a recently developed profile translation tool. The combination of the computationally efficient modelling chain with a thorough uncertainty sampling that considers two different representative concentration pathways, five configurations of global and regional climate models, three trajectories of mean sea-level rise, thousands of multivariate storms and different erosion-flooding couplings underlie the findings of this research in terms of total water level and flooded areas.

This work presents an approach to consider erosion-enhanced flooding at the climate change scale that has potential for improvement. On one hand, the simple translation rules used to upscale the shoreline movement to a two dimensional topobathymetry constitute a potentially inaccurate simplification of reality. The reference storm calculation for the short-term coupling approach does not correspond to any total water level condition used to force the flood model and was chosen as a balanced condition from a computational perspective. Beaches are assumed to be in good condition when modelling short-term effects on coastal flooding. Consideration of storm clustering, as occurs in many coastal sites worldwide, will significantly increase the weight of storm-induced short-term erosion in flooded areas. Also, the shoreline end-of-century projections used to drive morphodynamic evolution are highly uncertain themselves and rely on the assumption that the observed coastal response can be extrapolated to the future. All these shortcomings will be overcome by advances in the computational resources and the availability of long-term topobathymetric datasets via remote sensing to improve our knowledge of the coastal zone and to guide process- and physics-based models. This will enable running high-fidelity simulations to forecast the complete long-term coastal evolution. Until this point, reduced-complexity modelling frameworks, as the one developed in this research work, are the best alternative for risk-informed coastal

226

planning and adaptation to climate change.

CHAPTER 5

DEVELOPMENT OF IH-LANSLOC FOR LOCAL-SCALE STUDIES

In this Chapter, IH-LANS capabilities are extended to project not only the shoreline but the nearshore evolution yielding IH-LANSloc (Figure 5.1). The new version is ideally suited for local-scale analysis of the long-term response of natural and anthropized coasts. IH-LANSloc shares the modelling fundamentals of IH-LANS as it solves the shoreline evolution via a data-assimilated governing equation that accounts for longshore and cross-shore processes. Better process representation is attained as the complex interactions of waves propagating on a changing morphology are considered. This is achieved by using an advanced wave propagation model until the breaking point together with a profile translation tool that updates the bathymetric grid based on shoreline changes. IH-LANSloc is capable of modelling several man-made interventions like nourishments, seawalls, groynes and breakwaters but also the protection provided by natural ecosystems like mangroves, seagrasses or coral reefs. To test the model performance, different coastal settings with man-made interventions and natural ecosystems are simulated synthetically demonstrating the power of IH-LANSloc for coastal management and climate change adaptation in complex environments.
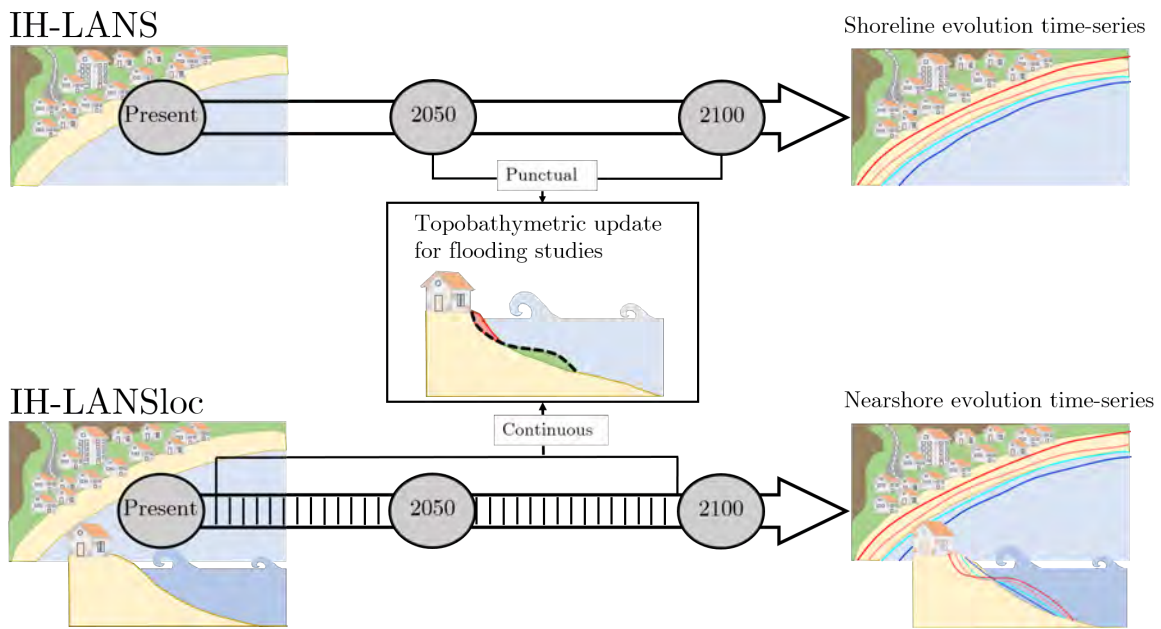
Figure 5.1: Comparison between IH-LANS and IH-LANSloc in terms of modelling outputs.

5.1. Introduction

Hindcasting and predicting how the coastal zone evolves is one of the major challenges in coastal engineering as it requires a deep understanding of the physical processes and their interactions together with accurate continental and oceanic forcings and boundary conditions. Furthermore, climate change adds another difficulty to the problem, namely uncertainty to future drivers, which may lead to an unprecedented coastal response (Wong et al., 2014; Collins et al., 2019).

In spite of the multiple sources of uncertainty conditioning the coastal response (Toimil et al., 2021a), the need to assess the nearshore effects of local adaptation measures is crucial for risk-informed decision-making (Toimil et al., 2020b). To this end, evaluating and ranking different adaptation measures in the context of climate change, requires efficient multi-scale models capable of solving the main physical processes while reducing the uncertainty of the problem. Although some progress has been made in recent years, there is significant room for modelling improvements (Ranasinghe, 2020). The focus should be placed on better representing the processes shaping the coastal system

and its response to hard and soft engineering interventions and nature based solutions, which may be achieved by intersecting the laws of physics and observations (Splinter and Coco, 2021).

When modelling the coastal response, there exist process-based models at different ranges of complexity (Lesser et al., 2004; Roelvink et al., 2009; García-Maribona et al., 2021), which are capable of precisely solving the coupled hydro-morphological evolution at the local scale in the short-term. However, reduced-complexity models are the best suited forecasting tool considering the scale and computational constraints imposed when modelling climate change-induced impacts. In the literature, one of the first multi-process reduced-complexity shoreline evolution model was developed by Vitousek et al. (2017c) (CoSMos-COAST) by combining a transect-based one-line model, a cross-shore model based on (Yates et al., 2009) and SLR-retreat following (Bruun, 1962). Additionally, they implemented a data-assimilation algorithm for filling the knowledge gaps of the coastal system via observations. Payo et al. (2017) created a novel model (CoastME) combining the vector-based one-line model (COVE) of Hurst et al. (2015), the inlet evolution model (ASMITA) of Stive (1998) and the soft cliff evolution model (SCAPE) developed by Walkden and Hall (2011). These models were integrated in a common spatial representation by dynamically altering the digital elevation model. Then, Robinet et al. (2018) developed a reduced-complexity model by combining the 2D cellular one-line model of Ashton et al. (2001) and the cross-shore model of Splinter et al. (2014). Antolínez et al. (2019) created a model (COCOONED) accounting for longshore processes via a transect-based one-line model, a cross-shore model considering short-term fluctuations and SLR following Miller and Dean (2004) and Bruun (1962) and a dune erosion model (Kriebel and Dean, 1993). Then, Roelvink et al. (2020) presented a simplified vector-based model (ShorelineS) capable of modelling complex forms due to alongshore transport alone and Tran and Barthélemy (2020) coupled a one-line model with the ShoreFor model (Splinter et al., 2014). IH-LANS, introduced in Chapter 2 solves for alongshore transport, cross-shore transport including SLR-induced retreat following Toimil et al. (2017a) and included a data-assimilation algorithm that introduced some improvements with reference to the Vitousek et al.

(2017c) model. Additionally, IH-LANS (Alvarez-Cuesta et al., 2021a) is capable of reproducing the shoreline response to anthropogenic interventions like groynes, seawalls, nourishments or breakwaters.

Although Vitousek et al. (2017c); Payo et al. (2017); Robinet et al. (2018); Antolínez et al. (2019); Roelvink et al. (2020); Tran and Barthélemy (2020); Alvarez-Cuesta et al. (2021a) can be used for regional and local-scale modelling, they fail to model wave propagation over uneven bathymetries as they rely on simple one dimensional wave breaking routines. Furthermore, high fidelity spectral representation of wave climate is oversimplified in these models via aggregated spectral parameters, which can lead to spurious descriptions of wave systems (Lobeto et al., 2021b) and their coastal impacts. Robinet et al. (2018) model uses the spectral wave model SWAN (Booij et al., 1999) to obtain breaking waves but the bathymetry is simplified by sweeping a Dean's shaped profile (Dean, 1991) along the coastline. Just IH-LANS and CoSMoS-COAST models are enriched by observations via data-assimilation and thus profit from reduced calibration uncertainty. The coastal response due to man-made interventions is tackled by Robinet et al. (2018); Roelvink et al. (2020); Alvarez-Cuesta et al. (2021a) but none of the models is capable of quantifying the effects of ecosystems like vegetation patches, coral reefs or mangroves regarding wave attenuation and subsequent coastal erosion. Furthermore, the shoreline evolution forecasted by the different models cannot be directly used to produce erosion-enhanced flooding projections.

To overcome these research gaps, an advanced reduced-complexity nearshore evolution model named IH-LANSloc is developed. The model solves the shoreline evolution considering longshore and short-term cross-shore processes as in IH-LANS but breaking waves are obtained by running the SWAN model over a dynamic topobathymetry. The initial topobathymetry is updated incrementally considering the shoreline movement using ShoreTrans (McCarroll et al., 2021), a profile translation tool based on heuristic rules. SLR-induced changes are modelled in ShoreTrans following Atkinson et al. (2018), which proposes a generalization of the Bruunian's response based on laboratory experiments. Thus, IH-LANSloc is born as the sum of IH-LANS, ShoreTrans and SWAN

and enables modelling the complete nearshore evolution over long-term time scales at a similar computational expense of running SWAN alone. IH-LANSloc outputs can be immediately used as the underlying topobathymetry for flooding models. Additionally, the enhanced process description in terms of wave propagation and morphodynamic modelling allows for considering the effects of different man-made interventions and nature-based solutions while model uncertainty is reduced by data-assimilation.

In the upcoming sections, the structure and characteristics of IH-LANSloc are described, emphasizing wave propagation and the topobathymetric update. Then, different synthetic cases are modelled in order to show model functionalities and highlight the power of IH-LANSloc for supporting local-scale coastal management.

5.2. Structure and functionalities of the model

As IH-LANS, IH-LANSloc is founded on three pillars which are an efficient two-step wave transformation, a multi-process shoreline evolution equation that considers long-shore and cross-shore transport and a data-assimilation algorithm for the calibration of free parameters.

The calculation flow diagram of IH-LANSloc is displayed in Figure 5.2. The differences with IH-LANS are highlighted in yellow and consists of the breaking wave propagation using SWAN model (Booij et al., 1999) and the topobathymetry update using ShoreTrans (McCarroll et al., 2021). The first step of the calculation flowchart consists of gathering all the necessary inputs at the study area. Then, the numerical domain formed by the computational grid for the two-step wave transformation needs to be defined together with the low resolution (LR) and high resolution (HR) transect-based shoreline discretization. The LR profiles are the rails of shoreline evolution while the HR profiles are used to update the topobathymetric grid for the area model computation and inherit the information of the LR profiles via distance-based interpolation. This dual discretization is needed as the LR profiles do not have enough resolution to update the terrain model and reducing LR spacing will compromise the numerical

stability of the shoreline evolution equation.

Nearshore waves are calculated at the offshore dynamic grid boundary via a statistical-numerical procedure described in Chapter 2 adapted from Camus et al. (2013). Then, wave and water level time series at the offshore points are further propagated to breaking using SWAN and drive shoreline changes by solving a multi-process shoreline evolution equation that accounts for longshore and cross-shore processes. Shoreline changes and free model parameters are corrected if observations are available via data-assimilation. Next, shoreline changes are transferred to the shoreface via a profile translation tool which considers process-specific heuristic kinematic rules for updating the topobathymetry that is used in the area propagation of the next step. To minimise the computational time, an efficient communication interface between IH-LANSloc and SWAN is developed to transfer the wave properties to the LR transects and the morphological changes from the HR transects to the SWAN grid.

5.2.1. Wave transformation

Wave propagation is done in two steps, Figure 5.3. The first step is the hybrid wave propagation using statistical and numerical tools to efficiently downscale offshore wave climate from global-scale models to the nearshore active domain considering a static offshore bathymetry. The second step propagation is done from the deepest part of the nearshore area to the shore using fully numerical propagation coupled with a dynamic topobathymetry, which changes over time considering erosion. The main difference introduced in this version of the model is that the breaking wave propagation is done using a 2D model instead of the 1D simplification of wave refraction through the Snell's law.

The wave propagation model implemented in IH-LANSloc to calculate breaking is SWAN, but the shoreline evolution model and the topobathymetry update routines are compatible with any other area wave model.

SWAN is a third generation wave model that solves the wave energy conservation equa-

Inputs

| Deep water wave climate | Water levels | Topo-bathymetry | Sediment characteristics | Shoreline observations | Boundary Conditions | Structures properties and nourishments |

Numerical domain definition

Wave transformation I: Hybrid nearshore wave propagation

Shoreline evolution loop

START OF COMPUTATION

Time step ti

Long-term trend?

Sinks and sources?

Wave transformation II: Propagation to breaking with SWAN

Yes

Yes

Calculate shoreline changes due to the long-term trend

Calculate shoreline changes due to sediment sinks and sources

Calculate LST gradients accounting for structures

Calculate cross-shore disequilibrium term

Calculate shoreline changes due to longshore transport

Calculate shoreline changes due to cross-shore transport

Multi-process governing equation

Calculate shoreline predicion at t_i

Shoreline observation?

Yes

Apply data-assimilation algorithm

Advance to next time step, $t_i = t_{i+1}$

No

Update topobathymetry with ShoreTrans

$t_i < t_{end}$

Yes

No

END OF COMPUTATION

Figure 5.2: IH-LANSloc calculation flowchart.

tion with sources and sinks: wind generation, white capping, bottom friction wave-wave interactions, dissipation due to vegetation fields and depth-induced breaking. In this

application, the stationary version is adopted:

$$\nabla[(\boldsymbol{C_g} + \boldsymbol{U})N] + \frac{\partial C_\theta N}{\partial \theta} + \frac{C_\sigma N}{\partial \sigma} = \frac{S_{tot}}{\sigma} \qquad (5.1)$$

where $N(x, y, \theta, \sigma)$ is the action density, θ is the wave direction, σ is the relative frequency, $\boldsymbol{C_g}$ is the wave group velocity in the geographical (x,y) space, $\boldsymbol{U}$ is the current velocity vector, C_θ is the action propagation speed in the $\theta-$space and C_σ is the propagation speed in the $\sigma-$space. Action density $N(x, y, \theta, \sigma)$ is equal to the energy density $E(x, y, \theta, \sigma)$ divided by the relative frequency: $N(x, y, \theta, \sigma) = E(x, y, \theta, \sigma)/\sigma$. The first term represents the change in action in the geographical propagation in space due to shoaling, the second term represents the depth and current-induced refraction, the third term models the frequency shifts due to variations in depth and currents and the term on the right hand side represents sink and source terms due to wind generation, whitecapping dissipation, wave-wave interactions, bottom friction, dissipation due to vegetation and depth-induced breaking.
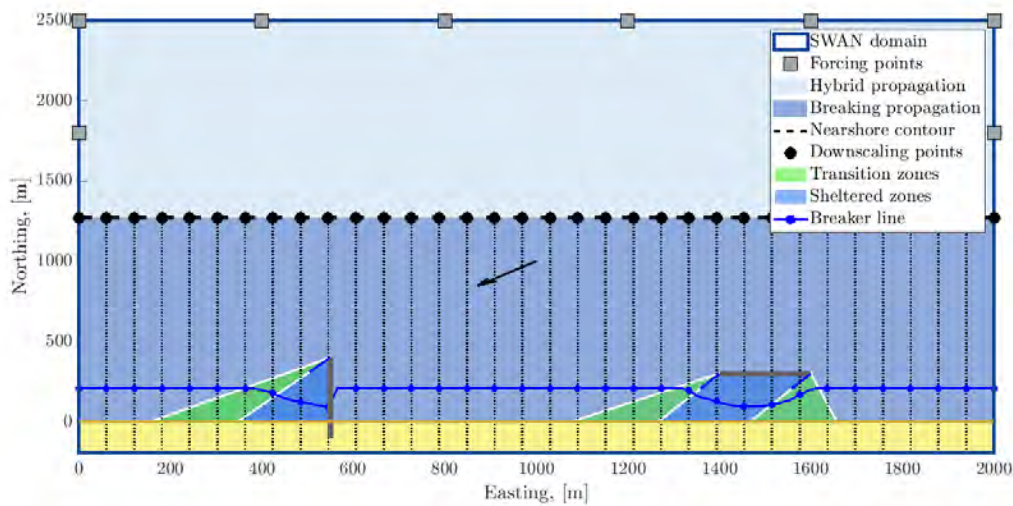
Figure 5.3: Schematic description of the two-step wave propagation.

5.2.2. Shoreline modelling

Total shoreline changes are the result of the sum of longshore and cross-shore contributions modelled at the LR transects (Equation 2.1). Longshore changes are calculated

based on gradients in alongshore sediment transport obtained from the CERC (USACE, 1984) expression, the contribution of sediment sinks or sources and the data-assimilated unresolved processes trend. On the other hand, wave and water level-driven cross-shore transport is modelled based on Miller and Dean (2004). Retreat due to SLR is not modelled following the Bruun's rule but following Atkinson et al. (2018) and considering the surveyed profiles. Additionally the modelling chain is enriched by observations as process-based shoreline outcomes and free model parameters are corrected via a data-assimilation algorithm based on the extended Kalman filter (the reader is referred to Appendix B for further details on the assimilation algorithm).

5.2.3. Topobathymetry update

Shoreline changes are transferred to the topobathymetry using ShoreTrans (McCarroll et al., 2021). ShoreTrans is a rules-based shoreface translation and sediment budgeting model, that updates surveyed profiles accounting for SLR following Atkinson et al. (2018), variations in sediment supply as in the classical one-line theory and storm erosion following Kinsela et al. (2017). The effects of shoreline armouring and non-erodible structures are also taken into account according to Beuzen et al. (2018). ShoreTrans is applied to the HR transects that inherit the longshore and cross-shore retreats from IH-LANSloc LR profiles and updates their geometry integrating the profile response to SLR. The numerical implementation of ShoreTrans is described in Section 4.2.2.

5.2.4. Bidirectional coupling of SWAN and IH-LANSloc

In order to couple IH-LANSloc and the 2D area wave model efficiently, a fast communication interface needs to be established between the numerical models. IH-LANSloc needs the wave characteristics from the SWAN grid at the computational LR transects to identify the breaking parameters and run the shoreline evolution governing equation. On the other hand, SWAN requires the updated topography grid from the IH-LANS HR transects. These exchanges are needed at every time step, so inefficient algorithms could dramatically increase the computational time. To this end, a simple routine is implemented in IH-LANSloc based on geometrical interpolation. Taking profit from

the fixed transect-based numerical discretization of IH-LANSloc, the position of the IH-LANSloc transects with respect to the SWAN grid does not change in time so two unique transformation matrices (one for each coupling direction IH-LANSloc-SWAN) are calculated at the beginning of the simulation and reused every time step. Thanks to this, a spatial field of a given quantity in SWAN is automatically transferred to the IH-LANSloc LR profiles by a simple multiplication. Similarly, the updated IH-LANSloc HR profiles are directly transferred to the SWAN grid by simple and fast predefined arithmetic operations.

The principle of geometric interpolation requires a domain Ω that can be discretized in subdomains $\sum \omega_i$ defined by their k vertices, (Figure 5.4a). Then, an interior point $\boldsymbol{x}$ can be defined by the coordinates of the containing element:

$$\boldsymbol{x} = \sum_k \hat{\gamma}_k(x, y)\boldsymbol{x_k} \tag{5.2}$$

where $\hat{\gamma}_k(x, y)$ are the geometric shape functions.

In the case of a triangular elements, the three geometric shape functions can be expressed in a reference triangular element:

$$\boldsymbol{x} = \sum_{k=1}^{3} \gamma_k(\xi, \eta)\boldsymbol{x_k} \tag{5.3}$$

Considering an affine transformation (Figure 5.4b), the general form of the shape functions and their properties are:

$$\gamma_k(\xi, \eta) = a_k\xi + b_k\eta + c_k, \quad \begin{cases} \gamma_k(\xi_l, \eta_l) = \delta_{kl} \\ \sum_k \gamma_k(\xi, \eta) = 1, \ \forall(\xi, \eta) \end{cases} \tag{5.4}$$

Thus, the shape functions in the reference element are:

$$\gamma_1 = \xi, \quad \gamma_2 = \eta, \quad \gamma_3 = 1 - \xi - \eta \tag{5.5}$$

The relationship between the real element coordinates (x_k, y_k) and the coordinates of
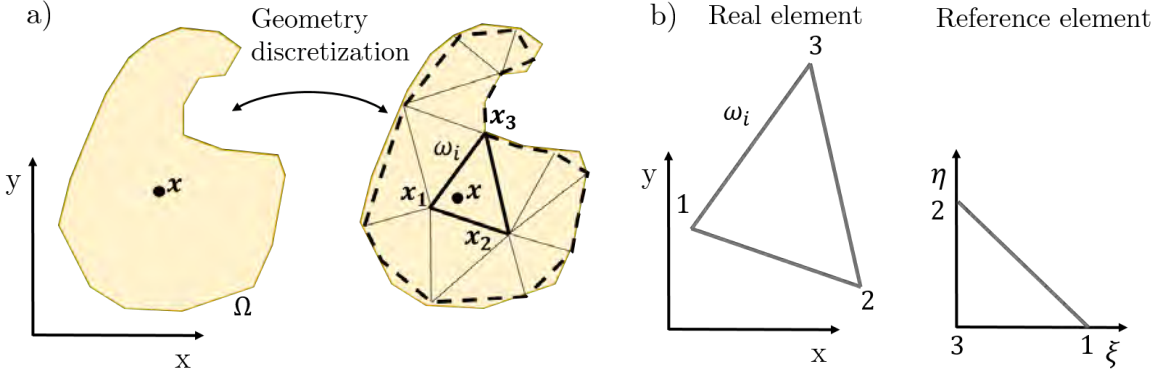
Figure 5.4: Schema of the geometric interpolation.

the reference element (ξ, η) is obtained by combining Equations 5.2 and 5.5:

$$\begin{bmatrix} \xi \\ \eta \end{bmatrix} = \frac{1}{det(\boldsymbol{J})} \begin{bmatrix} (y_2 - y_3)(x - x_3) + (x_3 - x_2)(y - y_3) \\ (y_3 - y_1)(x - x_3) + (x_1 - x_3)(y - y_3) \end{bmatrix} \tag{5.6}$$

where $det(\boldsymbol{J})$ is:

$$det(\boldsymbol{J}) = (x_1 - x_3)(y_2 - y_3) + (y_1 - y_3)(x_3 - x_2) \tag{5.7}$$

Thus, considering a wave model grid of any kind (structured or non-structured) formed by a set of w points and a set of transects defined by t LR points, a matrix $\boldsymbol{WT}$ is formed to transfer the wave properties evaluated at w points to the t LR points. The transfer matrix $\boldsymbol{WT}$ has t rows, one per transect point, and six columns corresponding to the three indices of the containing triangular element formed by the wave points and the three weights $\gamma_{\boldsymbol{WT}}$ associated with each of the three containing points and calculated following Equations 5.5, 5.6 and 5.7:

$$\boldsymbol{WT}_i = [w_{i,1}, w_{i,2}, w_{i,3}, \gamma_{\boldsymbol{WT}_{i,1}}, \gamma_{\boldsymbol{WT}_{i,2}}, \gamma_{\boldsymbol{WT}_{i,3}}]; \tag{5.8}$$

where $w_{i,l}$ denotes the vector position of the l vertex of the element containing the point t_i and $\gamma_{\boldsymbol{WT}_{i,l}}$ its weight. Given a scalar field P evaluated at the w grid points and considering the same interpolation scheme used for the geometry, the interpolated P_{t_i}

value at a point t_i is:

$$P_{t_i} = \gamma_{\boldsymbol{WT}_{i,1}} P_{w_{i,1}} + \gamma_{\boldsymbol{WT}_{i,1}} P_{w_{i,2}} + \gamma_{\boldsymbol{WT}_{i,1}} P_{w_{i,3}} \tag{5.9}$$
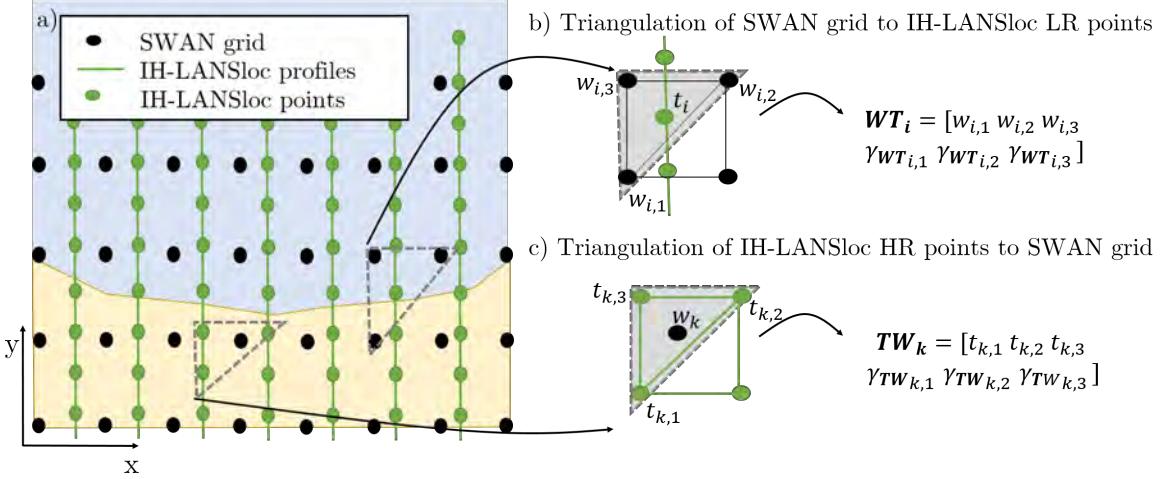
Figure 5.5: Interpolation scheme for the bidirectional coupling. For the ease of visualization, just a set of profiles and points are displayed in the figure. However part b) uses IH-LANSloc LR points while part c) employs IH-LANS HR points.

The matrix $\boldsymbol{WT}$ is calculated at the beginning of the simulation and then reused every time-step. Similarly, a $\boldsymbol{TW}$ matrix is assembled and enables transferring the properties from the t HR transect points to the wave grid data points. In this case, the $\boldsymbol{TW}$ matrix is formed by w rows, one per wave point and six columns: three for identifying the position of the t HR points enclosing the wave points and the associated weights. A schema of the procedure is displayed in Figure 5.5.

In order to calculate the breaking wave properties driving shoreline change, the scalar fields of significant wave height (H_s), mean and peak period (T_m, T_p), mean wave direction (θ) and percentage of breaking waves (Q_b) are transferred to the transect points via the $\boldsymbol{WT}$ matrix. The breaking wave properties $[H_{sb}, T_{mb}, T_{pb}, \theta_b]$ used for shoreline modelling are defined when the percentage of breaking waves Q_b exceeds a certain user-defined threshold. Then, the multi-process shoreline evolution equation is solved (Figure 5.2), the geometry of the computational transects is updated accordingly and this information is used to generate a new topobathymetric grid for the next time-step

via the $\boldsymbol{TW}$ matrix.

5.3. Modelling the effects of man-made interventions and natural ecosystems on shoreline evolution

Coupling IH-LANS and SWAN allows for better process representation which enables to model how man-made interventions and natural features influence the nearshore evolution. Groynes, breakwaters, seawalls, nourishments, rocky outcrops, coral reefs or vegetation fields are handled in IH-LANSloc by rigorous process-based modelling. Table 5.1 summarizes the different coastal features included in the model and how they impact the nearshore evolution by altering wave propagation and/or sediment transport. In the next subsection, further details regarding the implementation of the coastal features in IH-LANSloc are explained.

Feature	Wave propagation	Sediment transport
Groynes	Subgrid obstacle	Time-varying bypass coefficient
Breakwaters	Subgrid obstacle	-
Seawalls	-	Realistic boundary condition
Nourishments	Bathymetry change	Source term
Rocky outcrops	Subgrid obstacle / bathymetry change	-
Coral reefs	Subgrid obstacle / bathymetry change and increased bottom friction	-
Vegetation patches	Dissipation term	-[1]

Table 5.1: Modelling characteristics of the different coastal features inclued in IH-LANSloc.

5.3.1. Man-made interventions

Following IH-LANS, four different man-made interventions are implemented in IH-LANSloc by altering wave transformation and/or sediment transport. While the sediment transport effects of the man-made interventions in IH-LANSloc are inherited from

---

[1]In the current implementation of IH-LANSloc the sediment trapping effect of the vegetation is not considered.

IH-LANS, man-made wave-blocking features are modelled taking profit from SWAN obstacle implementation.

Groynes are shore-perpendicular structures that alter wave propagation by creating a shelter area in their lee side and compartmentalise the coast by blocking sediment transport. Their effect on wave propagation is modelled by a subgrid obstacle that blocks wave energy based on the transmission coefficient K_t. K_t can be a user-defined parameter ranging from 0 (impermeable structure) to 1 (permeable structure). In case of low-crested structures it can be calculated based on the formulation of d'Angremond et al. (1996):

$$K_t = -0.4\frac{F}{H_i} + 0.64\left(\frac{B_k}{H_i}\right)^{-0.31}(1 - \exp^{-0.5\xi_p}) \tag{5.10}$$

where B_k is the crest width of the structure, H_i is the incident wave height and $\xi_p = \tan\frac{\alpha}{\sqrt{H_i/L_{0p}}}$ is the Iribarren number, F is the freeboard and α the slope of the structure. Groynes also alter sediment transport by blocking the amount of sediment flowing from one computational cell to the next one. The proportion of solid flow trapped depends on the length of the groyne in the seaward side and the surfzone width following Equation 2.4.

Similarly, breakwaters are shore-parallel structures that stabilize the coast by creating a shelter area in their lee side without blocking sediment transport. They are also modelled as subgrid obstacles in SWAN via a user-defined transmission coefficient or by the d'Angremond et al. (1996) formulation.

An example of wave propagation in SWAN considering structures modelled as subgrid obstacles is displayed in Figure 5.6. In this case, the groynes are assumed to be impermeable ($K_t = 0$) while the breakwater blocks 60% of incoming wave energy ($K_t = 0.4$). The black line represent the breaking line and the dark arrows and the coloured circles the wave direction and have height at the breaking point used to feed the shoreline evolution governing equation. It is noticeable how the breaking line advances towards the coast, as wave height decreases, due to the sheltering effect exerted by the structures.
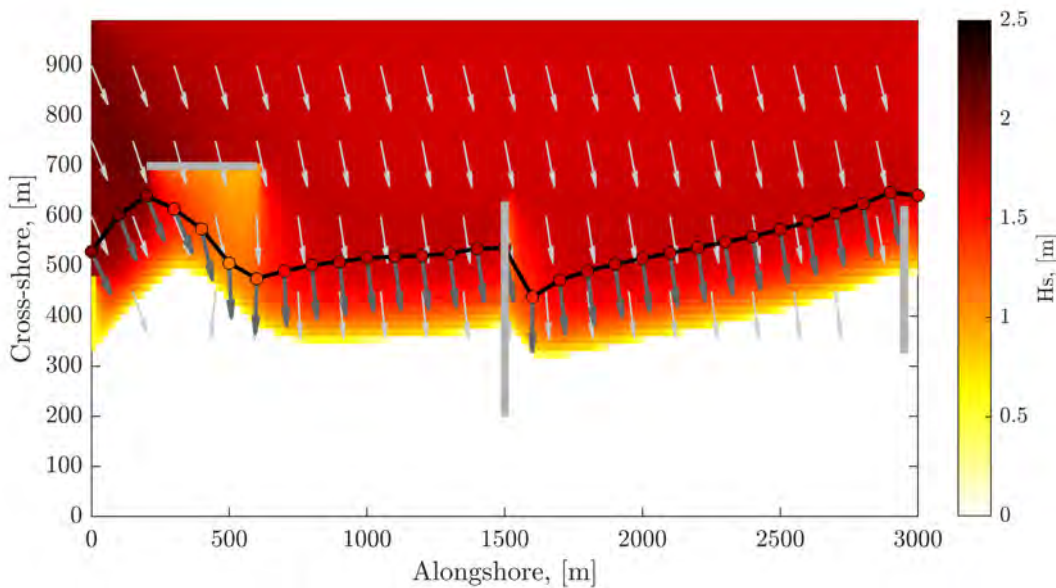
Figure 5.6: Example of propagation considering man-made structures and its breaking line.

Seawalls are coastal defences built in order to prevent shoreline retreat without altering wave propagation. They are modelled by altering sediment transport so as to ensure that the shoreline does not surpass the defence following Equation 2.5 as proposed by Hanson and Kraus (1986). Additionally, scouring due to the combination of SLR and/or storm retreat in front of a seawall is taken into account by the profile model following Beuzen et al. (2018) as described in Section 4.2.2.

Nourishments are integrated in the model as a source term in the shoreline evolution governing equation 2.1. The shoreline position upscales to the nearshore bathymetry via the profile translation tool and thus, wave propagation is also affected.

5.3.2. Rocky outcrops and coral reefs

While rocky outcrops modify wave propagation by blocking the energy transfer to the nearshore, coral reefs also induce wave dissipation due to breaking and an increase in bottom friction in their influence area. The energy passing through a rocky outcrop or a coral reef can be modelled in two ways: 1) via the transmission coefficient K_t following d'Angremond et al. (1996) or 2) via a real topobathymetric feature.

Additionally, coral reefs dissipate wave energy due to bottom friction. This is modelled via a sink term (S_{bf}) in Equation 5.1 defined as:

$$S_{bf} = -C_b \frac{\sigma^2}{g^2 \sinh^2 kd} E(\sigma, \theta) \tag{5.11}$$

where C_b is the bottom friction coefficient. Considering the formulation of Madsen et al. (1988), C_b is:

$$C_b = f_w \frac{g}{\sqrt{2}} U_{rms} \tag{5.12}$$

in which U_{rms} is:

$$U_{rms}^2 = \int_0^{2\pi} \int_0^\infty \frac{\sigma^2}{\sinh^2 kd} E(\sigma, \theta) d\sigma d\theta \tag{5.13}$$

f_w is a non-dimensional friction factor:

$$\frac{1}{4\sqrt{f_w}} + \log_{10}\left(\frac{1}{4\sqrt{f_w}}\right) = m_f + \log_{10}\left(\frac{a_b}{K_N}\right) \tag{5.14}$$

where $m_f = -0.08$, K_N is the bottom roughness length scale and a_b is a representative near-bottom excursion amplitude:

$$a_b^2 = 2 \int_0^{2\pi} \int_0^\infty \frac{1}{\sinh^2 kd} E(\sigma, \theta) d\sigma d\theta \tag{5.15}$$

An example of wave propagation over a coral reef is displayed in Figure 5.7. The reef is defined by the reef flat $B_{rf} = 50$ m, the reef base $B_r = 100$ m, the freeboard $h_r = 3$ m and the bottom roughness length scale $K_N = 0.3$ m. The reef is placed along the -6m contour line on the left side of the bay. It is modelled as a subgrid element following d'Angremond et al. (1996) formulation and bottom friction is considered as proposed by Madsen et al. (1988). Wave height and direction fields are shown and the breaking line properties for shoreline modelling are highlighted. The spatial fields evidence the sheltering effect done by the coral reef, which also translates to a breaking line displaced towards the coastline as wave height decreases.
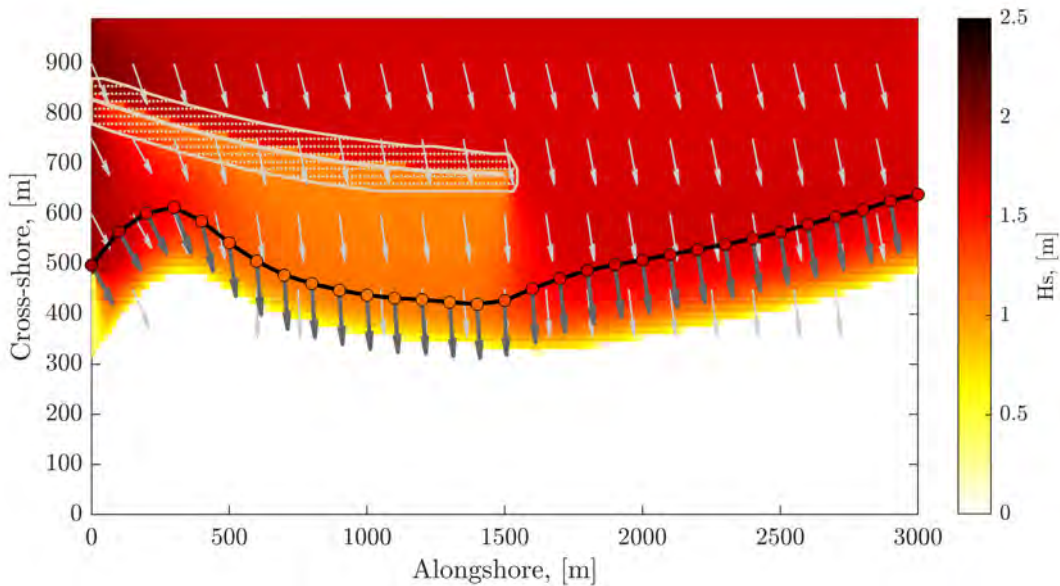
Figure 5.7: Example of propagation over a coral reef and its breaking line.

5.3.3.   Vegetation

Vegetation fields (mangroves, salt marshes, seagrasses, ...) induce wave damping, which is modelled in SWAN following the stratified version of the Mendez and Losada (2004) formulation proposed by Suzuki et al. (2012). This is included in Equation 5.1 through a dissipation term S_v in the frequency-direction space:

$$S_v(\sigma, \theta) = \frac{D_{tot}}{E_{tot}} E(\sigma, \theta) \tag{5.16}$$

Following Mendez and Losada (2004), D_{tot} is:

$$D_{tot} = -\frac{1}{2g\sqrt{\pi}} \overline{C}_D b_v N_v \left(\frac{g\overline{k}}{2\overline{\sigma}}\right) \frac{\sinh^3 \overline{k}\alpha h + 3\sinh \overline{k}\alpha h}{3k\cosh^3 \overline{k}h} H_{rms}^3 \tag{5.17}$$

where $\overline{\sigma}$ is the mean spectral frequency, $\overline{k}$ is the mean spectral wave number, $\overline{C}_D$ is the bulk drag coefficient, b_v is the stem diameter of the plant, αh is the plant height and N_v is the number of plants per square meter.

In order to show how vegetation patches influence wave propagation, a SWAN simulation is displayed in Figure 5.8. Both vegetation patches are defined by the drag

coefficient $C_D = 0.2$, the plant height $\alpha h = 3$ m, the plant width $b_v = 0.1$ m and the number of plants per square meter $N_v = 40$. Wave height and direction fields are shown and the breaking line properties for shoreline modelling are highlighted. The spatial fields evidence the sheltering effect done by the vegetation, which also translates to a breaking line displaced towards the coastline as wave height is dissipated.
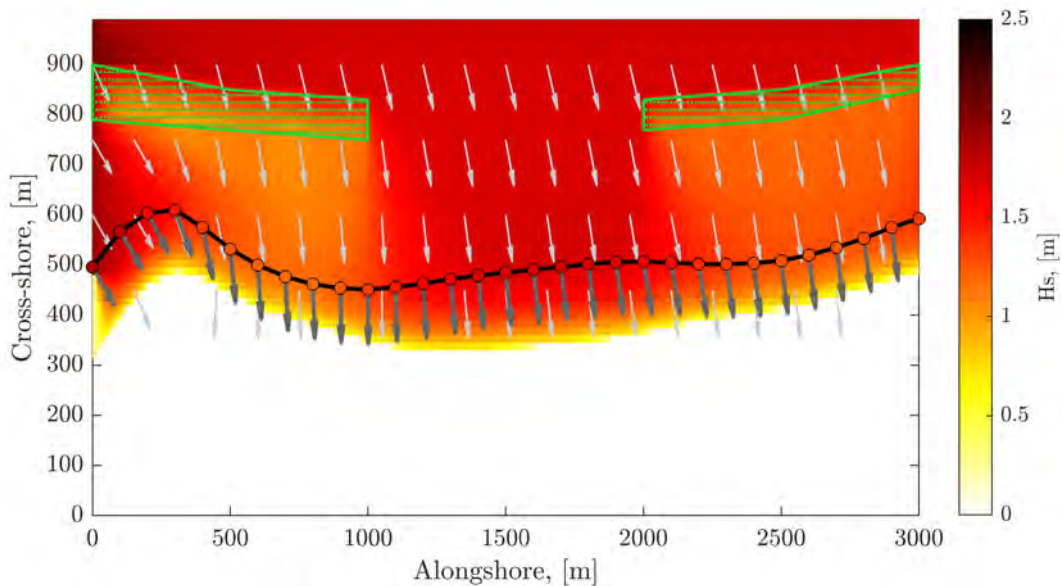
Figure 5.8: Example of propagation over a vegetation patch and its breaking line.

5.4. Synthetic cases

In order to test the ability of the model to handle different coastal features, four synthetic configurations are designed: 1) a base case without structures or natural ecosystems, 2) a case including structures, 3) a case including a coral reef and 4) a case including vegetation patches. In all these cases, the initial bathymetry, wave forcing and boundary conditions are the same and the only difference is the type of coastal feature introduced in the model.

The initial morphology modelled in the cases is a parabolic bay 3 km long. The bathymetry follows an equilibrium Dean's profile (Dean, 1991), the linear foreshore

slope is $\tan \beta_f = 0.05$, the berm height is $B = 3$ m and the depth of closure is $d_c = -5$ m. Wave climate at the boundaries of the nearshore domain is assumed constant and defined by a JONSWAP spectrum of $H_s = 2$ m, $T_p = 12$ s, $\theta_m = -40°$, peak enhancement factor $\gamma = 3.3$ and directional spreading $s = 30°$. No sediment exchanges occur on the left side (null Dirichlet flow boundary condition) but the line is hold in the right side (null Neumann flow boundary condition), enabling the sediment to exit the domain. So as to run IH-LANSloc, a SWAN grid of 15×15 m resolution is constructed and forced in all the three sea-side boundaries. The low resolution LR transects used to solve the shoreline evolution governing equation are spaced 100 meters while the high resolution HR transects that guide the topobathymetry update are 10 meters apart of each other. In this particular application, just longshore transport is considered and it is evaluated on a monthly basis considering a longshore transport constant of $K_1 = 50$ $m^{1/2}/day$.

The different cases are displayed in the first column in Figure 5.10 and the modelling key parameters of every case are summarized in Table 5.2. The first row represents the base case. The effect of man-made structures (groynes and breakwaters) is evaluated in the second case. Groynes are considered impermeable $K_t = 0$ while the breakwater transmission coefficient is set to 0.4. The third case consists of a coral reef placed along the -6 meters contour line spanning the left half of the bay. The coral reef geometrical parametrisation is taken from Escudero et al. (2021) and is determined by the reef flat width $B_{rf} = 50$ m, the reef base width $B_f = 100$ m and the reef freeboard $h_r = 3$ m. In order not to alter the bathymetry with respect to the base scenario, wave transmission over the reef is modelled following the low-crested structure formulation of d'Angremond et al. (1996). The increase in bottom friction in the influence area of the reef is taken into account by the bottom roughness length scale $K_N = 0.3$ m, which is in the same value range as found by Filipot and Cheung (2012). In case of sandy bottoms, the roughness length scale is $K_N = 0.05$ m. The fourth case considers two vegetation patches placed at the left and right margins of the -7 contour line. The vegetation patches are defined following one of the examples in Mendez and Losada (2004), where the drag coefficient is set to $C_D = 0.2$, the plant height is $\alpha h = 3$ m, the

plant width is $b_v = 0.1$ m and the number of plants per square meter is $N_v = 40$.

Case	Key parameters	Reference
Base	-	-
Structures	$K_{t,groyne} = 0$, $K_{t,breakwater} = 0.4$	-
Coral reef	$B_{rf} = 50$ m, $B_f = 100$ m, $h_r = 3$ m, $K_N = 0.3$ m	Escudero et al. (2021) Filipot and Cheung (2012)
Vegetation	$C_D = 0.2$, $\alpha h = 3$ m, $b_v = 0.1$ m, $N_v = 40$	Mendez and Losada (2004)

Table 5.2: Key parameters used to include the effects of the different coastal settings in wave modelling.
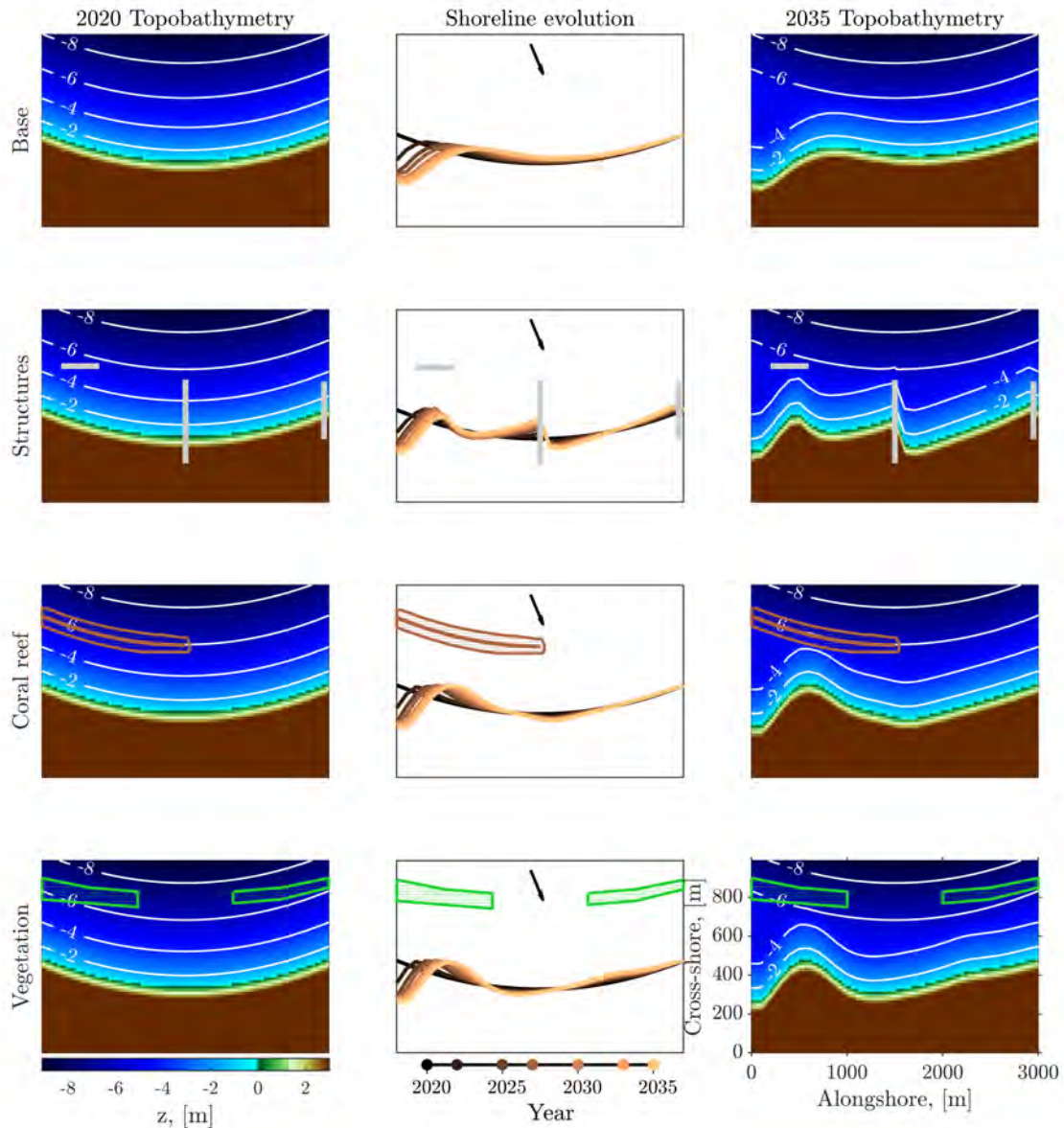
Figure 5.9: Configuration and results of the synthetic cases.

The shoreline evolution at different dates for the different cases is displayed in the second column in Figure 5.10. In every scenario, oblique wave incidence triggers a rightwards longshore transport that generates erosion in the left part of the bay. Placing man-made structures following the arrangement of the second synthetic case reduces the shoreline retreat in the left corner and compartmentalizes the bay by creating two isolated systems. However, the behaviour of the two compartments is the same, as they both tend to realign following the mean energy flux of the incoming waves. The third case shows how the coral reef acts as a submerged breakwater by limiting the energy reaching the coastline. The shoreline follows the same pattern as the base case but smoothed due to the smaller longshore transport and with a slight erosion highlighting the end of the coral reef sheltered area. Similarly, vegetation patches dissipate wave energy and limit potential longshore transport. In this case, a concave shape is formed in the middle of the bay, as it is not protected by the vegetated patches of the left and right extremes.

The third column in Figure 5.10 displays the final topobathymetry in 2035 for the different cases. It is clear how morphological changes do only occur in the active nearshore area, from the depth of closure to the berm. Due to the alignment of the breakwater, the coral reef and the vegetation patches and the longshore transport direction, a salient is formed in the left part of the bay. Looking at the behaviour of the right part, the second synthetic case achieves an orientation nearly in equilibrium with incoming waves. This is attained because the two halves of the bay are isolated by a groyne that blocks the longshore transport. The coral reef does not alter the shoreline evolution of the right half much while the location of the vegetation patches have an impact on the nearshore evolution by creating three zones, two of them protected from waves by vegetation and the central one which is totally exposed.

In order to quantitatively assess the effects of the different features on the nearshore evolution, three erosion indicators are extracted: the mean breaking wave height calculated as the mean in time and space of all the LR transects, the eroded volume and the shoreline retreat at the first transect in the left. Results are shown in Figure 5.10 and highlight how the offshore wave height of 2 m yields a mean breaking wave height

in the computational LR transects of 1.7 m in the base case, which reduces to 1.6 m in case of man-made structures are built and to less than 1.5 m when natural ecosystems are present. Similarly, the eroded volume in the base case of 680 dam^3 is greatly minimised in the rest of the cases reaching 450 dam^3 in the case with vegetation patches. Regarding the left transect retreat, the base scenario attains 250 m in 15 years, which is reduced by 30 to 40 m in presence of man-made structures, coral reefs or vegetation.
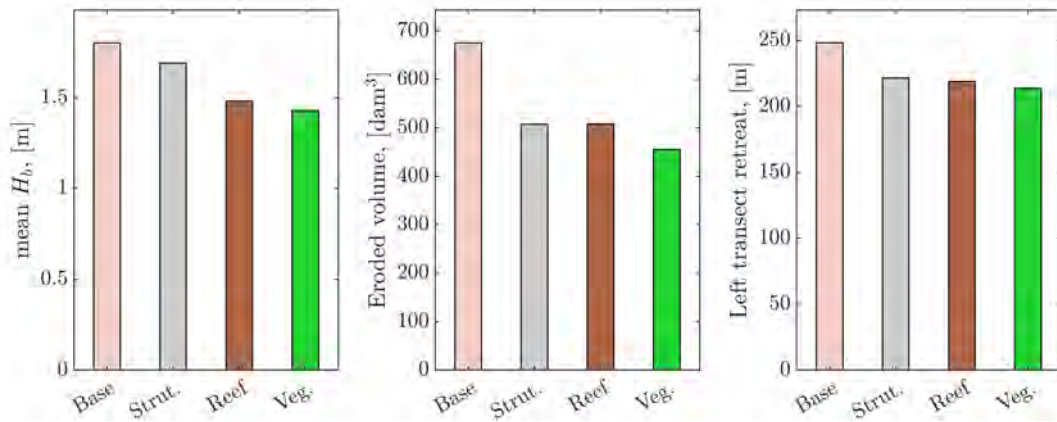
Figure 5.10: Comparison of erosion indicators for different configurations.

5.5. Conclusions

A novel nearshore evolution model named IH-LANSloc is presented and tested in synthetic cases. The model combines the shoreline evolution model IH-LANS, the profile translation model ShoreTrans and the spectral wave propagation model SWAN to achieve a high-fidelity description of the multi-scale morphodynamic evolution. Due to this enhanced process representation, a wide variety of coastal features ranging from man-made interventions to ecosystem services can be integrated in the analysis by considering their effects in wave propagation and sediment transport. Nearshore response to SLR distances from the Bruun's rule by employing heuristic kinematic rules applied to surveyed profiles validated under laboratory conditions. Also, the model can be enriched by observations following the data-assimilation algorithm inherited from the original IH-LANS implementation. The novel functionalities are tested in four synthetic cases proving the ability of IH-LANSloc of handling a wide variety of coastal features

representative of the sandy beaches.

The model provides the shoreline evolution but also the topobathymetry changes of the active zone, which implies that IH-LANSloc outputs can be directly used to model storm impacts or flooding (Gouldby et al., 2008; Roelvink et al., 2009; Leijnse et al., 2021). IH-LANSloc implementation is modular, so improved formulations, additional process parametrizations or data-assimilation schemes can be easily integrated.

IH-LANSloc incorporates efficient coupling routines between the different models so as to minimise the computational time, which is mainly constrained by the SWAN simulation. However, a centennial simulation at a spatial scale of several kilometers can take between 6-10 hours to complete, which is still compatible with the needs for uncertainty sampling in climate change-related studies.

The model can be used for assessing the coastal response in beaches affected by groynes, breakwaters or seawalls. Additionally, coastal areas with natural elements like rocky outcrops or coral reefs can be modelled. The coastal response to different coral reef bleaching scenarios and the protection benefits provided by mangroves or seagrass regarding coastal erosion can be evaluated. The model can also be used to evaluate different adaptation measures including classical engineering interventions, nature-based solutions or a combination of both. Thus, the model is a promising tool for forecasting relevant nearshore processes into the future and for assessing the performance of different adaptation strategies at most of the world's sandy coastlines in the context of climate change.

CHAPTER 6

CONCLUSIONS AND FUTURE WORK

6.1. Conclusions

In this work, an impact assessment framework composed of different models, tools and methodologies has been developed to improve erosion and flooding risk assessments and support climate change adaptation. The essential keystone of the research is the understanding of the main morphological processes occurring in the nearshore area at the long- and short-term time scales and their interactions through the development of a shoreline evolution model. The model is subsequently used to forecast the shoreline evolution and to provide the terrain boundary condition for erosion-enhanced flooding projections. The shoreline evolution model has been described in Chapter 2 and is capable of solving the relevant processes, the effects of man-made interventions and combines the physics-based equations with observations to achieve a better and more accurate response of the coastal zone. The model has been used to project the shoreline evolution considering the climate-related uncertainty sources yielding relevant information for risk-informed decision making and climate change adaptation in Chapter 3. Then, in Chapter 4, starting from the shoreline evolution projections, a novel methodology to generate erosion-enhanced flooding projections has been implemented. This has been done by upscaling the one-dimensional changes obtained from the shoreline

model to generate a two-dimensional erosion-updated topobathymetry considering long- and short-term morphological changes. Finally, in Chapter 5, all the advances in the research work have been wrapped up in a novel model capable of projecting not only the shoreline evolution but the nearshore topobathymetry while handling most of the sandy coastal settings worldwide.

According to the specific objectives set in Chapter 1, the main conclusions and improvements described throughout the document are presented hereinafter:

Objective 1 - Development of a shoreline evolution model

- A novel physics-based reduced-complexity shoreline evolution model capable of solving the main processes contributing to shoreline change has been developed. The model solves the shoreline evolution as the combination of longshore shoreline changes and cross-shore transport. The longshore contribution accounts for alongshore gradients in the sediment flow, sediment sinks and sources to model river discharges or dredging activities and a trend accounting for unresolved processes. Cross-shore transport is solved following the equilibrium model proposed by Toimil et al. (2017a) by combining the short-term cross-shore contribution modelled as Miller and Dean (2004) and the long-term response due to SLR following Bruun (1962).

- Physics-based equations of shoreline evolution have been enriched with observations via a data-assimilation algorithm based on the extended Kalman filter (Long and Plant, 2012; Vitousek et al., 2017c) so as to reduce the modelling uncertainty and produce better estimates. An alternative data-assimilation strategy has been proposed to avoid the spurious interactions between longshore and cross-shore processes in the Kalman filter.

- Man-made interventions like groynes, breakwaters, seawalls and nourishments have been integrated in the shoreline model in terms of wave propagation and sediment transport. Thank to this, the model can be used to model the shoreline evolution in anthropized environments and assess the coastal response to a variety of interventions.

Objective 2 - Development of a methodology to obtain shoreline evolution projections sampling climate-related uncertainty

- A methodology to develop projections of shoreline evolution considering climate-related uncertainty has been implemented by coupling efficient downscaling techniques with the shoreline evolution model. The nearshore downscaling procedure is capable of reproducing the nearshore wave climate from global wave and water level projections efficiently by combining statistical and dynamical tools. Then, the impact model is run with the nearshore dynamics and uncertainty sampling is accounted for by considering several radiative forcing scenarios, various global and regional climate model combinations and different sea level rise percentiles.

- From the hourly time series of shoreline evolution, relevant information for decision making has been unravelled. Permanent shoreline retreat, beach area loss, contribution of individual processes to shoreline change or non-stationary extreme shoreline retreat have been obtained. This data is a valuable guide for the identification of hotspots, adaptation needs and priorities in the context of climate change.

Objective 3 - Development of a methodology to include the erosion effect on flooding forecasts at multiple scales

- A novel regional scale emulator has been formulated by combining a state of the art local-scale emulator of linear variables with a multivariate directional model. By this improvement, the synthetic emulation of storm wave and water level parameters at several spatial forcing points for regional-scale analysis has been enabled.

- A comprehensive multi-scale erosion-enhanced topobathymetry generation method has been developed. To the author's knowledge, it is the first time that a topobathymetry is updated considering shoreline changes obtained from a data-assimilated shoreline model and a profile translation tool that applies heuristic kinematic rules to the surveyed profiles according to the long and short-term processes.

- A thorough analysis of the long- and short-term erosion effects on coastal flooding has been performed by analysing the total water level and the flooding extent. Results reveal that neglecting erosion on coastal flooding projections may blur, in the coastal settings studied, all the efforts in developing better wave and water level projections.

Objective 4 - Development of a nearshore evolution model for local-scale studies.

- To the author's knowledge, the first multi-scale coastal evolution model capable of solving the decadal nearshore evolution starting from the real topobathymetry has been developed. The nearshore model is conceived as the combination of the shoreline evolution model, the profile translation tool for updating the topobathymetry and an advanced wave propagation model.

- The coastal response to sea level rise has been modelled following heuristic kinematic rules applied to the surveyed profiles and not to theoretical ones, taking distance from the widely used Bruun's rule (Bruun, 1962). Furthermore, the response to sea level rise implemented in the nearshore model has been validated under laboratory conditions in Atkinson et al. (2018).

- Integrating in the nearshore model an advanced and continuously updated wave propagation model as SWAN, has given the nearshore model an unprecedented flexibility in modelling different sandy coastal settings. Thanks to this, the coastal response affected by the presence of coastal features like structures, rocky outcrops, coral reefs, mangroves or seagrasses can be evaluated and the benefits provided by these settings can be rigorously assessed.

6.2. Further work

This research constitutes the preliminary step towards an ambitious milestone, a digital twin of the coast (Losada, 2022). Following other initiatives like the digital twin of the Earth (Bauer et al., 2021), a digital twin of the coast is an information system that would expose users to a digital replication of the state and temporal evolution of the

coastal system conditioned by available observations and the laws of physics. It can be used for both monitoring and forecasting at multiple scales, assess model process errors and constrain missing physics through observations and machine learning. Additionally, the digital twin of the coast will provide a framework for optimisation of disaster prevention or adaptation strategies across multiple sectors without the need for an advanced knowledge of the coastal system. It would be a valuable tool to manage coastal areas and to support key elements of the blue economy like tourism or marine transport in the context of climate change. Even though the methodologies and tools are ready to be exploited, in order to bring the digital twin of the coast to life, substantial work needs to be done in the field of programming. Notably, the development of a common interface integrating all the methodologies, models and tools in an inter-operable and easy to use environment is a major coding challenge whose formidable effort will undoubtedly achieve positive returns in the short-term future.

Regarding the specific objectives, in spite of their fulfillment, some important elements emerged during the research process that need further attention in the future:

Regarding the development of the shoreline evolution model

- The fixed transect-based discretization adopted in the shoreline model needs to be upgraded to a more flexible vector-based discretization in which the shoreline is released from the transects and evolves as a string of points (Jiménez and Sánchez-Arcilla, 2004; Kaergaard and Fredsoe, 2013; Hurst et al., 2015; Roelvink et al., 2020). This will allow to model features like spit growth, high-angle wave instabilities and better reproduce curved coasts while rigorously respecting sediment conservation. A major challenge will be the implementation of data-assimilation within this shoreline discretization. This can be achieved by assimilating, in every time-step, the vector-based discretization to a transect-based discretization but with varying transect angle. As the string of points evolves freely, it is impossible to predict beforehand where the transects will be placed at a given time step, so the intersection between the time-varying transects and the observations cannot be computed in advance but iteratively in every time step.

257

- In order to widen the applicability of the model to different coastal settings world-wide, additional processes like cliff-retreat (Limber et al., 2018), tidal-inlet effects (Toimil et al., 2017a) or dune erosion (Antolínez et al., 2019) need to be included.

- Data-assimilation through the extended Kalman filter requires an analytically derived covariance matrix to weight observations and model outputs. This matrix is propagated iteratively from a combination of input process noise and initial covariance matrix which are complex to define as their physical sense is not clear. As an alternative, the covariance matrix can be approximated by forward propagating an ensemble of initial parameter estimates following the ensemble Kalman filter approach (Ibaceta et al., 2020; Vitousek et al., 2021). This will mean an extra computational expense as an ensemble of states needs to be propagated instead of a unique one, but in contrast, the covariance matrix, which plays a transcendental role in the Kalman filter results, can be obtained directly from the propagated ensemble in a more precise way. The ensemble Kalman filter has been successfully applied with cross-shore models, but the integration of this method in combined cross-shore and longshore models is definitely worth exploring.

- The cross-shore component of shoreline evolution is extremely difficult to calibrate as the short-term fluctuations are on the same temporal scale as the revisit time of most of the publicly available satellite campaigns. To this end, the integration of high-resolution low revisit time satellite campaigns is required to improve calibration under extreme conditions.

Regarding the development of a methodology to obtain shoreline evolution projections considering climate-related uncertainty

- Climate-related uncertainty has been properly sampled but a single model parametrisation, coming from the converged data-assimilation results, is retained. Further analysis on the effects of using different starting model parameters for calibration is required (d'Anna et al., 2020), which can be done by taking profit from implementing the ensemble Kalman filter approach.

- The data-assimilated long-term trend accounting for unresolved processes may yield erroneous results as time progresses during the forecast period. It is neces-

sary to properly bound its value and leave this trend as the last available resource by including in the modelling inputs all the processes that contribute to shoreline change. Narrowing down this value requires achieving a better representation of the physical processes and better observations to improve calibration. Then, the idea of linking the unresolved trend to coastal change drivers needs to be explored.

- Stationary free-model parameters have been used to produce future forecasts due to the lack of formulations linking large scale oceanographic drivers with impact model parameters. However, some authors acknowledge the fact that non-stationary parametrisations yield better results (Ibaceta et al., 2020; d'Anna et al., 2022b). In order to produce shoreline forecasts considering non-stationary parametrisations, the relationship between large scale drivers and free-model parameters needs to be defined. This is an extremely complex problem but the work of Montaño et al. (2021) may be combined with a statistical projection methodology similar to the one proposed by Camus et al. (2017) to achieve a climate-dependent impact model parametrisation.

Regarding the development of a methodology to include the erosion effects on flooding forecasts at multiple scales

- The nearshore response to sea level rise is extremely uncertain as projected water levels may trigger unseen effects. In spite of some punctual laboratory experiments, the hypothesis that profiles will follow sea level rise and will retreat landwards conserving volume will not be validated until a confirmation extracted from real evidence. Until that point, the development of numerical mirrors of reality via the implementation of high fidelity formulations (Cheng et al., 2017; García-Maribona et al., 2021) may be used to explore this behaviour and throw some light on the problem.

- The reference storm used to update the topobathymetry does not cover all the uncertainty associated with coastal erosion due to extreme events. Better uncertainty sampling is required considering the storm frequency and duration in order to jointly account for the effects of storm clustering and beach recovery on erosion-enhanced flooding projections.

- In order to fully assess erosion-enhanced flooding and the dynamic effects of short-term morphological changes on flooding, it is necessary to use a two dimensional process-based storm model like XBeach instead of a reduced-complexity flooding model like RFSM. In this way, every possible short-term feedback between hydrodynamics and morphodynamics will be considered.

Regarding the development of a nearshore evolution model for local-scale studies

- IH-LANSloc needs to be validated in real cases considering complex bathymetries and different coastal settings like anthropized environments and coral reef or vegetation-protected zones. Ideally, validation will be made considering not only the shoreline evolution but also bed levels.

- Better process implementation is needed, notably regarding the sediment trapping effect exerted by vegetation patches or coral reefs. To this end, advances in remote sensing will definitely help defining these transport parametrisations for different coastal settings.

- Using an advanced wave propagation model allows to obtain a detailed spectral description of the breaking wave climate. This information, which is blurred by aggregating wave parameters, could be exploited in frequency-direction dependent impact formulations that are currently unavailable. Just the longshore transport model by Van Rijn (2014) considers a light frequency-dependence via the percentage of swell waves in the sea state. As the previous item, the availability of observations through remote sensing will lead the way to novel and more accurate impact formulations.

6.3. Critical overview and way forward

The focus of the research has been placed to achieve a better understanding of how the coastal zone evolves in the long-term considering the multi-scale interactions at several coastal settings in the context of climate change. To this end, one of the key advances

is the combination, in the same model, of classical physics-based approaches with data-driven techniques. However, the main obstacle preventing progress in this field is due to the fact that sediment transport formulations are left well behind the advances in statistical techniques or hydrodynamics, with empirical models or concepts inherited unaltered from the past century. The longshore transport formulation implemented in this 2022 research is based on Pelnard-Considère (1956); USACE (1984), the long-term cross-shore model relies on the Brunn's rule (Bruun, 1962) and its generalizations. The short-term cross-shore behaviour is based on the Miller and Dean (2004) model, which comes from the work of Kriebel and Dean (1993), also linked to the 1962 Bruun's rule assumptions but adapted for the different temporal scale. This stagnation can be attributable to the inherent randomness of the complex flow-induced particle movement process whose physical description requires demanding field work for calibration and validation. Until now, measuring sediment concentration and morphological change implied extensive and expensive laboratory and field campaigns and the applicability range of the resulting empirical formulae is limited to site-specific conditions.

With reference to the target points for improvement, some research groups are making great efforts on using observations in order to improve existent formulations. The focus is placed on using time-varying and climate-dependent sediment transport parametrisations by exploiting data-assimilation approaches. This is certainly a field of research worth exploring, but also risky from the humble opinion of the inexperienced author. Time-varying parametrisations may overcomplicate models potentially leading to extremely uncertain forecasts. As a simple comparison, a linear model is not a valid approximation for a sinusoidal curve. Only if an appropriate time-varying slope model is adopted, the enhanced linear model could be a valid substitute for the trigonometric expression. However, determining the time-variation of the slope of the linear model is far more complicated than the model itself. Also, errors in the time-variation of the slope can compound making the enhanced linear model to diverge from the reference sinusoidal curve. This divergence will exceed the optimal stationary parametrisation of the linear model when fitting the sinusoidal curve, which is the case of zero slope (horizontal line). Thus, it may require less effort to look for another model capable of

reproducing the oscillating behavior of the sinusoidal curve than trying to fix a potentially wrong model using complicated parametrisations.

As an alternative way to move forward, the classical coastal engineering approach of separating profile (cross-shore) and plan (longshore) nearshore changes needs reconsideration. Isolating the longshore component from the cross-shore behaviour adds important modelling uncertainties due to the simplification of reality, as both processes occur and interact together. The longshore transport following the one-line theory assumes a uniform cross-shore transport distribution over a constant active area. Cross-shore transport under erosive conditions is linked to an approximate full cycle sinusoidal curve, generating erosion closer to the beachface and accretion at the bottom of the profile with a transition area in between. A coupled longshore and cross-shore response in terms of cross-shore sediment transport is thus the summation of a uniform distribution due to longshore transport and a sinusoidal curve due to cross-shore transport. By exploiting this fact and instead of trying to solve profile and plan response in isolation, a formulation relating this coupled cross-shore distribution of sediment transport and the active extent could be inferred based on wave and water level properties and geomorphological features through the combination of physics, observations and machine learning techniques. In this way, limitations like the constant depth of closure or berm height will be superseded. This formulation will reproduce the cross-shore distribution of sediment transport depending on the prevailing conditions. During calm periods, predominance of a sinusoidal curve with positive transport in the beach face and negative in the bar will simulate accretion and this situation will be reversed in case of energetic periods. A cross-shore sediment-transport distribution yielding a non-null enclosed area will represent a sediment imbalance due to longhshore transport, in a similar way as it occurs in nature.

It is unknown if future progress in nearshore modelling will come from non-stationary parametrisations or/and from improved formulations. However, it is widely acknowledged in the literature the transcendental role of global-coverage remote sensing observations in order to achieve a better description of the sediment transport processes in three

ways: by developing new and validating existent sediment transport formulations, by enabling calibration and by enriching the physics via machine learning approaches. Due to the advances in remote sensing, it is now possible to infer the shoreline position via satellite spectral information and even the topobathymetry and sediment concentration estimation is under development. By analogy with wave hydrodynamics, in the same way that the combination of buoy measurements and computational power boosted the state of the art from manual ray-tracking techniques to Navier-Stokes modelling passing through spectral wave propagation and phase resolving models; morphological observations, computational power and machine learning approaches will certainly drive the progress in nearshore sediment transport modelling, stuck since the 20th century.

APPENDIX A

CALCULATION OF WAVE PROPERTIES AT THE BREAKING POINT IN IH-LANS

In order to obtain breaking wave properties to feed the shoreline evolution governing equation, linear shoaling, refraction and depth-induced breaking are considered. For that purpose, wave energy conservation, Snell's law of refraction and a constant depth-induced breaker index (γ) of 0.55, are applied over each profile. Breaking wave properties without considering diffraction are calculated by iteratively solving Equation A.1.

$$H_{s_b} = H_{s_n} \sqrt{\frac{C_{g_n}}{\sqrt{gd_b}}} \sqrt{\frac{\cos(\alpha_n)}{\cos(\alpha_b)}} = \gamma d_b \qquad \text{(A.1)}$$

where H_{s_b} is the significant breaking wave height due to shoaling and refraction, H_{s_n} is the nearshore wave height, C_{g_n} is the linear nearshore wave group celerity, g is the gravity acceleration constant and d_b is the breaking depth and α_n and α_b are the angles between the nearshore wave crests and the breaker line respectively and the reference bathymetry contour. α_b is calculated through the Snell's law of refraction.

Following Snell's law, the reference bathymetry contour Dir_{bathy} is approximated by the shoreline orientation, which is updated every time-step considering the changes in the shoreline position Y of the adjacent transects, Figure A.1.

I
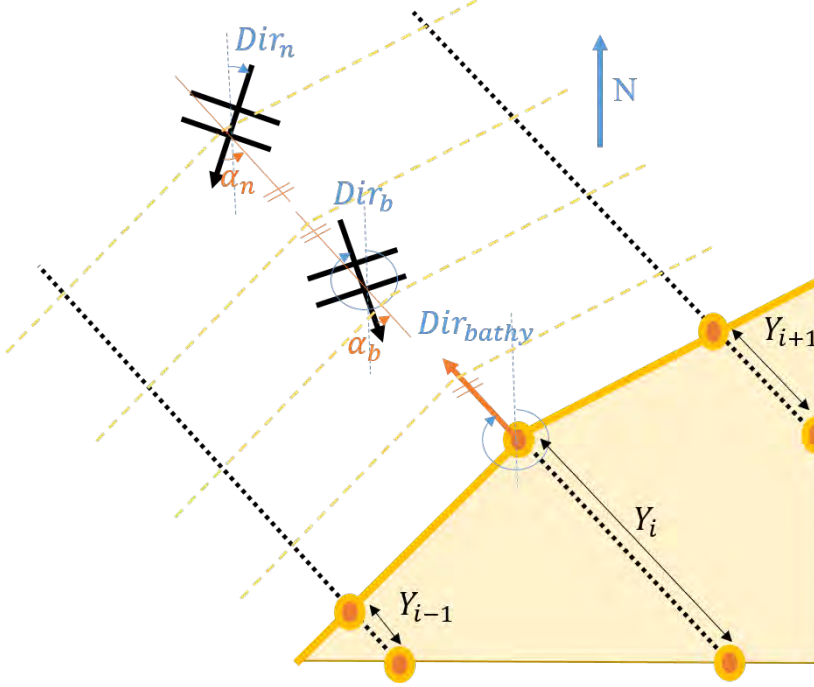
Figure A.1: Main angles in wave transformation II.

In order to model the effects of diffraction in the shoreline evolution model, empirical corrections of wave height and directions proposed by Kamphius (2000) for groynes and Dabees (2000) for parallel offshore breakwaters are applied with slight modifications.

Wave rays approaching a groyne at an angle are blocked by the structure, generating a longshore wave height gradient in the shelter zone, which is partially compensated by energy transfer from adjacent wave rays, Figure A.2a. Following Goda (1985) analysis of diffraction caused by random waves, Kamphius (2000) developed simple formulas to calculate wave height reduction and direction changes based on regression analysis. These formulas assume that the limiting transition zone angle is 90°, which implies an infinite transition zone if the coastline is straight. Considering that an infinite transition zone generates numerical instabilities, the transition zone is constrained in a similar way as in Hurst et al. (2015), by the limiting angle θ_r. The transition zone limits are calculated intersecting a wave ray parallel to θ_A with the shoreline. The ray is drawn at a distance G from the structures' tip in the shelter zone, and yields the point T. G is assumed to be 2.5 times the wave length.

When explicitly modelling the effects of structures, coupling hydrodynamics and morphodynamics is needed. Thus, to detect the transects in the shelter and transition zones, the breaker line without considering diffraction (known) is used as a proxy of the true breaking line. From the breaking depth d_b, the breaking width is obtained as $W_b^* = (d_b/A)^{1.5}$. Then, W_b^* is added to the time-varying shoreline position Y at each transect yielding the proxy of the breaker line position. The points of the breaker line proxy are then crossed with the shelter and transition zones to identify the geometric magnitudes needed apply the diffraction corrections in wave height and direction.

Breaking wave height considering diffraction $H_{s_{bd}}$ is obtained by multiplying H_{s_b} by a diffraction coefficient K_d calculated as follows:

$$K_d = \begin{cases} 0.71 - 0.0093\theta + 0.000025\theta^2, & \text{if } \theta \in [-90, 0] \\ 0.71 + 0.29 \left[\sin \left(90\frac{\theta}{\theta_r} \right) \right], & \text{if } \theta \in (0, \theta_r] \end{cases} \tag{A.2}$$

Diffraction effects of wave direction are modelled by the relationship proposed by Kamphius (2000):

$$\alpha_{bd} = \alpha_b K_d^{0.375} \tag{A.3}$$

Considering that waves are radiated through the tip of the structure, wave crests follow circular patterns centred at the diffracting point. In order to model this behaviour, a further decrease in wave angles needs to be accounted for in the sheltered zone:

$$\alpha_{bd} = \alpha_b K_d^{0.375} \left[\frac{2PB}{S(\tan(\alpha_s) + \tan(0.88\alpha_b))} \right], \text{ if } \theta < 0 \quad \text{and} \quad \frac{PB}{S} < \frac{1}{2}[\tan\alpha_s + \tan(0.88\alpha_b)] \tag{A.4}$$

In the case of parallel breakwaters, Dabees (2000) proposed a method to integrate diffraction-refraction in the calculation of wave direction, Figure A.2b. The method relies on the fact that due to water particles' inertia, waves are not radiated just through the structure's tip, but instead, they can be radiated from any point in between the extension of the structure a distance G and the tip of the structure. The transition zone is delimited by the structure's tip (point A), the intersection between a ray parallel to

θ_A at distance G from A and the shoreline (point T), and the shelter zone limit (point O).
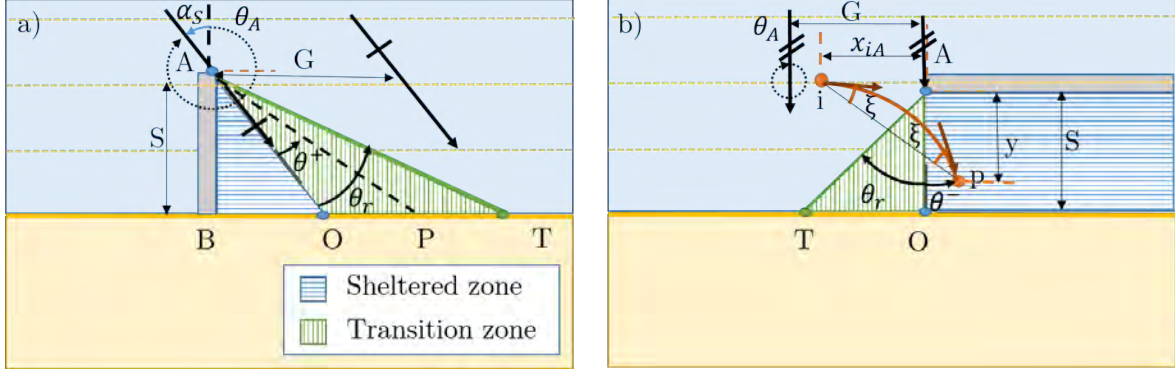
Figure A.2: Sketch of the main geometrical features to consider structures-induced diffraction. A) groyne case and b) infinite parallel breakwater with one diffraction tip. In both cases, the sheltered zone is delimited by the incoming wave ray at the diffracting tip and the transition zone is limited by the angle θ_r.

In the case of breakwaters, Equation A.2 is applied to calculate wave height reduction due to diffraction. Wave rays approaching at a point p located in the shelter zone are radiated though the point i. The distance x_{iA} from the point i to the breakwater tip A is obtained as follows:

$$x_{iA} = G\frac{y}{S} \tag{A.5}$$

where y is the distance from the point to the breakwater and S is the distance from the shoreline. Following Dabees (2000), the corrected wave breaking angle at point p is:

$$\alpha_P = \theta_{ip} - \xi \tag{A.6}$$

θ_{ip} is the angle of the straight line between points i and p and ξ is the difference of the actual ray angle from the straight line and is expressed as:

$$\xi = \tan^{-1}\left[\left(\frac{L_i - L_p}{L_i + L_p}\right)\tan\theta_{ip}\right] \tag{A.7}$$

where L_i and L_p are the wave lengths at points i and p.

In the case of a parallel breakwater with two diffracting points, the contribution from each tip is calculated independently and then combined by obtaining the mean wave

direction and wave height associated with the mean energy flux:

$$E_m \boldsymbol{Cg}_m = E_1 \boldsymbol{Cg}_1 + E_2 \boldsymbol{Cg}_2 \tag{A.8}$$

where E stands for wave energy, and $\boldsymbol{C_g}$ is the group celerity of points 1 and 2.

APPENDIX B

DATA-ASSIMILATION THROUGH THE EXTENDED KALMAN FILTER

Shoreline modelling is a non-linear dynamic problem and thus, the extended version of the Kalman filter (eKf) is applied in order to linearize the forecast equation at each time step. Conversely to previous studies (Long and Plant, 2012; Vitousek et al., 2017c), two different constants are considered depending on the retreating or advancing nature of the cross-shore shoreline movement.

The first step is the definition of the state vector $\mathbf{\Psi}$, which is the minimum number of variables and free-model parameters needed to advance the simulation one time step. In this case, the state vector accounts for longshore and cross-shore erosion/accretion processes, Equation B.1.

$$\mathbf{\Psi} = \left[\underbrace{Y_l, K_{ml}, vlt,}_{\mathbf{\Psi}_l} \underbrace{Y_c^-, Y_c^+, K_c^-, K_c^+}_{\mathbf{\Psi}_c} \right]^T \tag{B.1}$$

The search space of the parameters is not constrained by the eKf. This fact can eventually yield non-physical values of the free-model parameters. In order to avoid negative signs in the longshore constant K_1, its expression is reworked to an exponential form

$K_1(t) = K_{10} \exp(0.5 K_{ml}(t))$ following Vitousek et al. (2017c), where K_{10} the initial is estimate and K_{ml} is the assimilated variable. However this transformation is performed at the Kalman filter level and does not affect the process equation. The data-assimilation is performed considering the variable $K_{ml}(t)$ in $\mathbb{R}$ which is subsequently back-transformed and yields $K_1(t)$ in $\mathbb{R}^+$. A similar strategy was initially implemented with the cross-shore constants. Convergence times were substantially reduced and this approach was discarded as for reasonable uncertainty estimates of the cross-shore constants, the Kalman filter did not persistently fall in the negative range.

The eKf jointly resolves the process and the measurement equations at every transect:

$$\begin{cases} \boldsymbol{\Psi}_{t+1} = \boldsymbol{f}(t, \boldsymbol{\Psi}_t) + \boldsymbol{w} \\ y_{obs,t} = \boldsymbol{h}(t, \boldsymbol{\Psi}_t) + v \end{cases} \tag{B.2}$$

Where t is the time step, the functionals $\boldsymbol{f}(t, \boldsymbol{\Psi}_t)$ and $\boldsymbol{h}(t, \boldsymbol{\Psi}_t)$ denote the non-linear transformation in the process and measurements equations, $\boldsymbol{w}$ is the process noise with zero mean and $\boldsymbol{Q}$ covariance matrix assumed to be constant during the simulation and v is the measurement noise with zero mean and R variance. The fact of considering two different cross-shore rates for erosion and accretion implies a non-linear measurement equation. eKf performs a first order linearization of the system equations, which reads:

$$\begin{cases} \boldsymbol{\Psi}_{t+1} = \boldsymbol{F}_{t+1,t} \boldsymbol{\Psi}_t + \boldsymbol{w} \\ y_{obs,t} = \boldsymbol{H}_t \boldsymbol{\Psi}_t + v \end{cases} \tag{B.3}$$

where $\boldsymbol{H}_t$ is the measurement matrix and its value depends on the nature (erosive/accretive) of the cross-shore shoreline displacement and $\boldsymbol{F}_{t+1,t}$ is the Jacobian of the process transformation:

$$\boldsymbol{F}_{t+1,t} = \left. \frac{\partial \boldsymbol{f}(t, \boldsymbol{\Psi})}{\partial \boldsymbol{\Psi}} \right|_{\boldsymbol{\Psi} = \boldsymbol{\Psi}_t} \tag{B.4}$$

At a time step t, in which there is an observation available, a prior estimation of the state $\widetilde{\boldsymbol{\Psi}}_t$ is obtained by solving the process equation. Then, the eKf finds the optimal solution which minimizes the mean-square variance in the posterior state $\boldsymbol{\Psi}_t$ (Haykin

and Haykin, 2001). The posterior state at time t is:

$$\boldsymbol{\Psi}_t = \widetilde{\boldsymbol{\Psi}}_t + \boldsymbol{G}_t(y_{obs,t} - \boldsymbol{H}_t\widetilde{\boldsymbol{\Psi}}_t) \tag{B.5}$$

where the Kalman gain $\boldsymbol{G}_t$ weights the observation $y_{obs,t}$ and the process estimate of the state $\widetilde{\boldsymbol{\Psi}}_t$ to calculate the posterior state $\boldsymbol{\Psi}_t$.

In order to compute the Kalman gain $\boldsymbol{G}_t$, the a priori error covariance matrix $\widetilde{\boldsymbol{P}}_t$ is propagated throughout the analysis. Conversely to (Ibaceta et al., 2020; Vitousek et al., 2021), where the error covariance matrix is directly calculated from an ensemble of simulations, here it is analytically derived, (Equation B.6). The main advantage is the considerable save in computational time, as it does not require the propagation of an ensemble at every transect.

$$\widetilde{\boldsymbol{P}}_t = \boldsymbol{F}_{t,t-1}\boldsymbol{P}_{t-1}\boldsymbol{F}_{t,t-1}^T + \boldsymbol{Q} \tag{B.6}$$

Then, $\boldsymbol{G}_t$ is computed as follows:

$$\boldsymbol{G}_t = \widetilde{\boldsymbol{P}}_t\boldsymbol{H}_t^T(\boldsymbol{H}_t\widetilde{\boldsymbol{P}}_t\boldsymbol{H}_t^T + R)^{-1} \tag{B.7}$$

The posterior error covariance matrix is then:

$$\boldsymbol{P}_t = (\boldsymbol{I} - \boldsymbol{G}_t\boldsymbol{H}_t)\widetilde{\boldsymbol{P}}_t \tag{B.8}$$

So as to run the computation, the estimated state at initial time $\boldsymbol{\Psi}_0$, the initial error covariance matrix $\boldsymbol{P}_0$ that represents uncertainties in the initial estimate, the covariance of process noise $\boldsymbol{Q}$ which quantifies the inherent noise in the model and the measurement error R, are initialised.

The distinction between two different cross-shore constants is considered both in the initialization of the matrices $\boldsymbol{P}_0$ and $\boldsymbol{Q}$ and in the analysis. The main difference with respect to other approaches that consider a single cross-shore constant lies on the up-

date of error covariance matrices. Error covariance matrices associated with erosion $\boldsymbol{P}_c^-$ and accretion $\boldsymbol{P}_c^+$ cross-shore processes need to be independently updated just in the time steps when cross-shore retreat ($\partial Y_c/\partial t < 0$) or advance ($\partial Y_c/\partial t > 0$) takes place while the longshore-related terms in $\boldsymbol{P}_l^{+/-}$ are updated in every time-step.

Regarding the coupling between longshore and cross-shore processes in the data-assimilation algorithm, two alternative approaches are proposed. The independent approach performs the data-assimilation without considering interactions between longshore and cross-shore processes in the eKf. On the other hand, the coupled data-assimilation approach (Long and Plant, 2012; Vitousek et al., 2017c) couples all the processes in the eKf.

B.1.   Independent data-assimilation

In order to carry out the independent data-assimilation approach, an intermediate step is needed to extract from the time series of raw observations $Y_{obs}(t)$, the longshore component $Y_{obs,l}(t)$ and the cross-shore component $Y_{obs,c}(t)$. The different temporal scale of longshore and cross-shore processes enables the unravelling between components. In this application, a running mean is used to extract $Y_{obs,l}(t)$ while the residue is attributed to the cross-shore component $Y_{obs,c}(\text{t})$.

The procedure is detailed in Algorithm 1 and requires the definition of the initial longshore, cross-shore erosion and cross-shore accretion parameter state, covariance and process noise matrices which are defined in accordance with the state vectors $\boldsymbol{\Psi}_l = [Y_l, K_{ml}, vlt]^T$ and $\boldsymbol{\Psi}_c = [Y_c^-, Y_c^+, K_c^-, K_c^+]^T$. Also an error regarding the observations $Y_{obs,l}(t)$ and $Y_{obs,c}(t)$ needs to be specified (R_l, R_c respectively). This error is chosen to be bigger in the case of cross-shore observations because the unravelling technique tends to average detection errors in the longshore component. The sum of the errors R_l and R_c yields the total expected observation error. The measurement error in the case of longshore processes is $\boldsymbol{H}_l = [1, 0, 0]$ whereas for the case of cross-shore processes varies from erosive events $\boldsymbol{H}_c^- = [1, 0, 0, 0]$ and accretion events

$\boldsymbol{H}_c^+ = [0, 1, 0, 0]$. Three error covariance matrices are propagated through time, one for longshore processes P_l, cross-shore erosion $\boldsymbol{P}_c^-$ and cross-shore accretion $\boldsymbol{P}_c^+$. The matrix $\boldsymbol{P}_l$ is computed on every time-step whereas $\boldsymbol{P}_c^-$ and $\boldsymbol{P}_c^+$ just when an erosion or accretion event takes place.

B.2. Joint data-assimilation

In this case, the data-assimilation integrates longshore and cross-shore processes and is directly performed on the observed shoreline position $Y_{obs}(t)$. The method is detailed in Algorithm 2 and requires the definition of initial multi-process state vector, error covariance and noise matrices following the state vector definition of Equation B.1. The measurement vector behaves in a similar way as in the independent approach but integrates longshore and cross-shore processes to add-up to the observable shoreline position $Y_{obs}(t)$. Thus, when a cross-shore erosion event takes place, the measurement vector is $\boldsymbol{H}^- = [\boldsymbol{H}_l, \boldsymbol{H}_c^-] = [1, 0, 0, 1, 0, 0, 0]$ and in the case of cross-shore accretion $\boldsymbol{H}^+ = [\boldsymbol{H}_l, \boldsymbol{H}_c^+] = [1, 0, 0, 0, 1, 0, 0]$. In this case, two covariance matrices are propagated though the analysis, one for cross-shore erosion events $\boldsymbol{P}^-$ and another one for cross-shore accretive events $\boldsymbol{P}^+$. The cross-shore erosion related elements are updated when an erosion event takes place and similarly in the case of cross-shore accretion. However in the case of the longshore-related elements, they are updated every time-step in both matrices $\boldsymbol{P}^-$ and $\boldsymbol{P}^+$.

Algorithm 1 Independent data-assimilation

Initialize variables:
Define $\mathbf{\Psi}_{0,l}, \mathbf{P}_{0,l}, \mathbf{Q}_l, R_l, \mathbf{\Psi}_{0,c}, \mathbf{P}_{0,c}^-, \mathbf{Q}_c^-, \mathbf{Q}_c^+, R_c$
Shoreline evolution loop:
for $t \in [t_{ini} : \Delta t : t_{end}]$ **do**
    Update state: $\widetilde{\mathbf{\Psi}}_{t,l} = \boldsymbol{f}_l(t-1, \mathbf{\Psi}_{t-1,l}), \widetilde{\mathbf{\Psi}}_{t,c} = \boldsymbol{f}_c(t-1, \mathbf{\Psi}_{t-1,c})$
    Calculate the Jacobian of longshore processes (Eq. B.4): $\boldsymbol{F}_{t,t-1,l}$
    Update the longshore error covariance matrix (Eq. B.6): $\widetilde{\boldsymbol{P}}_{t,l}$
    if exists($y_{obs,t,l}$) **then**
        Compute Kalman gain (Eq. B.7): $\boldsymbol{G}_{t,l}$
        Update state vector (Eq. B.8): $\mathbf{\Psi}_{t,l}$
        Compute posterior error covariance matrix (Eq. B.8): $\boldsymbol{P}_{t,l}$
    else
        Update longshore posterior error covariance matrix and state:
        $\boldsymbol{P}_{t,l} = \widetilde{\boldsymbol{P}}_{t,l}, \mathbf{\Psi}_{t,l} = \widetilde{\mathbf{\Psi}}_{t,l}$
    end if
    if $\partial Y_c/\partial t < 0$ (cross-shore erosion) **then**
        Calculate the Jacobian of cross-shore processes (Eq. B.4): $\boldsymbol{F}_{t,t-1,c}^-$
        Update the cross-shore error covariance matrix (Eq. B.6): $\widetilde{\boldsymbol{P}}_{t,c}^-$
        if exists ($y_{obs,t,c}$) **then**
            Compute Kalman gain (Eq. B.7): $\boldsymbol{G}_{t,c}$
            Update state vector (Eq. B.5): $\mathbf{\Psi}_{t,c}$
            Compute/update posterior error covariance matrices (Eq. B.8):
            $\boldsymbol{P}_{t,c}^-, \boldsymbol{P}_{t,c}^+ = \boldsymbol{P}_{t-1,c}^+$
        else
            Update posterior error covaraince matrices and state:
            $\boldsymbol{P}_{t,c}^- = \widetilde{\boldsymbol{P}}_{t,c}^-, \boldsymbol{P}_{t,c}^+ = \boldsymbol{P}_{t-1,c}^+, \mathbf{\Psi}_{t,c} = \widetilde{\mathbf{\Psi}}_{t,c}$
        end if
    else(cross-shore accretion)
        Calculate the Jacobian of cross-shore processes (Eq. B.4): $\boldsymbol{F}_{t,t-1,c}^+$
        Update the cross-shore error covariance matrix (Eq. B.6): $\widetilde{\boldsymbol{P}}_{t,c}^+$
        if exists ($y_{obs,t,c}$) **then**
            Compute Kalman gain (Eq. B.7): $\boldsymbol{G}_{t,c}$
            Update state vector (Eq. B.5): $\mathbf{\Psi}_{t,c}$
            Compute/update posterior error covariance matrices (Eq. B.8):
            $\boldsymbol{P}_{t,c}^+, \boldsymbol{P}_{t,c}^- = \boldsymbol{P}_{t-1,c}^-$
        else
            Update posterior error covariance matrices and state:
            $\boldsymbol{P}_{t,c}^+ = \widetilde{\boldsymbol{P}}_{t,c}^+, \boldsymbol{P}_{t,c}^- = \boldsymbol{P}_{t-1,c}^-, \mathbf{\Psi}_{t,c} = \widetilde{\mathbf{\Psi}}_{t,c}$
        end if
    end if
end for

Algorithm 2 Joint data-assimilation

Initialize variables:
Define $\boldsymbol{\Psi}_{0,l}, \boldsymbol{P}_{0,l}, \boldsymbol{Q}_l, \boldsymbol{\Psi}_{0,c}, \boldsymbol{P}_{0,c}^-, \boldsymbol{Q}_c^-, \boldsymbol{Q}_c^+, R$
Assemble multi-process matrices: $\boldsymbol{\Psi}_0, \boldsymbol{P}_0^-, \boldsymbol{P}_0^+, \boldsymbol{Q}^-, \boldsymbol{Q}^+, R$
Shoreline evolution loop:
for $t \in [t_{ini} : \Delta t : t_{end}]$ **do**
    Update state: $\widetilde{\boldsymbol{\Psi}}_t = [\widetilde{\boldsymbol{\Psi}}_{t,l}, \widetilde{\boldsymbol{\Psi}}_{t,c}]$; $\widetilde{\boldsymbol{\Psi}}_{t,l} = \boldsymbol{f}_l(t-1, \boldsymbol{\Psi}_{t-1,l})$, $\widetilde{\boldsymbol{\Psi}}_{t,c} = \boldsymbol{f}_c(t-1, \boldsymbol{\Psi}_{t-1,c})$
    if $\partial Y_c/\partial t < 0$ (cross-shore erosion) **then**
        Calculate the Jacobian (Eq. B.4): $\boldsymbol{F}_{t,t-1}^-$
        Compute/Update the error covariance matrices (Eq. B.6):
$$\widetilde{\boldsymbol{P}}_t^-, \widetilde{\boldsymbol{P}}_t^+ = \begin{bmatrix} \widetilde{\boldsymbol{P}}_{t,l}^- & \boldsymbol{P}_{t-1,lc}^+ \\ \boldsymbol{P}_{t-1,lc}^+ & \boldsymbol{P}_{t-1,c}^+ \end{bmatrix}$$
        if exists$(y_{obs,t})$ **then**
            Compute Kalman gain (Eq. B.7): $\boldsymbol{G}_t$
            Update state vector (Eq. B.5): $\boldsymbol{\Psi}_t$
            Compute posterior error covariance matrix (Eq. B.8):
$$\boldsymbol{P}_t, \boldsymbol{P}_t^+ = \begin{bmatrix} \boldsymbol{P}_{t,l}^- & \boldsymbol{P}_{t-1,lc}^+ \\ \boldsymbol{P}_{t-1,lc}^+ & \boldsymbol{P}_{t-1,c}^+ \end{bmatrix}$$
        else
            Update posterior error covariance matrix and state:
            $\boldsymbol{P}_t^- = \widetilde{\boldsymbol{P}}_t^-$, $\boldsymbol{P}_t^+ = \widetilde{\boldsymbol{P}}_t^+$, $\boldsymbol{\Psi}_t = \widetilde{\boldsymbol{\Psi}}_t$
        end if
    else(cross-shore accretion)
        Calculate the Jacobian (Eq. B.4): $\boldsymbol{F}_{t,t-1}^+$
        Update the cross-shore error covariance matrix (Eq. B.6):
$$\widetilde{\boldsymbol{P}}_t^+, \widetilde{\boldsymbol{P}}_t^- = \begin{bmatrix} \widetilde{\boldsymbol{P}}_{t,l}^+ & \boldsymbol{P}_{t-1,lc}^- \\ \boldsymbol{P}_{t-1,lc}^- & \boldsymbol{P}_{t-1,c}^- \end{bmatrix}$$
        if exists $(y_{obs,t})$ **then**
            Compute Kalman gain (Eq. B.7): $\boldsymbol{G}_t$
            Update state vector (Eq. B.5): $\boldsymbol{\Psi}_t$
            Compute/update posterior error covariance matrices (Eq. B.8):
$$\boldsymbol{P}_t^+, \boldsymbol{P}_t^- = \begin{bmatrix} \boldsymbol{P}_{t,l}^+ & \boldsymbol{P}_{t-1,lc}^- \\ \boldsymbol{P}_{t-1,lc}^- & \boldsymbol{P}_{t-1,c}^- \end{bmatrix}$$
        else
            Update posterior error covaraince matrices and state:
            $\boldsymbol{P}_t^+ = \widetilde{\boldsymbol{P}}_t^+$, $\boldsymbol{P}_t^- = \widetilde{\boldsymbol{P}}_t^-$, $\boldsymbol{\Psi}_t = \widetilde{\boldsymbol{\Psi}}_t$
        end if
    end if
end for

APPENDIX C

SYNTHETIC GENERATION OF STORMS FOR REGIONAL-SCALE APPLICATIONS

C.1. Overview of the storm emulator

The multivariate storm emulator is composed of three modules: the peak period T_p module, the astronomical tide AT module and the statistical model, Figure C.1. The storm emulator is capable of generating statistically consistent extreme wave and water-level parameters.

The statistical model captures the dependence between the significant wave height H_s and mean wave period T_m at the director points, the storm surge SS at the water-level point and wave direction Dir at the link point. The T_p, due to its statistical behaviour, is modelled in an specific module via a heteroscedastic regression based on the mean wave period T_m. The astronomical tide is also modelled independently, as it is assumed to behave in a deterministic manner.
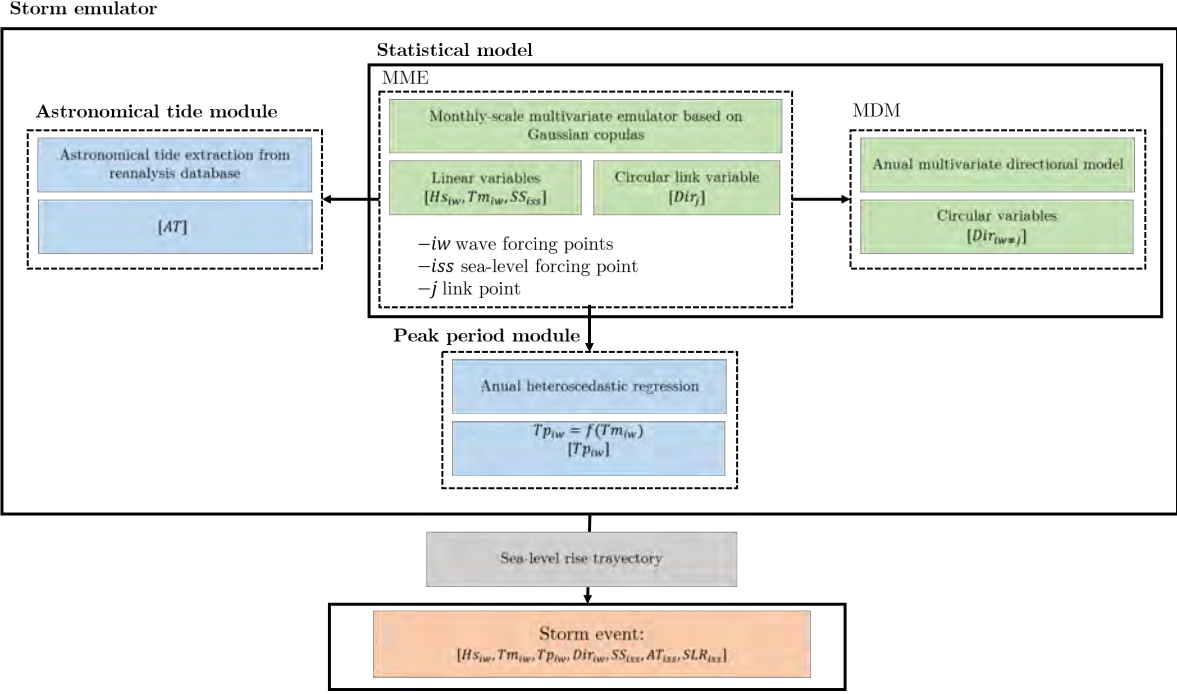
Figure C.1: Schematic representation of the storm emulator.

C.1.1. Statistical model

The statistical model is composed of a monthly-scale multivariate emulator (MME) based on Gaussian copulas (Lucio et al., 2020) and a multivariate directional model (MDM) (Mardia et al., 2008):

$$
f_{H_{s_{iw}},T_{m_{iw}},Dir_{iw},SS_{iss}}(H_{s_{iw}}, T_{m_{iw}}, Dir_{iw}, SS_{iss}) =
$$

$$
= \underbrace{f(H_{s_{iw}}, T_{m_{iw}}, Dir_j, SS_{iss})}_{MME} \cdot \underbrace{f(Dir_{iw \neq j}|Dir_j)}_{MDM} \tag{C.1}
$$

where $iw = 1, 2, ..., n$ and n the number of emulation points. iss is the water-level point and j is the link point between the MME model and the MDM model.

C.1.1.1. Inference of the MME model

The MME model based on Gaussian copulas models linear variables at every director point and a directional variable at the link point. Due to the flexibility of multivariate modelling using copulas, the joint distribution function is calculated though the marginal distribution function of the different variables and a copula function that

models the dependent structure. The MME distribution function of month l is:

$$
\begin{aligned}
F_{(H_{s_{iw}},T_{m_{iw}},Dir_j,SS_{iss},l)}&(H_{s_{iw}}, T_{m_{iw}}, Dir_j, SS_{iss}) = \\
&= \boldsymbol{C}(F(H_{s_{iw}}), F(T_{m_{iw}}), F(Dir_j), F(SS_{iss}); \boldsymbol{\Sigma}) = \\
&= \boldsymbol{C}_{\Sigma}(\Phi^{-1}(F(H_{s_{iw}})), \Phi^{-1}(F(T_{m_{iw}})), \Phi^{-1}(F(Dir_j)), \Phi^{-1}(F(SS_{iss})))
\end{aligned} \tag{C.2}
$$

where $\boldsymbol{\Sigma}$ is the correlation matrix of the variables $[H_{s_{iw}}, T_{m_{iw}}, Dir_j, SS_{iss}]$ in the space $[0,1]^{3nw+1}$. The marginal distribution functions follow a Generalised Extreme Value distribution: $H_{s_{iw}}, T_{m_{iw}}, SS_{iss} \sim GEV$ while the directional link variable is fitted to an empirical distribution.

The inference of the Gaussian multivariate model is done after fitting the marginal distribution functions. It consists of determining the correlation matrix $\boldsymbol{\Sigma}$ of the variables transformed in the normal space thorough the marginal distribution function $F(-)$.

C.1.1.2. Inference of the MDM model

For the statistical modelling of wave directions, the mixture model based on the multivariate von Mises distribution presented in Mardia et al. (2008), is used. The von Mises distribution is a circular equivalence of the Gaussian distribution and is limited by the fact that it can only model single-modal distributions or distributions with a single predominant direction. To sort this out, a mixture distribution composed of single-modal multivariate von Mises distributions is applied. A weighting procedure is developed to include the occurrence probability p_i of the predominant directions, Equation C.3.

$$
f_{\boldsymbol{\theta}}(\boldsymbol{\theta}) = \sum_{i=1}^{k} p_i T_{\boldsymbol{\theta} i}(\boldsymbol{\theta}) \tag{C.3}
$$

where $\boldsymbol{\theta}$ is the direction vector $[Dir_1, Dir_2, \dots Dir_n]$; k is the number of directional components of mixing; p_i is the probability of occurrence of each directional component; and $T_{\boldsymbol{\theta} i}(\boldsymbol{\theta})$ is the single-modal multivariate von Mises distribution. Once the number of mixing components k has been chosen, it is necessary to perform a classification in the observed storm event direction space. To this end, the K-means algorithm is applied together with an appropriate metric of angular distance. The result of the analysis is the classification of the set of storm directions at n director points into k subsets

$[\boldsymbol{\theta}_1, \boldsymbol{\theta}_2, ..., \boldsymbol{\theta}_k] \in \boldsymbol{\theta}_{1,2,...,n}$.

The calculation of the probability of occurrence of each directional component p_i consists of counting the number of elements in each cluster.

$$p_i = \frac{N_i}{N_t} \tag{C.4}$$

where N_i is the number of items in subset i; and N_t is the total number of elements in the study period.

Although the MME is inferred monthly, the MDM is inferred annually and considers monthly storm events. This is because of the limitation of the directional component classification, which drastically reduces the number of observations with which to fit the MDM. However, seasonality is not lost due to the link direction, which is modelled in the MME on a monthly scale.

Next, we fit the MDM to each subset of directions. The multivariate density function of $\boldsymbol{\theta}^T = [\theta_1, \theta_2, \ldots \theta_n] \in \mathbb{T}^n = [-\pi, \pi)^n$, being n the emulated points, is:

$$f_{\boldsymbol{\theta}}(\boldsymbol{\theta}) = [T(\boldsymbol{\kappa}, \boldsymbol{\Lambda})]^{-1} \exp[\boldsymbol{\kappa}^T c(\boldsymbol{\theta}, \boldsymbol{\mu}) + s(\boldsymbol{\theta}, \boldsymbol{\mu})^T \boldsymbol{\Lambda} s(\boldsymbol{\theta}, \boldsymbol{\mu})/2] \tag{C.5}$$

where $\boldsymbol{\theta}^T = [\theta_1, \theta_2, ..., \theta_n]$, $\boldsymbol{\mu}^T = [\mu_1, \mu_2, ...\mu_n] \in \mathbb{T}^n$, $\boldsymbol{\kappa}^T = [\kappa_1, \kappa_2, ..., \kappa_n] \in \mathbb{R}^n$, $\kappa_i > 0$ y $\boldsymbol{\Lambda} = \lambda_{ij} \in \mathbb{R}^{n \times n}$ with $\boldsymbol{\Lambda}^T = \boldsymbol{\Lambda}$ y $\lambda_{ii} = 0$,

$$c(\boldsymbol{\theta}, \boldsymbol{\mu}) = [\cos(\theta_1 - \mu_1), \cos(\theta_2 - \mu_2), ..., \cos(\theta_n - \mu_n)]$$

$$s(\boldsymbol{\theta}, \boldsymbol{\mu}) = [\sin(\theta_1 - \mu_1), \sin(\theta_2 - \mu_2), ..., \sin(\theta_n - \mu_n)]$$

$[T(\boldsymbol{\kappa}, \boldsymbol{\Lambda})]^{-1}$ is a normalisation constant which only has an analytical expression in the bivariate case:

$$T(\boldsymbol{\kappa}, \boldsymbol{\Lambda}) = T(\kappa_1, \kappa_2, \lambda) = 4\pi^2 \sum_{m=0}^{\infty} \binom{2m}{m} \frac{\lambda}{2}^{2m} \kappa_1^{-m} I_m(\kappa_1) \kappa_2^{-m} I_m(\kappa_2) \tag{C.6}$$

where $I_p(\kappa)$ is the modified Bessel function of order p.

When modelling three circular random variables, an analogous expression to Equation C.5 is:

$$f_{\boldsymbol{\theta}}(\theta_1, \theta_2, \theta_3) = [T(\boldsymbol{\kappa}, \boldsymbol{\Lambda})]^{-1}\Gamma(\theta_1, \theta_2, \theta_3) = [T(\boldsymbol{\kappa}, \boldsymbol{\Lambda})]^{-1} \exp[\kappa_1 \cos(\theta_1 - \mu_1)+$$
$$+\kappa_2 \cos(\theta_2 - \mu_2) + \kappa_3 \cos(\theta_3 - \mu_3) + \lambda_{12} \sin(\theta_1 - \mu_1) \sin(\theta_2 - \mu_2)+ \qquad \text{(C.7)}$$
$$+\lambda_{13} \sin(\theta_1 - \mu_1) \sin(\theta_3 - \mu_3) + \lambda_{23} \sin(\theta_2 - \mu_2) \sin(\lambda_3 - \mu_3)]$$

The constant $[T(\boldsymbol{\kappa}, \boldsymbol{\Lambda})]$, allows $f_{\boldsymbol{\theta}}(\boldsymbol{\theta})$ to be a density function:

$$[T(\boldsymbol{\kappa}, \boldsymbol{\Lambda})]^{-1} = \frac{1}{\iiint \Gamma(\boldsymbol{\theta}) \, d\boldsymbol{\theta}} \qquad \text{(C.8)}$$

In order to define the distribution in Equation C.5 for n director points, $n + n(n+1)/2$ parameters corresponding to $\boldsymbol{\mu}$, $\boldsymbol{\kappa}$, $\boldsymbol{\Lambda}$ need to be inferred. Since there is no explicit expression for the normalisation constant, the maximum likelihood estimator is implemented within an optimisation algorithm in which, at each iteration step, the normalisation constant for the set of parameters of the test is obtained. As the estimation using the maximum likelihood method is computationally expensive, here, the method of moments is employed to initialise an iterative algorithm for the maximisation of the pseudo-likelihood function.

Method of moments

In order to estimate the parameters $\boldsymbol{\mu}$, $\boldsymbol{\kappa}$, $\boldsymbol{\Lambda}$ for a n-dimensional multivariate von Misses distribution (at n forcing points), at point i, an estimate of $\hat{\mu}_i = \overline{x}_{0i}, \quad i \in [1, 2, ...n]$ where $\overline{x}_{0i}$ is the circular mean of the observed directional data $\boldsymbol{\theta}_i$. In the particular case of highly concentrated data, the matrices of concentrations $\boldsymbol{\kappa}$ and accuracies $\boldsymbol{\Lambda}$ are approximated from the circular covariance matrix $\boldsymbol{\Sigma}$ of the directional data matrix $\boldsymbol{\theta} = [\boldsymbol{\theta}_1, \boldsymbol{\theta}_2, ...\boldsymbol{\theta}_n]$:

$$\left(\boldsymbol{\Sigma}^{-1}\right)_{ii} = \kappa_i, \quad \left(\boldsymbol{\Sigma}^{-1}\right)_{ij} = -\lambda_{ij} \quad \text{if} \quad i \neq j \qquad \text{(C.9)}$$

The estimation of the covariance matrix $\hat{\boldsymbol{\Sigma}} = \overline{\boldsymbol{S}}$ by the method of moments is:

$$\overline{S}_{ij} = \frac{1}{n} \sum_{r=1}^{n} \sin(\theta_{ir} - \overline{x}_{0i}) \sin(\theta_{jr} - \overline{x}_{oj}) \tag{C.10}$$

Method of maximum pseudo-likelihood

Maximum pseudo-likelihood estimation (Besag, 1975) is based on conditional probabilities instead of the full density function. As such, the iterative calculation of the unknown normalisation constant at each step is avoided, saving computational time. The conditional probability distribution has the advantage that it's parameters are known a priori as it has the structure of a univariate von Mises distribution, (Equation C.11).

The pseudo-likelihood oestimator of an n-variate von Mises distribution, for a sample of m elements is:

$$PL = (2\pi)^{-pn} \prod_{j=1}^{n} \prod_{i=1}^{m} [I_o(\kappa_{j,rest}^{(i)})]^{-1} \exp[\kappa_{j,rest}^{(i)} \cos(\theta_{ji} - \mu_{j,rest}^{(i)})] \tag{C.11}$$

where for the $i - th$ observation, the coefficients of the conditional distribution are calculated as a function of the model parameters:

$$
\begin{aligned}
\mu_{j,rest}^{(i)} &= \mu_j + \tan^{-1}\left\{ \left[\sum_{l \neq j} \lambda_{jl} \sin(\theta_{li} - \mu_l) \right] / \kappa_j \right\} \\
\kappa_{j,rest}^{(i)} &= \left\{ \kappa_j^2 + \left[\sum_{l \neq j} \lambda_{jl} \sin(\theta_{li} - \mu_l) \right]^2 \right\}^{1/2}
\end{aligned} \tag{C.12}
$$

The inference of the model parameters consists of maximising the pseudo-likelihood (PL) function with respect to the $n+n(n+1)/2$ unknown parameters. PL maximisation is complex and computationally expensive. There are several methods in the literature used for multivariate maximisation, amongst them, the interior point method has been implemented via the Matlab builtin function `fmincon`.

C.1.2. Peak period module

The relationship between the mean wave period Tm and the peak period T_p is characterised by a progressive increase in variance. The assumption of heteroscedasticity is that T_m and T_p values follows a potential relationship, being the relationship between the variance of T_p and T_m linear. T_p is assumed to follow a normal distribution $T_p \sim \Phi(\mu_{T_p}, \sigma_{T_p})$.

$$\mu_{T_p} = a\mu_{T_m}^b, \quad \text{and} \quad \sigma_{T_p} = c\mu_{T_m} \tag{C.13}$$

So as to determine the coefficients a, b and c, the $T_m - T_p$ sample is divided into subsets for which the μ and σ statistics are calculated. Then, Equation C.13 is applied by fitting the pairs of values $\mu_{T_m} - \mu_{T_p}$ and $\mu_{T_m} - \sigma_{T_p}$

C.2. Synthetic emulation of storms

The synthetic generation starts from the MME based on Gaussian copulas from which a random vector of H_s, T_m, link Dir and SS is drawn. For this purpose, a random vector is drawn from the multivariate normal distribution $\Phi(0, \boldsymbol{\Sigma_l})$, where $\boldsymbol{\Sigma_l}$ is the correlation matrix of month l. A random realisation k, $[H_{s1}, H_{s2} \ldots, H_{sn}, T_{m1}, T_{m2}, \ldots, T_{mn}, Dir_j, SS_1]_k$ is obtained by inversely entering the marginals of each variable with the random vector from the $\Phi(0, \boldsymbol{\Sigma_l})$ distribution. The conditional link to the MDM is made via the variable Dir_j. Directions $Dir_{i\neq j}$ are obtained from the MDM by randomly extracting a realisation of the conditional density function $f_{Dir_{i\neq j}|Dir_j}(Dir_{i\neq j}|Dir_j)$. The density function conditioned on Dir_j are derived from the n-variate density function $f_{\boldsymbol{\theta}}(\boldsymbol{\theta})$ according to Equation C.14. The procedure based on conditional distributions is like the Gibbs sampling, which belongs to the family of Markov chain Monte Carlo (MCMC) methods.

$$f_{Dir_{i\neq j}|Dir_j}(Dir_{i\neq j}|Dir_j) = \frac{f_{\boldsymbol{\theta}}(\boldsymbol{\theta})}{f_{Dir_j}(Dir_j)} \tag{C.14}$$

T_p is obtained from the calibrated heteroscedastic model by means of T_m and T_p observations. Once T_m is known and assuming it is equal to μ_{T_m}, μ_{T_p} and σ_{T_m} can be calculated with Eq. S14. Then, T_p is obtained by drawing a random number from the distribution $\Phi(\mu_{T_p}, \sigma_{T_m})$. Finally, as AT is assumed to behave in a deterministic way,

it is randomly sampled from the *AT* time-series of month l from the GOT database.

APPENDIX D

CALIBRATION OF THE FLOOD MODELLING SUITE

On 19 January 2020, Storm Gloria hit Spain causing flooding and damage to the waterfront along the Mediterranean coastal stretch, affecting the study area. Storm Gloria was characterised by 0.25 m storm surges, significant wave heights of 5.5 m and peak periods up to 12 s (offshore conditions). Storm Gloria was simulated in order to calibrate XBeach (Roelvink et al., 2009) by comparing with flood extents and water marks obtained from satellite images and newspaper archives. For that purpose, nearshore waves of Chapter 3 at a resolution of 50 m (0.00045°) from the ERA5 hindcast (0.08°), storm surges from the ERA5 hindcast (0.08°) and reconstructed astronomical tides were used.

Water extent envelopes associated with Storm Gloria were used to calibrate the flood model suite composed by XBeach and RFSM-EDA (Jamieson et al., 2012). Satellite images from the Sentinel-2 campaign and discrete water marks from newspapers and publicly available videos that were recorded during the extreme event were used to delineate the water reach. Then, a sensitivity analysis was performed to get the XBeach parametrization that yielded the flood extent that best fitted the observations. The

following set of parameters was chosen: γ=0.5, $facAs$=0.1, $facSk$=0.1, $gwflow$=0, $wetslp$=0.3, and $sedcal$=1; where γ is the breaker parameter, $facAs$ is the calibration factor of time-averaged flows due to wave asymmetry, $facSk$ is the calibration factor of time-averaged flows due to wave skewness, $gwflow$ is the option for groundwater flow, $wetslp$ is the critical slope for underwater avalanching and $sedcal$ is the sediment transport coefficient. Maximum water heights modelled and the flood extent for the optimal set of parameters are displayed in Figure D.1 against the observed water-reach marks at different beaches in the study area.
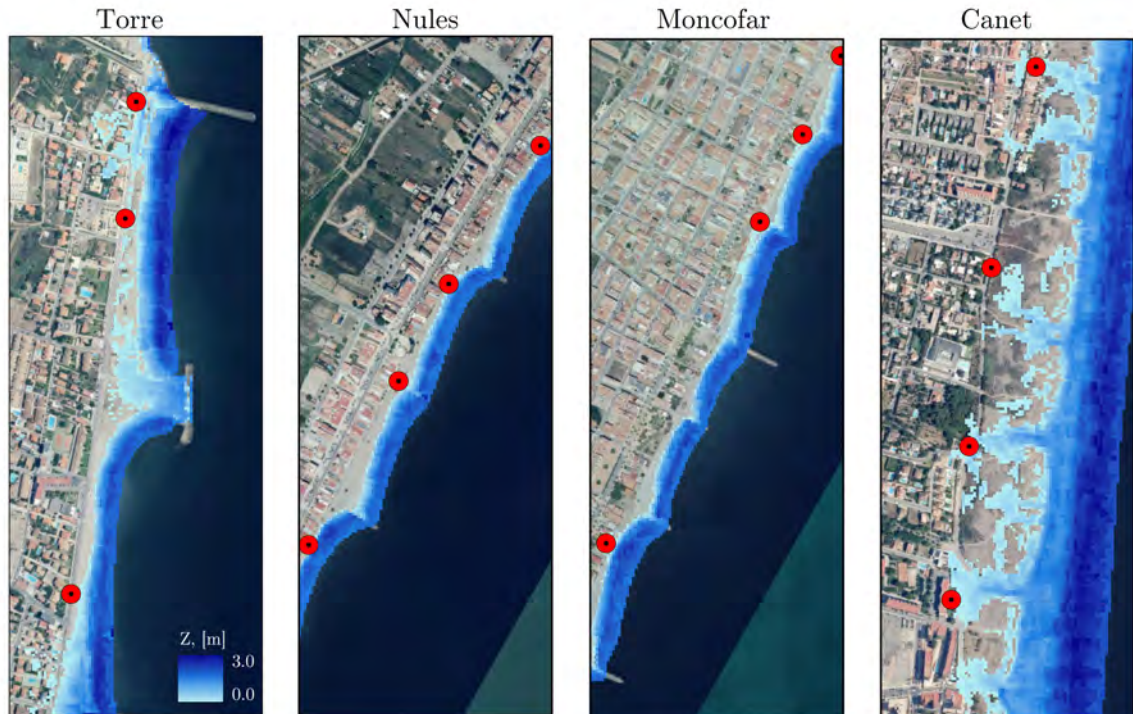
Figure D.1: Water height and flooding extent in Torre, Nules, Moncófar and Canet and the reference watermarks (red circles) at the peak of Storm Gloria.

APPENDIX E

SCIENTIFIC CONTRIBUTIONS DERIVED FROM THE PRESENT DISSERTATION

Peer-reviewed articles directly linked to the doctoral thesis:

1. Alvarez-Cuesta, M., Toimil, A., and Losada, I. J. 2021. Modelling long-term shoreline evolution in highly anthropized coastal areas. Part 1: Model description and validation. *Coastal Engineering,* 169(July):103960

2. Alvarez-Cuesta, M., Toimil, A., and Losada, I. J. 2021. Modelling long-term shoreline evolution in highly anthropized coastal areas. Part 2: Assessing the response to climate change. *Coastal Engineering,* 168(July):103961

3. Toimil, A., Alvarez-Cuesta, M. and Losada, I. J. 2022. Neglecting the coupled effect of coastal flooding and erosion can lead to spurious impact projections and maladaptation. *Under review in Coastal Engineering.* Submitted on April 2022.

Collaborations in peer-reviewed articles related to the topic of the thesis:

1. Thiéblemont, R., Le Cozannet, G., Rohmer, J., Toimil, A., Alvarez-Cuesta, M., Losada, I. J. 2021. Deep uncertainties in shoreline change projections: an extra-probabilistic approach applied to sandy beaches. *Natural Hazards and Earth*

System Sciences, 2015(January):1-24

2. Toimil, A., Camus, P., Losada, I., Alvarez-Cuesta, M., 2021. Visualising the uncertainty cascade in multi-ensemble probabilistic coastal erosion projections. *Frontiers in Marine Science*, 8(June):1-19

Oral presentations attended during the doctoral thesis:

1. Alvarez-Cuesta, M., Toimil, A., Losada, I. J. 2020. Una herramienta para el modelado de la evolución de la línea de costa en zonas fuertemente antropizadas en un clima incierto. *IV Congreso Transfronterizo sobre el Cambio Climático y Litoral (UHINAK).* Online meeting.

2. Alvarez-Cuesta, M., Toimil, A., Losada, I. J. 2021. Forecasting the shoreline evolution at highly anthropized coastal areas. *European Geosciences Union, EGU.* Online meeting.

3. Thiéblemont, R., Le Cozannet, G., Rohmer, J., Toimil, A., Alvarez-Cuesta, M., Losada, I. J. 2021. Deep uncertainties in shoreline change projections: an extra-probabilistic approach applied to sandy beaches. *European Geosciences Union, EGU.* Online meeting.

4. Toimil, A., Alvarez-Cuesta, M., Losada, I. J. 2021. On the need for uncertainty consideration in coastal erosion projections to support adaptation planning. *American Geophysical Union (AGU) .* Online meeting.

5. Alvarez-Cuesta, M., Toimil, A., Losada, I. J. 2022. IH-LANS: Una herramienta para el modelado de la línea de costa. *XVI Jornadas Españolas de Ingeniería de Costas y Puertos.* Vigo, Spain.

6. Alvarez-Cuesta, M., Toimil, A., Losada, I. J. 2022. Reduced-complexity modelling as a valuable tool to study the coastal impacts of climate change. *European Geosciences Union, EGU.* Online meeting.

BIBLIOGRAPHY

Almar, R., Ranasinghe, R., Bergsma, E. W., Diaz, H., Melet, A., Papa, F., Vousdoukas, M., Athanasiou, P., Dada, O., Almeida, L. P., et al. (2021). A global analysis of extreme coastal water levels with implications for potential coastal overtopping. *Nature Communications*, 12(1):1–9.

Alvarez-Cuesta, M., Toimil, A., and Losada, I. J. (2021a). Modelling long-term shoreline evolution in highly anthropized coastal areas . Part 1 : Model description and validation. *Coastal Engineering*, 169(July):103960.

Alvarez-Cuesta, M., Toimil, A., and Losada, I. J. (2021b). Modelling long-term shoreline evolution in highly anthropized coastal areas . Part 2 : Assessing the response to climate change. *Coastal Engineering*, 168(July):103961.

Anderson, D. L., Ruggiero, P., Mendez, F. J., Barnard, P. L., Erikson, L. H., O'Neill, A. C., Merrifield, M., Rueda, A., Cagigal, L., and Marra, J. (2021). Projecting climate dependent coastal flood risk with a hybrid statistical dynamical model. *Earth's Future*, pages 1–24.

Antolínez, J. A., Méndez, F. J., Anderson, D., Ruggiero, P., and Kaminsky, G. M. (2019). Predicting climate-driven coastlines with a simple and efficient multiscale model. *Journal of Geophysical Research: Earth Surface*, 124(6):1596–1624.

Aragonés, L., Serra, J. C., Villacampa, Y., Saval, J. M., and Tinoco, H. (2016). New methodology for describing the equilibrium beach profile applied to the Valencia's beaches. *Geomorphology*, 259:1–11.

Ashton, A., Murray, A. B., and Amoult, O. (2001). Formation of coastline features by large-scale instabilities induced by high-angle waves. *Nature*, 414(6872):296–300.

Ashton, A. D. and Murray, A. B. (2006). High-angle wave instability and emergent shoreline shapes: 1. Modeling of sand waves, flying spits, and capes. *Journal of Geophysical Research: Earth Surface*, 111(4).

Athanasiou, P., van Dongeren, A., Giardino, A., Vousdoukas, M., Gaytan-Aguilar, S., and Ranasinghe, R. (2019). Global distribution of nearshore slopes with implications for coastal retreat. *Earth System Science Data Discussions*, pages 1–29.

Athanasiou, P., van Dongeren, A., Giardino, A., Vousdoukas, M. I., Ranasinghe, R., and Kwadijk, J. (2020). Uncertainties in projections of sandy beach erosion due to sea level rise: an analysis at the European scale. *Scientific Reports*, 10(1):1–14.

Atkinson, A. L. and Baldock, T. E. (2020). Laboratory investigation of nourishment options to mitigate sea level rise induced erosion. *Coastal Engineering*, 161(November 2019):103769.

Atkinson, A. L., Baldock, T. E., Birrien, F., Callaghan, D. P., Nielsen, P., Beuzen, T., Turner, I. L., Blenkinsopp, C. E., and Ranasinghe, R. (2018). Laboratory investigation of the Bruun Rule and beach response to sea level rise. *Coastal Engineering*, 136(December 2017):183–202.

Bamunawala, J., Dastgheib, A., Ranasinghe, R., van der Spek, A., Maskey, S., Murray, A. B., Duong, T. M., Barnard, P. L., and Sirisena, T. A. (2020). A holistic modeling approach to project the evolution of inlet-interrupted coastlines over the 21st Century. *Frontiers in Marine Science*, 7(July):1–20.

Barnard, P. L., Erikson, L. H., Foxgrover, A. C., Hart, J. A. F., Limber, P., O'Neill, A. C., van Ormondt, M., Vitousek, S., Wood, N., Hayden, M. K., et al. (2019). Dynamic flood modeling essential to assess the coastal impacts of climate change. *Scientific Reports*, 9(1):1–13.

Bates, P. D. and De Roo, A. (2000). A simple raster-based model for flood inundation simulation. *Journal of Hydrology*, 236(1-2):54–77.

Bauer, P., Stevens, B., and Hazeleger, W. (2021). A digital twin of earth for the green transition. *Nature Climate Change*, 11(2):80–83.

Beck, M. W., Losada, I. J., Menéndez, P., Reguero, B. G., Díaz-Simal, P., and Fernández, F. (2018). The global flood protection savings provided by coral reefs. *Nature Communications*, 9(1):1–9.

Benavente, J., Del Río, L., Gracia, F. J., and Martínez-del Pozo, J. A. (2006). Coastal flooding hazard related to storms and coastal evolution in valdelagrana spit (cadiz bay natural park, sw spain). *Continental Shelf Research*, 26(9):1061–1076.

Bergillos, R. J., Masselink, G., and Ortega-Sánchez, M. (2017). Coupling cross-shore and longshore sediment transport to model storm response along a mixed sand-gravel coast under varying wave directions. *Coastal Engineering*, 129:93–104.

Besag, J. (1975). Statistical analysis of non-lattice data. *Journal of the Royal Statistical Society: Series D (The Statistician)*, 24(3):179–195.

Beuzen, T., Turner, I. L., Blenkinsopp, C. E., Atkinson, A., Flocard, F., and Baldock, T. E. (2018). Physical model study of beach profile evolution by sea level rise in the presence of seawalls. *Coastal Engineering*, 136(December 2017):172–182.

Bloemendaal, N., de Moel, H., Martinez, A. B., Muis, S., Haigh, I. D., van der Wiel, K., Haarsma, R. J., Ward, P. J., Roberts, M. J., Dullaart, J. C., et al. (2022). A globally consistent local-scale assessment of future tropical cyclone risk. *Science Advances*, 8(17):eabm8438.

Booij, N., Ris, R. C., and Holthuijsen, L. H. (1999). A third-generation wave model for coastal regions 1. Model description and validation. *Journal of Geophysical Research: Oceans*, 104(C4):7649–7666.

Brown, S., Nicholls, R. J., Hanson, S., Brundrit, G., Dearing, J. A., Dickson, M. E., Gallop, S. L., Gao, S., Haigh, I. D., Hinkel, J., et al. (2014). Shifting perspectives on coastal impacts and adaptation. *Nature Climate Change*, 4(9):752–755.

Bruun, P. (1962). Sea-level Rise as a cause of shore erosion. *J. Waterw. Harb. Div.*, 88(1):132.

Camus, P., Losada, I., Izaguirre, C., Espejo, A., Menéndez, M., and Pérez, J. (2017). Statistical wave climate projections for coastal impact assessments. *Earth's Future*, 5(9):918–933.

Camus, P., Mendez, F. J., Medina, R., and Cofiño, A. S. (2011). Analysis of clustering and selection algorithms for the study of multivariate wave climate. *Coastal Engineering*, 58(6):453–462.

Camus, P., Mendez, F. J., Medina, R., Tomas, A., and Izaguirre, C. (2013). High resolution downscaled ocean waves (DOW) reanalysis in coastal areas. *Coastal Engineering*, 72:56–68.

Cazenave, A. and Cozannet, G. L. (2014). Sea level rise and its coastal impacts. *Earth's Future*, 2(2):15–34.

Cheng, Z., Hsu, T. J., and Calantoni, J. (2017). SedFoam: A multi-dimensional Eulerian two-phase model for sediment transport and its application to momentary bed failure. *Coastal Engineering*, 119:32–50.

Collins, M., Sutherland, M., Bouwer, L., Cheong, S.-M., Frölicher, T., Jacot Des Combes, H., Koll Roxy, M., Losada, I. J., McInnes, K., Ratter, B., Rivera-Arriaga, E., Susanto, R. D., Swingedouw, D., and Tibig, L. (2019). Extremes, Abrupt Changes and Managing Risk. In *IPCC Special Report on the Ocean and Cryosphere in a Changing Climate* [Pörtner, H-O. et al. (eds.)], pages 589–655. Cambridge University Press, Cambridge, United Kingdom and New York, NY, USA.

Cooke, B. C., Jones, A. R., Goodwin, I. D., and Bishop, M. J. (2012). Nourishment practices on Australian sandy beaches: A review. *Journal of Environmental Management*, 113:319–327.

Cooper, J. A. G. and Pilkey, O. H. (2004). Sea-level rise and shoreline retreat: Time to abandon the Bruun Rule. *Global and Planetary Change*, 43(3-4):157–171.

Dabees, M. A. (2000). Efficient modeling of beach evolution. *Ph.D. Thesis, Queen´s University, Kingston, Ontario, Canada.*

d'Angremond, K., Van Der Meer, J. W., and De Jong, R. J. (1996). Wave transmission at low-crested structures. *Coastal Engineering Proceedings*, (25).

d'Anna, M., Castelle, B., Idier, D., Rohmer, J., Le Cozannet, G., Thieblemont, R., and Bricheno, L. (2021). Uncertainties in shoreline projections to 2100 at truc vert

beach (france): Role of sea-level rise and equilibrium model assumptions. *Journal of Geophysical Research: Earth Surface*, 126(8):e2021JF006160.

d'Anna, M., Idier, D., Castelle, B., Le Cozannet, G., Rohmer, J., and Robinet, A. (2020). Impact of model free parameters and sea-level rise uncertainties on 20-years shoreline hindcast: the case of Truc Vert beach (France). *Earth Surface Processes and Landforms*, (March).

d'Anna, M., Idier, D., Castelle, B., Rohmer, J., Cagigal, L., and Mendez, F. (2022a). Effects of stochastic wave forcing on probabilistic equilibrium shoreline response across the 21st century including sea-level rise. *Coastal Engineering*, 175:104149.

d'Anna, M., Idier, D., Castelle, B., Rohmer, J., Cagigal, L., and Mendez, F. (2022b). Effects of stochastic wave forcing on probabilistic equilibrium shoreline response across the 21st century including sea-level rise. *Coastal Engineering*, 175:104149.

Davidson, M. A., Turner, I. L., Splinter, K. D., and Harley, M. D. (2017). Annual prediction of shoreline erosion and subsequent recovery. *Coastal Engineering*, 130(October):14–25.

Dawson, R. J., Dickson, M. E., Nicholls, R. J., Hall, J. W., Walkden, M. J., Stansby, P. K., Mokrech, M., Richards, J., Zhou, J., Milligan, J., et al. (2009). Integrated analysis of risks of coastal flooding and cliff erosion under scenarios of long term change. *Climatic Change*, 95(1):249–288.

de Santiago, I., Camus, P., Gonzalez, M., Liria, P., Epelde, I., Chust, G., del Campo, A., and Uriarte, A. (2021). Impact of climate change on beach erosion in the Basque Coast, NE Spain. *Coastal Engineering*, 167:103916.

de Vriend, H. J., Capobianco, M., Chesher, T., de Swart, H. E., Latteux, B., and Stive, M. J. (1993). Approaches to long-term modelling of coastal morphology: A review. *Coastal Engineering*, 21(1-3):225–269.

Dean, R. G. (1991). Equilibrium beach profiles: characteristics and applications. *Journal of Coastal Research*, 7(1):53–84.

del Valle, R., Medina, R., and Losada, M. Á. (1993). Dependence of coefficient K on grain size. *Journal of Waterway, Port, Coastal and Ocean Engineering*, 119(5):568–574.

Duarte, C. M., Losada, I. J., Hendriks, I. E., Mazarrasa, I., and Marbà, N. (2013). The role of coastal plant communities for climate change mitigation and adaptation. *Nature Climate Change*, 3(11):961–968.

Dullaart, J., Muis, S., Bloemendaal, N., Chertova, M. V., Couasnon, A., and Aerts, J. C. (2021). Accounting for tropical cyclones more than doubles the global population exposed to low-probability coastal flooding. *Communications Earth & Environment*, 2(1):1–11.

Egbert, G. D. and Erofeeva, S. Y. (2002). Efficient inverse modeling of barotropic ocean tides. *Journal of Atmospheric and Oceanic Technology*, 19(2):183–204.

Erikson, L. H., O'Neill, A., Barnard, P. L., Vitousek, S., and Limber, P. (2017). Climate change-driven cliff and beach evolution at decadal to centennial time scales. *Coastal Dynamics 2017*, pages 125–136.

Escudero, M., Reguero, B. G., Mendoza, E., Secaira, F., and Silva, R. (2021). Coral reef geometry and hydrodynamics in beach erosion control in North Quintana Roo, Mexico. *Frontiers in Marine Science*, 8(September):1–17.

Evensen, G. (2003). The Ensemble Kalman Filter: Theoretical formulation and practical implementation. *Ocean Dynamics*, 53(4):343–367.

Falqués, A., Garnier, R., Ojeda, E., Ribas, F., and Guillen, J. (2008). Q2D-morfo: A medium to long term model for beach morphodynamics. *River, Coastal and Estuarine Morphodynamics: RCEM 2007 - Proceedings of the 5th IAHR Symposium on River, Coastal and Estuarine Morphodynamics*, 1:71–78.

Fasullo, J. T., Nerem, R., and Hamlington, B. (2016). Is the detection of accelerated sea level rise imminent? *Scientific Reports*, 6(1):1–7.

Filipot, J.-F. and Cheung, K. F. (2012). Spectral wave modeling in fringing reef environments. *Coastal Engineering*, 67:67–79.

García-Maribona, J., Lara, J. L., Maza, M., and Losada, I. J. (2021). An efficient RANS numerical model for cross-shore beach processes under erosive conditions. *Coastal Engineering*, 170:103975.

Gharagozlou, A., Dietrich, J. C., Karanci, A., Luettich, R. A., and Overton, M. F. (2020). Storm-driven erosion and inundation of barrier islands from dune-to region-scales. *Coastal Engineering*, 158:103674.

Goda, Y. (1985). *Random seas and design of maritime structures*, volume 33. University of Tokio Press.

Goldstein, E. B., Coco, G., and Plant, N. G. (2019). A review of machine learning applications to coastal sediment transport and morphodynamics. *Earth-Science Reviews*, 194(April):97–108.

Gomes da Silva, P., Coco, G., Garnier, R., and Klein, A. H. (2020). On the prediction of runup, setup and swash on beaches. *Earth-Science Reviews*, 204(October 2019):103148.

Gomes da Silva, P., Medina, R., González, M., and Garnier, R. (2018). Infragravity swash parameterization on beaches: The role of the profile shape and the morphodynamic beach state. *Coastal Engineering*, 136:41–55.

Gori, A., Lin, N., Xi, D., and Emanuel, K. (2022). Tropical cyclone climatology change greatly exacerbates US extreme rainfall-surge hazard. *Nature Climate Change*, 12(2):171–178.

Gouldby, B., Sayers, P., Mulet-Marti, J., Hassan, M., and Benwell, D. (2008). A methodology for regional-scale flood risk assessment. In *Proceedings of the Institution of Civil Engineers-Water Management*, volume 161, pages 169–182. Thomas Telford Ltd.

Grases, A., Gracia, V., García-León, M., Lin-Ye, J., and Sierra, J. P. (2020). Coastal flooding and erosion under a changing climate: Implications at a low-lying coast (Ebro Delta). *Water (Switzerland)*, 12(2).

Grilli, A., Spaulding, M. L., Oakley, B. A., and Damon, C. (2017). Mapping the coastal risk for the next century, including sea level rise and changes in the coastline: application to charlestown ri, usa. *Natural Hazards*, 88(1):389–414.

Gutierrez, B. T., Plant, N. G., and Thieler, E. R. (2011). A bayesian network to predict coastal vulnerability to sea level rise. *Journal of Geophysical Research: Earth Surface*, 116(F2).

Haigh, I. D., Pickering, M. D., Green, J. M., Arbic, B. K., Arns, A., Dangendorf, S., Hill, D. F., Horsburgh, K., Howard, T., Idier, D., et al. (2020). The tides they are a-changin': A comprehensive review of past and future nonastronomical changes in tides, their driving mechanisms, and future implications. *Reviews of Geophysics*, 58(1):e2018RG000636.

Hallegatte, S., Green, C., Nicholls, R. J., and Corfee-Morlot, J. (2013). Future flood losses in major coastal cities. *Nature Climate Change*, 3(9):802–806.

Hallermeier, R. J. (1980). A profile zonation for seasonal sand beaches from wave climate. *Coastal Engineering*, 4(C):253–277.

Hanson, H. (1989). Genesis: A Generalized Shoreline Change Numerical Model. *Journal of Coastal Research*, 5(1):1–27.

Hanson, H. and Kraus, N. C. (1986). Seawall constraint in shoreline numerical model. *Journal of Waterway, Port, Coastal and Ocean Engineering*, 1(6):1079–1083.

Hanson, H. and Kraus, N. C. (1989). Genesis: Generalized model for simulating shoreline change, report 1, technical reference / by Hans Hanson and Nicholas C. Kraus. Technical report.

Hay, C. C., Morrow, E., Kopp, R. E., and Mitrovica, J. X. (2015). Probabilistic reanalysis of twentieth-century sea-level rise. *Nature*, 517(7535):481–484.

Haykin, S. S. and Haykin, S. S. (2001). *Kalman filtering and neural networks*, volume 284. Wiley Online Library.

Heffernan, J. E. and Tawn, J. A. (2004). A conditional approach for multivariate extreme values. *Journal of the Royal Statistical Society. Series B: Statistical Methodology*, 66(3):497–546.

Hemer, M. A., Fan, Y., Mori, N., Semedo, A., and Wang, X. L. (2013). Projected changes in wave climate from a multi-model ensemble. *Nature Climate Change*, 3(5):471–476.

Hermans, T. H., Gregory, J. M., Palmer, M. D., Ringer, M. A., Katsman, C. A., and Slangen, A. B. (2021). Projecting global mean sea-level change using CMIP6 models. *Geophysical Research Letters*, 48(5):e2020GL092064.

Hinkel, J., Nicholls, R. J., Tol, R. S., Wang, Z. B., Hamilton, J. M., Boot, G., Vafeidis, A. T., McFadden, L., Ganopolski, A., and Klein, R. J. (2013). A global analysis of erosion of sandy beaches and sea-level rise: An application of DIVA. *Global and Planetary Change*, 111:150–158.

Hsu, J. R. and Silvester, R. (1990). Accretion behind single offshore breakwater. *Journal of Waterway, Port, Coastal and Ocean Engineering*, 116(3):362–380.

Hurst, M. D., Barkwith, A., Ellis, M. A., Thomas, C. W., and Murray, A. B. (2015). Exploring the sensitivities of crenulate bay shorelines to wave climates using a new vector-based one-line model. *Journal of Geophysical Research F: Earth Surface*, 120(12):2586–2608.

Ibaceta, R., Splinter, K. D., Harley, M. D., and Turner, I. L. (2020). Enhanced coastal shoreline modeling using an ensemble Kalman filter to include nonstationarity in future wave climates. *Geophysical Research Letters*, 47(22):1–12.

Idier, D., Paris, F., Le Cozannet, G., Boulahya, F., and Dumas, F. (2017). Sea-level rise impacts on the tides of the European Shelf. *Continental Shelf Research*, 137:56–71.

IHCantabria (2020). High-resolution projections of waves and water levels along the Spanish Coast. *Ministerio para La transición ecológica y el reto demográfico*.

Jamieson, S. R., Lhomme, J., Wright, G., and Gouldby, B. (2012). A highly efficient 2D flood model with sub-element topography. In *Proceedings of the Institution of Civil Engineers-Water Management*, volume 165, pages 581–595. Thomas Telford Ltd.

Jaramillo, C., Jara, M. S., González, M., and Medina, R. (2020). A shoreline evolution model considering the temporal variability of the beach profile sediment volume (sediment gain / loss). *Coastal Engineering*, 156(May 2019).

Jaramillo, C., Jara, M. S., González, M., and Medina, R. (2021). A shoreline evolution model for embayed beaches based on cross-shore, planform and rotation equilibrium models. *Coastal Engineering*, 169:103983.

Jevrejeva, S., Jackson, L. P., Riva, R. E., Grinsted, A., and Moore, J. C. (2016). Coastal sea level rise with warming above 2°C. *Proceedings of the National Academy of Sciences*, 113(47):13342–13347.

Jiménez, J. A. and Sánchez-Arcilla, A. (2004). A long-term (decadal scale) evolution model for microtidal barrier systems. *Coastal Engineering*, 51(8-9):749–764.

Jones, B. and O'Neill, B. C. (2016). Spatially explicit global population scenarios consistent with the shared socioeconomic pathways. *Environmental Research Letters*, 11(8):084003.

Kaergaard, K. and Fredsoe, J. (2013). A numerical shoreline model for shorelines with large curvature. *Coastal Engineering*, 74:19–32.

Kamphius, W. (1993). Alongshore sediment transport rate. *Journal of Waterway, Port, Coastal and Ocean Engineering*, 119(3):344–346.

Kamphius, W. (2000). *Introduction to Coastal Engineering and Management*. World Scientific, Singapore.

Karunarathna, H., Horrillo-Caraballo, J., Kuriyama, Y., Mase, H., Ranasinghe, R., and Reeve, D. E. (2016). Linkages between sediment composition, wave climate and beach profile variability at multiple timescales. *Marine Geology*, 381:194–208.

Kinsela, M. A., Morris, B. D., Linklater, M., and Hanslow, D. J. (2017). Second-pass assessment of potential exposure to shoreline change in New South Wales, Australia, using a sediment compartments framework. *Journal of Marine Science and Engineering*, 5(4).

Kopp, R. E., Horton, R. M., Little, C. M., Mitrovica, J. X., Oppenheimer, M., Rasmussen, D., Strauss, B. H., and Tebaldi, C. (2014). Probabilistic 21st and 22nd century sea-level projections at a global network of tide-gauge sites. *Earth's future*, 2(8):383–406.

Kriebel, D. L. and Dean, R. G. (1993). Convolution method for time-dependent beach-profile response. *Journal of Waterway, Port, Coastal, and Ocean Engineering*, 119(2):204–226.

Kristensen, S. E., Drønen, N., Deigaard, R., and Fredsoe, J. (2016). Impact of groyne fields on the littoral drift: A hybrid morphological modelling study. *Coastal Engineering*, 111:13–22.

Kroon, A., de Schipper, M. A., van Gelder, P. H., and Aarninkhof, S. G. (2020). Ranking uncertainty: Wave climate variability versus model uncertainty in probabilistic assessment of coastline change. *Coastal Engineering*, 158(February):103673.

Kulp, S. A. and Strauss, B. H. (2019). New elevation data triple estimates of global vulnerability to sea-level rise and coastal flooding. *Nature Communications*, 10(1):1–12.

Le Cozannet, G., Bulteau, T., Castelle, B., Ranasinghe, R., Wöppelmann, G., Rohmer, J., Bernon, N., Idier, D., Louisor, J., and Salas-y Mélia, D. (2019). Quantifying uncertainties of sandy shoreline change projections as sea level rises. *Scientific Reports*, 9(1):1–11.

Leaman, C. K., Harley, M. D., Splinter, K. D., Thran, M. C., Kinsela, M. A., and Turner, I. L. (2021). A storm hazard matrix combining coastal flooding and beach erosion. *Coastal Engineering*, 170:104001.

Leijnse, T., van Ormondt, M., Nederhoff, K., and van Dongeren, A. (2021). Modeling compound flooding in coastal systems using a computationally efficient reduced-physics solver: Including fluvial, pluvial, tidal, wind- and wave-driven processes. *Coastal Engineering*, 163(October 2020):103796.

Lentz, E. E., Thieler, E. R., Plant, N. G., Stippa, S. R., Horton, R. M., and Gesch, D. B. (2016). Evaluation of dynamic coastal response to sea-level rise modifies inundation likelihood. *Nature Climate Change*, 6(7):696–700.

Lesser, G. R., Roelvink, J. A., van Kester, J. A., and Stelling, G. S. (2004). Development

and validation of a three-dimensional morphological model. *Coastal Engineering*, 51(8-9):883–915.

Limber, P. W., Adams, P. N., and Murray, A. B. (2017). Modeling large-scale shoreline change caused by complex bathymetry in low-angle wave climates. *Marine Geology*, 383:55–64.

Limber, P. W., Barnard, P. L., Vitousek, S., and Erikson, L. H. (2018). A model ensemble for projecting multidecadal coastal cliff retreat during the 21st century. *Journal of Geophysical Research: Earth Surface*, 123(7):1566–1589.

Lin-Ye, J., García-León, M., Gràcia, V., Ortego, M., Lionello, P., and Sanchez-Arcilla, A. (2017). Multivariate statistical modelling of future marine storms. *Applied Ocean Research*, 65:192–205.

Lin-Ye, J., Garcia-Leon, M., Gracia, V., and Sanchez-Arcilla, A. (2016). A multivariate statistical model of extreme events: An application to the Catalan coast. *Coastal Engineering*, 117(August):138–156.

Little, C. M., Horton, R. M., Kopp, R. E., Oppenheimer, M., Vecchi, G. A., and Villarini, G. (2015). Joint projections of US East Coast sea level and storm surge. *Nature Climate Change*, 5(12):1114–1120.

Lobeto, H., Menendez, M., and Losada, I. J. (2021a). Future behavior of wind wave extremes due to climate change. *Scientific Reports*, 11(1):1–12.

Lobeto, H., Menendez, M., and Losada, I. J. (2021b). Projections of directional spectra help to unravel the future behavior of wind waves. *Frontiers in Marine Science*, 8:655490.

Long, J. W. and Plant, N. G. (2012). Extended Kalman Filter framework for forecasting shoreline evolution. *Geophysical Research Letters*, 39(13):1–6.

López-Dóriga, U., Jiménez, J. A., Valdemoro, H. I., and Nicholls, R. J. (2019). Impact of sea-level rise on the tourist-carrying capacity of Catalan beaches. *Ocean and Coastal Management*, 170(August 2018):40–50.

Losada, I. J. (2022). Un gemelo digital para apoyar la transformación de la costa española. *Revista de Obras Públicas*, 3635.

Losada, I. J., Toimil, A., Muñoz, A., Garcia-Fletcher, A. P., and Diaz-Simal, P. (2019). A planning strategy for the adaptation of coastal areas to climate change: The Spanish case. *Ocean and Coastal Management*, 182(April):104983.

Lucio, D., Tomás, A., Lara, J. L., Camus, P., and Losada, I. J. (2020). Stochastic modeling of long-term wave climate based on weather patterns for coastal engineering applications. *Coastal Engineering*, 161(January):103771.

Luettich, R. A., Westerink, J. J., Scheffner, N. W., et al. (1992). ADCIRC: an advanced three-dimensional circulation model for shelves, coasts, and estuaries. Report 1, Theory and methodology of ADCIRC-2DD1 and ADCIRC-3DL.

Luijendijk, A., Hagenaars, G., Ranasinghe, R., Baart, F., Donchyts, G., and Aarninkhof, S. (2018). The state of the world's beaches. *Scientific Reports*, 8(1):1–11.

Madsen, O. S., Poon, Y.-K., and Graber, H. C. (1988). Spectral wave attenuation by bottom friction: Theory. *Coastal Engineering Proceedings*, (21):34–34.

Marcos, M., Tsimplis, M. N., and Shaw, A. G. (2009). Sea level extremes in Southern Europe. *Journal of Geophysical Research: Oceans*, 114(C1).

Mardia, K. V., Hughes, G., Taylor, C. C., and Singh, H. (2008). A multivariate von Mises distribution with applications to bioinformatics. *Canadian Journal of Statistics*, 36(1):99–109.

Mardia, K. V., Jupp, P. E., and Mardia, K. (2000). *Directional statistics*, volume 2. Wiley Online Library.

Maspataud, A., Ruz, M. H., and Hequette, A. (2009). Spatial variability in post-storm beach recovery along a macrotidal Barred beach, Southern North Sea. *Journal of Coastal Research*, (SPEC. ISSUE 56):88–92.

McCall, R., de Vries, J. v. T., Plant, N., van Dongeren, A., Roelvink, J., Thompson, D., and Reniers, A. (2010). Two-dimensional time dependent hurricane overwash and erosion modeling at santa rosa island. *Coastal Engineering*, 57(7):668–683.

McCarroll, R. J., Masselink, G., Valiente, N. G., Scott, T., Wiggins, M., Kirby, J.-A., and Davidson, M. (2021). A rules-based shoreface translation and sediment budgeting tool for estimating coastal change: ShoreTrans. *Marine Geology*, 435:106466.

McGranahan, G., Balk, D., and Anderson, B. (2007). The rising tide: assessing the risks of climate change and human settlements in low elevation coastal zones. *Environment and Urbanization*, 19(1):17–37.

Melet, A., Teatini, P., Le Cozannet, G., Jamet, C., Conversi, A., Benveniste, J., and Almar, R. (2020). Earth observations for monitoring marine coastal hazards and their drivers. *Surveys in Geophysics*, 41(6):1489–1534.

Mendez, F. J. and Losada, I. J. (2004). An empirical model to estimate the propagation of random breaking and nonbreaking waves over vegetation fields. *Coastal Engineering*, 51(2):103–118.

Mentaschi, L., Vousdoukas, M., Voukouvalas, E., Sartini, L., Feyen, L., Besio, G., and Alfieri, L. (2016). Non-stationary extreme value analysis: a simplified approach for Earth science applications. *Hydrology and Earth System Sciences Discussions*, (February):1–38.

Mentaschi, L., Vousdoukas, M. I., Pekel, J.-F., Voukouvalas, E., and Feyen, L. (2018). Global long-term observations of coastal erosion and accretion. *Scientific Reports*, 8(1):1–11.

Mil-Homens, J., Ranasinghe, R., van Thiel de Vries, J. S., and Stive, M. J. (2013). Re-evaluation and improvement of three commonly used bulk longshore sediment transport formulas. *Coastal Engineering*, 75:29–39.

Miller, J. K. and Dean, R. G. (2004). A simple new shoreline change model. *Coastal Engineering*, 51(7):531–556.

Mitsuyasu, H., Tasai, F., Suhara, T., Mizuno, S., Ohkusu, M., Honda, T., and Rikiishi, K. (1975). Observations of the directional spectrum of ocean waves using a cloverleaf buoy. *Journal of Physical Oceanography*.

Montaño, J., Coco, G., Antolínez, J. A., Beuzen, T., Bryan, K. R., Cagigal, L., Castelle, B., Davidson, M. A., Goldstein, E. B., Ibaceta, R., Idier, D., Ludka, B. C., Masoud-Ansari, S., Méndez, F. J., Murray, A. B., Plant, N. G., Ratliff, K. M., Robinet, A., Rueda, A., Sénéchal, N., Simmons, J. A., Splinter, K. D., Stephens, S., Townend, I., Vitousek, S., and Vos, K. (2020). Blind testing of shoreline evolution models. *Scientific Reports*, 10(1):1–10.

Montaño, J., Coco, G., Cagigal, L., Mendez, F., Rueda, A., Bryan, K. R., and Harley, M. D. (2021). A multiscale approach to shoreline prediction. *Geophysical Research Letters*, 48(1):1–11.

Muis, S., Apecechea, M. I., Dullaart, J., de Lima Rego, J., Madsen, K. S., Su, J., Yan, K., and Verlaan, M. (2020). A high-resolution global dataset of extreme sea levels, tides, and storm surges, including future projections. *Frontiers in Marine Science*, 7:263.

Muñoz, D. F., Abbaszadeh, P., Moftakhari, H., and Moradkhani, H. (2022). Accounting for uncertainties in compound flood hazard assessment: The value of data assimilation. *Coastal Engineering*, 171:104057.

Narayan, S., Beck, M. W., Reguero, B. G., Losada, I. J., Van Wesenbeeck, B., Pontee, N., Sanchirico, J. N., Ingram, J. C., Lange, G.-M., and Burks-Copes, K. A. (2016). The effectiveness, costs and coastal protection benefits of natural and nature-based defences. *PloS One*, 11(5):e0154735.

Neumann, B., Vafeidis, A. T., Zimmermann, J., and Nicholls, R. J. (2015). Future coastal population growth and exposure to sea-level rise and coastal flooding-a global assessment. *PloS One*, 10(3):e0118571.

Nguyen, T. H., Ricci, S., Fatras, C., Piacentini, A., Delmotte, A., Lavergne, E., and Kettig, P. (2022). Improvement of flood extent representation with remote sensing data and data assimilation. *IEEE Transactions on Geoscience and Remote Sensing*, 60:1–22.

Nicholls, R. J. and Cazenave, A. (2010). Sea-level rise and its impact on coastal zones. *Science*, 328(5985):1517–1520.

OECD (2016). The ocean economy in 2030. *OECD Publishing*.

Oppenheimer, M., Glavovick, B. C., Hinkel, J., van de Wal, R., Magnan, A. K., Abd-Elgawad, A., Cai, R., Cifuenters-Jara, M., DeConto, R. M., Glosh, T., Hay, J., Isla, F., Marzeion, B., Meyssignac, B., and Sebesvari, Z. (2019). Sea Level Rise and Implications for Low-Lying Islands, Coasts and Communities. In *IPCC Special Report on the Ocean and Cryosphere in a Changing Climate* [Pörtner, H-O. et al.

(eds.)]. Cambridge University Press, Cambridge, United Kingdom and New York, NY, USA.

Ozasa, H. and Brampton, A. H. (1980). Mathematical modelling of beaches backed by seawalls. *Coastal Engineering*, 4(C):47–63.

Passeri, D. L., Bilskie, M. V., Plant, N. G., Long, J. W., and Hagen, S. C. (2018). Dynamic modeling of barrier island response to hurricane storm surge under future sea level rise. *Climatic Change*, 149(3):413–425.

Passeri, D. L., Hagen, S. C., Bilskie, M. V., and Medeiros, S. C. (2015). On the significance of incorporating shoreline changes for evaluating coastal hydrodynamics under sea level rise scenarios. *Natural Hazards*, 75(2):1599–1617.

Passeri, D. L., Hagen, S. C., Plant, N. G., Bilskie, M. V., Medeiros, S. C., and Alizad, K. (2016). Tidal hydrodynamics under future sea level rise and coastal morphology in the northern gulf of mexico. *Earth's Future*, 4(5):159–176.

Payo, A., Favis-Mortlock, D., Dickson, M., Hall, J. W., Hurst, M. D., Walkden, M. J., Townend, I., Ives, M. C., Nicholls, R. J., and Ellis, M. A. (2017). Coastal modelling environment version 1.0: a framework for integrating landform-specific component models in order to simulate decadal to centennial morphological changes on complex coasts. *Geoscientific Model Development*, 10(7):2715–2740.

Pelnard-Considère, R. (1956). Essai de theorie de l'evolution des formes de rivage en plages de sable et de galets. *Journées de L'hydraulique*, 4(1):289–298.

Pollard, J., Spencer, T., and Brooks, S. (2019). The interactive relationship between coastal erosion and flood risk. *Progress in Physical Geography: Earth and Environment*, 43(4):574–585.

Ranasinghe, R. (2016). Assessing climate change impacts on open sandy coasts: A review. *Earth-Science Reviews*, 160:320–332.

Ranasinghe, R. (2020). On the need for a new generation of coastal change models for the 21st century. *Scientific Reports*, 10(1):1–6.

Ranasinghe, R., Callaghan, D., and Stive, M. J. (2012). Estimating coastal recession due to sea level rise: Beyond the Bruun rule. *Climatic Change*, 110(3-4):561–574.

Ranasinghe, R., Swinkels, C., Luijendijk, A., Roelvink, D., Bosboom, J., Stive, M., and Walstra, D. J. (2011). Morphodynamic upscaling with the MORFAC approach: Dependencies and sensitivities. *Coastal Engineering*, 58(8):806–811.

Reguero, B. G., Losada, I. J., and Méndez, F. J. (2019). A recent increase in global wave power as a consequence of oceanic warming. *Nature Communications*, 10(1):1–14.

Reguero, B. G., Storlazzi, C., Gibbs, A. E., Shope, J. B., Cole, A. D., Cumming, K. A., and Beck, M. (2021). The value of us coral reefs for flood risk reduction. *Nature Sustainability*, 4:688–698.

Robinet, A., Idier, D., Castelle, B., and Marieu, V. (2018). A reduced-complexity

shoreline change model combining longshore and cross-shore processes: The LX-Shore model. *Environmental Modelling and Software*, 109(August):1–16.

Roelvink, D., Huisman, B., Elghandour, A., Ghonim, M., and Reyns, J. (2020). Efficient modeling of complex sandy coastal evolution at monthly to century time scales. *Frontiers in Marine Science*, 7(July):1–20.

Roelvink, D., Reniers, A., van Dongeren, A., van Thiel de Vries, J., McCall, R., and Lescinski, J. (2009). Modelling storm impacts on beaches, dunes and barrier islands. *Coastal Engineering*, 56(11):1133–1152.

Rueda, A., Camus, P., Tomás, A., Vitousek, S., and Méndez, F. (2016). A multivariate extreme wave and storm surge climate emulator based on weather patterns. *Ocean Modelling*, 104:242–251.

Sallenger, A. H., Doran, K. S., and Howd, P. A. (2012). Hotspot of accelerated sea-level rise on the Atlantic coast of North America. *Nature Climate Change*, 2(12):884–888.

Salvadori, G. and De Michele, C. (2004). Frequency analysis via copulas: Theoretical aspects and applications to hydrological events. *Water resources research*, 40(12).

Sánchez-García, E., Palomar-Vázquez, J. M., Pardo-Pascual, J. E., Almonacid-Caballer, J., Cabezas-Rabadán, C., and Gómez-Pujol, L. (2020). An efficient protocol for accurate and massive shoreline definition from mid-resolution satellite imagery. *Coastal Engineering*, 160:103732.

Sanuy, M. and Jiménez, J. A. (2021). Probabilistic characterisation of coastal storm-induced risks using bayesian networks. *Natural Hazards and Earth System Sciences*, 21(1):219–238.

Sanuy, M., Jiménez, J. A., Ortego, M. I., and Toimil, A. (2020a). Differences in assigning probabilities to coastal inundation hazard estimators: Event versus response approaches. *Journal of flood risk management*, 13:e12557.

Sanuy, M., Jiménez, J. A., and Plant, N. (2020b). A Bayesian Network methodology for coastal hazard assessments on a regional scale: The BN-CRAF. *Coastal Engineering*, 157(April 2019):1–10.

Sayol, J. M. and Marcos, M. (2018). Assessing Flood Risk Under Sea Level Rise and Extreme Sea Levels Scenarios: Application to the Ebro Delta (Spain). *Journal of Geophysical Research: Oceans*, 123(2):794–811.

Shchepetkin, A. F. and McWilliams, J. C. (2005). The regional oceanic modeling system (ROMS): A split-explicit, free-surface, topography-following-coordinate oceanic model. *Ocean Modelling*, 9(4):347–404.

Shi, F., Kirby, J. T., Harris, J. C., Geiman, J. D., and Grilli, S. T. (2012). A high-order adaptive time-stepping tvd solver for boussinesq modeling of breaking waves and coastal inundation. *Ocean Modelling*, 43-44:36–51.

Splinter, K. D. and Coco, G. (2021). Challenges and opportunities in coastal shoreline prediction. *Frontiers in Marine Science*.

Splinter, K. D., Turner, I. L., Davidson, M. A., Barnard, P., Castelle, B., and Oltman-Shay, J. (2014). A generalized equilibrium model for predicting daily to interannual shoreline response. *Journal of Geophysical Research: Earth Surface*, 119(9):1936–1958.

Stive, M. (1998). Morphodynamics of a tidal lagoon and adjacent coast. In *8th International Biennial Conference on Physics of Estuaries and coastal Seas, The Hague, The Netherlands, 1998*.

Stive, M. J., Aarninkhof, S. G., Hamm, L., Hanson, H., Larson, M., Wijnberg, K. M., Nicholls, R. J., and Capobianco, M. (2002). Variability of shore and shoreline evolution. *Coastal Engineering*, 47(2):211–235.

Stockdon, H. F., Holman, R. A., Howd, P. A., and Sallenger, A. H. (2006). Empirical parameterization of setup, swash, and runup. *Coastal Engineering*, 53(7):573–588.

Stripling, S., Panzeri, M., Blanco, B., Rossington, K., Sayers, P., and Borthwick, A. (2017). Regional-scale probabilistic shoreline evolution modelling for flood-risk assessment. *Coastal Engineering*, 121:129–144.

Suh, K. D. and Hardaway, C. S. (1995). Calculation of Tombolo in shoreline numerical model. *Proceedings of the Coastal Engineering Conference*, 3(August):2653–2667.

Suzuki, T., Zijlema, M., Burger, B., Meijer, M. C., and Narayan, S. (2012). Wave dissipation by vegetation with layer schematization in swan. *Coastal Engineering*, 59(1):64–71.

Syvitski, J. P., Kettner, A. J., Overeem, I., Hutton, E. W., Hannon, M. T., Brakenridge, G. R., Day, J., Vörösmarty, C., Saito, Y., Giosan, L., et al. (2009). Sinking deltas due to human activities. *Nature Geoscience*, 2(10):681–686.

Tebaldi, C., Ranasinghe, R., Vousdoukas, M., Rasmussen, D., Vega-Westhoff, B., Kirezci, E., Kopp, R. E., Sriver, R., and Mentaschi, L. (2021). Extreme sea levels at different global warming levels. *Nature Climate Change*, 11(9):746–751.

Thiéblemont, R., Le Cozannet, G., Rohmer, J., Toimil, A., Álvarez-Cuesta, M., and Losada, I. (2021). Deep uncertainties in shoreline change projections: an extra-probabilistic approach applied to sandy beaches. *Natural Hazards and Earth System Sciences*, 2015(January):1–24.

Thiéblemont, R., Le Cozannet, G., Toimil, A., Meyssignac, B., and Losada, I. J. (2019). Likely and high-end impacts of regional sea-level rise on the shoreline change of European sandy coasts under a high greenhouse gas emissions scenario. *Water (Switzerland)*, 11(12).

Toimil, A., Camus, P., Losada, I. J., and Alvarez-Cuesta, M. (2021a). Visualising the uncertainty cascade in multi-ensemble probabilistic coastal erosion projections. *Frontiers in Marine Science*, 8(June):1–19.

Toimil, A., Camus, P., Losada, I. J., Le Cozannet, G., Nicholls, R. J., Idier, D., and Maspataud, A. (2020a). Climate change-driven coastal erosion modelling in tem-

perate sandy beaches: Methods and uncertainty treatment. *Earth-Science Reviews*, 202:103110.

Toimil, A., Díaz-Simal, P., Losada, I. J., and Camus, P. (2018). Estimating the risk of loss of beach recreation value under climate change. *Tourism Management*, 68(March):387–400.

Toimil, A., Losada, I., and Camus, P. (2016). Metodología para el análisis del efecto del cambio climático en la inundación costera: aplicación a Asturias. *Ribagua*, 3(2):56–65.

Toimil, A., Losada, I. J., Camus, P., and Díaz-Simal, P. (2017a). Managing coastal erosion under climate change at the regional scale. *Coastal Engineering*, 128(August):106–122.

Toimil, A., Losada, I. J., Díaz-Simal, P., Izaguirre, C., and Camus, P. (2017b). Multi-sectoral, high-resolution assessment of climate change consequences of coastal flooding. *Climatic Change*, 145(3-4):431–444.

Toimil, A., Losada, I. J., Hinkel, J., and Nicholls, R. J. (2021b). Climate Risk Management Using quantitative dynamic adaptive policy pathways to manage climate change-induced coastal erosion. *Climate Risk Management*, 33(July):100342.

Toimil, A., Losada, I. J., Nicholls, R. J., Dalrymple, R. A., and Stive, M. J. (2020b). Addressing the challenges of climate change risks and adaptation in coastal areas: A review. *Coastal Engineering*, 156(December 2018).

Tolman, H. L. (2009). User manual and system documentation of WAVEWATCH-IIITM version 3.14. *Technical Note*, (3.14):220.

Tonnon, P. K., Huisman, B. J., Stam, G. N., and van Rijn, L. C. (2018). Numerical modelling of erosion rates, life span and maintenance volumes of mega nourishments. *Coastal Engineering*, 131(March 2017):51–69.

Tran, Y. H. and Barthélemy, E. (2020). Combined longshore and cross-shore shoreline model for closed embayed beaches. *Coastal Engineering*, 158(March).

Tsoukala, V., Katsardi, V., Hadjibiros, K., and Moutzouris, C. (2015). Beach erosion and consequential impacts due to the presence of harbours in sandy beaches in greece and cyprus. *Environmental Processes*, 2(1):55–71.

Turner, I. L., Harley, M. D., Almar, R., and Bergsma, E. W. (2021). Satellite optical imagery in coastal engineering. *Coastal Engineering*, 167:103919.

USACE (1984). Shore Protection Manual. *Department of the Army, Waterways Experiment Station, 1*, II.

van Ormondt, M., Nelson, T. R., Hapke, C. J., and Roelvink, D. (2020). Morphodynamic modelling of the wilderness breach, fire island, new york. part i: Model set-up and validation. *Coastal Engineering*, 157:103621.

Van Rijn, L. C. (2014). A simple general expression for longshore transport of sand, gravel and shingle. *Coastal Engineering*, 90:23–39.

Van Wellen, E., Chadwick, A. J., and Mason, T. (2000). A review and assessment of longshore sediment transport equations for coarse-grained beaches. *Coastal Engineering*, 40(3):243–275.

Vitousek, S. and Barnard, P. L. (2015). A nonlinear, implicit one-line model to predict long-term shoreline change. *Proceedings of the Coastal Sediments*, pages 1–14.

Vitousek, S., Barnard, P. L., Fletcher, C. H., Frazer, N., Erikson, L., and Storlazzi, C. D. (2017a). Doubling of coastal flooding frequency within decades due to sea-level rise. *Scientific Reports*, 7(1):1–9.

Vitousek, S., Barnard, P. L., and Limber, P. (2017b). Can beaches survive climate change? *Journal of Geophysical Research: Earth Surface*, 122(4):1060–1067.

Vitousek, S., Barnard, P. L., Limber, P., Erikson, L., and Cole, B. (2017c). A model integrating longshore and cross-shore processes for predicting long-term shoreline response to climate change. *Journal of Geophysical Research: Earth Surface*, 122(4):782–806.

Vitousek, S., Cagigal, L., Montaño, J., Rueda, A., Mendez, F., Coco, G., and Barnard, P. L. (2021). The application of ensemble wave forcing to quantify uncertainty of shoreline change predictions. *Journal of Geophysical Research: Earth Surface*, pages 1–43.

Vos, K., Harley, M. D., Splinter, K. D., Simmons, J. A., and Turner, I. L. (2019). Sub-annual to multi-decadal shoreline variability from publicly available satellite imagery. *Coastal Engineering*, 150(April):160–174.

Vousdoukas, M. I., Mentaschi, L., Hinkel, J., Ward, P. J., Mongelli, I., Ciscar, J.-C., and Feyen, L. (2020a). Economic motivation for raising coastal flood defenses in europe. *Nature Communications*, 11(1):1–11.

Vousdoukas, M. I., Mentaschi, L., Voukouvalas, E., Bianchi, A., Dottori, F., and Feyen, L. (2018a). Climatic and socioeconomic controls of future coastal flood risk in europe. *Nature Climate Change*, 8(9):776–780.

Vousdoukas, M. I., Mentaschi, L., Voukouvalas, E., Verlaan, M., Jevrejeva, S., Jackson, L. P., and Feyen, L. (2018b). Global probabilistic projections of extreme sea levels show intensification of coastal flood hazard. *Nature Communications*, 9(1):1–12.

Vousdoukas, M. I., Ranasinghe, R., Mentaschi, L., Plomaritis, T. A., Athanasiou, P., Luijendijk, A., and Feyen, L. (2020b). Sandy coastlines under threat of erosion. *Nature Climate Change*, 10(3):260–263.

Wahl, T., Plant, N. G., and Long, J. W. (2016). Probabilistic assessment of erosion and flooding risk in the northern gulf of mexico. *Journal of Geophysical Research: Oceans*, 121(5):3029–3043.

Walkden, M. and Hall, J. (2005). A predictive mesoscale model of the erosion and profile development of soft rock shores. *Coastal Engineering*, 52(6):535–563.

Walkden, M. and Hall, J. (2011). A mesoscale predictive model of the evolution and management of a soft-rock coast. *Journal of Coastal research*, 27(3):529–543.

Wang, N., Chen, Q., and Chen, Z. (2022). Reconstruction of nearshore wave fields based on physics-informed neural networks. *Coastal Engineering*, page 104167.

Wong, P. P., Losada, I. J., Gattuso, J.-P., Hinkel, J., Khattabi, A., McInnes, K., Saito, Y., and Sallenger, A. (2014). Coastal systems and low-lying areas. In *Climate Change 2014: Impacts; Adaptation and Vulnerability. Part A: Global and Sectoral Aspects. Contribution of the Working Group II to the Fifth Assesment Report of the Intergovernmental Panel on Climate Change* [Field, C. B. et al (eds.)], pages 361–409. Cambridge University Press. Cambridge, United Kingdom and New York, NY, USA.

Woodruff, J. D., Irish, J. L., and Camargo, S. J. (2013). Coastal flooding by tropical cyclones and sea-level rise. *Nature*, 504(7478):44–52.

Yates, M. L., Guza, R. T., and O'Reilly, W. C. (2009). Equilibrium shoreline response: Observations and modeling. *Journal of Geophysical Research: Oceans*, 114(9):1–16.

Zacharioudaki, A. and Reeve, D. E. (2011). Shoreline evolution under climate change wave scenarios. *Climatic Change*, 108(1):73–105.

Zijlema, M., Stelling, G., and Smit, P. (2011). Swash: An operational public domain code for simulating wave fields and rapidly varied flows in coastal waters. *Coastal Engineering*, 58(10):992–1012.